UNIVERSITY OF SOUTHAMPTON

FACULTY OF ENGINEERING, SCIENCE & MATHEMATICS

OPTOELECTRONICS RESEARCH CENTRE

FIBRE OPTICAL PARAMETRIC DEVICES FOR LARGE FREQUENCY-SHIFT WAVELENGTH CONVERSION

by

Gysbert Johannes van der Westhuizen

Thesis for the degree of Doctor of Philosophy

December 2012

University of Southampton

ABSTRACT

FACULTY OF ENGINEERING, SCIENCE AND MATHEMATICS

OPTOELECTRONICS RESEARCH CENTRE

Doctor of Philosophy

FIBRE OPTICAL PARAMETRIC DEVICES FOR LARGE FREQUENCY-SHIFT WAVELENGTH CONVERSION

by Gysbert Johannes van der Westhuizen

In this thesis, I investigate fibre optical parametric amplifiers (OPA) and oscillators (OPO), in terms of their potential for efficient large frequency-shift wavelength conversion. The underlying physical mechanism of fibre four wave mixing (FWM) offers simultaneous up-conversion and down-conversion in frequency to arbitrary wavelengths, determined by the pump wavelength and chromatic dispersion of the fibre. Using optical pulses from an ytterbium-doped fibre master-oscillator power-amplifier (MOPA), at a wavelength of 1080 nm, I experimentally and numerically evaluate the suitability of various fibres for frequency up-conversion towards the visible spectrum. The use of an Yb-doped fibre source allows for all-fibre integration with fibre optical parametric devices, potentially making it a viable alternative to expensive bulk sources currently employed in the sub-1-µm spectral region.

To accommodate an all-fibre configuration, the first part of the thesis numerically investigates polarization maintaining (PM) as well as higher-order mode fibres for phase-matched FWM at relatively modest pump peak powers (< 1 kW). Experiments using the PM fibre in an OPA configuration, and employing multiple seeding arrangements, are subsequently presented. Here, it is found that the influence of fibre inhomogeneity, coupled with a relatively small parametric bandwidth and competing nonlinear processes, severely impairs the conversion efficiency from the 1080 nm pump wave to the anti-Stokes wave at 840 nm.

The work in the second part of the thesis reports on the use of higher-order dispersion phase-matching in a photonic crystal fibre (PCF). In the OPA configuration, this approach proves more efficient and demonstrates parametric conversion over 142 THz to an anti-Stokes wave at 715 nm. The PCF is also reconfigured into an all-fibre uni-directional ring-cavity OPO, for which the dependence on nonlinear converter length, out-coupling ratio, pump pulse duration and intra-cavity filtering are studied. Using a PCF length of 18 m and 800 ps pump pulses with sub-kW peak powers, this all-fibre OPO demonstrates, what is believed to be, a record in-fibre pump-to-anti-Stokes conversion efficiency in excess of 10% over 142 THz.

Finally, computer simulations, aimed at realising a dispersion engineered PCF for an enhanced parametric gain bandwidth, is carried out for a pump wavelength around 1 µm. PCF designs of this type, using GeO_2-doped core regions, are identified for arbitrary frequency-shift FWM. It is demonstrated that these fibres can enhance the parametric bandwidth by up to three orders of magnitude, which can lead to a significant reduction in the sensitivity of FWM to fibre inhomogeneities. An increased parametric bandwidth should furthermore enable the use of pump sources that are not currently considered to be viable. The fibres are finally also considered in terms of fabrication tolerances.

Table of Contents

List of Figures

List of Tables

List of Abbreviations

AS	Anti-Stokes
AWG	Arbitrary Waveform Generator
BPF	Band-Pass Filter
CW	Continuous Wave
DC	Double-Clad
DSF	Dispersion-Shifted Fibre
EDFA	Erbium-Doped Fibre Amplifier
EM	Electromagnetic
EOM	Electro-Optic Modulator
ESA	Excited-State Absorption
FBG	Fibre Bragg-Grating
FEM	Finite Element Method
FWM	Four Wave Mixing
GV	Group Velocity
GVD	Group Velocity Dispersion
HE	Hybrid Electric
LD	Laser Diode
LMA	Large Mode-Area
LP	Linearly Polarized
MFD	Mode-Field Diameter
MI	Modulation Instability
MM	Multimode
MOPA	Master-Oscillator Power-Amplifier
NA	Numerical Aperture
NLSE	Nonlinear Schrödinger Equation
OPA	Optical Parametric Amplifier
OPG	Optical Parametric Generator
OPO	Optical Parametric Oscillator
OSA	Optical Spectrum Analyser
PBGF	Photonic Band-Gap Fibre

PCF	Photonic Crystal Fibre
PER	Polarization Extinction Ratio
PM	Polarization Maintaining
PMD	Polarization-Mode Dispersion
PRF	Pulse Repetition Frequency
RE	Rare-Earth
RF	Radio Frequency
RIP	Refractive Index Profile
RNF	Refracted Near-Field
SAP	Stress-Applying Parts
SBS	Stimulated Brillouin Scattering
SC	Supercontinuum
SM	Single-Mode
SP	Single-Polarization
SPM	Self-Phase Modulation
SRO	Singly-Resonant Oscillator
SRS	Stimulated Raman Scattering
SSFM	Split-Step Fourier Method
SVEA	Slowly-Varying-Envelope Approximation
TE	Transverse Electric
TFB	Tapered Fibre Bundle
TLS	Tunable Laser Source
TM	Transverse Magnetic
VBG	Volume Bragg-Grating
WDM	Wavelength Division Multiplex
XPM	Cross-Phase Modulation
YDF	Ytterbium-Doped Fibre
YDFA	Ytterbium-Doped Fibre Amplifier
YDFL	Ytterbium-Doped Fibre Laser
ZDW	Zero-Dispersion Wavelength

Academic Thesis: Declaration of Authorship

I, Gysbert van der Westhuizen, declare that the thesis entitled; Fibre Optical Parametric Devices for Large Frequency-Shift Wavelength Conversion, and the work presented in the thesis are both my own, and have been generated by me as the result of my own original research.

I confirm that:

[1] this work was done wholly or mainly while in candidature for a research degree at this University;

[2] where any part of this thesis has previously been submitted for a degree or any other qualification at this University or any other institution, this has been clearly stated;

[3] where I have consulted the published work of others, this is always clearly attributed;

[4] where I have quoted from the work of others, the source is always given. With the exception of such quotations, this thesis is entirely my own work;

[5] I have acknowledged all main sources of help;

[6] where the thesis is based on work done by myself jointly with others, I have made clear exactly what was done by others and what I have contributed myself;

[7] parts of this work have been published as:

- G.J. Van der Westhuizen and J. Nilsson, "Fiber optical parametric oscillator for large frequency-shift wavelength conversion," *IEEE J. Quantum Electon.*, vol. 47, no. 11, pp. 1396-1403 (2011).
- G.J. Van der Westhuizen and J. Nilsson, "All-fiber optical parametric oscillator, pumped by an all-fiber Yb-based MOPA," *Conference on Lasers and Electro-Optics (CLEO)*, Baltimore (2011).
- G.J. Van der Westhuizen and J. Nilsson, "All-fibre OPO system for visible wavelengths," *International Quantum Electronics Conference (IQEC) and Conference on Lasers and Electro-Optics (CLEO) Pacific Rim*, Sydney (2011).

Signed: Gysbert van der Westhuizen

Date: 21/12/2012

Acknowledgements

First and foremost I would like to thank my supervisor, Professor Johan Nilsson, for welcoming me into his research group in 2008, and for waiting patiently as I took my time to write this thesis. His guidance remains invaluable and the experience of the past five years has enriched my life forever. I also sincerely appreciate his financial support over the last three months of my stay in Southampton.

I would also like to thank the other members of the High Power Fibre Laser (HPFL) group, for all their support during my stay at the ORC. A special thank you to Dr. Christophe Codemard, Dr. Jean-Noel Maran and Dr. Carl Farrell who taught me the tricks of the trade of working with optical fibres. I also thank Dr. Junhua Ji and Dr. Luis Vasquez-Zuniga for endless discussions and for their company on smoke-breaks in what was often miserable weather.

I furthermore thank Professor Jayanta Sahu and his group for the fabrication of Yb-doped fibres used throughout this thesis, as well as for assistance with fibre characterisation; Dr. Morten Ibsen for fibre Bragg gratings supplied on several occasions; Dr. Kang-Kang Chen for the use of his MOPA source in an experiment; Dr. Peter Horak and Dr. Francesco Poletti for discussions on nonlinear fibre optics and the modelling thereof; Dr. Radan Slavik, Dr. Florian Kienlè and Mr. Jae Daniel for ad-hoc assistance with lab equipment and fibre preparation; and finally Mr. Simon Butler and his team for practical assistance in the lab.

Lastly, I would like to thank my loving wife, Marguerite, for disrupting her career and life by accompanying me to England. The past five years were challenging at times, but she took it in her stride and gave me a life outside of the lab, and for that I love her.

I am finally grateful to the ORC and its management for providing me with the studentship that enabled my PhD studies.

Chapter 1

Introduction

Prior to the 1960 discovery of the ruby laser [1], an optical medium was presumed linear in its response to an incident electro-magnetic field. The high optical intensities accessible from lasers however enabled several observations to the contrary. It was found, for example, that the medium's refractive index exhibits an intensity dependence and that the light-matter interaction can alter an incident wave's optical frequency. As a consequence, the nonlinear interaction enables electro-magnetic fields to interact with co- (or counter) propagating fields, through the influence of the medium, thereby violating the principle of superposition. The implications of these discoveries were, and still are, far-reaching and lead to the development of the field of research known as nonlinear optics [2].

Nonlinear optical phenomena are categorised by the order of the nonlinearity, derived from a Taylor series expansion of the optical medium's polarization density about the electric field. Most nonlinearities of practical interest are therefore either of second-order or third-order. Both second and third-order nonlinear processes were initially observed in bulk crystalline or liquid media, since these are characterised by relatively large nonlinear optical coefficients. Whilst optical fibres were available at the time, relatively small nonlinear optical coefficients and high transmission losses precluded their use. Low loss optical fibres only truly became an option for nonlinear experiments in 1970, after significant refinement in their fabrication [3]. In contrast to bulk nonlinear media, for which alignment and beam overlap remained a complication, the waveguide property of low loss optical fibres afforded unprecedented interaction

lengths. The relatively diminutive size of the fibre core furthermore meant that the efficiency of the nonlinear process, defined as the product of the optical intensity and the interaction length, for a given wavelength and power, can be larger by a factor of 10^7 – 10^9, relative to that in a bulk medium [4]. These properties, together with the interesting dynamics resulting from the coupling of nonlinear effects and fibre dispersion, were responsible for the rapid development in the field of nonlinear fibre optics during the 1970s and early 1980s (refer to ref. [5] for a detailed account).

Progress in the early years of nonlinear fibre optics relied almost exclusively on silica fibre, as a result of the medium's relatively superior transmission properties. However, since the silica molecule exhibits inversion symmetry, silica fibre has a virtually non-existent second-order nonlinearity. Although it is possible to induce a second-order nonlinearity through the process of poling, the approach is elaborate and will not be considered here [6]. Third-order nonlinear processes therefore present the lowest order nonlinearities on offer in silica fibres. Processes included in this category are Stimulated Brillouin Scattering (SBS), Stimulated Raman Scattering (SRS), Self-Phase Modulation (SPM), Cross-Phase Modulation (XPM) and Four Wave Mixing (FWM). These nonlinear processes often co-exist in a fibre-optic system, in which case the dominant contribution depends on the properties of the fibre waveguide as well as the spectral attributes and power of the incident field.

Whilst nonlinear effects can be undesired and even devastating if left unchecked, they offer unique attributes that make them valuable to a large range of applications. Wavelength conversion is a fine example. Laser sources, irrespective of the applicable medium, require a mechanism for optical gain. In fibre lasers, for example, optical gain is afforded by so-called rare-earth (RE) doping. The RE ions are optically excited (typically by means of a semiconductor diode laser), resulting in emission at what is usually a longer wavelength. The absorption and emission wavelengths are determined by the atomic transitions associated with the energy level structure of the RE ions. This means that laser emission is only available at wavelengths for which gain media with the appropriate energy level structure exist. Consequently, there are windows in the visible and near-infrared spectra for which laser quality light is not available. It is in this regard that nonlinear processes can be used to extend the wavelength coverage available from conventional lasers.

The process of fibre FWM is one approach that offers great potential as a versatile wavelength converter [7]. In its simplest configuration, FWM can be initiated from a single incident optical field. Two photons from this so-called degenerate pump wave are annihilated, leading to the simultaneous creation of one photon at a lower frequency (Stokes) and one photon at a higher frequency (anti-Stokes), so as to conserve energy. The frequency separation between the pump and Stokes (or anti-Stokes) waves can assume any value up to the second-harmonic limit, provided that the fibre dispersion is suitable. This condition on the fibre dispersion is known as phase-matching and is equivalent to the requirement of momentum conservation. Since fibre dispersion can be tailored by changing the fibre dimensions and material composition [8], fibre FWM offers a promising route to laser quality light at practically any wavelength for the appropriate choice of pump wavelength. Practical implementations of fibre FWM are encountered in either an optical parametric amplifier (OPA) or optical parametric oscillator (OPO) configuration. An OPA is a single-pass FWM device seeded at either the Stokes or anti-Stokes wavelength, such that the seeded component is amplified, whilst the un-seeded component is generated from noise. Oscillators, on the other hand, are typically noise-seeded at both the Stokes and anti-Stokes and rely on optical feedback at one, or even both wavelengths, to increase the conversion rate.

To date, the success of nonlinear optical devices as wavelength converters can largely be attributed to progress in bulk optical parametric amplifiers and oscillators (refer to [9] and references therein). These sources offer excellent conversion efficiencies over large frequency separations as well as wavelength tuneability. However, in contrast to fibre FWM, bulk optical parametric mixing devices are based on the second-order nonlinearity and therefore only allow down-conversion of the incident frequency. They are furthermore relatively expensive and susceptible to misalignment. In contrast, optical fibre is inexpensive and robust, and offers the possibility of a compact fully-integrated all-fibre wavelength converter. These properties have been instrumental in the success of fibre Raman amplifiers and lasers in general [10], as well as in optical communication systems (refer to [11] and references therein). Whilst SRS typically only allows for frequency down-conversion, the process is self-phase-matched for a frequency separation determined by the energy level structure of the medium. For this reason, fibre FWM, for which phase-matching needs

to be achieved in an active manner, proves relatively challenging, but also promises greater flexibility.

Phase-matched fibre FWM can be realised in two distinct ways. Assuming a degenerate pump and a fibre with a single zero-dispersion wavelength (ZDW) , the first approach pumps the fibre just inside the anomalous group velocity dispersion (GVD) regime. This results in phase-matching over a relatively broad bandwidth about the pump wavelength. Of greater interest for the purpose of wavelength conversion, is the second approach, where the fibre is pumped in the normal GVD regime. In this case, phase-matching can be achieved in a number of ways, each of which allows for phase-matched FWM to spectrally distant narrow bands. Whereas the narrow bandwidth associated with the second approach is often desired, it places strict requirements on the fibre dispersion, which has to be uniform along the length of the fibre to maintain phase-matching. It is therefore important to optimise the parametric bandwidth, which scales inversely with an increase in fibre length (assuming perfect phase-matching). To reduce the impact of fluctuations in the fibre dispersion, short fibres are therefore required, which in turn demands an increased pump power for efficient conversion.

The past decade has seen renewed interest in fibre FWM for the purpose of wavelength conversion. This may be attributed to a number of technological advancements. Perhaps the most important is the progress that has been made in RE-doped fibre lasers and amplifiers [12]. Particularly double-cladding ytterbium-doped fibre devices have been demonstrated as exceptionally versatile high power laser sources, in both the CW and pulsed operating regimes. Progress in fibre design and fabrication is another contributing factor to the resurgence in large frequency-shift fibre FWM research. Smaller mode-field diameters and improved longitudinal uniformity in conventional solid-core fibres, as well as photonic crystal fibres, are constantly enabling record conversion efficiencies to wavelengths throughout the visible and near-infrared spectra. The combination of these technologies looks set to unlock the potential of fibre FWM as a viable alternative to existing nonlinear wavelength converters.

1.1 Historical Overview

Degenerate fibre FWM, or three-wave mixing, was first demonstrated in 1974 by R. H. Stolen et. al., working at Bell Labs [7]. Using pump pulses from a frequency doubled

Nd:YAG laser, phase-matching was accomplished for a frequency-shift of 85 THz, through the use of higher-order spatial modes. The dispersion characteristics of higher-order spatial modes offered a relatively straightforward route to phase-matching, and subsequent experimental work therefore focussed on exploring different mode combinations [13] - [16]. In 1980, Washio et. al. reported the first demonstration of fundamental mode fibre FWM [17]. This approach, relying on the waveguide's higher-order dispersion, showed that phase-matching can be achieved when pumping close to the fibre's ZDW in the normal GVD regime. Subsequent results confirmed that the phase-matched frequency-shift depends on the frequency separation between the pump wavelength and ZDW [18], [19]. Around the same time, Stolen and co-workers continued their pioneering work by demonstrating an alternative approach to fundamental mode fibre FWM. Here, phase-matching relied on the polarization-multiplicity of the fundamental fibre mode and resulted in frequency-shifts of up to 30 THz for birefringence values of the order of 10^{-4} [20]. By this time, fibre FWM and parametric amplification was well understood [21]. Although the performance of fibre OPAs was not comparable to Raman amplifiers [22], their potential, specifically as wavelength converters, was undeniable.

During the mid-to-late 1980s, interest in optical fibre communication systems started to grow. What followed was an intense period of research aimed at discovering suitable optical amplifiers. This research culminated in the 1986 discovery of the erbium-doped fibre amplifier (EDFA) at the University of Southampton [23]. The associated progress in the fabrication of RE-doped fibre lasers and amplifiers, as well as diode laser technology, rejuvenated interest in fibre FWM, which had been experiencing a period of relative inactivity. The renewed interest was furthermore spurred on by the 1986 in-fibre demonstration of so-called modulation instability [24], [25]. Mathematically, this nonlinear process is simply the time-domain description of a fibre FWM process in which the pump wave is positioned inside the anomalous GVD regime. The previously discovered phase-matching processes function by balancing the phase mismatch contributions attributed to material and waveguide dispersion. In contrast, the modulation instability process uses pump-wave induced SPM to cancel the phase mismatch attributed to dispersion. Although the resultant phase-matched frequency-shift is comparatively small, the parametric gain bandwidth can span hundreds of nanometres [26]. The combination of high gain and a bandwidth that can

exceed those of EDFAs and Raman amplifiers generated considerable interest from the telecommunication community. Progress since the latter half of the 1990s also benefitted from the first demonstration of a so-called highly-nonlinear dispersion-shifted fibre [27]. These fibres enabled the use of modulation-instability-based amplifiers in the all-important 1550 nm spectral window, thereby making it available to a host of potential applications. For an excellent overview of telecommunication-related performance results and applications, the interested reader is referred to Ref. [28].

The development of fibre-based technologies that accompanied the rise of the telecommunication era, invariably also held benefits for technology aimed at non-telecommunication applications. Progress in the fabrication of passive and RE-doped fibres are examples of particular interest for large frequency-shift FWM. These improvements were complemented by the realisation of double-cladding fibres, which enabled the use of multimode pump diodes, to improve the power scalability of single-mode fibre lasers and amplifiers in a drastic way [29], [30]. Another important milestone during the latter half of the 1990s was the discovery of index-guiding photonic crystal fibres (PCF) [31]. Instead of using dopant materials to raise the index of the core, the cladding of this typically single-material fibre is covered with air-holes to guide light via the process of modified total internal reflection. PCF immediately attracted interest from the nonlinear optics research community for two reasons. Firstly, these fibres can be designed to have very large waveguide dispersion, which can be used to shift the fibre's ZDW to values below that of the silica material. Secondly, PCF offers the possibility of a wavelength-independent mode-field diameter, which effectively allows for a single guided mode over a large spectral range. Over the past decade, these technological advances resulted in a resurgence in research activity into large frequency-shift fibre FWM. The following is a brief overview of notable trends and achievements.

The ability of PCF to shift the ZDW enabled researchers to achieve phase-matching through the use of higher-order dispersion and a variety of pump sources. Q-switched or mode-locked Nd:YAG and Nd:YVO_4 lasers proved particularly popular as pump sources in OPA experiments, since the picosecond pulse widths and low repetition rates of these enabled high peak powers and therefore afforded relatively good conversion efficiencies [32] - [34]. Similar experiments explored the wavelength tuneability of the large-shift FWM process using ultra-short pulses from a Ti:sapphire

laser [35], as well as nanosecond pulses and even continuous wave (CW) radiation from a dye laser [36]. Phase-matched FWM were also realised through the use of different polarization modes [37], [38], as well as higher-order spatial modes [39], [40]. For the latter case, a PCF with a germania-doped core was chosen, since it was found that these allow even greater design flexibility [41]. Other novel applications and concepts included the demonstration of FWM in a air-guided photonic band-gap fibre (PBGF) [42], as well as the theoretical treatment of degenerate FWM in a solid-core PBGF [43].

Whilst optical parametric generation and amplification were also demonstrated in conventional fibre (see Ref. [44], for example), these could not quite match the large frequency-shift conversion efficiencies of PCF-based devices. This is primarily a consequence of the reliance on relatively low power EDFA pump sources which precludes an adequate parametric bandwidth. To overcome this limitation, the use of the optical parametric oscillator (OPO) configuration proved remarkably successful [45]. Impressive conversion efficiencies at moderate frequency separations were demonstrated in all-fibre [46] and hybrid free-space [47] ring-cavities using nanosecond pulses and CW radiation from a tunable laser source (TLS)-seeded EDFA pump, respectively. Similar experiments have recently been used to demonstrate wavelength tunability up to 2 μm [48] - [50], as well as excellent conversion efficiencies and watt-level output powers (albeit at smaller frequency-shifts) for CW pump waves [51] and nanosecond pump pulses [52]. Research on OPO devices at alternative pump wavelengths has also been a topic of interest over the past decade. As such, moderately efficient PCF-based OPOs have been demonstrated in hybrid free-space ring cavities [53], [54] as well as linear cavities [55], at pulse widths ranging from tens of picoseconds to tens of nanoseconds. For a detailed discussion on these devices, the interested reader is referred to Ref. [56], where similar implementations, relying on an anomalous GVD pump source, are also treated.

1.2 Motivations

In recent years, researchers have started to realise the value of ytterbium-doped fibre lasers (YDFL) and amplifiers (YDFA) as pump sources for large frequency-shift fibre FWM devices. In contrast to bulk alternatives like Nd:YAG, YDFA pump sources offer unrivalled flexibility and power scalability, particularly in the so-called master

oscillator power-amplifier (MOPA) configuration. Pump sources based on YDFA technology have been used, for example, to illustrate up-conversion efficiencies in excess of 30% at frequency-shifts larger than 120 THz in optical parametric generators [57][58]. In these experiments, the combination of picosecond pump pulses with high peak powers and short PCF nonlinear converters resulted in large parametric bandwidths. These bandwidths in turn made the phase-matching, and thus the FWM conversion efficiency, more resilient to longitudinal fibre inhomogeneities. However, a high peak pump power often precludes the use of an all-fibre configuration in order to avoid unwanted nonlinearities, thereby forfeiting a principle advantage of fibre sources. A demonstration of an all-fibre pump-OPA source, based on the combination of YDFA and PCF technology, was however reported very recently [59]. Here, the authors managed to achieve a pump to anti-Stokes conversion efficiency of about 15% at a frequency-shift of 85 THz, in a 0.6 m long PCF, using 50 ps pump pulses with a peak power of roughly 3.6 kW at 1030 nm. In contrast to results at pump wavelengths around 1 μm, efficient all-fibre pump-OPA (and OPO) configurations for pump wavelengths in the 1550 nm spectral region have become relatively common (refer to Section 1.1). Notably, these devices typically utilise nanosecond pump pulses and dispersion-shifted fibre lengths ranging from tens to hundreds of metres.

The purpose of this thesis is to investigate methods whereby practical and efficient large frequency-shift FWM can be realised at YDFA pump wavelengths. In addition to the previously-mentioned advantages of YDFA technology, the motivation for its use is two-fold. Firstly, it offers the potential for large frequency-shift up-conversion towards visible wavelengths, where spectroscopy applications in particular stand to benefit from the ytterbium gain medium's flexibility in terms of pulse width and wavelength tuneability. Although the spectral range in question can be accessed via conventional solid-state technology, such as Ti:sapphire lasers, these are expensive and sensitive, which can make them impractical. Other fibre-based pump sources, like EDFAs, are similarly unsuitable, since these do not allow for conversion to sub-1 μm wavelengths. The potential of YDFA-based pump sources to be integrated into all-fibre OPA or OPO devices is further motivation for its use. An all-fibre solution offers excellent stability as well as reliability in terms of beam quality and power delivery, potentially making it a viable alternative to current bulk sources.

In contrast to the brute-force high pump power approach followed in some of the previous research investigations on this topic, the work presented in this thesis considers the use of nanosecond pulses and relatively modest pump powers (1 kW). As a result of the reduced pump power, longer fibre lengths will be considered in order to maintain optimal conversion efficiency. This approach is common for fibre OPA and OPO devices operating in the 1550 nm spectral region, where they have proved very successful. However, their success, especially at large frequency-shifts, may in part be attributed to the use of dispersion-shifted fibres and the excellent longitudinal uniformity of these. A uniform fibre is crucial to maintain coherent FWM, particularly since both a reduction in pump power and increase in fibre length reduces the parametric gain bandwidth. For this reason, this thesis considers the use of telecommunication-grade fibre to achieve large frequency-shift FWM. Since the ZDWs of these typically range from 1300 nm to 1600 nm, they do not lend themselves to phase-matching through the use of higher-order dispersion for pump wavelengths around 1 µm. The investigation therefore evaluates the possibility of using higher-order spatial modes, as well as polarization modes, to achieve phase-matching. The combination of these techniques in conventional fibres and 1 µm pump wavelengths has not received much attention since the middle 1980s. Therefore, given the immense progress that has been made for pump sources, passive fibres and fibre components, it is time to re-evaluate the potential of these techniques. In addition, the work presented here considers higher-order dispersion phase-matching in a photonic crystal fibre. This allows for, at least, qualitative comparisons of the findings from the respective investigations and provides insight into the applicability of the considered techniques.

1.3 Thesis Outline

Chapter 2 follows the introduction and historical overview of this chapter with a review of the theory relevant to an understanding of fibre FWM. It starts with an introduction on the principle of waveguiding and the significance of optical modes. This leads into a discussion on the important topic of chromatic dispersion, which is considered within the context of multimode fibres, polarization maintaining fibres as well as photonic crystal fibres. The second part of Chapter 2 deals with nonlinear phenomena in fibres. After a brief introduction on Brillouin and Raman scattering, FWM is considered with

particular attention to the underlying physics and the mechanisms for phase-matching. The chapter is concluded with an overview of the most important properties of ytterbium-doped fibre sources.

The ytterbium-doped fibre master-oscillator power-amplifier configuration, employed as pump source in the majority of experiments reported in this thesis, are described in Chapter 3. This includes an overview of the characteristics of the seed lasers and fibre amplifiers developed throughout the iterative approach that was followed to optimise performance for FWM in an all-fibre system.

Chapter 4 provides details on a numerical and experimental investigation into the plausibility of fibre optical parametric amplification in conventional telecommunication fibres. The first part of the chapter describes a numerical model that calculates a fibre's dispersion from its refractive index profile. Next, these dispersion characteristics are used to evaluate phase-matching combinations in readily available multimode and polarization maintaining (PM) fibres. This, together with solutions to the equations that govern FWM in the respective fibres, are then used to identify the PM fibre as a more suitable choice for the experimental phase reported in the second half of the chapter. Here, FWM in the PM fibre is evaluated in the OPA configuration using a pulsed, as well as CW, seed laser, and the pump MOPA of Chapter 3. Experiments in an un-seeded optical parametric generator (OPG) configuration, employing pump sources with alternative characteristics, are also presented.

Chapter 5 considers higher-order dispersion phase-matching in PCF. After a short overview of the chosen fibre's properties and their implications for phase-matching, experimental results are presented on the use of this fibre in the OPG configuration. This leads into a discussion on the role of competing nonlinearities and the motivation behind the decision to reconfigure the single pass OPG into a ring-cavity OPO. The PCF-based OPO is first implemented using a hybrid free-space setup, but is eventually integrated into an all-fibre pump-OPO configuration. The rest of the chapter is dedicated to a structured overview of the characteristics of an all-fibre OPO, with particular attention to the influence of out-coupling ratio, PCF length, pump pulse width and intra-cavity filtering.

The use of a relatively low pump peak power and long nonlinear converter leads to a reduced parametric bandwidth, which makes the large frequency-shift FWM

process sensitive to longitudinal inhomogeneities in the fibre. This process has a disruptive influence on FWM conversion. The numerical analysis of Chapter 6 explores the possibility of increasing the parametric bandwidth by engineering of the dispersion, and subsequently the phase-matching. Designs based on PCFs with germania-doped core-regions forms the basis of the approach. It is found that the additional degrees of freedom, provided by the doping concentration and uniformly doped radius, can lead to an optimised parametric bandwidth.

Chapter 7 finally provides a summary on the main results and conclusions throughout this thesis. Suggestions on further experimental work are also provided here.

1.4 References

[1] T.H. Maiman, "Stimulated optical radiation in ruby masers," *Nature*, vol. 187, pp. 493 (1960).
[2] N. Bloembergen, *Nonlinear Optics*, W.A. Benjamin, Reading, MA, 1965.
[3] F.P. Kapron, D.B. Keck and R.D. Maurer, "Radiation losses in glass optical waveguides," *Appl. Phys. Lett.*, vol. 17, no. 10, pp. 423-425 (1970).
[4] G.P. Agrawal, "Nonlinear fiber optics: its history and recent progress," *J. Opt. Soc. Am. B*, vol. 28, no. 12, pp. A1-A10 (2011).
[5] R.H. Stolen, "The early years of fiber nonlinear optics," *J. Lightw. Technol.*, vol. 26, no. 9, pp. 1021-1031 (2008).
[6] V. Pruneri, G. Bonfrate, P.G. Kazansky, D.J. Richardson, N.G. Broderick, J.P. de Sandro, G. Simonneau, P. Vidakovic and J.A. Levenson, "Greater than 20%-efficient frequency doubling of 1532-nm nanosecond pulses in quasi-phase-matched germanosilicate optical fibers," *Opt. Lett.*, vol. 24, pp. 208-210 (1999).
[7] R.H. Stolen, J.E. Bjorkholm and A. Ashkin, "Phase-matched three-wave mixing in silica fiber optical waveguides," *Appl. Phys. Lett.*, vol. 24, no. 7, pp. 308-310 (1974).
[8] D. Gloge, "Weakly guiding fibers," *Appl. Opt.*, vol. 10, no. 10, pp. 2252-2258 (1971).
[9] M.H. Dunn and M. Ebrahimzadeh, "Parametric generation of tunable light from continuous-wave to femtosecond pulses," Science, vol. 286, no. 5444, pp. 1513-1517 (1999).
[10] Y. Feng, J.R. Taylor and D.B. Calia, "150 W highly-efficient Raman fiber laser," *Opt. Express*, vol. 17, no. 26, pp. 23678-23683 (2009).
[11] M.N. Islam, ed., Raman Amplifiers for Telecommunications, Springer, 2003.
[12] D.J. Richardson, J. Nilsson and W.A. Clarkson, "High power fiber lasers: current status and future perspectives," *J. Opt. Soc. Am. B*, vol. 27, no. 11, pp. B63-B92 (2010).
[13] R.H. Stolen, "Phase-matched-stimulated four-photon mixing in silica-fiber waveguides," *IEEE J. Quantum Electron.*, vol. QE-11, no. 3, pp. 100-103 (1975).
[14] C. Lin and M.A. Bösch, "Large-Stokes-shift stimulated four-photon mixing in optical fibers," *Appl. Phys. Lett.*, vol. 38, no. 7, pp. 479-481 (1981).

[15] K.O. Hill, D.C. Johnson and B.S. Kawasaki, "Efficient conversion of light over a wide spectral range by four-photon mixing in a multimode graded-index fiber," *Appl. Opt.*, vol. 20, no. 6, pp. 1075-1079 (1981).

[16] E.M. Dianov, E.A. Zakhidov, A. Ya Karasik, P.V. Mamyshev and A.M. Prokhorov, "Stimulated four-photon mixing in glass fibres," *Sov. Phys. JETP Lett.*, vol. 34, pp. 38-42 (1981).

[17] K. Washio, K. Inoue and T. Tanigawa, "Efficient generation of near-I.R. stimulated light scattering in optical fibres pumped in low-dispersion region at 1.3 μm," *Electron. Lett.*, vol. 16, no. 9, pp. 331-333 (1980).

[18] C. Lin, W.A. Reed, A.D. Pearson and H.-T. Shang, "Phase matching in the minimum-chromatic-dispersion region of single-mode fibers for stimulated four-photon mixing," *Opt. Lett.*, vol. 6, no. 10, pp. 493-495 (1981).

[19] C. Lin, W.A. Reed, A.D. Pearson, H.-T. Shang and P.F. Glodis, "Designing single-mode fibres for near-IR (1.1-1.7 μm) frequency generation by phase-matched four-photon mixing in the minimum chromatic dispersion region," *Electron. Lett.*, vol. 18, no. 2, pp. 87-89 (1982).

[20] R.H. Stolen, M.A. Bösch and C. Lin, "Phase matching in birefringent fibers," *Opt. Lett.*, vol. 6, no. 5, pp. 213-215 (1981).

[21] R.H. Stolen and J.E. Bjorkholm, "Parametric amplification and frequency conversion in optical fibers," *IEEE J. Quantum Electron.*, vol. QE-18, no. 7, pp. 1062-1072 (1982).

[22] J.P. Pocholle, J. Raffy, M. Papuchon and E. Desurvire, "Raman and four photon mixing amplification in single mode fibers," *Optical Engineering*, vol. 24, pp. 600-608 (1985).

[23] R.J. Mears, L. Reekie, I.M. Jauncey and D.N. Payne, "High-gain rare-earth-doped fiber amplifier at 1.54 μm," *Optical Fiber Communication Conference* (Reno, Nevada), W12 (1987).

[24] A. Hasegawa and W.F. Brinkman, "Tunable coherent IR and FIR source utilizing modulation instability," *IEEE J. Quantum Electron.*, vol. QE-16, pp. 694-697 (1980).

[25] K. Tai, A. Hasegawa and A. Tomita, "Observation of modulation instability in optical fibers," *Phys. Rev. Lett.*, vol. 56, pp. 135-138 (1986).

[26] M.E. Marhic, N. Kagi, T.K. Chiang and L.G. Kazovsky, "Broadband fiber optical parametric amplifiers," *Opt. Lett.*, vol. 21, pp. 573-575 (1996).

[27] M.J. Holmes, D.L. Williams and R.J. Manning, "Highly nonlinear optical fiber for all optical processing applications," *IEEE Photon. Technol. Lett.*, vol. 7, pp. 1045-1047 (1995).

[28] M.E. Marhic, Fiber Optical Parametric Amplifiers, Oscillators and Related Devices, Cambridge Univ. Press, 2008.

[29] J.D. Kafka, "Laser diode pumped fiber laser with pump cavity," U.S. patent 4,829,529 (1989).

[30] R.D. Maurer, "Optical waveguide light source," U.S. patent 3,808,549 (1974).

[31] J.C. Knight, T.A. Birks, P.St.J. Russell and D.M. Atkin, "All-silica single-mode optical fiber with photonic crystal cladding," *Opt. Lett.*, vol. 21, no. 19, pp. 1547-1549 (1996).

[32] W.J. Wadsworth, N. Joly, J.C. Knight, T.A. Birks, F. Biancalana and P .St. J. Russell, "Supercontinuum and four-wave mixing with Q-switched pulses in endlessly single-mode photonic crystal fibers," *Opt. Express*, vol. 12, no. 2, pp. 299-309 (2004).

[33] T. Sloanes, K. McEwan, B. Lowans and L. Michaille, "Optimisation of high average power optical parametric generation using a photonic crystal fiber," *Opt. Express*, vol. 16, no. 24, pp. 19724-19733 (2008).

[34] L. Velazquez-Ibarra, A. Diez, E. Silvestre, M.V. Andres, M.A. Martinez and J.L. Lucio, "Pump power dependence of four-wave mixing parametric wavelengths in normal dispersion photonic crystal fibers," *IEEE Photon. Technol. Lett.*, vol. 23, no. 14, pp. 1010-1012 (2011).

[35] J. Yuan, X. Sang, C. Yu, Y. Han, G. Zhou, S. Li and L. Hou, "Highly efficient anti-Stokes signal conversion by pumping in the normal and anomalous dispersion regions in the fundamental mode of photonic crystal fiber," *J. Lightw. Technol.*, vol. 29, no. 19, pp. 2920-2926 (2011).

[36] G.K.L. Wong, A.Y.H. Chen, S.G. Murdoch, R. Leonhardt, J.D. Harvey, N.Y. Joly, J.C. Knight, W.J. Wadsworth and P.St.J. Russell, "Continuous-wave tunable optical parametric generation in a photonic-crystal fiber," *J. Opt. Soc. Am. B*, vol. 22, no. 11, pp. 2505-2511 (2005).

[37] R.J Kruhlak, G.K.L. Wong, J.S.Y. Chen, S.G. Murdoch, R. Leonhardt, J.D. Harvey, N.Y. Joly and J.C. Knight, "Polarization modulation instability in photonic crystal fibers," *Opt. Lett.*, vol. 31, no. 10, pp. 1379-1381 (2006).

[38] P. Dupriez, F. Poletti, P. Horak, M.N. Petrovich, Y. Jeong, J. Nilsson, D.J. Richardson and D.N. Payne, "Efficient white light generation in secondary cores of holey fibers," *Opt. Express*, vol. 15, no. 7, pp. 3729-3736 (2007).

[39] Labruyère, V. Tombelaine, P. Leproux, V. Couderc, F. Gerôme, G. Humbert, J. Kobelke, K. Schuster and H. Bartelt, "Intermodal four-wave mixing in structured-core photonic crystal fiber: Experimental results," *CLEO/IQEC*, CFS3 (2009).

[40] Labruyère, P. Leproux, V. Couderc, V. Tombelaine, J. Kobelke, K. Schuster, H. Bartelt, S. Hilaire, G. Huss and G. Mélin, "Structured-core GeO_2-doped photonic-crystal fibers for parametric and supercontinuum generation," *IEEE Photon. Technol. Lett.*, vol. 22, no. 16, pp. 1259-1261 (2010).

[41] Y.P. Yatsenko, A.D. Pryamikov, V.M. Mashinsky, M.E. Likhachev, A.O. Mavritsky, E.M. Dianov, A.N. Guryanov, V.F. Khopin and M.Y. Salgansky, "Four-wave mixing with large Stokes shifts in heavily Ge-doped silica fibers," *Opt. Lett.*, vol. 30, no. 15, pp. 1932-1934 (2005).

[42] S.O. Konorov, E.E. Serebryannikov, D.A. Akimov, A.A. Ivanov, M.V. Alfimov and A.M. Zheltikov, "Phase-matched four-wave mixing of sub-100-TW/cm^2 femtosecond laser pulses in isolated air-guided modes of a hollow photonic-crystal fiber," *Phys. Rev. E*, vol. 70, pp. 066625-1 – 066625-5 (2004).

[43] P.D. Rasmussen, J. Lægsgaard and O. Bang, "Degenerate four wave mixing in solid core photonic bandgap fibers," Opt. Express, vol. 16, no. 6, pp. 4059-4068 (2008).

[44] M.E. Marhic, K.K.Y. Wong and L.G. Kazovsky, "Wide-band tuning of the gain spectra of one-pump fiber optical parametric amplifiers," *IEEE J. Sel. Topics Quantum Electron.*, vol. 10, no. 5, pp. 1133-1141 (2004).

[45] W. Margulis and U. Österberg, "Four-photon fiber laser," *Opt. Lett.*, vol. 12, no. 7, pp. 519-521 (1987).

[46] G.K.L. Wong, S.G. Murdoch, R. Leonhardt, J.D. Harvey and V. Marie, "High-conversion-efficiency widely-tunable all-fiber optical parametric oscillator," *Opt. Express*, vol. 15, no. 6, pp. 2947-2952 (2007).

[47] T.Q. Xu, S.G. Murdoch, R. Leonhardt and J.D. Harvey, "Raman-assisted continuous-wave tunable all-fiber optical parametric oscillator," *J. Opt. Soc. Amer. B*, vol. 26, no. 7, pp. 1351-1356 (2009).

[48] Y. Zhou, K.K.Y. Cheung, S. Yang, P.C. Chui and K.K.Y. Wong, "Ultra-widely tunable, narrow linewidth picosecond fiber-optical parametric oscillator," *IEEE Photon. Technol. Lett.*, vol. 22, no. 23, pp. 1756-1758 (2010).

[49] Gershikov, E. Shumakher, A. Willinger and G. Eisenstein, "Fiber parametric oscillator for the 2 μm wavelength range based on narrowband optical parametric amplification," *Opt. Lett.*, vol. 35, no. 19, pp. 3198-3200 (2010).

[50] B.P.-P. Kuo, N. Alic, P.F. Wysocki and S. Radic, "Simultaneous wavelength-swept generation in NIR and SWIR bands over combined 329-nm band using swept-pump fiber optical parametric oscillator," *J. Lightw. Technol.*, vol. 29, no. 4, pp. 410-416 (2011).

[51] R. Malik and M. E. Marhic, "Narrow-linewidth tunable continuous-wave fiber optical parametric oscillator with 1W output power," *ECOC 2010*, paper Th.10.C.5.

[52] Y.Q. Xu, K.F. Mak and S.G. Murdoch, "Multiwatt level output powers from a tunable fiber optical parametric oscillator," *Opt. Lett.*, vol. 36, no. 11, pp. 1966-1968 (2011).

[53] J.D. Harvey, R. Leonhardt, S. Coen, G.K.L. Wong, J.C. Knight, W.J. Wadsworth and P. St. J. Russell, "Scalar modulation instability in the normal dispersion regime by use of a photonic crystal fiber," *Opt. Lett.*, vol. 28, no. 22, pp. 2225-2227 (2003).

[54] K. Cook, C. Xiong and W.J. Wadsworth, "Enhanced four-wave mixing and parametric oscillator in photonic crystal fiber," *J. Opt. A: Pure Appl. Opt.*, vol. 9, pp. 1095-1099 (2007).

[55] Y.Q. Xu, S.G. Murdoch, R. Leonhardt and J.D. Harvey, "Widely tunable photonic crystal fiber Fabry-Perot optical parametric oscillator," *Opt. Lett.*, vol. 33, no. 12, pp. 1351-1353 (2008).

[56] J.E. Sharping, "Microstructure fiber based optical parametric oscillators," *J. Lightw. Technol.*, vol. 26, no. 14, pp. 2184-2191 (2008).

[57] D. Nodop, C. Jauregui, D. Schimpf, J. Limpert and A. Tünnermann, "Efficient high-power generation of visible and mid-infrared light by degenerate four-wave mixing in a large-mode-area photonic-crystal fiber," *Opt. Lett.*, vol. 34, no. 22, pp. 3499-3501 (2009).

[58] L. Lavoute, J.C. Knight, P. Dupriez and W.J. Wadsworth, "High power red and near-IR generation using four wave mixing in all integrated fiber laser systems," *Opt. Express*, vol. 18, no. 15, pp. 16193-16205 (2010).

[59] M. Baumgartl, T. Gottschall, J. Abreu-Afonso, A. Diez, T. Meyer, B. Dietzek, M. Rothhardt, J. Popp, J. Limpert and A. Tünnermann, "Alignment-free, all-spliced fiber laser source for CARS microscopy based on four-wave-mixing," *Opt. Express*, vol. 20, no. 19, pp. 21010-21018 (2012)

Chapter 2

Background

Chapter 2 provides an overview of the background theory relevant to an understanding of fibre optical parametric devices. The focus is on the fibre waveguide and the nonlinear processes supported by this medium. The chapter is concluded with a summary of the pump source technology chosen for the experimental investigations to follow in Chapters 3 through 5. Only the most important subjects are covered and whilst the content will serve only as a reference to later chapters, appropriate references are provided throughout, for the interested reader.

2.1 Optical Fibre Waveguides

An optical fibre is a dielectric structure that confines electromagnetic (EM) radiation through the process of waveguiding. Although various materials and shapes are possible, optical fibres are traditionally cylindrical and consist primarily of silica glass.

Typical optical fibres have outer diameters of ~125 μm. Governed by the transparency of the dielectric material that makes up the optical fibre, these waveguides are usually employed in the visible and near infrared portions of the EM spectrum. In this limit, where the radiation's wavelength (say, 1 μm) is small in comparison to the fibre dimensions, waveguiding can be described through ray optics. To this end, we consider a so-called step-index fibre (refer to Figure 2.1) [1].

A step-index fibre is made up of two distinct regions, known as the core and cladding. As the name suggests, the core is located within the cladding, and is characterized by a refractive index, n_1. The cladding is similarly characterized by a refractive index n_2, such that $n_1 > n_2$. The relative increase in the core refractive index is achieved by doping silica (for example) with a material with a higher refractive index, such as germania.

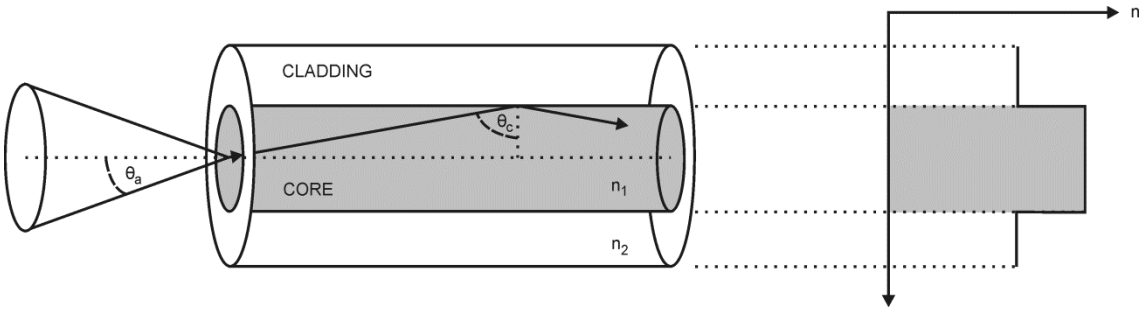

Figure 2.1: Schematic of a step-index optical fibre, indicating the core, cladding and angles relevant to waveguiding. The core refractive index, n_1, is larger than that of the cladding, n_2.

Consider an optical ray, propagating in a plane that passes through the fibre's optical axis. According to the Fresnel equations and Snell's law, the incident ray will undergo refraction and reflection at the core-cladding interface [2]. The proportionality of the refracted and reflected power will depend on the angle of incidence, with respect to the normal. In general, a larger angle results in a reduction in power transmission, up to a critical angle (θ_c) at which the incident power is reflected in full. Beyond the critical angle, the ray is said to undergo total internal reflection. From Snell's law, the critical angle follows as:

$$\theta_c = \sin^{-1}\frac{n_2}{n_1} \tag{2.1}$$

Rays satisfying equation 2.1 are confined to the core, whilst all other rays rapidly *leak* from the core through consecutive interface encounters.

The condition for waveguiding, as outlined above, has implications for the light-gathering capacity of the fibre core. An optical ray propagating from air, into the fibre core, will be refracted. Snell's law can thus once more be used to calculate allowed incidence angles, necessary to ensure total internal reflection:

$$\theta_a = \sin^{-1}\sqrt{\mathrm{n}_1^2 - \mathrm{n}_2^2} = \sin^{-1}\mathrm{NA} \tag{2.2}$$

This angle defines the acceptance cone of the optical fibre and is a function of the fibre's so-called numerical aperture (NA). From Figure 2.1 it is clear that rays incident at angles greater that θ_a will not be guided. The numerical aperture is an important quantity, which, along with the core dimensions, dictates the guidance characteristics of step-index fibres.

The preceding ray representation is a simplification of a more involved wave representation, wherein a ray is assumed perpendicular to the wave's phase front. By considering the conditions imposed on different rays by a common phase front, it is simple to derive a phase-matching condition for the discrete ray angles, $\varphi > \theta_c$, for which waveguiding will occur [3], [4]. Each of the allowed angles (φ), which depend on the radiation wavelength, fibre core size and fibre NA, therefore corresponds to an allowed EM wave. Since the phase front of a particular EM wave is subject to interference, the resulting EM field distribution, or mode, becomes a standing wave in the fibre's transverse plane. In this way, a fibre may support a large number of modes at a given wavelength.

Whereas geometrical optics provides an intuitive picture on the origin of waveguiding, a rigorous treatment involves Maxwell's equations and solutions to the subsequent wave equation. In this section we shall briefly outline the most important aspects of such a treatment, with an emphasis on obtaining solutions to the relevant equations. The remainder of the section will then be dedicated to a discussion on the waveguiding properties of typical dielectric media and the implications for the theory used to describe light-matter interaction.

2.1.1 Optical Fibre Modes

For a dielectric material, where both the current density and electric charge density are zero, Maxwell's equations may be written as [1],

$$\nabla \times \mathbf{H}(\mathbf{r}, \mathrm{t}) = \frac{\partial \mathbf{D}(\mathbf{r}, \mathrm{t})}{\partial \mathrm{t}} \tag{2.3}$$

$$\nabla \times \mathbf{E}(\mathbf{r}, \mathrm{t}) = -\frac{\partial \mathbf{B}(\mathbf{r}, \mathrm{t})}{\partial \mathrm{t}} \tag{2.4}$$

$$\nabla \cdot \mathbf{D}(\mathbf{r}, \mathrm{t}) = 0 \tag{2.5}$$

$$\nabla \cdot \mathbf{B}(\mathbf{r}, \mathrm{t}) = 0 \tag{2.6}$$

where **r** and t denote the spatial and temporal dependence, respectively.

The electric and magnetic field vectors (**E** and **H**) are related to the electric displacement and magnetic flux density (**D** and **B**) by the constitutive relations. The constitutive relations describe the macroscopic properties of the medium through which the fields traverse. For the purpose of obtaining the mode field distributions and the corresponding mode propagation constants, the dielectric medium is assumed to be linear. In a linear medium the induced electric polarization ($\mathbf{P}(\mathbf{r}, \mathrm{t})$) is directly proportional to the electric field via the electric susceptibility (χ_e). Similarly, the magnetization ($\mathbf{M}(\mathbf{r}, \mathrm{t})$) is directly proportional to the magnetic field through the magnetic susceptibility (χ_m). In general, $\chi_e(\mathbf{r})$ and $\chi_m(\mathbf{r})$ are tensors. The constitutive relations therefore become:

$$\mathbf{D}(\mathbf{r}, \mathrm{t}) = \varepsilon_0\big(1 + \chi_e(\mathbf{r})\big)\mathbf{E}(\mathbf{r}, \mathrm{t}) = \varepsilon(\mathbf{r})\mathbf{E}(\mathbf{r}, \mathrm{t}) \tag{2.7}$$

$$\mathbf{B}(\mathbf{r}, \mathrm{t}) = \mu_0\big(1 + \chi_m(\mathbf{r})\big)\mathbf{H}(\mathbf{r}, \mathrm{t}) = \mu(\mathbf{r})\mathbf{H}(\mathbf{r}, \mathrm{t}) \tag{2.8}$$

The constants ε_0 and μ_0 are the vacuum permittivity and vacuum permeability, respectively. However, due to the non-magnetic nature of the dielectric, $\chi_m(\mathbf{r})$ may be taken as zero [5]. For the time being, we also assume that the propagation medium is isotropic ($\varepsilon(\mathbf{r})$ independent of field polarization).

Equations 2.7 and 2.8 may be used to rewrite Maxwell's equations. Based on the underlying assumption of a monochromatic optical field, the resultant expressions are satisfied by time-harmonic solutions, allowing us to write the vector fields as $\mathbf{E}(\mathbf{r}, \mathrm{t}) = \mathbf{E}(\mathbf{r})e^{\mathrm{j}\omega t}$ and $\mathbf{H}(\mathbf{r}, \mathrm{t}) = \mathbf{H}(\mathbf{r})e^{\mathrm{j}\omega t}$, for angular frequency ω. Here, $\mathbf{E}(\mathbf{r})$ and $\mathbf{H}(\mathbf{r})$ are the complex amplitudes of the electric and magnetic fields [1]. Clearly, the time-derivative of $\mathbf{E}(\mathbf{r}, \mathrm{t})$, for example, will now simply translate into multiplication by a factor jω (where $\mathrm{j} = \sqrt{-1}$). With the time-derivatives removed, Maxwell's equations in their new form may be combined to yield the following wave equation for $\mathbf{E}(\mathbf{r})$:

$$\nabla \times \nabla \times \mathbf{E}(\mathbf{r}) = \omega^2 \mu_0 \varepsilon(\mathbf{r})\mathbf{E}(\mathbf{r}) \tag{2.9}$$

A similar expression for $\mathbf{H}(\mathbf{r})$ may be derived in the same way. For a low-loss dielectric medium, the imaginary part of the complex quantity $\varepsilon(\mathbf{r})$, may be neglected. In this case, the real part of the permittivity is related to the medium's refractive index by $\varepsilon(\mathbf{r}) = \varepsilon_0 n^2(\mathbf{r})$. If we now consider a wave propagating along the optical axis of a lossless, perfectly cylindrical waveguide (say z), the field-phasor solution to equation 2.9 will have the following form [6],

$$\mathbf{E}(\mathbf{r}) = \mathbf{E}(x, y, z) = \mathbf{E}_0(x, y)e^{-j\beta z} \tag{2.10}$$

where β is the mode propagation constant. Substituting equation 2.10 into equation 2.9 leads to a so-called eigenvalue problem, where $\mathbf{E}_0(x, y)$ represents the eigenvector corresponding to an eigenvalue β.

Solutions for step-index fibres:

Equation 2.9 accounts for possible spatial variation in the permittivity and therefore describes wave propagation in inhomogeneous media. In the case of a step-index fibre (refer to Figure 2.1), the refractive index distribution may however be divided into homogeneous zones (i.e., core and cladding). In this case, the permittivity within a specific zone may be taken as position independent ($\varepsilon(\mathbf{r}) = \varepsilon$), resulting in the following simplified wave equation:

$$\nabla^2\mathbf{E}(\mathbf{r}) = k^2\mathbf{E}(\mathbf{r}) \tag{2.11}$$

Equation 2.11 is called the Helmholtz equation and the quantity $k = (n\omega)/c$ denotes the propagation constant (wavevector), where c is the speed of light in vacuum. Substituting equation 2.10 into equation 2.11 gives rise to the following eigenvalue problem [6]:

$$\nabla_T^2\mathbf{E}_0(x, y) = (k^2 - \beta^2)\mathbf{E}_0(x, y) \tag{2.12}$$

Here, $\nabla_T^2 = \frac{\partial^2}{\partial x^2} + \frac{\partial^2}{\partial y^2}$ is the transverse Laplacian. Solutions to equation 2.12 and the equivalent expression for $\mathbf{H}(\mathbf{r})$ can be found by re-casting the eigenvalue problem into cylindrical coordinates. For a step-index fibre, the mode propagation constants of the guided modes will be limited according to $k_2 < \beta < k_1$. Equation 2.12 therefore differs

for the core and cladding, depending on the sign of $(k^2 - \beta^2)$. To this end, two parameters are defined as follows:

$$\mathrm{U}^2 = a^2(k_1^2 - \beta^2), \qquad \text{for } \beta < k_1 \tag{2.13}$$

$$\mathrm{W}^2 = a^2(\beta^2 - k_2^2), \qquad \text{for } \beta > k_2 \tag{2.14}$$

U and W are so-called mode parameters, normalized with respect to the fibre core radius (a). Both resulting expressions are Bessel differential equations, which are satisfied by Bessel functions of the first kind (J) and modified Bessel functions of the second kind (K), in the core and cladding, respectively. Matching the fields at the core-cladding boundary, using the relevant boundary conditions, eventually yields a dispersion equation from which solutions to the mode fields and mode propagation constants can be found. Since the procedure for deriving the dispersion equations are well documented in several reference guides (see [6] for example), it will not be repeated here. It is however instructive to consider certain aspects of the theory.

The sum of equations 2.13 and 2.14 is a constant that depends on the design parameters of a step-index fibre:

$$\mathrm{V} = a\sqrt{k_1^2 - k_2^2} = ak_0\mathrm{NA} \tag{2.15}$$

NA is the numerical aperture defined in equation 2.2, whilst $k_0 = (2\pi)/\lambda$ is the vacuum wavevector, where λ represents the vacuum wavelength. The quantity V is commonly referred to as the normalized frequency, or V-number, and provides an elegant measure of the number of modes supported by a given fibre, at a given wavelength. Inspection of equation 2.15 reveals that the V-number decreases for an increase in wavelength . It therefore follows that a specific fibre will support more modes at shorter wavelengths. Clearly then, a wavelength exists for which the V-number becomes small enough for the fibre to support only a single (spatial) mode. This is called the single-mode cut-off wavelength and it can be shown to occur for $\mathrm{V_c} \approx 2.405$ [6]. In a similar way, cut-off wavelengths are defined for all the higher-order modes.

Fibre modes can generally be classified into three groups, namely transverse electric (TE), transverse magnetic (TM) and hybrid modes (HE and EH). Each group is associated with a particular dispersion equation, based on the relevant field components.

Solving the dispersion equation analytically is extremely complex, especially for hybrid modes, where the electric and magnetic fields have axial components. It is therefore common to employ the weakly-guiding approximation, under which $(n_1/n_2 \approx 1)$. In this case, the axial field components are weak in comparison to the transverse field components, allowing us to represent all fibre modes using a unified dispersion equation [7], [4]:

$$\mathrm{U}\frac{\mathrm{J}_{l-1}(\mathrm{U})}{\mathrm{J}_{l}(\mathrm{U})} = \mathrm{W}\frac{\mathrm{K}_{l-1}(\mathrm{W})}{\mathrm{K}_{l}(\mathrm{W})}, \qquad l = \begin{cases} 1 & \text{for } \mathrm{TE}_{0\mathrm{m}},\ \mathrm{TM}_{0\mathrm{m}} \\ q+1 & \text{for } \mathrm{EH}_{q\mathrm{m}} \\ q-1 & \text{for } \mathrm{HE}_{q\mathrm{m}} \end{cases} \tag{2.16}$$

In equation 2.16, J and K are the mentioned Bessel functions, whilst the subscripts *q* and *m* are the mode order and radial mode order, respectively. By using the weakly-guiding approximation, the real fibre modes may be grouped together according to their mode orders. Since the mode propagation constants for the real modes within every group are degenerate in this approximation, they can be superimposed to yield linearly polarized (LP_{lm}) modes [8]. Since equation 2.16 is transcendental, a graphical or numerical approach is still required to solve for the mode fields and propagation constants. For the case of conventional fibres, it however presents a significant simplification for a small penalty in accuracy.

In the single-mode regime, for which $\mathrm{V} < 2.405$, very useful approximate analytical solutions for quantities of interest have been derived. Of particular importance is the so-called normalized propagation constant, which may be calculated from the design parameters of the fibre alone, according to [8]:

$$\mathrm{b}_{\mathrm{eff}} = \frac{(\beta/\mathrm{k}_0)^2 - \mathrm{n}_2^2}{\mathrm{n}_1^2 - \mathrm{n}_2^2} = 1 - \left[\frac{1+\sqrt{2}}{1+(4+\mathrm{V}^4)^{1/4}}\right]^2 \tag{2.17}$$

As before, n_1 and n_2 denote the refractive index of the core and cladding, respectively. Similarly, it has been shown that the mode field diameter (MFD) may be calculated from the following empirical relation [9],

$$\mathrm{MFD} = 2a\left[0.65 + \frac{1.619}{\mathrm{V}^{3/2}} + \frac{2.879}{\mathrm{V}^6}\right] \tag{2.18}$$

where *a* denotes the core radius. Although these expressions are strictly applicable to step-index fibres, they often prove very useful in the evaluation of real fibres.

Solutions for arbitrary refractive index distributions:

The preceding theory is often applicable to real fibres, for which the refractive index profile is approximately step-index. However, once the refractive index distribution of a fibre becomes more involved, analytical formulations to the boundary conditions between homogeneous zones may become impossible. Furthermore, in the case of index-guiding photonic crystal fibres (PCF), the index-contrast between the dielectric cladding and the air-holes precludes the use of the weakly-guiding approximation [10]. Representations of real fibre cross-sections, treated throughout this thesis, are shown in Figure 2.2. Optical characterization of these fibres require solutions to equation 2.9, or an equivalent expression. To this end, numerical procedures have to be considered.

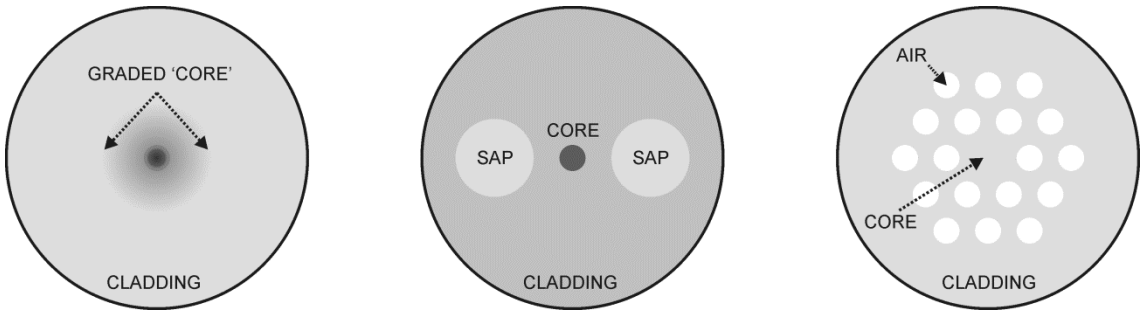

(a) (b) (c)

Figure 2.2: Illustrations of real fibre cross-sections encountered in this thesis. (a) A graded-index fibre, where the core refractive index is a gradual function of the fibre radius. (b) A PANDA polarization-maintaining (PM) fibre, with stress-applying parts (SAP) in its cladding. (c) A photonic crystal fibre (PCF) with a triangular air-hole lattice in its cladding.

The numerical procedure of choice throughout this thesis is provided by the commercial software COMSOL [11] and makes use of the finite element method (FEM). The FEM solves the eigenvalue equation, associated with equation 2.9, by approximating the boundary value problem as a linear system of integral equations, using Galerkin's method of weighted residuals. By dividing the computational domain into a number of small triangular subdomains, the FEM greatly simplifies the implementation of Galerkin's method. The linear system of integral equations are finally solved through an iterative method [10], [4].

The FEM thus provides us with the mode propagation constants and corresponding mode fields at a single frequency for a given optical fibre. In Chapters 4 and 5 this method will be applied to commercial fibres for the purpose of studying their suitability as optical parametric amplifiers. The following section will be concerned with the frequency dependence of the solutions, obtained from the software.

2.1.2 Chromatic Dispersion

A complete evaluation of the guidance characteristics of a fibre needs to account for the frequency dependence of the optical mode's propagation constant, called chromatic dispersion. Chromatic dispersion may be decomposed into a contribution due to the bulk material and a contribution due to waveguiding.

In the near infrared spectral region, the dispersion of a bulk material is well approximated by the Sellmeier equation [12]:

$$n^2(\lambda) = 1 + \sum_{j=1}^{3} \frac{B_j \lambda^2}{\lambda^2 - \lambda_j^2} \tag{2.19}$$

The wavelengths, λ_j, are the resonance wavelengths at which the specific medium absorbs light, while the constants, B_j, indicate the strength of each resonance. As mentioned in the introduction to Section 2.1, the radial variation in the refractive index of an optical fibre is accomplished by doping a host material (SiO_2 for example) with another material. These so-called dopant materials can be categorized as index increasing or index decreasing, depending on whether they increase or decrease the refractive index of the host. In this work we shall only consider silica-based fibres for which the Sellmeier coefficients (λ_j and B_j) are given by Fleming [13]. A number of dopants, such as GeO_2, P_2O_5, B_2O_3 and F, will be considered and their Sellmeier coefficients can be found in [12] and [13] (also see [14] and [15]).

In order to calculate the complete material dispersion, associated with an arbitrarily doped portion of the fibre, it is necessary to include the dispersion of the host medium and the dopant medium. From the respective Sellmeier coefficients, the refractive index of the host material (n_0) and the refractive index of the host, doped with a known concentration (m_+) of an index increasing dopant (n_+) (for example),

can be calculated at a given wavelength, λ. Using these values, the corresponding refractive index at λ for an arbitrary doping concentration (m) can be calculate from [16]:

$$n = \left[n_0^2 + \frac{m}{m_+}(n_+^2 - n_0^2)\right]^{1/2} \tag{2.20}$$

Here, the doping concentrations are typically specified in units of % (mol).

Even in the absence of material dispersion, the optical mode of a fibre still depends on frequency. This so-called waveguide dispersion is related to the V-number's dependence on wavelength (refer to equation 2.15). Physically, the confinement of the mode field changes with wavelength, leading to a change in the mode field distribution relative to the waveguide structure and its associated refractive index distribution. As a result, the mode experiences a change in its so-called effective refractive index (n_{eff}). The effective refractive index of a given mode is related to the mode propagation constant through:

$$\beta(\omega) = \frac{n_{eff}(\omega)\omega}{c} \tag{2.21}$$

By considering a Taylor expansion of the mode propagation constant, about a central frequency ω_0, the effects of chromatic dispersion may be isolated [5]:

$$\beta(\omega) = \beta_0 + \beta_1(\omega - \omega_0) + \frac{1}{2}\beta_2(\omega - \omega_0)^2 + \cdots \tag{2.22}$$

$$\beta_m = \left(\frac{d^m\beta}{d\omega^m}\right)_{\omega=\omega_0} \tag{2.23}$$

Here, the parameter β_1 denotes the inverse of the group velocity of a pulse, associated with a spectrum about ω_0. From equation 2.23 it follows that β_2 denotes the dispersion in the group velocity and is subsequently called the group-velocity dispersion (GVD) parameter. Chromatic dispersion in fibres is historically presented by the dispersion parameter (D) and is related to the GVD as follows:

$$D = -\frac{2\pi c}{\lambda^2}\beta_2 \tag{2.24}$$

Figure 2.3(a) shows the wavelength dependence of the core (3.5% GeO_2-doped SiO_2), cladding (pure SiO_2) and effective refractive index, for the fundamental mode (LP_{01}) and a higher-order mode (LP_{11}), of a typical step-index fibre ($a = 4.15$ μm). It is clear that the n_{eff}-values for both guided modes are bound by the refractive index values for the core and cladding. For wavelengths longer than 1.32 μm, the refractive index of the cladding exceeds the effective index of the LP_{11} mode, resulting in the V-number (equation 2.15) dropping below 2.405, and the mode reaching cut-off (see Section 2.1.1). Figure 2.3(b) shows the dispersion (D) associated with the core and cladding materials, as well as the total chromatic dispersion of the LP_{01} and LP_{11} modes of the fibre. The values for the zero material dispersion wavelength of the core and cladding are 1.288 μm to 1.273 μm, respectively (see inset Figure 2.3(b)). This increase is consistent with the linearity in equation 2.18 and the general observation that a higher core refractive index will increase the wavelength of zero material dispersion. It is also found that the influence of waveguide dispersion results in a further increase in the zero dispersion wavelength (ZDW) of the fundamental mode. This increase may be attributed to the negative contribution from waveguide dispersion in the spectral region about the zero material dispersion wavelength [4]. In fact, the ZDW can similarly be increased beyond 1.6 μm, through the use of smaller cores, higher levels of core doping, and additional features in the refractive index distribution of the fibre. The dispersion of the LP_{11} mode in Figure 2.3(b) remains negative over the wavelength range of interest and terminates at its cutoff wavelength.

Dispersion and the ZDW are of great importance for pulse propagation and nonlinear processes in fibres. In particular, it governs the phase-matching process that is crucial for fibre FWM. The theory related to FWM follows in Section 2.3. For the time being, it is sufficient to note that the short-wavelength side with respect to the ZDW is called the normal-dispersion regime ($D < 0$), whilst the long-wavelength side is called the anomalous-dispersion regime ($D > 0$).

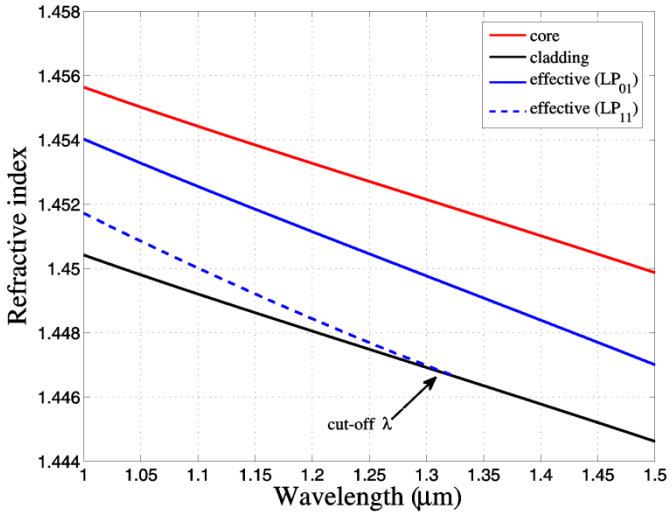

(a)

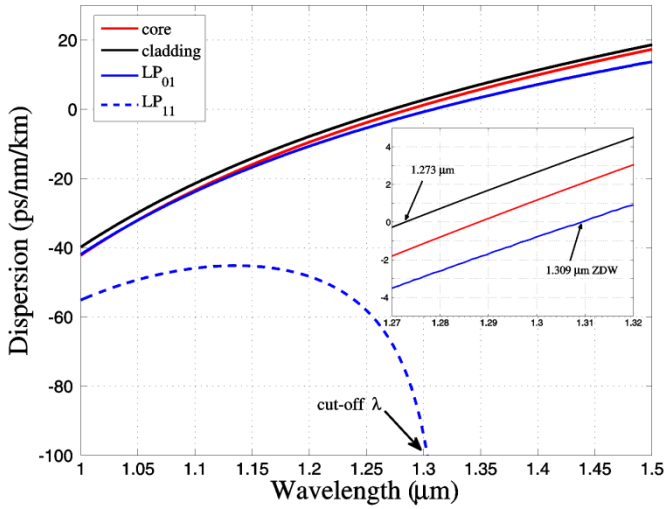

(b)

Figure 2.3: (a) Wavelength dependence of the core (SiO_2 / 3.5% GeO_2), cladding (SiO_2) and effective refractive index for the LP_{01} and LP_{11} modes. (b) Dispersion parameter associated with the core and cladding material, as well as the total chromatic dispersion for the LP_{01} and LP_{11} modes. Both graphs indicate the cut-off wavelength for the LP_{11} mode. The inset to (b) shows an increase in the zero dispersion wavelength (ZDW) for the LP_{01} mode (1.309 μm), relative to that of the cladding material (1.273 μm).

2.1.3 Modal Birefringence

The theory of Section 2.1.1 assumed an isotropic material with perfect cylindrical symmetry. An optical fibre satisfying these assumptions is called an ideal fibre. In an ideal fibre, the fundamental mode is two-fold degenerate. The two degenerate

fundamental modes are however distinguishable through their mutually orthogonal polarizations. If one of these modes is excited, it will propagate with its polarization unperturbed [5].

Real fibres have cross sections which are not precisely symmetrical. These asymmetries are due to manufacturing flaws as well as external stress acting on the fibre, leading to anisotropy. As a result of these imperfections, the degeneracy of the fundamental mode is broken and the mode propagation constants differ from each other. Since the imperfections in real fibres also vary along the length of the fibre, the amount by which the mode propagation constants differ from each other also vary. This leads to random changes in the polarization of an excited mode [5].

The random changes in the polarization of the fundamental mode may be prevented through the introduction of a large amount of birefringence. This birefringence can be initiated through geometrical anisotropy (elliptical core) or by the application of stress [4]. The intentional birefringence introduces two orthogonal principae axes in the fibre. The magnitude of the material birefringence is defined as the difference between the refractive index along each of the principle axes, $B_0 = |n_x - n_y|$. If light is polarized parallel to either of these principle axes, its polarization will be maintained as it propagates along the fibre. Hence, these types of fibres are called polarization maintaining (PM) fibres. Since the method of stress-induced birefringence has been proven to be the most effective for fibres relevant to this thesis [4], I shall briefly consider it here.

A typical preform for the fabrication of PM fibre, has a circular core, a circular cladding and a so-called stress-applying part (SAP) on either side of the core (see, for example, the PANDA fibre in Figure 2.2(b)). The SAPs can have a variety of shapes and sizes, both of which influence the resulting birefringence. The different fibre regions (core, cladding and SAP) all have different elastic and thermal properties. Since the fibre is drawn at high temperatures and then cooled down, the differences in these properties lead to the formation of stress. The magnitude of the induced stress as well as the resulting material birefringence, over the fibre cross-section, may be calculated using COMSOL [17]. The numerical procedure relies upon the plane-strain approximation, whereby a zero-valued strain in the z-direction (along the fibre axis), is

assumed. This approximation is justified for an optical fibre, where the transverse dimensions are small compared to its length [18], [19].

COMSOL uses the FEM to relate the thermal displacements, corresponding to a given temperature change (ΔT), to the strain tensor components (ε_{ij}). From ε_{ij} and the relevant material's properties, which includes Poisson's ratio (ν), Young's modulus (E) and the thermal expansion coefficient (α), the stress tensor components (σ_{ij}) are calculated. The stress tensor components are related to the refractive index tensor components through [19],

$$n_x = n_{x0} + C_1\sigma_x + C_2\sigma_y \tag{2.25}$$

$$n_y = n_{y0} + C_2\sigma_x + C_1\sigma_y \tag{2.26}$$

in what is known as the photo-elastic effect. The refractive indices, n_{x0} and n_{y0}, correspond to a stress-free material. By subtracting equation 2.26 from equation 2.25, the following expression for the material birefringence is obtained:

$$B_0 = (n_{x0} - n_{y0}) + C(\sigma_x - \sigma_y) \tag{2.27}$$

Here, the constant $C = C_1 - C_2$ is known as the relative stress-optic coefficient. The first term accounts for geometrical anisotropy and is negligible for the PANDA fibre of Figure 2.2(b). The second term represents the contribution from stress-induced birefringence.

The values for n_x and n_y, obtained from COMSOL's structural mechanics module, may now be passed on to the RF module (from Section 2.1.1) to solve for the mode propagation constants and mode field distributions in a PM fibre. In Chapter 4 this approach will be applied to a real PM fibre to investigate how the modal birefringence, defined as $B_m = |n_{eff,x} - n_{eff,y}|$, may be exploited for the purpose of fibre FWM.

2.1.4 Photonic Crystal Fibres

The term photonic crystal fibre refers to a broad range of waveguides, all characterized by a periodic transverse microstructure [20]. In this thesis, we shall only concern ourselves with index-guiding PCF, on which a brief introduction follows.

An example of the cross-section of a typical PCF is shown in Figure 2.2(c). The fibre consists of a single material (silica), covered with a triangular lattice of circular air-holes. By removing the central air-hole, a so-called silica defect is formed, which acts as the fibre core. The fibre structure can be entirely described by the pitch (Λ) and relative diameter of the air-holes (d/Λ), where the pitch is the distance between the centres of adjacent air-holes. The guidance mechanism in an index-guiding PCF is essentially the same as for a conventional all-solid fibre. The air-holes in the microstructured cladding reduce its effective refractive index (not to be confused with the modal index), resulting in light being confined to the silica core via a modified form of total internal reflection [21].

In analogy to the theory for step-index fibres (Section 2.2.1), the guidance characteristics of a PCF may be expressed in terms of a normalized frequency (V). Although various definitions for the V-number of a PCF have been proposed [22], [23], the definition by Koshiba and Saitoh proves particularly useful [24]:

$$V_{eff} = k_0 a_{eff} \sqrt{n_1^2 - n_2^2} \tag{2.28}$$

Here, the core radius a_{eff} is assumed to have a magnitude of $\Lambda/\sqrt{3}$, whilst n_1 and n_2 denote the refractive index of the core and effective refractive index of the cladding, respectively. The refractive index of the photonic crystal cladding is defined as the effective index of the fundamental space-filling mode of the triangular air-hole lattice, n_{FSM} [22].

Experimental observations revealed that light at short wavelengths ($\lambda \ll \Lambda$) are able to *resolve* the air-holes, leading to mode fields being confined primarily to the silica portions of the cladding (i.e. $n_{FSM} \approx n_{silica}$). In contrast, as the wavelength becomes comparable to the pitch, the mode field will be distributed over the silica-air structure, resulting in a lowered value for n_{FSM} [21]. This property of PCF has profound consequences for its guidance characteristics. As for a step-index fibre (equation 2.15), a decrease in wavelength will lead to an increase in V_{eff}. However, whereas the NA of a step-index fibre has a weak dependence on wavelength, the NA of a PCF shows significant dispersion due to the wavelength dependence of n_{FSM}. Consequently, a reduction in wavelength leads to a reduced NA, thus counter-acting the increase in k_0.

This scenario is in contrast with that of a step-index fibre, where the V-number and therefore the number of guided modes approaches infinity in the short wavelength limit. In fact, for a suitable choice of design parameters (Λ, d), it is possible to have a single guided mode irrespective of wavelength [22]. From the definition in equation 2.28, the single-mode cutoff condition for PCF was confirmed to be $V_{eff} < 2.405$ [24]. According to this value, it was subsequently determined, and experimentally confirmed, that so-called endlessly single-mode guidance can be achieved for $d/\Lambda < 0.43$.

The equivalence in the cut-off conditions for a step-index fibre (equation 2.15) and PCF (equation 2.28) confirms that the two waveguides are governed by the same basic physics [23]. In light of this, equations 2.17 and 2.18 apply to PCF within certain limits of the design parameters [24]. Although these approximate results are useful, they still require a value for n_{FSM}, which typically calls for a numerical solution to equation 2.9. However, based on the formalism of Ref. [24], empirical relations for V_{eff} and the corresponding W-parameter, defined as

$$W = k_0 a_{eff} \sqrt{n_{eff}^2 - n_2^2} \tag{2.29}$$

were determined from detailed FEM simulations (refer to equation 2.14) [25]. Consistent with equation 2.28, n_2 denotes n_{FSM}. Both empirical relations have the following form,

$$X\left(\frac{\lambda}{\Lambda}, \frac{d}{\Lambda}\right) = A_1 + \frac{A_2}{1 + A_3 \exp(A_4 \lambda/\Lambda)} \tag{2.30}$$

where

$$A_i = a_{i0} + a_{i1}\left(\frac{d}{\Lambda}\right)^{b_{i1}} + a_{i2}\left(\frac{d}{\Lambda}\right)^{b_{i2}} + a_{i3}\left(\frac{d}{\Lambda}\right)^{b_{i3}} \tag{2.31}$$

Here, X denotes V_{eff} or W, and the values of the fitting parameters depend on their respective sets of coefficients (a_{i0} to a_{i3} and b_{i1} to b_{i3}), given in Ref. [25]. By using these empirical relations, V_{eff} can be used to calculate n_{FSM}, which in turn can be used to calculate n_{eff}, once W is known.

For the purpose of obtaining accurate results for the chromatic dispersion of a PCF, the FEM of Section 2.1.1 is still used to solve the wave equation (equation 2.9). However, since the numerical approach can be time consuming, equation 2.30 and the corresponding coefficients are very useful for the purpose of quickly evaluating the chromatic dispersion of the fundamental mode, for a given set of design parameters. The reported accuracy, relative to FEM solutions, of less than 0.15% for $\lambda/\Lambda < 1.5$ and $W > 0.1$, is also sufficient in most cases. This is illustrated by the comparison in Figure 2.4, where black circles are the FEM-calculated dispersion for a fibre having $\Lambda = 6.6$ μm and $d/\Lambda = 0.46$, and the blue line is the results from the empirical relations.

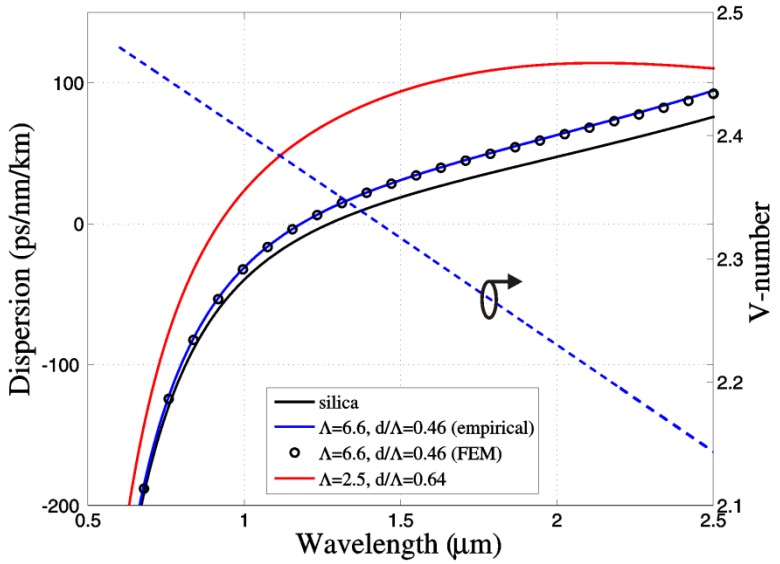

Figure 2.4: Chromatic dispersion calculated from the FEM (black circles) and from empirical relations (blue lines), for a PCF characterized by $\Lambda = 6.6$ μm and $d/\Lambda = 0.46$ (left-hand axes). The material dispersion for silica (black line) and the chromatic dispersion for another PCF ($\Lambda = 2.5$ μm and $d/\Lambda = 0.64$: red line), are also shown. The wavelength-dependent V-number, corresponding to the blue curve, is given on the right-hand axes, illustrating the range of single-mode guidance.

The strong waveguide dispersion associated with PCF, through the characteristics of n_{FSM}, can drastically influence the chromatic dispersion of the waveguide. Through the appropriate choice of Λ and d, a positive contribution from waveguide dispersion can shift the ZDW well below the zero material dispersion wavelength of silica (black line in Figure 2.4). This is the case for both fibres in Figure 2.4, where the blue ($\Lambda = 6.6$ μm and $d/\Lambda = 0.46$) and red ($\Lambda = 2.5$ μm and $d/\Lambda = 0.64$) lines have ZDWs of 1182 nm

and 920 nm, respectively. The dispersion can similarly be tailored to give a ZDW in the visible spectrum, or an ultra-flat dispersion profile [26]. The dashed blue line in Figure 2.4 (right-hand axes) furthermore gives the V-number, as a function of wavelength for the case with $\Lambda = 6.6$ μm and $\mathrm{d}/\Lambda = 0.46$. The result clearly illustrates the role of $\mathrm{n_{FSM}}$ in extending the single-mode wavelength range of the PCF.

2.2 Nonlinear Phenomena in Fibres

Through the course of formulating the wave equations of Section 2.1, the dielectric medium was assumed linear. Although this assumption is valid when the EM fields are relatively weak, it cannot describe the response of the medium for the case of intense fields. It is then necessary to consider a more general expression for the induced polarization in the medium,

$$\mathbf{P}(\mathbf{r},\mathrm{t}) = \varepsilon_0\left(\chi^{(1)}\cdot\mathbf{E} + \chi^{(2)}\cdot\mathbf{E}\cdot\mathbf{E} + \chi^{(3)}\cdot\mathbf{E}\cdot\mathbf{E}\cdot\mathbf{E} + \cdots\right) \tag{2.32}$$

where $\mathbf{E} = \mathbf{E}(\mathbf{r},\mathrm{t})$, and where the susceptibility tensors ($\chi^{(j)}$) are assumed to be independent of spatial coordinate **r** (homogeneous medium). The first term in equation 2.32 is the linear contribution to the polarization, which gives rise to the refractive index of the medium, $\mathrm{n}^2 = 1 + \chi^{(1)}$ (refer to Section 2.1.1). The terms proportional to $\chi^{(2)}$ and $\chi^{(3)}$ have a nonlinear dependence on the electric field and lead to so-called nonlinear effects. Nonlinear effects influence light propagation in a variety of ways. Depending on the attributes of the incident light and propagation medium, different terms in the expansion for $\chi^{(2)}$ and $\chi^{(3)}$ will dominate. Since we are only concerned with silica-based fibre, which is a centrosymmetric medium, the effects from $\chi^{(2)}$ are absent [26]. The lowest-order nonlinear effects in fibres are therefore associated with the third-order nonlinear susceptibility ($\chi^{(3)}$).

Nonlinearities may be sub-categorized as either parametric or nonparametric processes. The word parametric refers to a system where the initial and final quantum mechanical states of the system are identical [26]. As such, parametric processes involve transitions between the molecular ground level and so-called virtual levels, whilst nonparametric processes involve transitions between real levels. The distinction is important, since parametric processes are characterized by a real susceptibility and

conservation of photon energy. For this reason, parametric processes are also called *elastic*. In contrast, nonparametric processes involve an imaginary contribution to the susceptibility, and may be described as *inelastic* as a result of energy exchange with the medium.

Although nonlinearities are often undesired due to their influence on the spectral and temporal properties of incident light, they can be employed in a host of constructive ways. For the purpose of this thesis, the most important application is wavelength conversion. In this section I will give an overview of the third-order nonlinearities applicable to a study of fibre optical parametric amplifiers and oscillators. As far as nonparametric processes are concerned, we will consider stimulated inelastic scattering. Following this, the parametric processes of nonlinear refraction and four-wave mixing will be introduced.

2.2.1 Stimulated Inelastic Scattering

Stimulated inelastic scattering processes are of great consequence for light propagation in a fibre medium. Here, the emphasis is on two of these processes in particular, namely stimulated Raman scattering (SRS) and stimulated Brillouin scattering (SBS). Both SRS and SBS are consistent with a picture wherein an incident photon (ω_p) is annihilated, leading to the creation of a photon at reduced energy (ω_s) along with a phonon at frequency $\Omega = \omega_p - \omega_s$, thereby conserving energy and momentum. Subsequently, the evolution of the so-called pump (I_p) and Stokes (I_s) intensities along the fibre, for both processes, may described as follows [5]:

$$\frac{dI_p}{dz} = -\frac{\omega_p}{\omega_s} g I_p I_s - \alpha_p I_p \tag{2.33}$$

$$\frac{dI_s}{dz} = q g I_p I_s - \alpha_s I_s \tag{2.34}$$

Here, g is the applicable gain coefficient (related to $\chi^{(3)}$), whilst α_p and α_s denote the fibre attenuation at the pump and Stokes wavelengths, respectively. The frequency ratio in equation 2.33 accounts for the loss associated with the phonon. Depending on whether equation 2.34 describes forward propagating SRS or backward propagating SBS, the constant q has a value of 1 or -1. Whilst backward propagating SRS can also

occur, the forward propagating process has a lower threshold and dominates in the absence of seeding, assuming a pulsed pump source.

Whilst the origin and mathematical description for SRS and SBS are very similar, their associated gain spectra differ substantially. Not only does this lead to different threshold conditions, but it also determines the circumstances under which either process can be enhanced or suppressed. For this reason, we briefly consider them separately.

Stimulated Raman scattering:

Quantum mechanically, the generated SRS phonon, mentioned in the preceding general discussion, corresponds to an increase in the vibrational energy state of an interacting molecule. The process can also occur in reverse, where the vibrational energy of the molecule is reduced, upon the annihilation of a lower-energy photon, leading to the creation of a higher-energy photon (called the anti-Stokes process). The probability of the anti-Stokes process is however relatively small at thermal equilibrium, owing to the Boltzmann distribution [26].

As a result of the amorphous nature of silica glass, the discrete molecular vibrational frequencies spread out to form a continuum. This leads to SRS having a very broad gain spectrum of up to 40 THz, relative to the pump frequency. The peak of the gain spectrum is typically located at a downshifted frequency of 13.2 THz, where g_R has a value of 1×10^{-13} m/W, at a wavelength of 1 μm [5]. This value for g_R assumes co-polarized pump and Stokes waves. When the pump and Stokes waves are however orthogonally polarized, or if one wave is unpolarized, the gain coefficient has been shown to reduce by a factor 10, or 2, respectively [27]. The gain coefficient furthermore shows a dependence on the fibre composition. For the typical case of a GeO_2-doped fibre core (see Section 2.1.2), the maximum value of g_R may experience an enhancement of up to 8 times, whilst the peak remains at roughly 13 THz [28].

Solutions to equations 2.33 and 2.34 describe the growth of the Stokes wave in the presence of pump depletion and fibre loss. However, if we neglect the influence of pump depletion (first term in equation 2.33), a simple analytical expression for the SRS gain (G_R) may be derived. For the case where $\alpha_s = \alpha_p = \alpha$, the solution in units of nepers is given by [29],

$$G_R = \frac{g_R P_p L_{eff}}{A_{eff}} \tag{2.35}$$

where the effective interaction length follows as:

$$L_{eff} = \frac{(1 - e^{-\alpha L})}{\alpha} \tag{2.36}$$

In equation 2.35, $P_p = I_p A_{eff}$, where A_{eff} denotes the effective core area of the fibre. The SRS threshold may be defined as the input pump power for which the output Stokes power equals the output pump power. This so-called critical pump power represents an upper limit to the pump power, after which the assumption of negligible pump depletion is violated. According to this definition, the SRS gain required to reach threshold was calculated as $G_R \approx 16$ Np, from which the critical pump power may be calculated [29]. The calculated gain may be converted from nepers to decibels using, $G_R[\mathrm{dB}] = 4.343 \times G_R[\mathrm{Np}]$.

The preceding mathematical description of SRS is strictly only applicable to continuous wave (CW) pump and Stokes light. When pump pulses are used, the temporal dynamics must be accounted for via the inclusion of dispersion. From a comparison of the CW (equations 2.33 through 2.35) and time-dependent theories, the most important difference is found to occur as a result of group-velocity mismatch between the pump and Stokes pulses (refer to Section 2.1.2). Since the pulses for the pump and Stokes waves are centred about different wavelengths, their group-velocities are different and the pulses will therefore only overlap over a certain propagation distance. This distance is called the walk-off length and is calculated using [5]:

$$L_W = \frac{T_0}{\left|\beta_1(\lambda_p) - \beta_1(\lambda_s)\right|} \tag{2.37}$$

β_1 is defined in equations 2.22 and 2.23, whilst T_0 denotes pulse width. For the case of a conventional fibre, where the role of waveguide dispersion is minimal, the relative group delay (denominator in equation 2.37) may be calculated from the material dispersion of silica. At pump and Stokes wavelengths of 1080 nm and 1134 nm,

respectively, we find roughly 1 ps/m. Since this thesis is only concerned with fibre lengths ≤ 200 m, group-velocity mismatch will only become a concern for SRS if pulse widths well below 1 ns are used. Note that these values will be different for PCF, where the waveguide dispersion is substantial. In this so-called quasi-CW regime, where the influence of group-velocity mismatch is limited, equations 2.33 through 2.35 are approximately valid.

Stimulated Brillouin scattering:

Whereas SRS is characterized by an optical phonon, SBS is associated with an acoustic phonon. As the acoustic wave propagates through the optical medium, it modulates the refractive index through the process of electrostriction [26]. This leads to a moving grating. When a sufficiently intense pump wave co-propagates in the optical medium, it undergoes Bragg diffraction. The diffracted wave is at a downshifted frequency (Stokes), owing to the Doppler effect associated with the moving grating [5]. The backward-propagating Stokes wave now interferes with the incident pump wave which reinforces the acoustic wave. In turn, the reinforced acoustic wave will scatter more of the incident pump wave, which will interfere constructively with the existing Stokes wave. Provided that the attributes of the acoustic wave are such that frequency and momentum are conserved, the amplitudes of the acoustic and Stokes waves can build up rapidly. SBS is typically initiated through thermally excited acoustic phonons.

In contrast to SRS, SBS has a very narrow gain spectrum ($\Delta\nu_B$), ranging from 10 MHz to 100 MHz. This relatively small value is related to the acoustic phonon lifetime (T_B), which has a value of approximately 10 ns. Relative to the pump frequency, the Brillouin gain peak is downshifted with a value ranging from 10 GHz to 100 GHz. The SBS frequency-shift and gain bandwidth are proportional to $1/\lambda$ and $1/\lambda^2$, respectively. The SBS frequency- shift furthermore shows an inverse dependence on the GeO_2 doping concentration in the fibre core. In spite of these relationships, the peak SBS gain coefficient (g_B) remains roughly constant at a value of 5×10^{-11} m/W. This can be explained at the hand of the SBS gain bandwidth's inherent proportionality to $1/\lambda^2$. The decrease in g_B at longer wavelengths is counter-acted by a narrowing of the gain spectrum [5]. In analogy to the SRS gain coefficient, the quoted value for g_B assumes co-polarized pump and Stokes waves. It has been shown that this value is reduced by a factor 1.5 for randomly varying relative polarization angles [30].

The peak SBS gain coefficient is nearly three orders of magnitude larger than the value for SRS. The SBS critical pump power may therefore be expected to be significantly lower than that of SRS. Using the same approach as before (equations 2.33 and 2.34), an analytical expression for the SBS gain can be calculated. The solution in units of nepers is given by [29], [31],

$$G_B = \frac{g_B P_p L_{eff}}{A_{eff}} \left(1 + \frac{\Delta\nu_p}{\Delta\nu_B}\right)^{-1} \tag{2.38}$$

where $\Delta\nu_p$ is the linewidth of the pump source, and the other parameters have their usual meanings. The SBS gain required to reach threshold was calculated as $G_B \approx 21$ Np [29]. From equation 2.38 and the threshold value for G_B it is clear that the SBS critical pump power can be substantially lower than of SRS. However, for the case of CW waves, the effective SBS gain coefficient may be significantly reduced if the pump linewidth exceeds the SBS bandwidth (see bracketed terms in equation 2.38). Also in the quasi-CW regime, the SBS threshold can be increased by using a pulse width short in comparison to the acoustic phonon lifetime.

2.2.2 Four-Wave Mixing

In the presence of third-order nonlinearity, the refractive index may be written as $n^2 = 1 + \chi_{eff}$, by re-casting equation 2.32 as $\mathbf{P} = \varepsilon_0\left(\chi^{(1)} + \chi^{(3)} \cdot \mathbf{E} \cdot \mathbf{E} + \cdots\right)\mathbf{E} = \varepsilon_0 \chi_{eff} \mathbf{E}$ [26]. This expression is analogous to the definition of the *linear* refractive index (now denoted by n_0) of Section 2.1 (refer to equations 2.7 and 2.9). A direct comparison implies the following modified relation for the refractive index [5]:

$$n = n_0 + n_2 |\mathbf{E}|^2 \tag{2.39}$$

Here, $n_2 = \frac{3}{8n}\Re\left(\chi^{(3)}\right)$ is the nonlinear index coefficient (or nonlinear refractive index). In general $\chi^{(3)}$, and subsequently n_2, depends on frequency, fibre composition and polarization. It is however common throughout the literature to approximate n_2 as frequency independent [5]. In this case, its value for silica fibre may nominally be taken as of 2.6×10^{-20} m^2/W, where a linearly polarized field is assumed.

The intensity-dependent term in equation 2.39 is responsible for so-called nonlinear refraction, which leads to many interesting nonlinear effects. Generally, the processes of self-phase modulation (SPM) and cross-phase modulation (XPM) are dominant. SPM involves a self-induced intensity-dependent phase-shift in a propagating optical field. Mathematically, its influence can be understood by considering the accumulated phase of a propagating optical field, given by $\phi = \mathrm{n}k_0\mathrm{L}$. XPM may similarly be explained as the intensity-dependent phase-shift in an optical field, induced by a field at a second frequency. Both processes are related to spectral broadening and also play an important role in the workings of more involved nonlinear processes, such as four-wave mixing (FWM). The nature of this involvement follows in the discussion of Section 2.3.

FWM refers to a nonlinear interaction among four optical waves [32]. In analogy to SRS and SBS, the FWM process relies on the conservation of energy and momentum. However, as a result of the active participation of the optical medium, momentum conservation is guaranteed for the scattering processes of Section 2.2.1. This is not the case for FWM, where significant transfer of energy between the interacting waves will only take place if the following conditions are satisfied:

$$\omega_1 + \omega_2 = \omega_3 + \omega_4 \tag{2.40}$$

$$\beta_1 + \beta_2 = \beta_3 + \beta_4 \tag{2.41}$$

Physically, equation 2.40 corresponds to a process in which two photons at frequencies ω_1 and ω_2 are annihilated, whilst one photon at a higher frequency (ω_3) and one at a lower frequency (ω_4), with respect to $\omega_c = (\omega_1 + \omega_2)/2$, are created. In keeping with Section 2.2.1, components at frequencies ω_1 and ω_2 are associated with optical pump waves, whilst the generated low frequency and high frequency components are called Stokes and anti-Stokes waves, respectively. Four optical modes satisfying equation 2.41 are said to be phase-matched. From the discussion on chromatic dispersion (Section 2.1.2), it is clear that the phase-matching process depends on the material composition and dimensions of the optical waveguide. Note that the notation for the mode

propagation constants of the four waves can be confused with the Taylor series coefficients of equations 2.22 and 2.23. It is therefore important to consider the context. In practice, FWM can be observed for intense pump waves, in the presence or absence of external seeding at the Stokes and anti-Stokes wavelengths. When no power at ω_3 and ω_4 are supplied, both waves will be initiated from noise and the process is called optical parametric generation (OPG). Alternatively, seed power may be provided at ω_3, for example, in which case the interaction will lead to amplification at the anti-Stokes wave, as well as power conversion from the pump waves to the Stokes wave. In this case, the anti-Stokes process is called optical parametric amplification (OPA), whilst the Stokes process may be referred to as wavelength conversion. With the conditions of equations 2.40 and 2.41 satisfied, FWM offers very attractive features. Specifically for the purpose of wavelength conversion, examples include:

(1) Waves can be generated, or amplified, at arbitrary wavelengths, depending on the pump wavelengths and fibre dispersion.

(2) Waves can be generated, or amplified, at higher frequencies than that corresponding to the pump waves.

(3) The FWM gain bandwidth can be tailored through the choice of fibre and pump source.

(4) Devices based on fibre FWM are compatible with all-fibre architectures, where they stand to benefit from the associated relative mechanical and thermal stability.

These features are illustrated in the next section, where the mathematical descriptions of fibre FWM and phase-matching are treated. Here, we shall also derive an expression for the FWM gain coefficient, to enable a comparison to the scattering processes of Section 2.2.1.

2.3 Properties of FWM

The process of FWM may be described by a set of coupled equations, similar to equations 2.33 and 2.34 for SRS and SBS. The interaction, which leads to energy transfer between the waves, is facilitated through a number of mechanisms. The aim here is to show the origin of these mechanisms and how they contribute to the phenomenon of FWM.

In the following it will be assumed that the optical fields are linearly polarized and maintain their polarization with propagation along the waveguide. The preservation of the field polarizations allow for a scalar approach. For a homogeneous medium and the general form of the polarization (equation 2.32), equation 2.9 may then be rewritten as:

$$\nabla^2 \mathrm{E}(\mathrm{r},\mathrm{t}) - \frac{1}{\mathrm{c}^2}\frac{\partial^2 \mathrm{E}(\mathrm{r},\mathrm{t})}{\partial \mathrm{t}^2} = \mu_0 \frac{\partial^2 \mathrm{P}(\mathrm{r},\mathrm{t})}{\partial \mathrm{t}^2} \tag{2.42}$$

It is straightforward to verify that equation 2.42 reduces to the Helmholtz equation (equation 2.11) if $\chi^{(3)}$ is taken as zero. In this limit, equation 2.42 is satisfied by the time-harmonic field leading to the phasor solution of equation 2.10. In analogy, the full field, consisting of a single frequency component, for the case $\chi^{(3)} \neq 0$, may be written as:

$$\mathrm{E}(\mathrm{r},\mathrm{t}) = \mathrm{E}_0(\mathrm{r})\mathrm{e}^{\mathrm{j}\omega\mathrm{t}-\mathrm{j}\beta\mathrm{z}} \tag{2.43}$$

The real field, consisting of four frequency components, may similarly be expressed as,

$$\begin{aligned} \mathrm{E}(\mathrm{r},\mathrm{t}) &= \frac{1}{2}\sum_{\mathrm{k}=1}^{4}\left[\mathrm{E}_{0,\mathrm{k}}(\mathrm{r})\mathrm{e}^{\mathrm{j}\omega_\mathrm{k}\mathrm{t}-\mathrm{j}\beta_\mathrm{k}\mathrm{z}} + \mathrm{c.c.}\right] \\ &= \frac{1}{2}\sum_{\mathrm{k}=1}^{4}\left[\mathrm{F}_\mathrm{k}(\mathrm{x},\mathrm{y})\mathrm{A}_\mathrm{k}(\mathrm{z})\mathrm{e}^{\mathrm{j}\omega_\mathrm{k}\mathrm{t}-\mathrm{j}\beta_\mathrm{k}\mathrm{z}} + \mathrm{c.c.}\right] \end{aligned} \tag{2.44}$$

where $F_k(x,y)$ is the transverse mode field distribution of the k'th mode. The amplitude of the slowly varying envelope of the mode, $A_k(z)$, is introduced here and has an explicit z-dependence in anticipation of power transfer between the fields [3]. Equations 2.32 (for $\chi^{(2)} = 0$) and 2.44 are now substituted into equation 2.42. For relatively small differences in the frequencies of the four interacting modes, $\chi^{(3)}$ may be taken as frequency independent. The resulting expression for the nonlinear contribution to the polarization-term on the right-hand side of equation 2.42 is, $\frac{\chi^{(3)}}{c^2}\frac{\partial^2}{\partial t^2}[\mathrm{E}(\mathrm{r},\mathrm{t})]^3$. The expansion of the electric field, as given by equation 2.44, leads to a large number of terms. However, by considering terms at a single frequency $\omega_k = \omega_1$, and by assuming

that the four frequency components conserve energy (equation 2.40), a propagation equation for $A_k(z)$ is obtained [33][1]:

$$F_1 \frac{dA_1}{dz} = \frac{j\omega_1 n_2}{c}\{[F_1^2|A_1|^2 + 2(F_2^2|A_2|^2 + F_3^2|A_3|^2 + F_4^2|A_4|^2)]F_1A_1 + 2F_2F_3F_4A_2^*A_3A_4e^{j\Delta\beta z}\} \tag{2.45}$$

The simplified form of equation 2.45 may be attributed to the use of the slowly varying envelope approximation (SVEA). Following the approach of Section 2.2.2, $\chi^{(3)}$ is absorbed into the nonlinear index coefficient (n_2). The phase mismatch is defined as:

$$\Delta\beta = \beta_3 + \beta_4 - \beta_1 - \beta_2 \tag{2.46}$$

For the remainder of this text, we shall be concerned with the partially degenerate case where two of the four frequency components are equal and satisfy $2\omega_1 = \omega_3 + \omega_4$. Furthermore, the two photons at frequency ω_1 propagate in the same spatial mode and will be associated with the pump wave (subscript p), whilst ω_3 and ω_4 are the anti-Stokes (subscript a) and Stokes (subscript s) waves, respectively. By restricting the analysis to linearly polarized modes, equation 2.45 for the pump, as well as similar equations for the anti-Stokes and Stokes waves, may be rewritten [33]:

$$\frac{dA_p}{dz} = \frac{j\omega_p n_2}{c}\left[f_{pp}|A_p|^2A_p + 2A_p(f_{pa}|A_a|^2 + f_{ps}|A_s|^2) + 2f_{ppas}A_p^*A_aA_se^{j\Delta\beta z}\right] \tag{2.47}$$

$$\frac{dA_a}{dz} = \frac{j\omega_a n_2}{c}\left[f_{aa}|A_a|^2A_a + 2A_a\left(f_{ap}|A_p|^2 + f_{as}|A_s|^2\right) + f_{aspp}A_s^*(A_p)^2e^{-j\Delta\beta z}\right] \tag{2.48}$$

$$\frac{dA_s}{dz} = \frac{j\omega_s n_2}{c}\left[f_{ss}|A_s|^2A_s + 2A_s\left(f_{sp}|A_p|^2 + f_{sa}|A_a|^2\right) + f_{sapp}A_a^*(A_p)^2e^{-j\Delta\beta z}\right] \tag{2.49}$$

The transverse coordinate dependence is confined to the constants f_{ij} and f_{ijkl}, known as the overlap integrals. The overlap integrals are defined as,

$$f_{ij} = \frac{\langle|F_i|^2|F_j|^2\rangle}{\langle|F_i|^2\rangle\langle|F_j|^2\rangle} \tag{2.50}$$

[1] the x- and y-dependence of F as well as the z-dependence of A are not explicitly indicated in equation 2.45 and in the rest of this chapter

$$f_{ijkl} = \frac{\langle F_i^* F_j^* F_k F_l \rangle}{\left[\langle |F_i|^2 \rangle \langle |F_j|^2 \rangle \langle |F_k|^2 \rangle \langle |F_l|^2 \rangle \right]^{1/2}} \tag{2.51}$$

and is a measure of the extent to which modes can interact. Following the notation of Agrawal [5], angled brackets indicate integration with respect to the x- and y-coordinates. In this instance equation 2.46 simplifies to $\Delta\beta = \beta_a + \beta_s - 2\beta_p$.

The first term on the right-hand side of equations 2.47 to 2.49 is the contributions from SPM, as discussed in Section 2.2.2. Similarly, the second and third terms are the contributions from XPM, i.e. the interaction of each wave with every other optical wave in the medium. The other wave may be at a different frequency, propagate in a different transverse mode or propagate in the opposite direction. It should be noted that the phase shift contribution due to XPM has twice the magnitude of the contribution due to SPM (assuming waves of equal intensity). The final term in the coupled amplitude equations represents four-wave mixing (FWM). The FWM term couples the three distinct waves (in the degenerate case) and depends on the degree of phase-matching. Although the derivation neglects fibre loss, its influence may become relevant. In this case, the right-hand side of equations 2.47 to 2.49 may each be supplemented by the loss term, $-(\alpha_k/2)A_k$, where $k = p, a, s$.

The coupled amplitude equations represent a full description of the FWM process under CW and quasi-CW conditions, accounting for pump depletion and spatial overlap of the modes. The equations are easily solved by means of a numerical method and may even be solved analytically [34], [35]. Whilst the full solution is treated in the following section, it is instructive to first consider the process under simplified conditions. As a first approach, we consider a FWM process characterized by a relatively small value of the so-called frequency-shift, $\Omega = \omega_a - \omega_p = \omega_p - \omega_s$. Assuming single-mode conditions, the overlap integrals of equations 2.50 and 2.51 are approximately equal and can be described by the effective area parameter, $A_{eff} = 1/f_{ij} \approx 1/f_{ijkl}$. In this case, equations 2.47 to 2.49 may be simplified by defining the nonlinear parameter,

$$\gamma = \frac{\omega n_2}{c A_{eff}} \tag{2.52}$$

where ω is the nominal frequency for the process. The resultant expressions may now be de-coupled for appropriately normalized amplitudes, $A_k = \sqrt{P_k}e^{i\phi_k}$, which yields [36], [37]:

$$\frac{\mathrm{dP_p}}{\mathrm{dz}} = -4\gamma\sqrt{\mathrm{P_p^2 P_a P_s}}\sin\theta \tag{2.53}$$

$$\frac{\mathrm{dP_a}}{\mathrm{dz}} = 2\gamma\sqrt{\mathrm{P_p^2 P_a P_s}}\sin\theta \tag{2.54}$$

$$\frac{\mathrm{dP_s}}{\mathrm{dz}} = 2\gamma\sqrt{\mathrm{P_p^2 P_a P_s}}\sin\theta \tag{2.55}$$

$$\frac{\mathrm{d}\theta}{\mathrm{dz}} = \Delta\beta + \gamma\left(2\mathrm{P_p} - \mathrm{P_a} - \mathrm{P_s}\right) + \gamma\left[\sqrt{\mathrm{P_p^2 P_a}/\mathrm{P_s}} + \sqrt{\mathrm{P_p^2 P_s}/\mathrm{P_a}} - 4\sqrt{\mathrm{P_a P_s}}\right]\cos\theta \tag{2.56}$$

Here, $\mathrm{P_k}$ and ϕ_k are the power and phase associated with wave k, whilst $\theta(\mathrm{z}) = \Delta\beta\mathrm{z} + \phi_\mathrm{a} + \phi_\mathrm{s} - 2\phi_\mathrm{p}$ denotes the relative phase of the waves. It is clear that equations 2.53 to 2.55 governs the evolution of the respective powers. Similarly, equation 2.56 governs the evolution of the relative phase, and is referred to as the total phase mismatch. In this form, the FWM interaction can be understood as follows. As the waves propagate through the medium, they exchange power, depending on the magnitude of the relative phase. The total phase mismatch is dependent on the linear phase mismatch ($\Delta\beta$), as well as a nonlinear contribution (terms proportional to γ). When $\theta \approx \pi/2$, the third term in equation 2.56 becomes negligible, leading to a zero-valued total phase mismatch. This corresponds to power transfer from the pump to the Stokes and anti-Stokes waves. Once pump depletion starts to occur, the second term in equation 2.56 results in a non-zero value for the total phase mismatch, causing the relative phase to change accordingly. In the same way, a relative phase of $-\pi/2$ will lead to power transfer from the Stokes and anti-Stokes waves to the pump wave [38].

If we now consider the scenario where a strong pump wave is phase-matched to weak Stokes and anti-Stokes waves, such that $P_p \gg P_{a,s}$ and $\theta \approx \pi/2$ over the propagation distance of interest, the total phase mismatch becomes [39], [32]:

$$\frac{\mathrm{d}\theta}{\mathrm{dz}} \approx \Delta\beta + 2\gamma\mathrm{P_p} = \kappa \tag{2.57}$$

In this scenario, where pump depletion is negligible, equation 2.47 for the pump wave may be solved by setting the XPM and FWM terms to zero. The resultant expression for the pump amplitude may then be substituted into equations 2.48 and 2.49, in which the SPM terms and XPM terms, related to the interaction between the Stokes and anti-Stokes waves, are also set to zero. For a given set of boundary conditions, the equations for the Stokes and anti-Stokes amplitudes may then be solved analytically. The solution for the Stokes power for the case where no anti-Stokes power is provided becomes [32]:

$$P_s(L) = P_s(0)\left(1 + \left[\frac{\gamma P_p}{g}\sinh(gL)\right]^2\right) \tag{2.58}$$

where,

$$g = \sqrt{(\gamma P_p)^2 - (\kappa/2)^2} \tag{2.59}$$

As before, L denotes fibre length, whilst g is the FWM (or parametric) gain coefficient. By dividing both sides of equation 2.58 by $P_s(0)$, an expression for the unsaturated single pass Stokes gain (G_s) is obtained. The unsaturated anti-Stokes wavelength conversion efficiency is related to this quantity by, $G_a = G_s - 1$. The Stokes gain for perfect phase-matching ($\kappa = 0$) can be calculated in dB units, using $G_s[\text{dB}] \approx 10\log_{10}\left[\frac{1}{4}e^{2\gamma P_p L}\right]$.

The maximum value for the parametric gain coefficient is obtained for perfect phase-matching and has a value of γP_p. Using equation 2.52, this may be rewritten to reflect the expression, $g_{max} = 2\pi n_2/\lambda$. At a wavelength of 1 μm, we therefore have a value of 1.63×10^{-13} m/W, which is found to be larger than the SRS gain coefficient (refer to Section 2.2.1).

When the quasi-CW regime no longer applies, equations 2.47 to 2.49 require considerable adjustments. As before (refer to Section 2.2.1), the validity of the quasi-CW regime is determined from the walk-off length (equation 2.37), which may be significantly shorter than that associated with SRS. Additionally, the pump pulse shape influences the accuracy of the quasi-CW approach, due to the varying influence of the nonlinear contribution to the total phase mismatch. The theoretical case of a square pulse is the exception here, since the so-called nonlinear phase-shift will remain

constant over the pulse duration. Based on the influence of the nonlinear phase-shift, the preceding formalism is valid for pulse widths of no less than 100 ps, conditional on walk-off being negligible [33]. For shorter pulse widths, an accurate description of FWM requires the solution to one or more nonlinear Schrödinger equations (NLSE), which include the effects of dispersion and even SRS [5]. The NLSE is typically solved numerically using the so-called split-step Fourier method (SSFM). The SSFM works by separating the dispersive and nonlinear terms and by solving them independently over very short distances (or *steps*). Apart from this spatial discretization, which is related to the accuracy of the approach, the solution requires a time-frequency discretization. The number of points required for temporal and spectral computation windows spanning T_{span} and F_{span}, respectively, is given by the sampling theorem as $N_p = T_{span} F_{span}$ [40]. Therefore, although the NLSE formalism provides a useful tool, it is not always feasible. Consider, for example, a pump pulse width of the order of 1 ns and a FWM interaction covering a range of 300 THz (refer to Chapters 4 and 5). In this case, the required number of points can easily exceed 10^6, which would require an unacceptable computation time. For this reason, the NLSE was not employed in the work of this thesis.

At this point it is worth noting that the FWM process may equivalently be described by means of modulation instability (MI) [37], [41]. Although the mathematical frameworks are different, MI is essentially the time domain equivalent to the frequency domain description used here for FWM (refer to [42] and [43]).

2.3.1 General Solutions to the Coupled Amplitude Equations

To appreciate the way in which SPM, XPM and pump depletion influences the FWM process, we consider a general example. The pump and Stokes powers are P_p=50 W and P_s=0.1 mW, whilst the anti-Stokes wave is generated from noise. The power contained in the noise at the anti-Stokes wavelength is approximated as 0.1 μW [36]. For simplicity, the difference in photon energy is neglected from the calculation and a nominal wavelength of 1080 nm is used throughout. It is also assumed that the overlap integrals are all equal, allowing the use of a single A_{eff}-value. For a choice of A_{eff}=85 μm^2, γ becomes 1.8 $W^{-1}km^{-1}$ (n_2= 2.6×10^{-20} m^2/W).

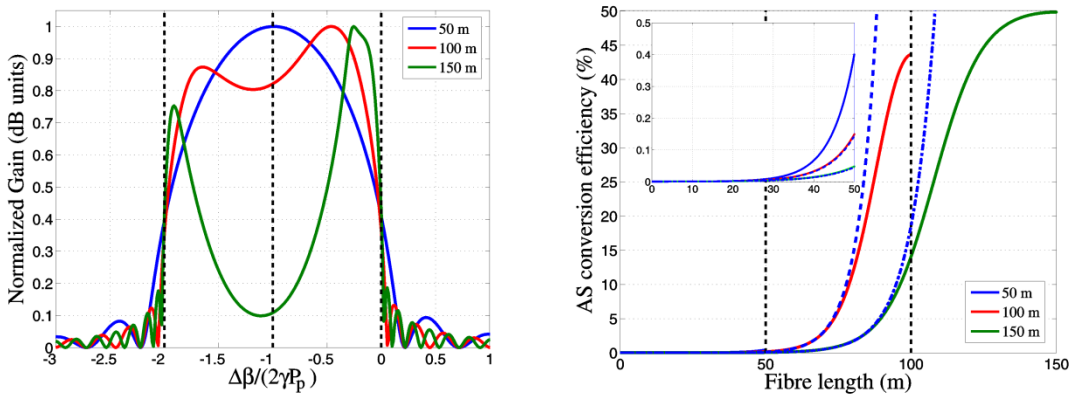

(a) (b)

Figure 2.5: (a) Normalized parametric gain as a function of the normalized phase mismatch for P_p=50 W, P_s=0.1 mW, P_a=0.1 μW and γ=1.8 $W^{-1}km^{-1}$, for three lengths of fibre. The difference in photon energy is neglected, whilst a single value is assumed for the nonlinear parameter. (b) Anti-Stokes power conversion efficiency for all three fibre lengths. Blue curves represent solutions from equation 2.58, whilst red and green curves are the solutions to equations 2.53 to 2.56 (or equivalently, equations 2.47 to 2.49).

Figure 2.5(a) gives the normalized gain (in units of dB) over a range of phase mismatch values. The phase mismatch is normalized to $2\gamma P_p$ to facilitate a comparison of the results to equations 2.57 and 2.59. Three fibre lengths were used in the calculation. For the shortest fibre (50 m), the blue curve shows the result. In this regime, pump depletion is negligible and the analytical result (equation 2.58) exactly matches the numerically calculated result (equations 2.53 to 2.56). The gain exists over a range $-4\gamma P_p < \Delta\beta < 0$, with the peak gain located at $\Delta\beta = -2\gamma P_p$. As the fibre length is extended to 100 m (red curve) or 150 m (green curve), pump depletion plays an increasingly important role. As a consequence, the value for Δβ corresponding to peak gain is changed. Figure 2.5(b) gives the anti-Stokes power conversion efficiency for the 50 m case (see inset: solid blue curve), 100 m case (red curve) and 150 m case (green curve), at the peak Δβ-values identified from Figure 2.5(a). Additional blue curves represent the associated analytical results for the cases of 100 m (dashed) and 150 m (dashed-dotted). From this it is clear that the analytical expression grossly over-estimates the gain in the regime where pump depletion sets in. Figure 2.5(b) furthermore shows that nearly-complete pump depletion is theoretically possible.

It is important to note that pump depletion leads to a scenario where, depending on the phase mismatch value, the anti-Stokes power conversion efficiency is not necessarily a maximum at the fibre output. This can be inferred from Figure 2.5, but is

shown explicitly in Figure 2.6(a), where pump depletion occurs in the middle of the fibre, after which the direction of power flow is reversed. This periodic nature of the solutions is well documented and is consistent with analytical formulations [34], [35], [44].

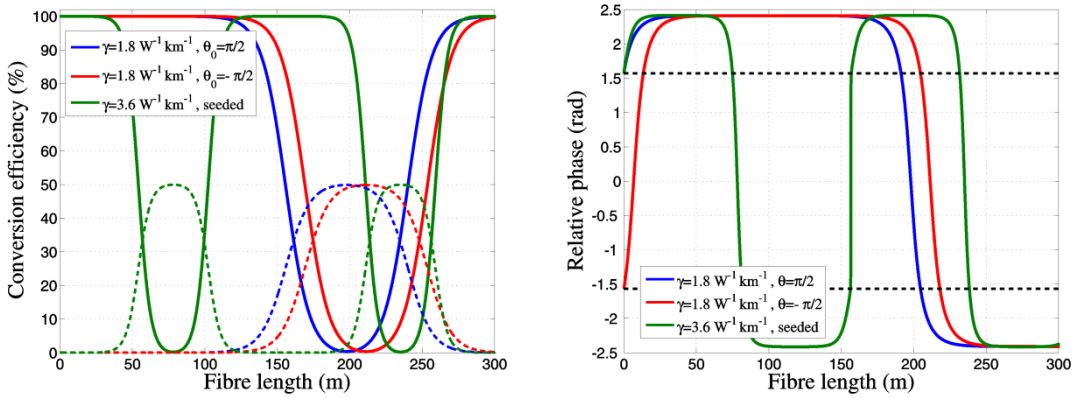

(a) (b)

Figure 2.6: (a) Power conversion efficiency as a function of fibre length for P_p=50 W, P_s=0.1 mW, P_a=0.1 μW and γ=3.8 $W^{-1}km^{-1}$ (green curves), and P_p=50 W, P_s=0.1 μW, P_a=0.1 μW and γ=1.8 $W^{-1}km^{-1}$ (blue and red curves). Blue and red curves are characterized by initial relative phases of π/2 and - π/2, respectively. Solid and dashed lines differentiate between pump and Stokes (or anti-Stokes) waves. (b) Phase evolution for the cases treated in (a).

The blue and red curves in Figure 2.6(a) were calculated for the case where the Stokes and anti-Stokes waves build up from noise (the other parameters are identical to before). In contrast to the seeded arrangement of Figure 2.5, the power transfer associated with the blue and red curves depend on the initial relative phase. The evolution of the phase for both cases follows in Figure 2.6(b). A value of $\theta_0 = \pi/2$ (blue) results in the most efficient conversion. Compared to $\theta_0 = -\pi/2$ (red), complete pump depletion occurs for a ~10 m reduction in fibre length. This can also be verified from Figure 2.6(b), where maximum power transfer corresponds to the zero-crossing of the relevant curve [45]. In a similar way, the power transfer for a process in which the Stokes and anti-Stokes waves are seeded, will be phase sensitive [46]. A comparison of both results to the green curve in Figure 2.5(b) shows that seeding at the Stokes (or anti-Stokes) wavelength leads to a significant reduction (>50 m) in the fibre length required for complete pump depletion. The green curves in Figures 2.6(a) and (b) also show the power and phase evolution for the following set of initial conditions: P_p=50 W, P_s=0.1 mW, P_a=0.1 μW and γ=3.6 $W^{-1}km^{-1}$ (A_{eff}=42 μm^2). From a comparison to Figure

2.5(b), it is clear that a two-fold increase in the nonlinear parameter results in roughly twice the rate of power transfer. A similar result can be achieved through a two-fold increase in the pump power.

2.3.2 Phase-matching Regimes

Phase-matching in optical fibres can be realized in a number of ways. For a given fibre, the phase-matched wavelengths will depend on the dispersion and choice of pump wavelength. To help illustrate the different regimes for phase-matching, it is useful to rewrite equation 2.57 [5]:

$$\begin{aligned}\kappa &= \left(n_a\omega_a + n_s\omega_s - 2n_p\omega_p\right)/c + \left(\Delta n_a\omega_a + \Delta n_s\omega_s - 2\Delta n_p\omega_p\right)/c + 2\gamma P_p \\ &= \Delta\beta_M + \Delta\beta_W + \Delta\beta_{NL}\end{aligned} \tag{2.60}$$

By decomposing the effective refractive index as $n_{eff} = n + \Delta n$, the contributions to the phase mismatch from material (n) and waveguide (Δn) dispersion are separated. The nonlinear phase-shift is also re-branded as the nonlinear phase mismatch. It is additionally instructive to expand the individual terms in equation 2.46, for the linear phase mismatch ($\Delta\beta_M + \Delta\beta_W$), about the pump frequency, using the Taylor series of equation 2.22 [47]:

$$\Delta\beta = \beta_2\Omega^2 + \beta_4\Omega^4/12 + \cdots \tag{2.61}$$

Equation 2.61 generally applies provided that the frequency-shift is not exceedingly large. The accuracy may however be improved by including the next even higher-order term, $\beta_6\Omega^6/360$. In the following, we will consider three approaches for phase-matching. The discussion makes reference to Figure 2.7, detailing important aspects of each approach.

The first and most common approach is shown in Figure 2.7(a). Here, phase-matching is achieved by positioning the pump wavelength in the anomalous dispersion regime ($D > 0$, $\beta_2 < 0$). It is then typical to neglect the second term in equation 2.61, from which it follows that the linear phase mismatch is negative. Note however that the approximation of neglecting $\beta_4\Omega^4/12$ is only valid provided that $\lambda_p \neq \lambda_0$ (where λ_0 is the ZDW). Since β_2 is typically not too large, and is dominated by the material dispersion in the case of conventional fibres, $\Delta\beta_M + \Delta\beta_W$ may be balanced by the

positive influence of $\Delta\beta_{NL}$ [48]. The resultant gain spectrum is located about the pump frequency and can extend over tens, or even hundreds, of nanometers. For this reason, this approach for phase-matching is popular in the field of telecommunications, where several low-power signals can be amplified simultaneously [33].

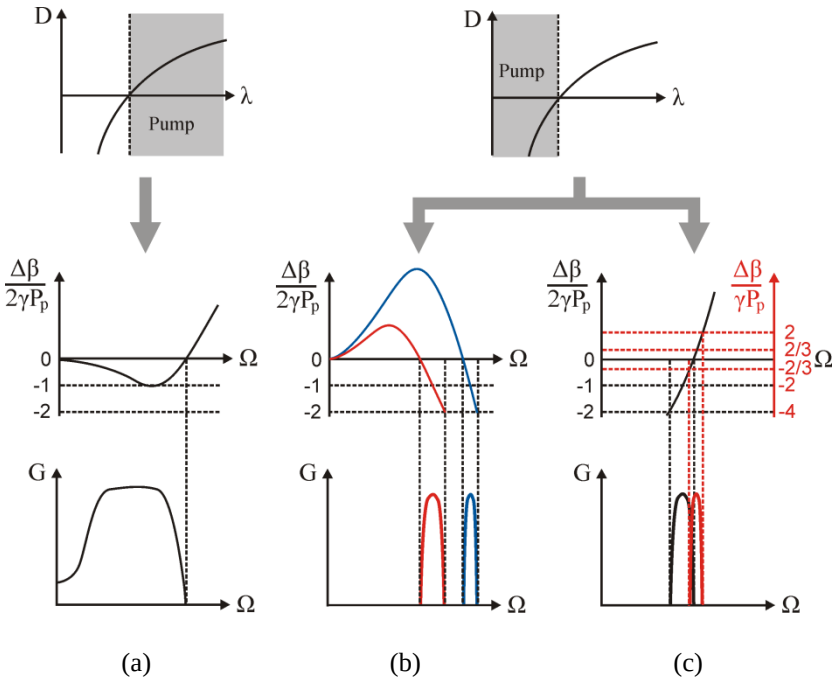

Figure 2.7: Schematic detailing the origin and properties of three approaches for phase-matching in optical fibres. (a) An anomalous dispersion pump wavelength results in a broad gain region, about the pump wavelength. Phase-matching is mainly attributed to the opposite influences of $\Delta\beta_M + \Delta\beta_W$ and $\Delta\beta_{NL}$. (b) A normal dispersion pump wavelength results in a narrow, isolated gain region. Phase-matching is achieved through the opposite influences of $\Delta\beta_M$ and $\Delta\beta_W$, provided that $\beta_4 < 0$. (c) Same result as for (b). In this case, phase-matching results from an interaction between waves with different spatial (left-hand y-axis) or polarization modes (right-hand y-axis). Once again, $\Delta\beta_W$ counter-acts $\Delta\beta_M$. Refer to the main text for an explanation on the significance of the right-hand y-axis.

The phase-matching processes of interest to this thesis are detailed in Figure 2.7(b) and (c). Both cases require the pump wavelength to be positioned within the normal dispersion regime ($D < 0$, $\beta_2 > 0$). However, in contrast to the preceding case (Figure 2.7(a)), the influence of $\Delta\beta_{NL}$ is essentially negligible in determining the phase-matched wavelengths [32], [42]. Note however that $\Delta\beta_{NL}$ still affects the parametric bandwidth (refer to discussion below). Phase-matching must therefore be satisfied by

balancing the influences of $\Delta\beta_M$ and $\Delta\beta_W$. Since this may be accomplished in three different ways, of which two correspond to Figure 2.7(c), we consider them separately.

For the case of Figure 2.7(b), the phase-matching process can be understood by considering equation 2.61. Starting from an initial value of zero for the fully degenerate case, $\Delta\beta$ experiences positive growth as the frequency-shift increases. In this way, $\Delta\beta$ can become very large for $\Omega < \Omega_{\text{critical}}$, where Ω_{critical} depends on the proximity of the pump wavelength to the ZDW. As the critical frequency-shift approaches, a negative contribution from the term proportional to Ω^4 leads to a turning point, after which $\Delta\beta$ decreases to a negative value [49], [50]. It is therefore clear that this phase-matching approach requires $\beta_2 > 0$ and $\beta_4 < 0$, at the pump wavelength [51]. These conditions are satisfied in the normal dispersion regime of bulk silica [50]. However, the influence of waveguide dispersion can drastically alter the values of β_2 and β_4, especially in the case of PCF. The process therefore relies on a delicate balance between $\Delta\beta_M$ and $\Delta\beta_W$. The phase-matched frequency-shift associated with this process is proportional to $\lambda_0 - \lambda_p$ and can be deduced from equation 2.61, as $\Omega = \sqrt{-12\beta_2/\beta_4}$. In contrast, the gain bandwidth for this process typically has an inverse dependence on $\lambda_0 - \lambda_p$. Both these aspects are illustrated in Figure 2.8, where the small-signal gain (equation 2.58), as a function of wavelength, is given for four pump wavelengths. For this example, the fibre dispersion associated with the blue curve in Figure 2.4 was used.

Figure 2.7(c) is applicable to two processes. In the first of these (left-hand y-axis), the required negative value for $\Delta\beta_W$ is obtained through the use of higher order spatial modes [52], [53]. This method therefore relies on the mode dependence of the waveguide dispersion. Two pump photons at the same frequency (degenerate FWM), can be either in the same spatial mode or in different modes. Similarly, the Stokes and anti-Stokes photons need not be in the same spatial mode. In fact, the combination of higher-order modes is only limited by the overlap integrals of equations 2.50 and 2.51. Whilst different mode combinations will yield different phase-matched frequency-shift values, the general shape of the curve relating the phase mismatch and frequency-shift can also vary. For the representative case of Figure 2.7(c), a large negative $\Delta\beta_W$ dominates over the positive contribution of $\Delta\beta_M$ for smaller values of Ω, but is eventually compensated. The reverse scenario is equally likely. Whereas the formation of the gain spectrum is essentially similar to that of Figure 2.7(b), the process is not

explicitly dependent on $\lambda_0 - \lambda_p$. It is also worth noting that, apart from the so-called *divided pump process* where the pump power is divided between the same two modes as the Stokes and anti-Stokes [53], $\Delta\beta$ is not zero at $\Omega = 0$.

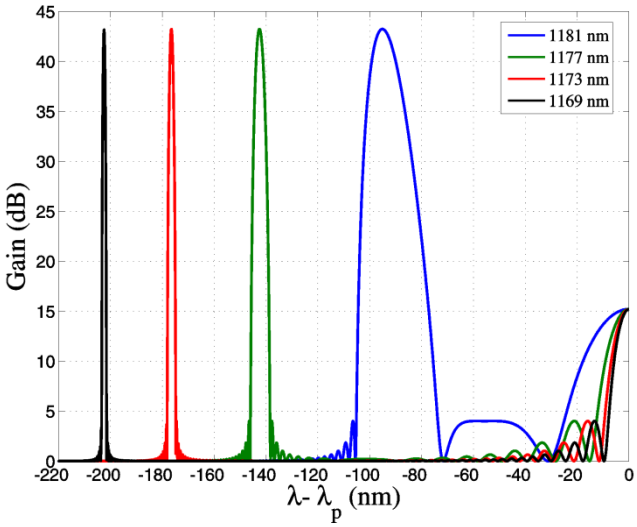

Figure 2.8: Parametric gain spectrum as a function of pump wavelength, in the normal dispersion regime. The fibre has a ZDW of 1182 nm (refer to blue dispersion curve in Figure 2.4). As the separation between the pump and zero-dispersion wavelengths increases, the frequency-shift associated with the gain region becomes larger and the gain bandwidth becomes smaller.

The second phase-matching process related to Figure 2.7(c) is that of birefringence matching (right-hand y-axis) [54]. In this approach, a negative value for $\Delta\beta_W$ results from the use of different polarization modes in a birefringent fibre (refer to Section 2.1.3). The orthogonal principae axes in a linearly birefringent fibre are commonly called the slow and fast axis. This terminology originates from the principle that light travels slower when polarized along the axis associated with n_{eff}^{x}, provided that $n_{eff}^{x} > n_{eff}^{y}$. A negative contribution from $\Delta\beta_W$ can be realized by polarizing the pump wave along the slow axis, whilst polarizing the anti-Stokes and Stokes waves along the fast axis. The linear phase mismatch for the birefringent process ($\Delta\beta_{xy}$) may then be rewritten as [33],

$$\begin{aligned}\Delta\beta_{xy} &= \left[\tilde{n}_a^y\omega_a + \tilde{n}_s^y\omega_s - 2\left(B_m + \tilde{n}_p^y\right)\omega_p\right]/c \\ &= \Delta\beta_y - 2B_m\omega_p/c\end{aligned} \tag{2.62}$$

where $B_m = \tilde{n}^x - \tilde{n}^y$ is the previously defined modal birefringence (Section 2.1.3) and $\Delta\beta_y$ is the linear phase mismatch for the *isotropic* process, where all four photons are co-polarized along the fast axis. Furthermore, $\tilde{n}$ denotes the effective refractive index, for which the subscript and superscript indicate the associated wavelength and polarization, respectively. In analogy to equation 2.61, $\Delta\beta_y$ may be expanded in a Taylor series. It is common to make the assumption that B_m is frequency independent, in which case $\Delta\beta_y = \Delta\beta_x \approx \beta_2\Omega^2$. The second term in equation 2.62 may then be regarded as an additional manifestation of $\Delta\beta_W$, resulting in an expression for the phase-matched frequency-shift, $\Omega = \sqrt{2B_m\omega_p/(\beta_2 c)}$.

An interesting difference between birefringence matching and the other above-mentioned phase-matching processes, may be explained at the hand of Figure 2.7(c). In accordance with Figure 2.5(a), the gain associated with phase-matched FWM between co-polarized waves exists over the range $-4\gamma P_p < \Delta\beta < 0$, with the peak gain located at $\Delta\beta = -2\gamma P_p$ (refer to the left-hand y-axis). Equation 2.57 therefore implies a positive contribution from $\Delta\beta_{NL}$ to the total phase mismatch. For cross-polarized interacting waves, the magnitude of $\chi^{(3)}$ is reduced to roughly a third of its co-polarized value (refer to the discussion in Chapter 4). The resulting contribution from $\Delta\beta_{NL}$ is negative and leads to a total phase mismatch (equation 2.57) of $\kappa = \Delta\beta - 2\gamma P_p/3$. It therefore follows that gain exists over the range $-2\gamma P_p/3 < \Delta\beta < 2\gamma P_p$, with the peak located at $\Delta\beta = 2\gamma P_p/3$ (refer to the right-hand y-axis). It is important to note that these values are applicable to the specific configuration of interest, where the degenerate pump wave is polarized along the slow fibre axis. By polarizing the four waves in a different manner, several other phase-matching options are possible [55], [56]. One other combination is equivalent to the divided pump process from the preceding discussion on the use of higher-order spatial modes. The specifics of this approach are however left for the discussion in Chapter 4.

A very useful expression for calculating the small-signal parametric bandwidth for the processes of Figure 2.7, is provided by Stolen and Bjorkholm [32]:

$$\Delta\Omega_B = \Delta\kappa_B \frac{d\Omega}{d(\Delta\beta)_{\Delta\beta=0}} \tag{2.63}$$

Here, $\Delta\kappa_B = 2\sqrt{(\pi/L)^2 + (\gamma P_p)^2}$ is the so-called mixing bandwidth and is related to equation 2.58. The individual terms in the mixing bandwidth can be motivated by considering small-signal gain distributions, similar to that of the blue curve in Figure 2.5(a). The derivative in equation 2.63 is determined from the slope of the phase mismatch curve in the vicinity of its zero-crossing (refer to schematics in the middle row of Figure 2.7). From this definition, the parametric bandwidth defines the frequency range over which the phase mismatch is sufficiently small for the parametric gain, in linear units, to remain larger than $4G_{max}/\pi^2$. Similar to the case of SBS, the effective parametric gain will be reduced if the pump linewidth exceeds the parametric bandwidth. The parametric bandwidth therefore translates into a so-called pump acceptance bandwidth.

2.3.3 Optical Parametric Generators, Amplifiers and Oscillators

Practical implementations of degenerate fibre FWM can be categorized into four main groups, as illustrated in Figure 2.9. The primary distinction between these groups is the mechanism for seeding. The processes of Figure 2.9(a) and (b) have previously been introduced (refer to section 2.2.2). Both processes involve a single pass through the gain fibre, but whereas FWM is initiated by noise photons for the case of an optical parametric generator (OPG), the optical parametric amplifier (OPA) is seeded externally. An OPG may however be converted into an optical parametric oscillator (OPO) through the introduction of feedback [57]. For the case of a linear cavity (Figure 2.9(c)), this feedback is typically provided by fibre Bragg gratings (FBG). The input FBG must be transparent at λ_p, but highly reflective at λ_a, assuming a resonant anti-Stokes wave. Similarly, the output FBG must be transparent at λ_p and λ_s, whilst being partially reflective at λ_a. The noise-generated anti-Stokes and Stokes waves will then grow with propagation distance, after which the Stokes, pump and a fraction of the anti-Stokes waves are coupled out of the fibre. The remainder of the anti-Stokes wave is reflected, resulting in a singly-resonant bi-directional oscillator [33]. Since the backward-propagating resonant wave of a bi-directional oscillator will interact with the forward-propagating waves through the processes of SPM and XPM, a uni-directional OPO may be preferable. One configuration for a uni-directional OPO is given in Figure 2.9(d). Similar to the case of the OPA in Figure 2.9(b), a wavelength-division

multiplexer (WDM) is used to combine the pump and resonant anti-Stokes (or Stokes) waves. A tap-coupler is used to extract a portion of the power, while the remaining power is recycled. The use of a band-pass filter (BPF) allows for singly-resonant operation.

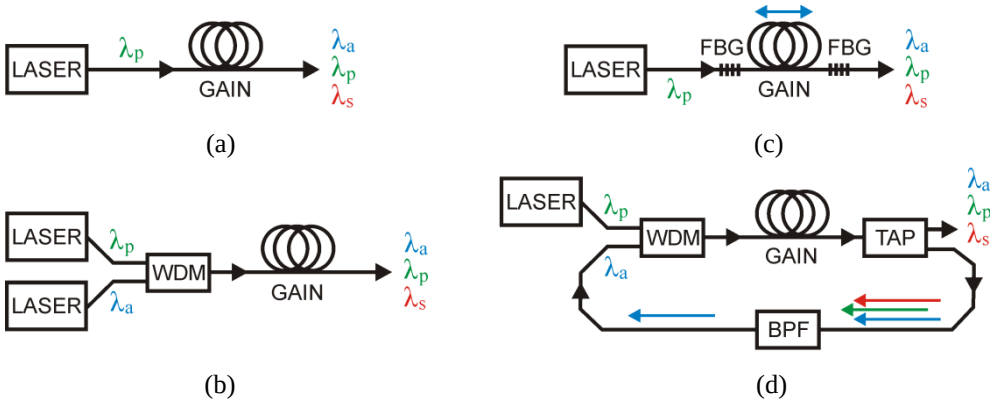

Figure 2.9: Schematic diagram showing the four most common practical implementations of degenerate fibre FWM. (a) An optical parametric generator, for which only a pump wave is incident on the gain fibre. (b) An optical parametric amplifier, for which a seed wave, at the anti-Stokes wavelength, is injected at the gain fibre input. A wavelength-division multiplexer (WDM) combines pump and anti-Stokes light. (c) A bi-directional optical parametric oscillator, where fibre Bragg gratings (FBG) are used to form a cavity, resonant at the anti-Stokes wavelength. (d) A uni-directional fibre optical parametric oscillator. A tap-coupler is used to split the output power from the gain fibre. The inclusion of a band-pass filter ensures that the cavity is singly-resonant at the anti-Stokes wavelength.

In the absence of fibre loss, the OPO reaches a so-called steady-state once $P_r(L)T = P_r(0)$, where T denotes the total cavity transmission and the subscript r is used for the resonant FWM component [33]. As an example, consider a linear cavity with a 100% reflectivity (R_1) on the one end and a 70% reflectivity (R_2) on the other, resulting in T=0.7. If we restrict ourselves to the case of pump pulses in the regime where walk-off is negligible, interactions between the forward and backward-propagating pulses may be neglected. The preceding quasi-CW FWM theory may then be applied, in an iterative manner, to calculate the intra-cavity powers that will satisfy the steady-state condition for a given pump power and fibre length. The resulting intra-cavity powers for the pump and resonant anti-Stokes waves are given in Figure 2.10 by solid and dashed lines, respectively. For the purpose of comparing the results to those of Figures 2.5 and 2.6, for the OPA configuration, the calculation used P_p=50 W, P_s=0.1 μW and γ=1.8 $W^{-1}km^{-1}$. Once again, the difference in photon energy is neglected. In

addition to the result for a cavity transmission of 0.7 (green curves), Figure 2.10 also shows results for T=0.3 (blue curves) and T=0.5 (red curves). Each calculation was performed using the Δβ-value corresponding to peak gain. From the fibre length required for nearly-complete pump depletion, it is clear that feedback leads to a significant increase in the FWM efficiency [42]. The decrease in threshold is related to the intra-cavity power of the resonant wave, which may exceed the input pump power, depending on the cavity transmission. In particular, a larger value for the cavity transmission leads to a greater reduction in the FWM threshold. The intra-cavity power of the Stokes wave, for the case of T=0.7, is given by the green dashed-dotted curve. The Stokes power for the cases of T=0.3 and T=0.5 is similarly related to the anti-Stokes power by a constant offset that is equal to the difference in initial powers.

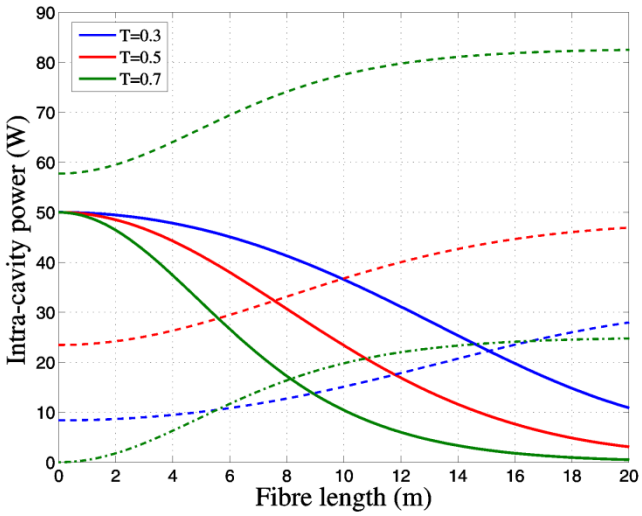

Figure 2.10: Fibre OPO intra-cavity powers for three values of the cavity-transmission (T), at their respective optimised linear phase mismatch values. Solid and dashed lines are used for the pump and resonant anti-Stokes waves, respectively. The dashed-dotted green curve shows the power evolution for the Stokes wave corresponding to T=0.7.

2.3.4 Practical Considerations

So far, Section 2.3 has been concerned with FWM under ideal conditions. However, in reality, the fibre medium is manufactured to a finite precision and external influences may also have an impact on the FWM efficiency. In the following, we briefly consider some of the mechanisms responsible for a departure from the preceding idealized FWM.

In practice, the dimensions and doping concentrations of a fibre do not remain constant along its length. Small variations in these manufacturing quantities lead to variations in the dispersion of the fibre. From Section 2.3.2 it is clear that the fibre dispersion, and in particular the ZDW, plays an important role in the phase-matching process. For this reason, so-called longitudinal fibre inhomogeneity presents a significant limitation to the FWM efficiency and has been studied extensively [58], [59], [60]. The process is typically treated by considering the distribution of the fluctuations in the core diameter along the fibre length as either periodic or stochastic. A figure of merit for the parametric gain may then be defined as the product of the length over which the fluctuations occur and the amplitude of the fluctuations. For random fluctuations, results indicate that the largest fluctuation length scale is typically of the same order as the fibre length. For this reason, longer fibres show a greater sensitivity to longitudinal inhomogeneity [61]. It furthermore follows that parametric processes associated with larger frequency-shifts are affected more severely, for a given figure of merit [62], [61]. This result is consistent with the previously established correlation between the frequency-shift and the parametric bandwidth.

The fibre dispersion can also fluctuate as a result of changes in temperature, pressure or strain. In fact, measurements on dispersion-shifted fibres indicate a linear relationship between temperature and ZDW with a slope of 0.03 nm/^{o}C [63]. For large frequency-shift FWM, this effect can therefore easily become significant, especially if its influence is localised. It is worth mentioning that a position-dependent ZDW can be used to tailor the FWM gain profile. Experiments to this end have been performed, using the temperature dependence of the ZDW [64], but also by simply splicing fibres with slightly different values of λ_0 together [65].

For non-PM fibres, small departures from circular symmetry, for example, can lead to random birefringence (refer to Section 2.1.3). The combined effects of random birefringence and nonlinear polarization rotation lead to position and time-dependent changes in the relative polarization of the interacting FWM waves [5]. As the terms in the coupled amplitude equations (2.47 to 2.49) depend on the relative polarization of the waves, this effect can be very detrimental to FWM. Studies have shown that the reduction in average parametric gain, as well as the fluctuation in the gain, relative to the average, is proportional to the phase-matched frequency-shift [66].

2.4 Ytterbium-Doped Fibre Sources

As stated in Chapter 1, the aim of this thesis is to investigate the feasibility of fibre FWM as an approach to wavelength conversion. Specifically of interest is the ability of FWM to generate up-converted frequencies, which can be implemented to construct a flexible light source in the visible and near-infrared parts of the spectrum. Since conservation of energy restricts the FWM anti-Stokes frequency to the second harmonic of the pump frequency, the pump wavelength should not exceed 1.3 μm.

Fortunately, the 1 μm spectral region is host to a number of potential pump sources, including bulk crystalline and fibre-based gain media. A fibre-based laser represents a natural choice as a pump source for fibre FWM devices, since it allows for all-fibre integration and can lead to compact and robust systems. Moreover, fibre lasers are capable of high gain and high power, whilst maintaining a single transverse mode.

As far as fibre lasers are concerned, ytterbium-doped silica remains the preferred gain medium by virtue of its high efficiency, broad gain bandwidth and power-scaling ability [67]. It is for these reasons that Yb-doped fibre lasers (YDFL) and amplifiers (YDFA) were also chosen for the work of this thesis. In this Section we therefore briefly consider some of the properties that make Yb-doped fibre (YDF) gain media so appealing. The spectroscopic features of ytterbium in silica as well as some general features of ytterbium's use as gain medium are reviewed in Section 2.4.1. This is followed by the discussion of Section 2.4.2, where we consider the most important technological advancements in the field of high-brightness, high-power fibre sources. Finally, Section 2.4.3 introduces the important concept of the master-oscillator power-amplifier (MOPA).

2.4.1 Spectroscopy and General Properties

To illustrate the spectroscopic properties of ytterbium, we shall make use of its energy level diagram (in a silica host), shown in Figure 2.11 [68]. Both the ground-state ($^2F_{7/2}$) and excited-state ($^2F_{5/2}$) manifolds are split into a number of sublevels as a result of the crystal-field (Stark) interaction. As opposed to Yb in a bulk crystalline material, Yb-doped silica is subject to strong line broadening leading to Stark transitions that are not fully resolved at room temperature. For this reason Yb-doped silica has a very broad

bandwidth for absorption and emission [69]. The manifolds are separated in energy by 10000 cm^{-1}, which is large enough not to be susceptible to nonradiative decay as a result of multiphonon emission.

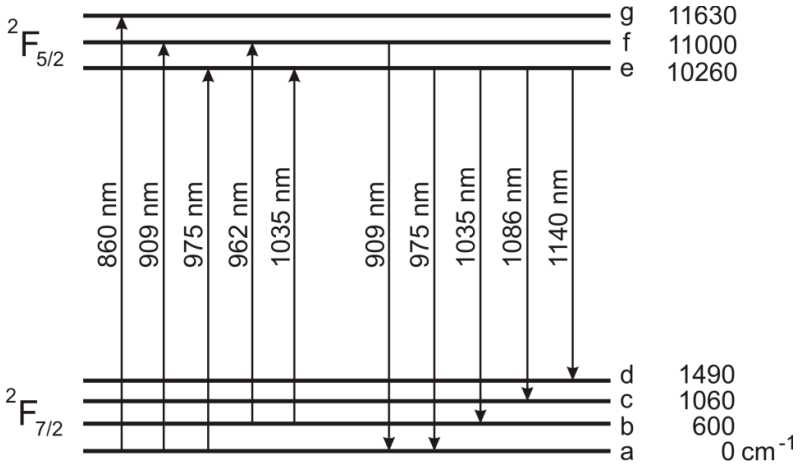

Figure 2.11: Energy level diagram for Yb^{3+} in germano-aluminosilicate [68]. Energy levels in the ground-state ($^2F_{7/2}$) and excited-state ($^2F_{5/2}$) manifolds are labelled, along with their energy separation from the ground-state. Wavelengths corresponding to various transitions are indicated.

Due to its relatively simple spectroscopy, ytterbium is not subject to processes such as excited-state absorption (ESA) or concentration quenching. Consequently, higher concentrations of Yb-ions can be incorporated into the glass host, resulting in higher pump absorption per unit length. This attribute, together with a characteristic low quantum defect, is responsible for the superior conversion efficiency and power-scaling properties of Yb [70]. The broad emission bandwidth furthermore makes Yb ideal for use as a wavelength tunable laser, or for short pulse amplification. Particularly favourable for pulse amplification, is Yb's long upper-state lifetime of between 0.8 and 1.5 ms, which allows for a high energy-storage capacity.

The exact fibre composition of Yb-doped silica fibres is known to have an influence on the cross-sections for absorption and emission [71], [72]. Whereas Yb-doping is essential for laser action, the core of the fibre is doped with germanium or phosphorus to increase the refractive index for guiding. Other elements such as aluminium are added to the fibre composition due to the fact that it increases the solubility of the fibre, thereby greatly alleviating clustering of ytterbium ions. Aluminium as a dopant has the added advantage of controlling the radial ytterbium doping profile [69]. Although Ge-doping does not lead to significant changes in the

cross-section distribution, Al-doping is preferred over P-doping if a pump wavelength at 910 nm is desired [73], [74]. Al-doping however has the disadvantage of being more prone to photodarkening, compared to P-doping for example [75]. Since the photodarkening effect is strongly related to the population inversion levels at which the laser or amplifier is operated, this effect is manageable in the quasi-CW regime. The Yb-doped fibres used in the experiments of this thesis all have a germano-aluminosilicate composition, of which the cross-section distribution can be found in the paper by Paschotta et al. [72].

Figure 2.11 also indicates the different transitions that occur between the sublevels of the ground-state and excited-state manifolds. In accordance with the Boltzmann distribution for ytterbium at room temperature, the strongest absorption and emission transition occurs between level a and level e of the ground-state and excited-state manifold, respectively. This energy difference corresponds to a wavelength of 975 nm. The absorption band, extending from 800 nm to 1100 nm, shows a secondary peak at a wavelength of ~910 nm. Both peaks are at wavelengths for which high power laser diodes are readily available. The emission band extends from 900 nm to 1200 nm and has a secondary peak at ~1035 nm. Due to the small thermal populations in levels c, d, f, g, and to a lesser extent, b, transitions from these levels are not dominant. Especially the absorption transitions do however play a significant role as far as the lasing wavelength is concerned, since they result in reabsorption of the signal light. Although reabsorption takes place at all wavelengths for which the absorption and emission bands overlap, its effect diminishes for longer wavelengths (≥1080 nm). For this reason, ytterbium is often described as a three-level gain medium for shorter signal wavelengths, whilst it approaches the behaviour seen in four-level gain media at longer wavelengths [68]. The correct fibre length for laser action at a specific wavelength is therefore a function of gain and reabsorption and has been the subject of several studies [72], [76].

2.4.2 Key Technologies

In addition to the steady progress that has been made in the fabrication of low loss optical fibres, a number of key technological advancements have lead to a remarkable increase in the output powers of fibre laser sources. The most revolutionary of these was the advent of double-clad (DC) fibres [77] (also see [78]).

Similar to the fibre of Figure 2.1, the DC fibre consists of a core and a much larger cladding. The cladding is however surrounded by a second cladding of lower refractive index. In this way, the inner cladding forms an additional waveguide that overlaps the core region. Typically the rare-earth dopant (Yb for our purposes) is contained in the core region. A pump beam, launched into the (inner) cladding, is therefore progressively absorbed into the core as it propagates down the fibre. For this reason, the modal characteristics of the laser emission are still determined by the waveguide properties of the core. However, since the cladding has a significantly larger acceptance cone than the core (refer to Section 2.1), multi-mode (MM) laser diodes (LD) may now be employed as pump sources. Advances in the area of high-power MM LD sources for the purpose of so-called cladding pumping therefore present another enabling technology for power-scaling of fibre lasers.

An obvious drawback of cladding pumping, compared to core pumping, is the increased absorption length due to a significantly lower overlap between the pump beam and doped area. In fact, some of the cladding modes never interact with the doped region, leading to unabsorbed pump power and therefore a decreased efficiency. For this reason, DC fibres typically require some element to break the circular symmetry of the inner cladding. This can, for instance, be achieved by using a D-shaped or hexagonal inner cladding.

For pump powers of several hundred watts, DC fibre technology is commonly employed using a free-space pump launch. However, specifically for the purpose of increasing the power-scalability of all-fibre laser sources, the tapered fibre bundle (TFB) provides an elegant solution [79]. In its simplest configuration, this device combines several MM input fibres in a taper, where their respective powers are transferred to a single MM output fibre. Alternatively, a single mode fibre is bundled along with the MM fibres and the output fibre is itself a DC fibre. In this way, the output fibre can be spliced directly to a DC doped fibre in an end-pumped amplifier configuration.

2.4.3 All-fibre Master-Oscillator Power-Amplifier

Although free-space pump launch configurations was employed during the work of this thesis, it was primarily used as a first approach for the characterization of fibres and

components. The experimental results to follow in Chapters 3 through 5 are therefore based on fiberized configurations, on which a brief introduction follows.

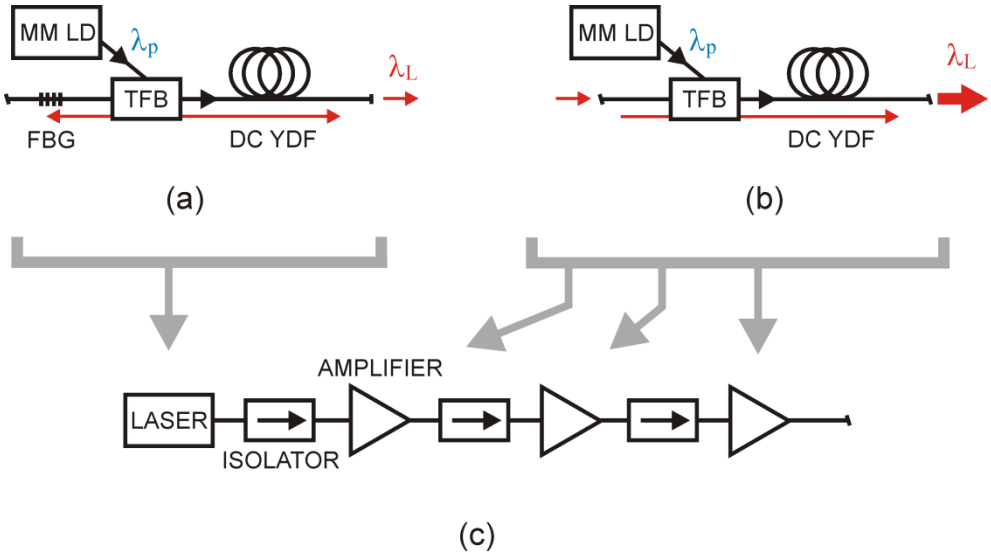

Figure 2.12: Experimental configuration for: (a) a simple linear laser oscillator, (b) a laser amplifier and (c) a master-oscillator power-amplifier, consisting of a laser (or SM LD) and three cascaded amplifiers, all separated by in-line fibre isolators. In all cases, the gain fibre is a double-clad ytterbium-doped fibre and pumping occurs via a tapered fibre bundle.

Figure 2.12(a) shows the basic configuration of a CW linear laser oscillator. It consists of a DC YDF, pumped by a single MM LD, via a TFB. Feedback at the lasing wavelength (λ_L) is achieved through the use of an FBG, designed for high reflectivity at λ_L, on the one end, and a flat fibre cleave on the other. The flat fibre cleave results in a 4% Fresnel reflection, leading to the formation of a standing wave. The configuration is slightly more complicated than that of Figure 2.12(b) for a fibre amplifier. In this case, both fibre ends are terminated by angled cleaves to avoid feedback into the fibre core. Consequently, laser light makes a single pass through the DC YDF and is amplified through stimulated emission.

High power fibre lasers often offer little in the way of control over the spectral and temporal (in the case of pulsed systems) properties of the output [67]. It these cases it may be preferable to adopt an approach whereby a low power seed laser, with the desired properties, are power-scaled through the use of cascaded fibre amplifiers. This is the foundation of the master-oscillator power-amplifier (MOPA) configuration. The concept is illustrated in Figure 2.12(c). Through the use of TFBs and similar fibre components, the setup can be completely fiberized. The seed laser and amplifier stages

are typically separated by in-line isolators. This is done to avoid backward propagating light from depleting the population inversion in the preceding amplifier, whereby catastrophic damage may be caused.

2.5 References

[1] B.A.E. Saleh and M.C. Teich, *Fundamentals of Photonics*, John Wiley and Sons, Inc., 1991.

[2] E. Hecht, *Optics*, 3rd ed., Addison-Wesley, 1998.

[3] D. Marcuse, *Theory of Dielectric Optical Waveguides*, Academic Press, New York and London, 1974.

[4] K. Okamoto, *Fundamentals of Optical Waveguides*, 2nd ed., Academic Press, 2006.

[5] G.P. Agrawal, *Nonlinear Fiber Optics*, 3rd ed., Academic Press, 2001.

[6] J.A. Buck, *Fundamentals of Optical Fibers*, 2nd ed., John Wiley and Sons, Inc., 2004.

[7] A.W. Snyder, "Asymptotic expression for eigenfunctions and eigenvalues of dielectric optical waveguides," *IEEE Trans. On Microwave Theory and Tech.*, vol MTT-17, pp. 1130-1138 (1969).

[8] D. Gloge, "Weakly guiding fibers," *Appl. Opt.*, vol. 10, no. 10, pp. 2252-2258 (1971).

[9] D. Marcuse, "Loss analysis of single-mode fiber splices," *The Bell System Technical Journal*, vol. 56, no. 5, pp. 703-718 (1977).

[10] F. Poletti, "Direct and inverse design of microstructured optical fibres," Ph.D. dissertation, Optoelectronics Research Centre, University of Southampton (2007).

[11] COMSOL Multiphysics, *RF Module User's Guide*, Copyright 1994-2007.

[12] J.W. Fleming, "Material dispersion in lightguide glasses," *Electron. Lett.*, vol. 14, no. 11, pp. 326-328 (1978).

[12] J.W. Fleming, "Dispersion in GeO_2-SiO_2 glasses," *Appl. Opt.*, vol. 23, no. 24, pp. 4486-4493 (1984).

[13] A.K. Sharma and R.B.D. Gupta, "Influence of dopants on the performance of a fiber optic surface plasmon resonance sensor," *Opt. Commun.*, vol. 274, pp. 320-326 (2007).

[14] J.W. Yu and K. Oh, "New in-line fiber band pass filters using high silica dispersive optical fibers," *Opt. Commun.*, vol. 204, pp. 111-118 (2002).

[15] Fiber CAD, Version 1.5, Optiwave Corporation, Copyright 2000.

[16] COMSOL Multiphysics, *Structural Mechanics Module User's Guide*, Copyright 1994-2007.

[17] P.L. Chu and R.A. Sammut, " Analytical method for calculation of stresses and material birefringence in polarization-maintaining optical fiber," *J. Lightw. Technol.*, vol. LT-2, no. 5, pp. 650-662 (1984).

[18] K. Okamoto, T. Hosaka and T. Edahiro, "Stress analysis of optical fibers by a finite element method," *IEEE J. Quantum Electron.*, vol. QE-17, no.10, pp. 2123-2129 (1981).

[19] P.St.J. Russell, "Photonic-crystal fibers," *J. Lightw. Technol.*, vol. 24, no. 12, pp. 4729-4749 (2006).

[20] J.C. Knight, T.A. Birks, P.St.J. Russell and D.M. Atkin, "All-silica single-mode optical fiber with photonic crystal cladding," *Opt. Lett.*, vol. 21, no. 19, pp. 1547-1549 (1996).
[21] T.A. Birks, J.C. Knight and P.St.J. Russell, "Endlessly single-mode photonic crystal fiber," *Opt. Lett.*, vol. 22, no. 13, pp. 961-963 (1997).
[23] N.A. Mortensen, J.R. Folkenberg, M.D. Nielsen and K.P. Hansen, "Modal cutoff and the V parameter in photonic crystal fibers," *Opt. Lett.*, vol. 28, no. 20, pp. 1879-1881 (2003).
[24] M. Koshiba and K. Saitoh, "Applicability of classical optical fiber theories to holey fibers," *Opt. Lett.*, vol. 29, no. 15, pp. 1739-1741 (2004).
[25] K. Saitoh and M. Koshiba, "Empirical relations for simple design of photonic crystal fibers," *Opt. Express*, vol. 13, no. 1, pp. 267-274 (2005).
[26] R.W. Boyd, *Nonlinear Optics*, 3rd ed., Academic Press, 2008.
[27] R.H. Stolen, "Polarization effects in fiber Raman and Brillouin lasers," *IEEE J. Quantum Electron.*, vol. QE-15, no.10, pp. 1157-1160 (1979).
[28] S.T. Davey, D.L. Williams, B.J. Ainslie, W.J.M. Rothwell and B. Wakefield, "Optical gain spectrum of GeO_2-SiO_2 Raman fibre amplifiers," *IEE Proceedings*, vol. 136, no. 6, pp. 301-306 (1989).
[29] R.G. Smith, "Optical power handling capacity of low loss optical fibers as determined by stimulated Raman and Brillouin scattering," *Appl. Opt.*, vol. 11, no.11, pp. 2489-2494 (1972).
[30] M.O. Van Deventer and A.J. Boot, "Polarization properties of stimulated Brillouin scattering in single-mode fibers," *J. Lightw. Technol.*, vol. 12, no. 4, pp. 585-590 (1994).
[31] E. Lichtman, A.A. Friesem, R.G. Waarts and H.H. Yaffe, "Stimulated Brillouin scattering excited by two pump waves in single-mode fibers," *J. Opt. Soc. Am. B*, vol. 4, no. 9, pp. 1397-1403 (1987).
[32] R.H. Stolen and J.E. Bjorkholm, "Parametric amplification and frequency conversion in optical fibers," *IEEE J. Quantum Electron.*, vol. QE-18, no. 7, pp. 1062-1072 (1982).
[33] M.E. Marhic, Fiber Optical Parametric Amplifiers, Oscillators and Related Devices, Cambridge Univ. Press, 2008.
[34] Y. Chen and A.W. Snyder, "Four-photon parametric mixing in optical fibers: effect of pump depletion," *Opt. Lett.*, vol. 14, no. 1, pp. 87-89 (1989).
[35] C.J. McKinstrie, G.G. Luther and S.H. Batha, "Signal enhancement in collinear four-wave mixing," *J. Opt. Soc. Am. B*, vol. 7, no. 3, pp. 340-344 (1990).
[36] A. Vatarescu, "Light conversion in nonlinear monomode optical fibers," *J. Lightw. Technol.*, vol. LT-5, no. 12, pp. 1652-1659 (1987).
[37] G. Cappellini and S. Trillo, "Third-order three-wave mixing in single-mode fibers: exact solutions and spatial instability effects," *J. Opt. Soc. Am. B*, vol. 8, no. 4, pp. 824-838 (1991).
[38] K. Inoue and T. Mukai, "Signal wavelength dependence of gain saturation in a fiber optical parametric amplifier," *Opt. Lett.*, vol. 26, no. 1, pp. 10-12 (2001).
[39] J. Hansryd, P.A. Andrekson, M. Westlund, J. Li and P.-O. Hedekvist, "Fiber-based optical parametric amplifiers and their applications," *IEEE J. Sel. Topics Quantum Electron.*, vol. 8, no. 3, pp. 506-520 (2002).
[40] J.M. Dudley, G. Genty and S. Coen, "Supercontinuum generation in photonic crystal fiber," *Rev. Mod. Phys.*, vol. 78, no. 4, pp. 1135-1184 (2006).
[41] E.A. Golovchenko and A.N. Pilipetskii, "Unified analysis of four-photon mixing, modulational instability, and stimulated Raman scattering under various

polarization conditions in fibers," *J. Opt. Soc. Am. B*, vol. 11, no. 1, pp. 92-101 (1994).

[42] J.D. Harvey, R. Leonhardt, S. Coen, G.K.L. Wong, J.C. Knight, W.J. Wadsworth and P.St.J. Russell, "Scalar modulation instability in the normal dispersion regime by use of a photonic crystal fiber," *Opt. Lett.*, vol. 28, no. 22, pp. 2225-2227 (2003).

[43] S. Pitois and G. Millot, "Experimental observation of a new modulational instability spectral window induced by fourth-order dispersion in a normally dispersive single-mode optical fiber," *Opt. Commun.*, vol. 226, pp. 415-422 (2003).

[44] S.J. Garth, "Small-frequency-shift stimulated-four-photon mixing in optical fibers: optimum phase-matching conditions," *Appl. Opt.*, vol. 31, no. 6, pp. 742-745 (1992).

[45] C.J. McKinstrie, X.D. Cao and J.S. Li, "Nonlinear detuning of four-wave interactions," *J. Opt. Soc. Am. B*, vol. 10, no. 10, pp. 1856-1869 (1993).

[46] M.E. Marhic, K.K.Y. Wong, M.C. Ho and L.G. Kazovsky, "92% pump depletion in a continuous-wave one-pump fiber optical parametric amplifier," *Opt. Lett.*, vol. 26, no. 9, pp. 620-622 (2001).

[47] M.E. Marhic, K.K.Y. Wong and L.G. Kazovsky, "Wide-band tuning of the gain spectra of one-pump fiber optical parametric amplifiers," *IEEE J. Sel. Topics Quantum Electron.*, vol. 10, no. 5, pp. 1133-1141 (2004).

[48] N. Kagi, T.-K. Chiang, M.E. Marhic and L.G. Kazovsky, "Fibre optical parametric amplifier operating near zero-dispersion wavelength," *Electron. Lett.*, vol. 31, no. 22, pp. 1935-1937 (1995).

[49] K. Washio, K. Inoue and T. Tanigawa, "Efficient generation of near-I.R. stimulated light scattering in optical fibres pumped in low-dispersion region at 1.3 μm," *Electron. Lett.*, vol. 16, no. 9, pp. 331-333 (1980).

[50] C. Lin, W.A. Reed, A.D. Pearson and H.-T. Shang, "Phase matching in the minimum-chromatic-dispersion region of single-mode fibers for stimulated four-photon mixing," *Opt. Lett.*, vol. 6, no. 10, pp. 493-495 (1981).

[51] S.J. Garth and C. Pask, "Four-photon mixing and dispersion in single-mode fibers," *Opt. Lett.*, vol. 11, no. 6, pp. 380-382 (1986).

[52] R.H. Stolen, J.E. Bjorkholm and A. Ashkin, "Phase-matched three-wave mixing in silica fiber optical waveguides," *Appl. Phys. Lett.*, vol. 24, no. 7, pp. 308-310 (1974).

[53] R.H. Stolen, "Phase-matched-stimulated four-photon mixing in silica-fiber waveguides," *IEEE J. Quantum Electron.*, vol. QE-11, no. 3, pp. 100-103 (1975).

[54] R.H. Stolen, M.A. Bösch and C. Lin, "Phase matching in birefringent fibers," *Opt. Lett.*, vol. 6, no. 5, pp. 213-215 (1981).

[55] R.K. Jain and K. Stenersen, "Phase-matched four-photon mixing processes in birefringent fibers," *Appl. Phys. B*, vol. 35, pp. 49-57 (1984).

[56] P.N. Morgan and J.M. Liu, "Parametric four-photon mixing followed by stimulated Raman scattering with optical pulses in birefringent optical fibers," *IEEE J. Quantum Electron.*, vol. 27, no. 4, pp. 1011-1021 (1991).

[57] W. Margulis and U. Österberg, "Four-photon fiber laser," *Opt. Lett.*, vol. 12, no. 7, pp. 519-521 (1987).

[58] K. Inoue, "Four-wave mixing in an optical fiber in the zero-dispersion wavelength region," *J. Lightw. Technol.*, vol. 10, no. 11, pp. 1553-1561 (1992).

[59] M. Karlsson, "Four-wave mixing in fibers with randomly varying zero-dispersion wavelength," *J. Opt. Soc. Am. B*, vol. 15, no. 8, pp. 2269-2275 (1998).

[60] M. Farahmand and M. De Sterke, "Parametric amplification in presence of dispersion fluctuations," *Opt. Express*, vol. 12, no. 1, pp. 136-142 (2004).

[61] J.S.Y. Chen, S.G. Murdoch, R. Leonhardt and J.D. Harvey, "Effect of dispersion fluctuations on widely tunable optical parametric amplification in photonic crystal fibers," *Opt. Express*, vol. 14, no. 20, pp. 9491-9501 (2006).

[62] B. Kibler, C. Billet, J.M. Dudley, R.S. Windeler and G. Millot, "Effects of structural irregularities on modulational instability phase matching in photonic crystal fibers," *Opt. Lett.*, vol. 29, no. 16, pp. 1903-1905 (2004).

[63] F.C. Byron, M.A. Bedgood, A. Finney, C. McGauran, S. Savory and I. Watson, "Shifts in zero dispersion wavelength due to pressure, temperature and strain in dispersion shifted singlemode fibres," *Electron. Lett.*, vol. 28, no. 18, pp. 1712-1714 (1992).

[64] K.K.Y. Wong, M.E. Marhic and L.G. Kazovsky, "Temperature control of the gain spectrum of fiber optical parametric amplifiers," *Opt. Express*, vol. 13, no. 12, pp. 4666-4673 (2005).

[65] L. Provino, A. Mussot, E. Lantz, T. Sylvestre and H. Maillotte, "Broadband and flat parametric amplifiers with multisection dispersion-tailored nonlinear fiber arrangement" *J. Opt. Soc. Am. B*, vol. 20, no. 7, pp. 1532-1537 (2003).

[66] Q. Lin and G.P. Agrawal, "Effects of polarization-mode dispersion on fiber-based parametric amplification and wavelength conversion," *Opt. Lett.*, vol. 29, no. 10, pp. 1114-1116 (2004).

[67] D.J. Richardson, J. Nilsson and W.A. Clarkson, "High power fiber lasers: current status and future perspectives," *J. Opt. Soc. Am. B*, vol. 27, no. 11, pp. B63-B92 (2010).

[68] H.M. Pask, R.J. Carman, D.C. Hanna, A.C. Tropper, C.J. Mackechnie, P.R. Barber and J.M. Dawes, "Ytterbium-doped silica fiber lasers: Versatile sources for the 1-1.2 μm region," *IEEE J. Sel. Topics Quantum Electron.*, vol. 1, no. 1, pp. 2-13 (1995).

[69] M.J.F Digonnet, ed., *Rare Earth Doped Fiber Lasers and Amplifiers*, 2nd ed., Marcel Dekker, Inc., 2001.

[70] Y. Jeong, J.K. Sahu, D.N. Payne and J. Nilsson, "Ytterbium-doped large-core fiber laser with 1.36 kW continuous-wave output power," *Opt. Express*, vol. 12, no. 25, pp. 6088-6092 (2004).

[71] M.J. Weber, J.E. Lynch, D.H. Blackburn and D.J. Cronin, "Dependence of the stimulated emission cross sections of Yb^{3+} on host glass composition," *IEEE J. Quantum Electron.*, vol. QE-19, no. 10, pp. 1600-1608 (1983).

[72] R. Paschotta, J. Nilsson, A.C. Tropper and D.C. Hanna, "Ytterbium-doped fiber amplifiers," *IEEE J. Quantum Electron.*, vol. 33, no. 7, pp. 1049-1056 (1997).

[73] K. Lu and N.K. Dutta, "Spectroscopic properties of Yb-doped silica glass," *J. Appl. Phys.*, vol. 91, no. 2, pp. 576-581 (2002).

[74] J. Nilsson, W.A. Clarkson, R. Selvas, J.K. Sahu, P.W. Turner, S.-U. Alam and A.B. Grudinin, "High-power wavelength-tunable cladding-pumped rare-earth-doped silica fiber lasers," *Opt. Fiber Technol.*, vol. 10, pp. 5-30 (2004).

[75] M. Engholm and L. Norin, "Preventing photodarkening in ytterbium-doped high power fiber lasers; correlation to the UV-transparency of the core glass," *Opt. Express*, vol. 16, no. 2, pp.1260-1268 (2008).

[76] C.R. Giles and E. Desurvire, "Modeling erbium-doped fiber amplifiers," *J. Lightw. Technol.*, vol. 9, no. 2, pp. 271-283 (1991).

[77] J.D. Kafka, "Laser diode pumped fiber laser with pump cavity," U.S. patent 4,829,529 (1989).

[78] R.D. Maurer, "Optical waveguide light source," U.S. patent 3,808,549 (1974).
[79] D.J. DiGiovanni and A.J. Stentz, "Tapered fiber bundles for coupling light into and out of cladding-pumped fiber devices," U.S. patent 5,864,644 (1999).

Chapter 3

Ytterbium-Doped Fibre MOPA

From the discussion in Chapter 2, it should be evident that efficient four-wave mixing places several requirements on the pump source. This is particularly true for FWM processes associated with large frequency-shifts, for which the parametric bandwidth is typically quite small. In this case, the appropriate pump source should have a narrow spectral linewidth and should furthermore be capable of kW-level output powers. It is then also crucially important to ensure a high spectral purity, since seeding of competing nonlinearities can easily allow their dominance, especially when the phase-matching is degraded. Satisfying these requirements is not trivial, especially when an all-fibre pump source is additionally preferred. However, the modular approach of the MOPA architecture allows one to satisfy these requirements in stages, thereby providing the ideal pump source solution.

This chapter is dedicated to an overview of the pulsed pump MOPA, used in the majority of the optical parametric amplifier and oscillator experiments to follow in Chapters 4 and 5. Since the system was improved throughout the work of this thesis, different experiments correspond to different pump source characteristics. For this reason, the chapter details three distinct permutations of the MOPA, using one of two possible seed lasers. Section 3.1 describes the attributes of the MOPA seed lasers, whilst Section 3.2 elaborates on the performance of the cascaded amplifier stages.

3.1 MOPA Seed Source

Depending on the desired MOPA characteristics, several seed laser sources may be considered. For pulsed MOPA systems in particular, the choice of seed laser will be different depending on the intended pulse duration regime. If picosecond or femtosecond pulses are required, the MOPA seed will typically be a mode-locked laser. Nanosecond pulsed lasers can similarly be constructed through the introduction of an intra-cavity Q-switching mechanism. The pulse durations associated with these sources are typically a few nanoseconds or longer. If still longer pulse durations are required, direct modulation of the laser diode current becomes an option. For pulse durations ranging between 200 ps and 5 ns, external modulation of a CW laser through the use of a fast electro-optic modulator (EOM) provides a flexible solution. The rapid modulation capabilities of EOMs not only allow for (almost) arbitrary pulse durations at arbitrary repetition frequencies, but also enable pulse shaping [1] and generation of bursts.

For the work of this thesis, the pulse duration regime of interest was determined by considering a number of factors. Firstly, the large frequency-shift FWM processes of interest are typically subject to differential group delays of the order of 10 ps/m. Since walk-off results in a significant reduction in the FWM efficiency, the pump pulse duration should preferably exceed 100 ps. It is worth noting that this restriction can be circumvented through the use of highly-nonlinear FWM fibres. However, the small core diameters associated with highly-nonlinear fibres may preclude an all-fibre device due to splice losses, and a limitation on the power scalability. For this reason, our considerations are based on the nonlinear attributes of more typical fibres, instead. Secondly, if the pump pulse duration exceeds a few ns, the SBS threshold is reduced significantly (refer to Chapter 2) for the case of (near) transform-limited pulses like ours. Not only can this lead to a scenario where SBS dominates over FWM in the nonlinear converter, but SBS may in fact also disrupt the amplification process throughout the MOPA. Finally, it is worth considering the average-power-handling capabilities of common fibre-components used in the construction of all-fibre systems. Typically, fused fibre couplers, for example, may be limited to about 10 W average power, although powers at the 100 W level have been reported in state-of-the-art demonstrations [2]. In order to reach kW-level peak powers it is therefore required to operate the pump source at a duty cycle of ~1%. However, in an OPO, a low pulse

repetition frequency (PRF) will require a long intra-cavity fibre length for the purpose of synchronous pumping, which may result in unacceptable losses and nonlinear degradation (refer to Chapter 5). This effectively places an upper limit on the pump pulse duration required for a desired peak power.

Based on the preceding considerations, it was decided to construct a MOPA for operation in the sub-5 ns pulse duration regime. For this reason, the CW seed laser is modulated external to the cavity, prior to being amplified. This section gives an overview of two CW seed sources used in the experiments of Chapters 4 and 5.

3.1.1 Ytterbium-Doped Fibre Ring-Laser

As a first approach, a seed laser was constructed from available fibre-optic components. The chosen configuration was a uni-directional fibre ring laser. The experimental setup is given in Figure 3.1. Unless otherwise stated, all fibres and fibre-components may be assumed to be polarization maintaining (PM).

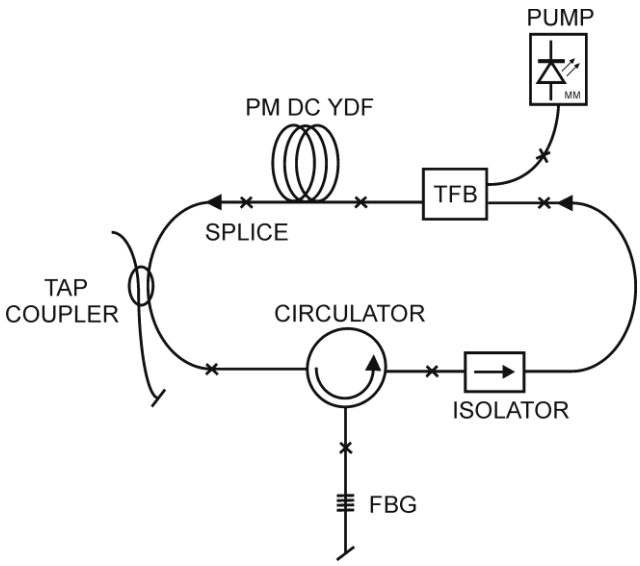

Figure 3.1: Experimental setup for the double-clad (DC) ytterbium-doped fibre (YDF) ring laser. A fibre Bragg grating (FBG) at a centre wavelength of 1079 nm is used to filter the laser feedback. TFB: Tapered fibre bundle.

The PM double-clad (DC) ytterbium-doped fibre (YDF) for the ring laser was manufactured by Liekki (Yb1200-10/125) and has a core diameter and NA of 11 μm and 0.076, respectively [3]. The aluminosilicate YDF has a length of 10 m and is specified to have a cladding absorption of 1.8 dB/m at a wavelength of 920 nm. A single

MM pump diode, emitting at a wavelength around 910 nm (JDS uniphase [4]), is spliced to a 6+1:1 TFB (Avensys Tech [5]), which is in turn sliced to the YDF. Each of the TFB's six multi-mode (MM) input fibres have a core diameter of 105 μm and a NA of 0.22. The double-clad TFB output fibre has a core diameter and NA of 5 μm and 0.14, respectively. As a result of the MFD-mismatch (refer to equation 2.18), it proved difficult to reduce the splice loss between the TFB and YDF below 2 dB for the signal. The splice between the TFB and YDF is coated with a low refractive-index polymer to ensure guidance of the pump light in the cladding. The splice at the output of the YDF is similarly coated with a high-index polymer to remove residual pump light from the cladding.

Laser feedback is facilitated through the use of a circulator (Opto-Link corporation [6]) and a single polarization (SP) fibre isolator (AFW Technologies [7]). The functionality of the circulator is two-fold. Firstly, it enforces uni-directional propagation within the cavity. Secondly, the circulator accommodates the spectral filter, provided here by a fibre Bragg-grating (FBG). The in-house fabricated FBG has a centre wavelength of 1079 nm and a 3-dB bandwidth of 0.1 nm[2]. The SP isolator enforces single polarization conditions in the ring laser. This is achieved by introducing large losses for light propagating in the fast axis of the PM fibre, allowing light orientated along the slow axis to saturate the gain in the YDF. This then prevents power build-up in the fast-axis polarization.

Laser light is extracted from the cavity through the use of a fibre coupler (Gooch & Housego [8]), with a coupling ratio of 80/20, at 1079 nm. Initially, the output coupler was arranged to couple 20% of the light back into the cavity. However, since the cavity has high losses due to the presence of the circulator (4 dB in total), isolator (2 dB), TFB-YDF splice (~1.8 dB) and FBG (~3 dB), the output coupler's ports were exchanged. With 80% of the light coupled back into the cavity, the intra-cavity power is increased, leading to stronger gain saturation and in turn larger suppression of ASE. Increased intra-cavity power requires greater care, since both the circulator and isolator have maximum power handling ratings of 300 mW. For this reason, the output-coupler is located prior to these low-power components, directly following the YDF output. The

[2] Courtesy of Morten Ibsen

un-spliced output coupler pigtails, as well as any other loose fibre ends, are terminated by angled cleaves to prevent feedback from Fresnel reflections at the glass-air interface.

Figure 3.2(a) shows the ring laser output power as a function of absorbed pump power. The threshold pump power is 0.63 W and the slope efficiency is 3.7%. The low value for the slope efficiency is a result of the high intra-cavity losses and the low output coupling. Despite the poor efficiency, the CW output power is sufficient, since the power-handling of the EOM is a mere 30 mW (refer to Section 3.2). Figure 3.2(b) gives the ring laser output spectrum at a power of 42 mW, measured using an Ando AQ-6317 optical spectrum analyser (OSA) at a resolution of 0.1 nm. The spectrum reveals a high extinction ratio of over 60 dB, at the laser wavelength. The ASE envelope, stretching from ~1060 nm to 1200 nm, has its peak around 1095 nm. This value suggests that the YDF is longer than required for a laser wavelength of 1079 nm, at the operating pump power of 1.15 W [9]. At the maximum OSA resolution of 0.01 nm, a measurement of the ring laser linewidth gives 30 pm. The polarization extinction ratio (PER) of the ring laser, operating at an output power of 42 mW, was measured to 15 dB.

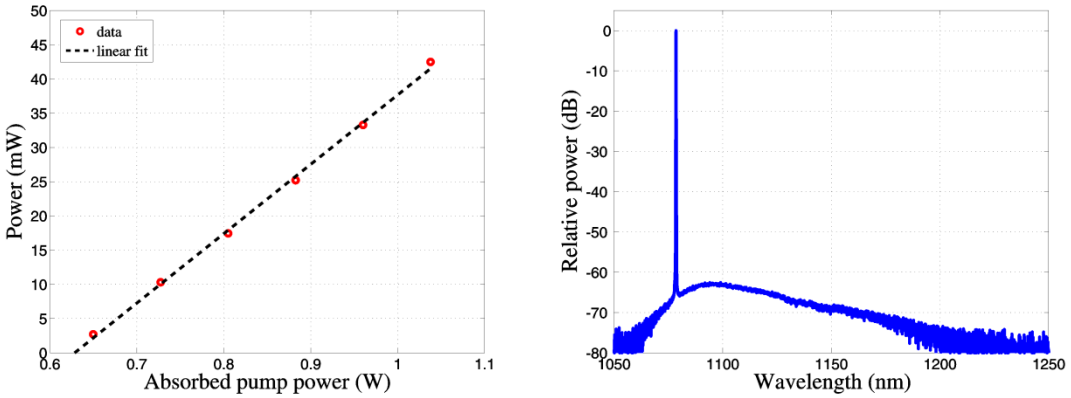

(a) (b)

Figure 3.2: (a) Ring laser output power at 1079 nm as a function of absorbed pump power. (b) Output spectrum at a power of 42 mW (spectral resolution: 0.1 nm).

3.1.2 Laser Diode Seed Source

For the experiments described in the latter part of this thesis, the ring laser MOPA seed was replaced by a single-mode laser diode at a wavelength of 1080 nm (Lumics [10]). This substitution was primarily motivated by the inclusion of an EOM with a

higher power handling rating, of 100 mW. The new EOM enabled the use of a higher-power seed source, which in turn allowed for sufficient gain saturation in the first amplifier stage at lower duty cycles than before.

Figure 3.3(a) gives the power characteristics of the Lumics SM diode, whilst Figure 3.3(b) gives the corresponding output spectrum at a power of 103 mW. As a result of FBG stabilization, the diode displayed a linewidth identical to that of the ring laser (30 pm). Transmission measurements through a single polarization isolator also confirmed an excellent PER.

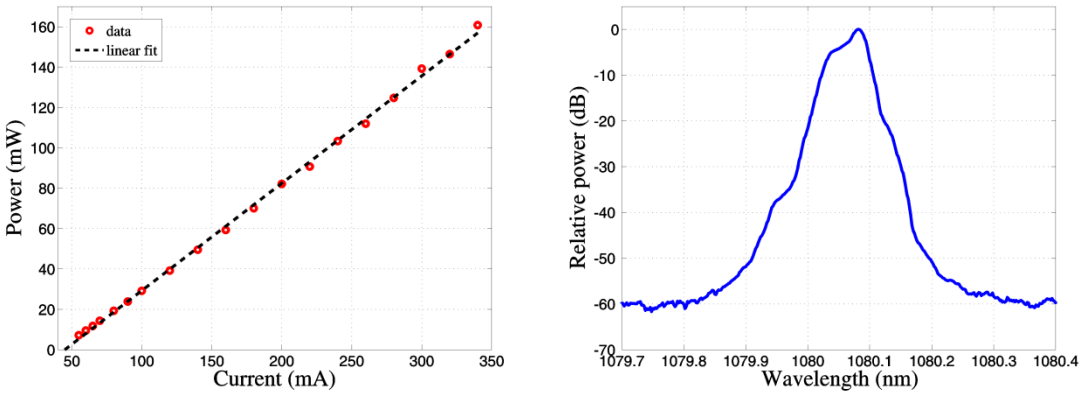

(a) (b)

Figure 3.3: (a) Lumics SM diode output power at 1080 nm as a function of pump current. (b) Output spectrum at a power of 103 mW (spectral resolution: 0.01 nm).

3.2 Amplifier Characterisation

As stated in the introduction, the characteristics of the MOPA may be sub-categorized into three groups. However, the general architecture depicted in the schematic of Figure 3.4 is applicable regardless. The CW seed source, with an output power in the range 30 mW to 100 mW, is protected by a SP isolator (AFW Technologies) and spliced to an 80/20 tap-coupler (Gooch & Housego). This tap-coupler removes 20% of the light at ~1080 nm and is used primarily to monitor the seed laser characteristics. The 80% port is spliced to the EOM (intensity modulator). Initial experiments made use of a 10 GHz Eospace EOM [11]. This component was eventually replaced by a 5 GHz Selex EOM with improved power handling [12]. The radio frequency (RF) input to the EOM typically consisted of square pulses of duration 200 ps to 2.5 ns, at repetition frequencies ranging from 1 MHz to 5 MHz. Depending on the required modulation

speeds, the RF signal was provided by either a 150 MHz pulse generator (Agilent 8110A), or by the combination of a 4 GHz arbitrary waveform generator (Tektronix AWG710) and a 1 GHz RF-amplifier (Mini-Circuits ZHL-2-8). In addition to RF modulation, a DC bias voltage is also applied to the EOM. The bias voltage ensures that the EOM is operated at the optimum pulse extinction ratio. As the EOM is very sensitive to counter-propagating radiation, it is followed by a second SP isolator, which is spliced to the input of the amplifier chain.

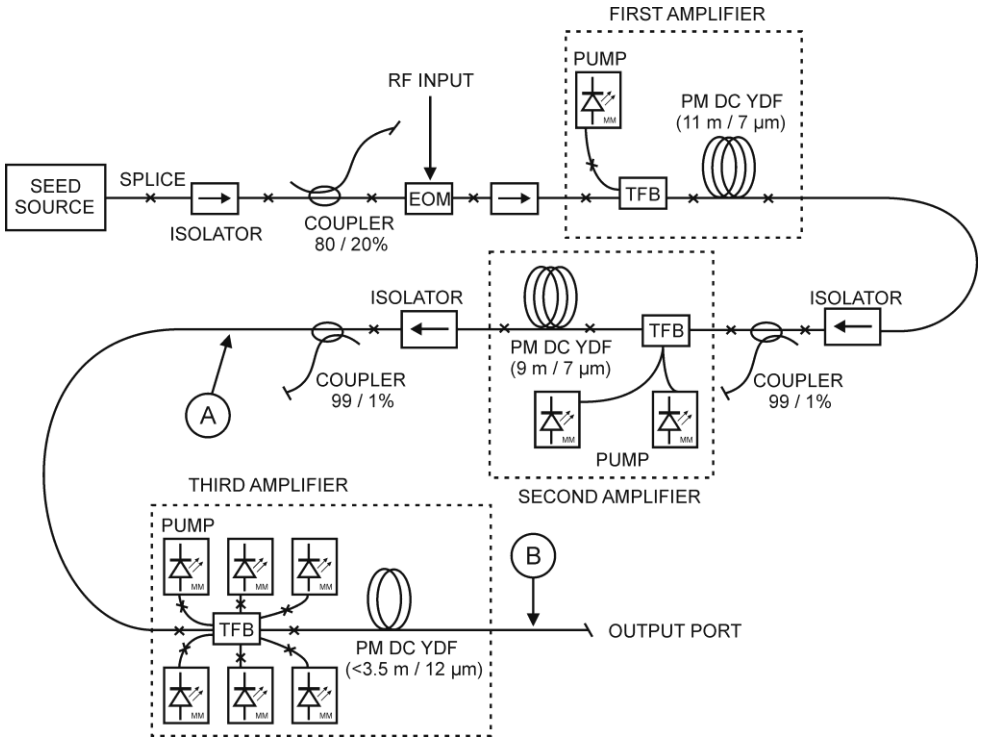

Figure 3.4: Experimental setup for the MOPA. Refer to the main text for details. A and B are markers that indicate the positions of the narrow-band spectral filter and band-pass-filter-integrated isolator, respectively (refer to Sections 3.2.2 and 3.2.3 in the main text). All fibre-components are PM.

All three amplifier stages consist of a co-pumped aluminosilicate PM DC YDF. The YDF used for the first and second amplifiers was fabricated in-house (T0278-L30178)[3]. This fibre has a core diameter and NA of 7 µm and 0.1, respectively. The MFD at the seed wavelength is calculated to be 8.6 µm. Since this YDF has a specified absorption of 1 dB/m (at 915 nm), it was decided to use device lengths of 11 m and 9 m, for the first and second amplifier, respectively. The 6+1:1 TFB used in all amplifier

[3] Courtesy of Jayanta Sahu

stages has a MFD of 6.8 μm (Gooch & Housego). For this reason, the T0278-L30178 YDF and TFB spliced well. In contrast, the splice between the TFB and third amplifier YDF gave a loss of ~1.5 dB. The loss is mainly attributed to this YDF having a larger MFD for the purpose of minimizing unwanted nonlinearities within the amplifier. The third amplifier YDF was acquired from Coractive (DC-Yb-PM-12/125-10-01) and has a core diameter of 12 μm and an NA of 0.1 [13]. Whilst the corresponding V-number, at 1080 nm, has a value of 4.1, a beam quality measurement confirmed single-mode guidance ($M^2 < 1.1$). Since this fibre has a large 915 nm cladding absorption of 3.2 dB/m, the device length never exceeded 3.5 m.

Amplifier stages are separated by SP isolators from Shinkosha [14] (post amplifier-1) and Agiltron [15] (post amplifier-2), as well as low-ratio tap-couplers. The isolators protect the seed laser and pre-amplifiers from counter-propagating light, but also ensure an acceptable PER (~15 dB) throughout the system. Tap-couplers allow for easy evaluation of the amplifier powers, spectra and temporal characteristics. A portion of the power from the post amplifier-1 tap-coupler is continuously monitored on a power meter that provides feedback to an analog-to-digital converter. The converter, in turn, is connected to a computer, which uses a simple algorithm to adjust the DC-bias input to the EOM via a digital-to-analog converter. In this way, the EOM is always assured to have the appropriate bias to keep the pulse ER optimized under changing thermal and mechanical conditions.

3.2.1 YDFL-Seeded MOPA

The low power handling rating and high insertion loss (3.8 dB) of the EOM, together with a low duty-cycle modulation (≤1.25%), results in first-amplifier input average powers of around 30 μW. Despite this low value, the amplifier gain is sufficiently saturated, with the output spectrum displaying an ER >30 dB at 1079 nm, at a spectral resolution of 0.1 nm (see Figure 3.5(b)). Also shown in Figure 3.5(a) is the amplifier average output power, as a function of absorbed pump power, for 2.5 ns pulses at a PRF of 5 MHz. The first amplifier was typically operated at average output powers around 7 mW, with an associated amplifier gain of ~24 dB.

Figure 3.6 similarly shows the output average power and spectrum from the second amplifier, for the above mentioned modulation parameters. From the spectrum,

it is clear that the ER of the signal, relative to the ASE envelope, has degraded from the first amplifier. This is a result of further amplification of the ASE originating from the YDFL and first amplifier. The spectral noise furthermore extends out to 1140 nm, where it provides seed photons for the first order Raman Stokes. Since the peak powers in the second amplifier and subsequent fibre components are of the order of 100 W, SRS start to build up and can grow to unacceptable levels inside the third amplifier. To mitigate this effect, the second amplifier was mostly operated at an average power of no more than 640 mW.

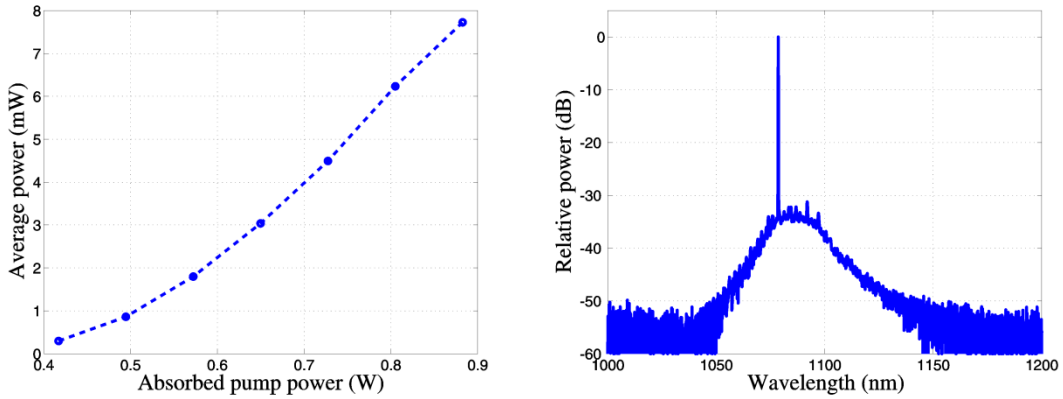

(a) (b)

Figure 3.5: (a) YDFL-seeded first amplifier output at 1079 nm, as a function of pump power. (b) Output spectrum at an average power of 6.2 mW (spectral resolution: 0.1 nm). Modulation parameters: 2.5 ns pulses at 5 MHz.

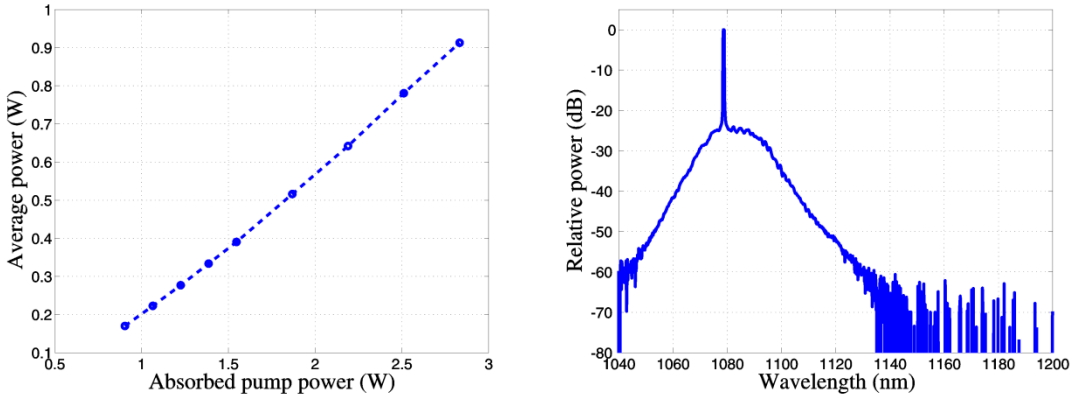

(a) (b)

Figure 3.6: (a) Second amplifier output at 1079 nm, as a function of pump power. (b) Output spectrum at an average power of 640 mW (spectral resolution: 0.5 nm). Modulation parameters: 2.5 ns pulses at 5 MHz.

The third and final amplifier's average output power, as a function of absorbed pump power, is shown in Figure 3.7(a). The measured values correspond to a YDF length of 3.3 m. Whilst the output power did not show any signs of saturation and the available pump power was more than adequate, the MOPA was typically operated at a modest average output power of 4 W. This was necessitated by the emergence of SRS. The MOPA output spectrum, at an average power of 4 W, is shown in Figure 3.7(b) for duty cycles of 1.25% (2.5 ns pulses at 5 MHz) and 0.2% (1 ns pulses at 2 MHz). Whereas the spectrum for a duty cycle of 1.25% (blue) shows initial signs of SRS, the spectrum for 0.2% shows significant levels of SRS at the first and second Stokes, as well as the first-order Raman anti-Stokes. Not only does this level of SRS compromise the spectral purity of the FWM pump source, leading to competing nonlinearities, but it also depletes the power at 1079 nm. Significant levels of SPM and possibly XPM are inevitable, too, at these levels of nonlinear interaction.

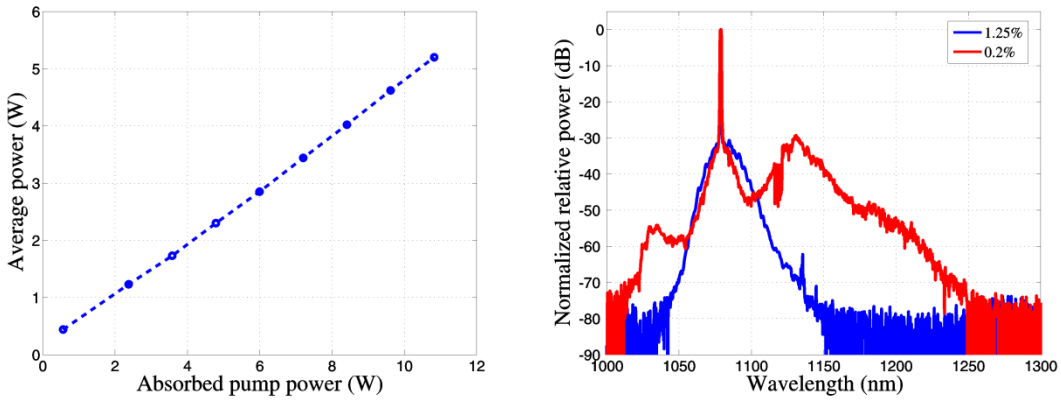

(a) (b)

Figure 3.7: (a) Third amplifier (3.3 m YDF) output at 1079 nm, as a function of pump power. (b) Output spectrum at an average power of 4 W, for a duty cycle of 1.25% (2.5 ns pulses at 5 MHz) and 0.2% (1 ns pulses at 2 MHz). (spectral resolution: 1 nm).

3.2.2 YDFL-Seeded MOPA: Improved Setup

In order to access higher peak powers, changes were made to reduce the impact of SRS in the MOPA. To this end, a tunable narrowband spectral filter (Agiltron [15]) was included following the second amplifier in the setup of Figure 3.4, at the position marked by A. Figure 3.8(a) gives the average power from the second amplifier, as measured at the output of the spectral filter for a duty cycle of 0.2% (1 ns pulses at 2

MHz). As before, the second amplifier was operated at a pump power of 2.2 W. This time the resultant output power was 258 mW, primarily attributed to 1 dB and 2.3 dB insertion losses at the fibre isolator and tunable filter, respectively. The output spectrum from the filter, with its 1 nm bandwidth centred at 1079 nm, is given in Figure 3.8(b). The effect of the filter, whereby out-of-band light is suppressed by up to 30 dB, is easily verified from a comparison to the spectrum of Figure 3.6(b).

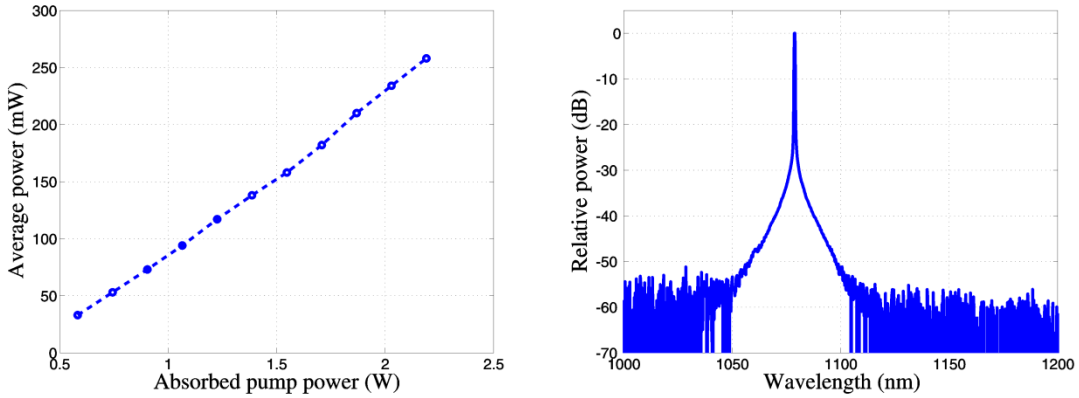

(a) (b)

Figure 3.8: (a) Second amplifier output via a narrowband filter, at 1079 nm, as a function of pump power. (b) Output spectrum, via a narrowband filter, at an average power of 258 mW (spectral resolution: 0.5 nm). Modulation parameters: 1 ns pulses at 2 MHz.

Although the presence of the narrowband filter lead to reduced seeding at the SRS wavelengths inside the third amplifier, additional measures were required to optimise the spectral purity at the MOPA output. It was therefore decided to reduce the third amplifier's YDF to a length of 2.3 m. Although a shorter YDF resulted in a reduction of absorbed power, it also reduced the effective length for SRS. The shorter YDF furthermore lead to a shift in the gain peak towards shorter wavelengths, subsequently lessening the contribution of ASE to SRS seeding. The resultant power and spectral characteristics are shown in Figure 3.9. At an identical launched pump power, the MOPA average output power of 3.8 W represents a slight reduction relative to the 3.3 m YDF. Also the output spectrum (blue) compares favourably to the corresponding duty cycle in Figure 3.7(b). Not only is the spectrum free from SRS features, but the ER at 1079 nm is also noticeably enhanced.

In the absence of appropriate high power fibre isolators and filters, some initial experiments relied on a free-space launch from the MOPA. This enabled the use of high

power free-space isolators. In terms of additional filtering, volume Bragg-gratings (VBG) were preferred over short-pass dichroic mirrors, primarily due to their narrow pass-bands (0.5 nm), high suppression (>60 dB) and low loss (<0.2 dB). The red curve in Figure 3.9(b) gives the spectrum of light diffracted off the VBG, for an incident spectrum similar to the blue curve.

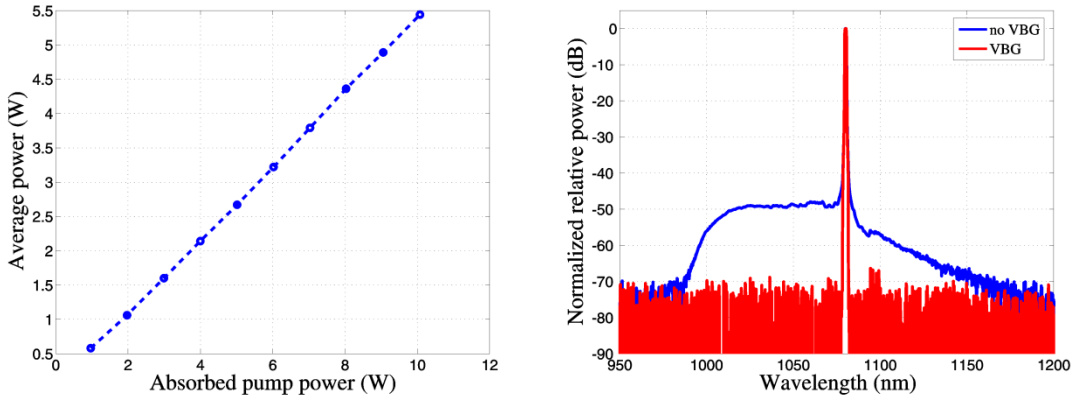

(a) (b)

Figure 3.9: (a) Third amplifier (2.3 m YDF) output at 1079 nm, as a function of pump power. (b) Output spectrum at an average power of 3.8 W, in the absence (blue) and presence (red) of a VBG spectral filter (spectral resolution: 1 nm).

3.2.3 Diode-Seeded MOPA

In the final MOPA configuration, used in the experiments reported towards the latter part of Chapter 5, the emphasis shifted and an all-fibre FWM pump source became a priority. Whilst the experimental setup for the external modulation and amplifier chain remained unchanged from that of Figure 3.4, including the improvements of Section 3.2.2, the YDFL seed laser was replaced by the 1080 nm Lumics diode of Section 3.1.2. More importantly, a band-pass-filter-integrated fibre isolator, at a centre wavelength of 1080 nm, was incorporated following the third amplifier, at the position marked by B (see Figure 3.4). This component was developed in collaboration with Shinkosha to have a customised set of properties [14], including a relatively high power handling rating (2 W), broad pass-band (1060 – 1082 nm), large out-of-band suppression (1100 – 1120 nm >25 dB, 1120 – 1145 nm >50 dB) and large mode-area fibre pigtails (Nufern PM085 LNA). The performance of the first and second amplifiers were found to be qualitatively similar to the results of Figures 3.5 and 3.8. However, the presence of the

fibre isolator-filter affected the characteristics of the third amplifier, and consequently the MOPA output.

The MOPA average power, as measured from the band-pass-filter-integrated fibre isolator output, is given in Figure 3.10(a). The output power was limited to 2.2 W, by the damage limit of the fibre isolator-filter. The damage limit was determined to be around 3.4 W average power, based on a low power measurement of the component's insertion loss (1.9 dB) and an accidental destructive measurement. This insertion loss, together with an additional 0.5 dB loss associated with the splice between the YDF and fibre isolator-filter pigtail, is responsible for the reduced slope in Figure 3.10(a). The output spectrum at a duty cycle of 0.2%, shown in Figure 3.10(b), compares well to the VBG-filtered spectrum of Figure 3.9(b). Despite the all-fibre nature of the power delivery, SRS power levels are below the measurement threshold, at a spectral resolution of 1 nm.

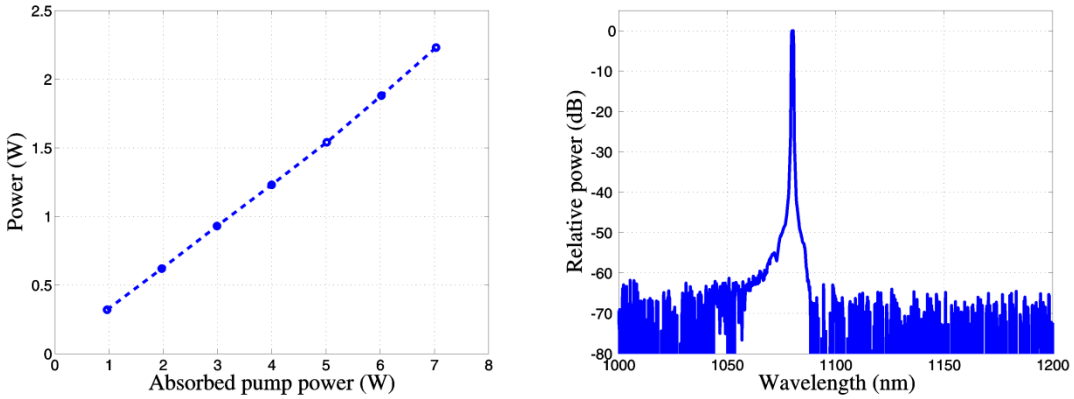

(a) (b)

Figure 3.10: (a) Lumics-seeded third amplifier (2.3 m YDF) output via a band-pass-integrated fibre isolator, at 1080 nm, as a function of pump power. (b) Output spectrum, via a band-pass-integrated fibre isolator, at an average power of 2.3 W (spectral resolution: 1 nm).

Shown in Figure 3.11 is the spectral linewidth of the output from the Lumics-seeded MOPA, for two power values. It is clear that the 3 dB linewidth is almost invariant to the effect of SPM, which only succeeds in generating small satellite features, as can be expected for optical pulses with a super-Gaussian profile [16].

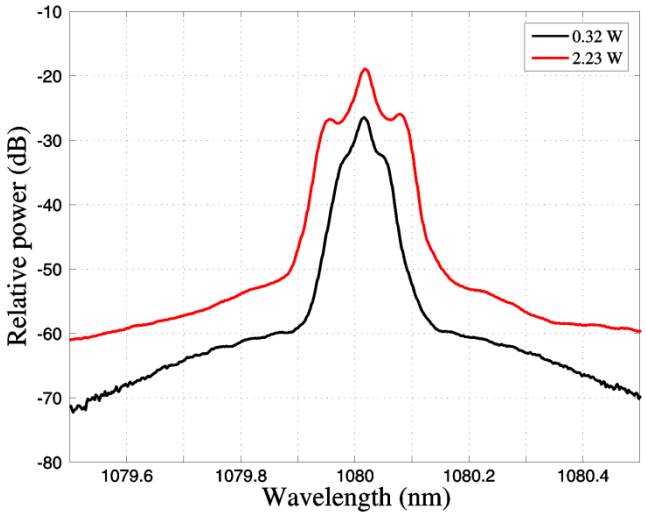

Figure 3.11: Lumics-seeded MOPA output linewidths at low power and at maximum power (spectral resolution: 0.01 nm). As a result of the square pulse shape, the MOPA linewidth is resilient to the broadening effect of SPM.

3.3 References

[1] D.J. Richardson, J. Nilsson and W.A. Clarkson, "High power fiber lasers: current status and future perspectives," *J. Opt. Soc. Am. B*, vol. 27, no. 11, pp. B63-B92 (2010).
[2] Y. Feng, L.R. Taylor and D.B. Calia, "150 W highly-efficient Raman fiber laser," *Opt. Express*, vol. 17, no. 26, pp. 23678-23683 (2009).
[3] Information available at: www.nlight.net
[4] Information available at: www.jdsu.com
[5] Information available at: www.itflabs.com
[6] Information available at: www.optolinkcorp.com
[7] Information available at: www.afwtechnologies.com.au
[8] Information available at: www.goochandhousego.com
[9] R. Paschotta, J. Nilsson, A.C. Tropper and D.C. Hanna, "Ytterbium-doped fiber amplifiers," *IEEE J. Quantum Electron.*, vol. 33, no. 7, pp. 1049-1056 (1997).
[10] Information available at: www.lumics.com
[11] Information available at: www.eospace.com
[12] Information available at: www.crisel-instruments.it/selex/
[13] Information available at: www.coractive.com
[14] Information available at: www.shinkosha.com
[15] Information available at: www.agiltron.com
[16] G.P. Agrawal, *Nonlinear Fiber Optics*, 3rd ed., Academic Press, 2001.

Chapter 4

OPA Using Conventional Fibre

This chapter details the results from an initial investigation into large frequency-shift FWM. The approach considers conventional, non-microstructured fibres for the nonlinear converter. This decision was based on the rationale that the impact of the previously mentioned longitudinal inhomogeneities (refer to Section 2.3.4) would be less severe in conventional fibres, for which the manufacturing techniques are more mature.

Section 4.1 is devoted to results from numerical models that were used to identify fibres of interest. Experimental results from the chosen fibre, in noise-seeded and externally seeded configurations, follow in Section 4.2. The chapter is concluded with a brief summary of important results and their implications.

4.1 Evaluation of Fibres

In this section, the process whereby different commercial fibres were investigated in terms of their potential for FWM, is detailed. The process essentially consists of two stages. In the first stage, the procedure outlined in the following paragraphs is used to evaluate the dispersion and phase-matching properties of real fibres (Section 4.1.1). Stage two subsequently demonstrates how the phase-matching properties and waveguide attributes of the chosen fibres influence the optimal fibre length required for FWM, under ideal conditions (Section 4.1.2).

Since the dispersion properties of commercial fibres are typically only specified for a narrow spectral range about the telecommunications window, a method to extract the dispersion over the desired range was required. Whilst fibre dispersion can be measured in a variety of ways [1], the methods often involve long fibre samples and short broadband pulses, or time consuming free-space alignment. For this reason, a numerical procedure was used to calculate fibre dispersion, using measured values for the refractive index profiles (RIP) as input parameters.

The numerical procedure, used to obtain the mode propagation constants and mode fields of a real fibre at a specific wavelength, λ, can be explained at the hand of the following:

1. The fibre RIP is measured using the refracted near-field (RNF) method, at a wavelength of $\lambda_0 = 630$ nm[4]. Examples of measured RIPs for commercial fibres, considered during the initial stages of our investigation, are given in Figure 4.1(a) to (d). For simplicity, the refractive index distributions of these fibres were assumed to be circularly symmetric. In what follows, the Pirelli Freelight fibre (Figure 4.1(d)) will be used for reference purposes.
2. From the RIP and the value for the refractive index of pure SiO_2 at λ_0, n_0, the presence of dopants can be identified. In the case of the Freelight fibre, the presence of an index-increasing dopant is identified. The dopant is assumed to be GeO_2.
3. Using the Sellmeier coefficients of the doped material, specified at a certain doping concentration, m_+, the Sellmeier equation (equation 2.19) is used to calculate the refractive index of the doped material, n_+, at λ_0.
4. The refractive index of the medium may now be obtained for an arbitrary doping concentration, m, through the use of the following equation (identical to equation 2.20):

$$n = \left[n_0^2 + \frac{m}{m_+}(n_+^2 - n_0^2)\right]^{1/2} \tag{4.1}$$

[4] courtesy of Robert Standish

5. Equation 4.1 enables the mapping of the measured RIP into a doping index profile (n(r)→ m(r)).
6. The Sellmeier equation may now again be used to calculate the refractive index of the doped material (m_+) and SiO_2 at the wavelength of interest, λ.
7. The values of n_+ and n_0 at λ together with m(r) are substituted into equation 4.1 to obtain the RIP at λ.

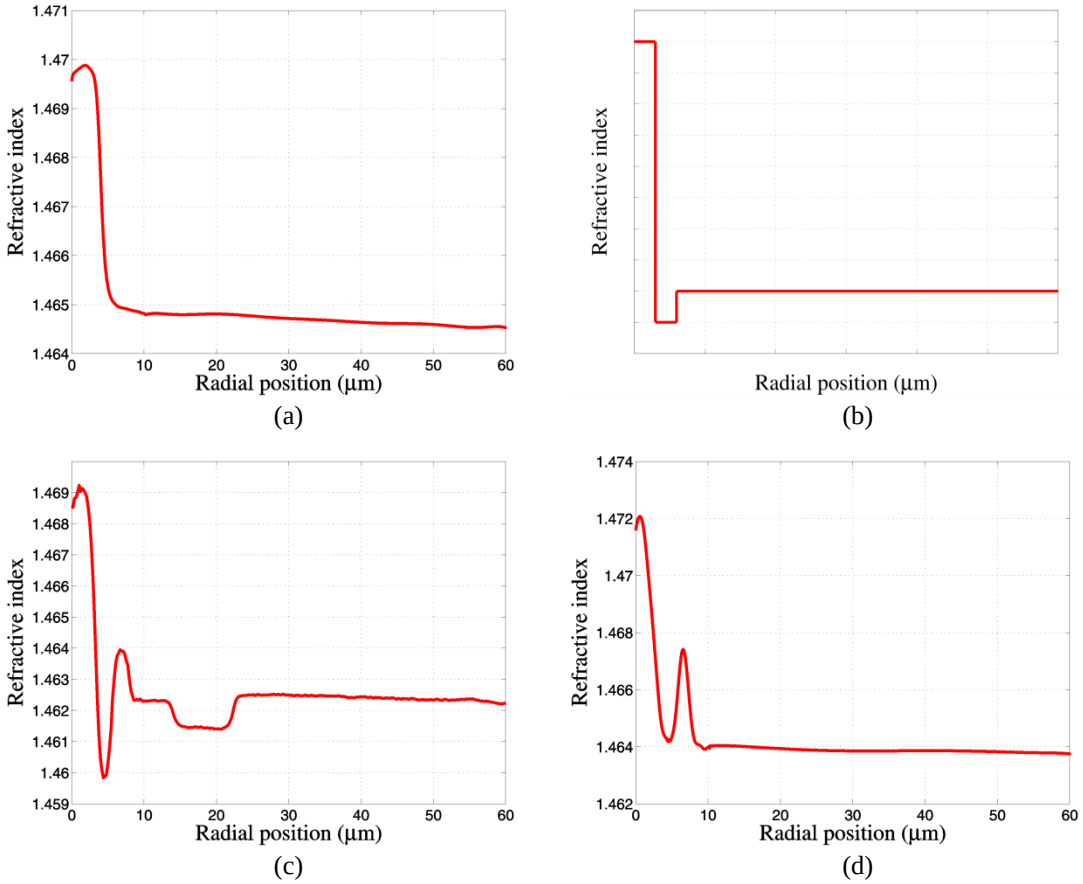

Figure 4.1: RIPs used in a numerical procedure for the calculation of fibre dispersion: (a) Corning SMF-28, (b) Sumitomo HNLF (representative), (c) Lucent Truewave and (d) Pirelli Freelight.

By repeating the above procedure over a range of wavelengths (λ), and by solving the wave equation (Chapter 2.1.1) for n(r,λ), the total dispersion for a given fibre is obtained. As an example, Figure 4.2 shows the calculated total dispersion for the Freelight fibre, which is found to compare well to measured values[5].

[5] courtesy of a time-of-flight measurement, performed by Carl Farrell

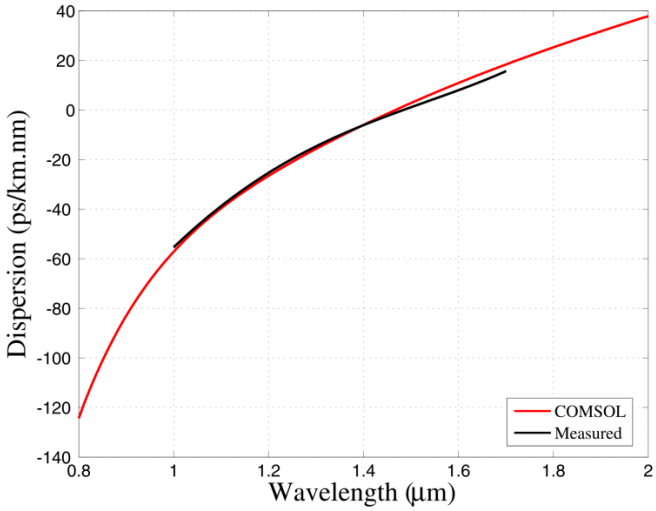

Figure 4.2: Comparison between the measured and calculated values for the total dispersion of the Freelight fundamental mode.

The dispersion of the effective refractive index allows us to search for phase-matched components according to $\Delta\beta = \beta_a + \beta_s - 2\beta_p$ (see Chapter 2.3). This is done by assigning a constant value to the pump frequency (ω_p), whilst varying the frequency-shift ($\Omega = \omega_a - \omega_p = \omega_p - \omega_s$). As Ω is varied, ω_a and ω_s assume specific values, which, together with ω_p, satisfy the conservation of energy requirement. The value of n_{eff} at each of the relevant frequencies is obtained through interpolation of the calculated dispersion. The phase mismatch is calculated before a new value for ω_p is chosen and the process is repeated. The application of this approach follows next.

4.1.1 Phase-Matching Calculations

The fibres shown in Figure 4.1 all have ZDWs in excess of 1273 nm, which is the zero material dispersion wavelength for silica. Consequently, the intended FWM pump wavelength in the range 1060-1080 nm, is normally dispersive ($\beta_2 > 0$). According to the discussion in Chapter 2.3.2, these fibres may therefore lend themselves to co-polarized fundamental mode phase-matching (refer to Figure 2.7(b)). However, when the wavelength difference between the pump and ZDW becomes too large (100 nm or more), the value of β_2 can become enormous. In this case, a large negative contribution from β_4 is required as compensation, to achieve phase-matching. Provided that the fibre dispersion results in a negative β_4, this critical value will only be reached for very large

values of the frequency-shift, if a solution is in fact physically realizable. Large phase-matched frequency-shifts are also correlated with small parametric bandwidths (for the co-polarized fundamental mode process), leading to extremely inefficient FWM in real fibres (refer to Chapter 2.3.2). It is therefore clear that the preceding conventional fibres preclude the use of co-polarized fundamental mode FWM. For this reason, an investigation into the plausibility of using the mixed higher-order spatial mode phase-matching process of Figure 2.7(c), was conducted [2], [3]. The findings of this study is covered next.

Before we proceed with a discussion on the use of higher-order modes, as a method for phase-matching, the following should be noted. The modes obtained from the COMSOL software are fully vectorial (refer to Chapter 2.1.1). In contrast, the coupled amplitude equations (equations 2.47 to 2.49) and the accompanying overlap integrals (equations 2.50 and 2.51) were derived under the approximation of linearly polarized (LP) fields. For this reason, the consolidated approach presented below employs a superposition of the calculated COMSOL vector modes (refer in Chapter 2.1.1).

As for Section 4.1, we start off by considering the Pirelli Freelight fibre. This fibre supports five modes in the wavelength range 800 nm to 1700 nm. From the cut-off wavelengths and the available modes, a number of possible mode combinations for multi-mode phase-matching were identified. These include $LP_{11}^{p} LP_{02}^{a} LP_{11}^{s}$ (for $\lambda_p \leq 1210$ nm), $LP_{02}^{p} LP_{21}^{a} LP_{02}^{s}$ (for $\lambda_p \leq 1010$ nm) and $LP_{02}^{p} LP_{21}^{a} LP_{11}^{s}$ (for $\lambda_p \leq 1130$ nm), where a superscript indicates the relevant frequency component for a given mode. The modes of the latter combination are shown in Figure 4.3, where different colours illustrate the relative field amplitude.

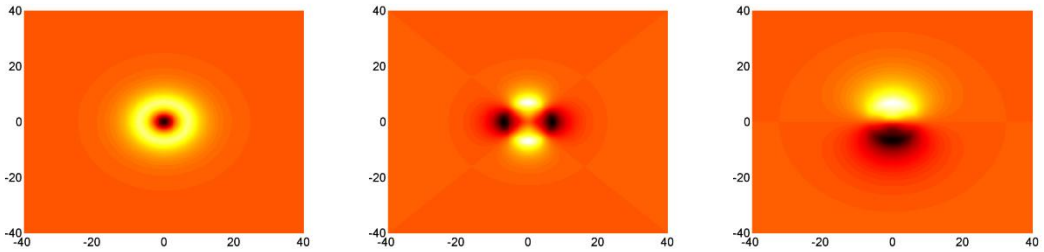

(a) (b) (c)

Figure 4.3: Combination of higher-order Freelight modes resulting in phase-matching: (a) LP_{02}^{p}, (b) LP_{21}^{a}, (c) LP_{11}^{s}.

For λ_p = 1060 nm, Figure 4.4(a) gives the phase-matched frequency-shift for the $LP_{02}^{p} LP_{21}^{a} LP_{11}^{s}$ combination. In accordance with the discussion of Chapter 2.3.2, the positive contribution from $\Delta\beta_M$ is initially dominated by a large negative contribution from $\Delta\beta_W$, resulting from the specific combination of interacting modes. However, as the frequency-shift is increased beyond 10 THz, the phase mismatch starts to reduce, eventually leading to a zero-valued mismatch at $\Omega/(2\pi) \approx 58$ THz. Figure 4.4(b) shows the signal and idler wavelengths as a function of the frequency-shift. Solid and dashed black lines are used to indicate the wavelength values at zero-mismatch and the modal cut-off wavelengths, respectively. It is clear that both modes are guided at 58 THz. The process is summarised by the phase-matching diagram of Figure 4.4(c), where the phase-matched wavelengths are displayed as a function of pump wavelength for values in the range 980 nm to 1130 nm.

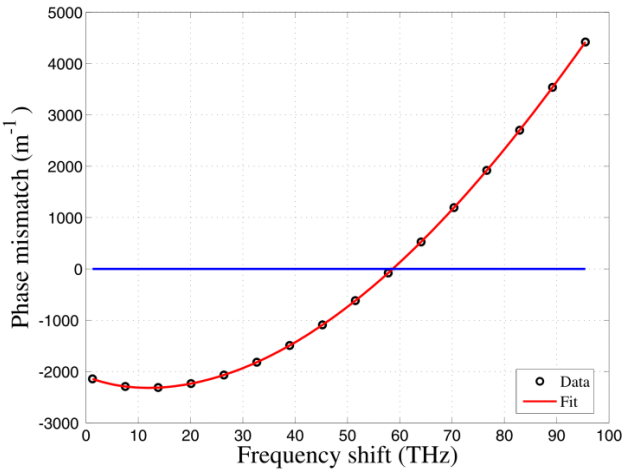

(a)

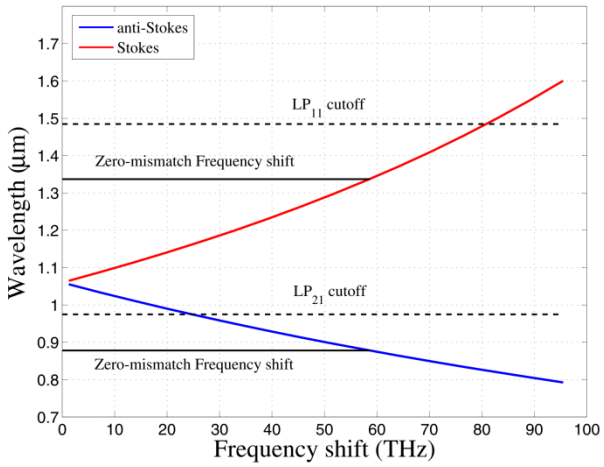

(b)

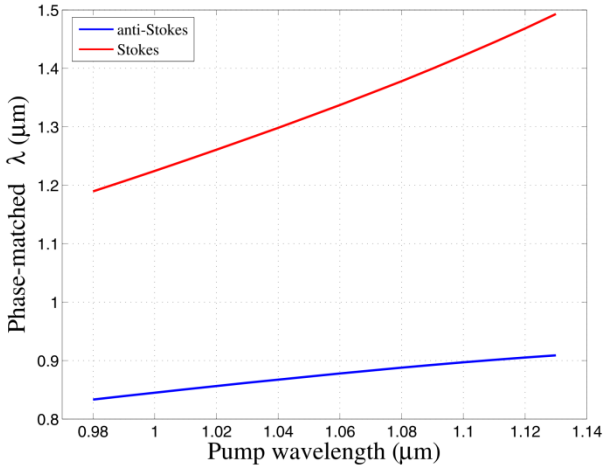

(c)

Figure 4.4: (a) Phase mismatch for the $LP_{02}^{p}LP_{21}^{a}LP_{11}^{s}$ combination at increased values for the frequency-shift for λ_p = 1060 nm. (b) Cut-off wavelengths for the relevant modes. (c) Phase-matching diagram for the combination of higher-order Freelight modes.

From equations 2.50 and 2.51 we may now calculate the overlap integrals for the higher-order mode combination of Figure 4.3. The values of the overlap integrals (f_{ij} or f_{ijkl}) should reveal the extent to which the respective modes will be able to exchange power. In FWM literature a quantity called the effective area, defined as $A_{eff} = 1/f$ for f_{ij} or f_{ijkl}, is often used to describe this interaction strength for the processes of SPM, XPM and FWM [4]. The value of A_{eff} is useful since it can be compared to the cross-sectional area of the fibre core. Since the Freelight fibre does not have a clearly defined core, the A_{eff} values for a hypothetical fundamental-mode phase-matching process, at a frequency-shift of 58 THz, can be calculated as reference. This was done, yielding a value of 40 μm^2 for the FWM A_{eff}-parameter. In contrast, the corresponding value for the case of Figure 4.3 approached infinity. Whilst the value of 40 μm^2 makes sense in terms of the dimensions of the Freelight fibre 'core' area, the higher-order mode value essentially indicates zero-overlap. Closer inspection however revealed that this result is consistent in terms of symmetry considerations and equivalently holds for the other two higher-order mode combinations identified for the Freelight fibre ($LP_{11}^{p}LP_{02}^{a}LP_{11}^{s}$ and $LP_{02}^{p}LP_{21}^{a}LP_{02}^{s}$). For an LP_{lm} mode, the analytical expressions for the mode fields, together with the numerator in equation 2.51, may be used to show that at least one of the following three equations should be satisfied for non-zero overlap:

$$l_a - l_s = 0$$

$$|l_a - l_s| = 2l_p \qquad (4.2)$$
$$l_a + l_s = 2l_p$$

Here, l denotes the azimuthal mode number as defined for an LP mode, whilst the subscripts a, s and p again refer to the anti-Stokes, Stokes and pump wavelength components, respectively. Analysis of the remaining fibres in Figure 4.1 revealed less higher-order modes than that obtained for the Freelight fibre. Consequently, the only possible mode combinations that were found to be suitable for phase-matching, did not satisfy the conditions of equation 4.2. The following section gives a brief overview of a higher-order mode combination for which the conditions of equation 4.2 are satisfied, in order to get an idea of the typical A_{eff}-values that can be obtained with this phase-matching method.

4.1.1.1 Multi-mode fibre

The RIP of the Freelight fibre was used as starting point in the search for alternative higher-order mode combinations. The approach here was to stretch the RIP in the radial direction by a factor φ, whilst keeping the cladding radius fixed to 60 µm. In this way φ = 1 simply returns the dimensions of the Freelight fibre. In terms of a step-index fibre this procedure is equivalent to an increase in the core radius. For discussion purposes, this fibre is labelled the 'Adjusted Freelight' fibre.

Using the preceding approach, the dispersion was computed over a range of φ-values. For each of the resultant fibres, the phase mismatch for various mode combinations, was calculated. To reduce the number of calculations, whilst retaining all the results relevant to the aim, as stated in Chapter 1, a pre-defined frequency-shift was used. This frequency-shift of roughly 70 THz was obtained by fixing λ_p and λ_a to 1060 nm and 850 nm, respectively (λ_s = 1408 nm).

In addition to shifting the cutoff wavelengths of the existing Freelight higher-order modes to longer wavelengths, a stretch of the RIP introduced additional guided modes. This resulted in a greater rate of increase in the number of mode combinations, that had to be evaluated in terms of phase-matching, for larger values of φ. Most of the mode combinations could however be discounted on the basis of the modes reaching cut-off or the conditions for non-zero overlap. Among the remaining mode

combinations a number of phase-matching options were identified. The two results that showed the most promise are the $LP_{02}^{p}LP_{12}^{a}LP_{11}^{s}$ combination at φ = 1.06 and the $LP_{11}^{p}LP_{02}^{a}LP_{02}^{s}$ combination at φ = 1.36. Figure 4.5(a) shows a comparison of the Adjusted Freelight RIP with φ = 1.36 and the Freelight RIP. The phase mismatch solution for the case φ = 1.06 is given in Figure 4.5(b). Calculation of the effective area for FWM give values of 601 μm^2 and 1127 μm^2 for the cases of φ = 1.06 and φ = 1.36, respectively. The $LP_{02}^{p}LP_{12}^{a}LP_{11}^{s}$ combination was therefore found to be the most feasible option for higher-order mode phase-matching at the given frequency-shift.

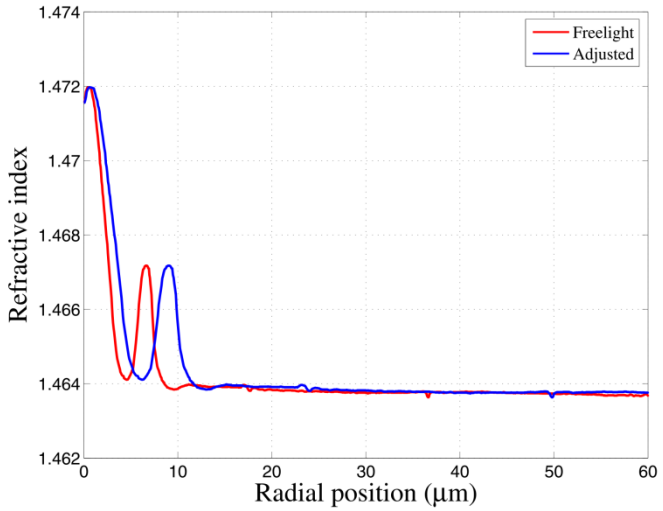

(a)

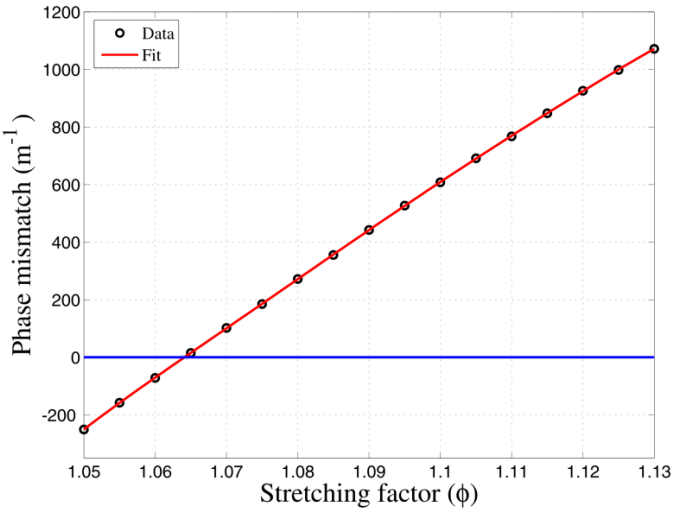

(b)

Figure 4.5: (a) RIPs for the Freelight and Adjusted Freelight (φ = 1.36) fibres. (b) Phase mismatch for the Adjusted Freelight $LP_{02}^{p}LP_{12}^{a}LP_{11}^{s}$ mode combination at various values of φ, for a 70 THz frequency-shift. Zero-mismatch occurs at φ = 1.06.

4.1.1.2 Polarization maintaining fibre

Compared to the hypothetical A_{eff}-parameter, computed for the fundamental mode of the Freelight fibre, the preceding higher-order mode A_{eff}-parameter of the Adjusted Freelight fibre ($\varphi = 1.06$) implies an order of magnitude relative decrease in the rate of power transfer via FWM (refer to Section 2.3.1). It is interesting to compare these values to that accessible through birefringence phase-matching in a PM fibre [5]. The general details of this approach were covered in the discussion of Section 2.3.2, in reference to Figure 2.7(c). Here, I will only give an overview of the application of this technique and the subsequent results.

To investigate birefringence phase-matching, the Fujikura SM98-PS-U25A PM fibre, was used. This fibre uses stress-induced birefringence to maintain the polarization of a mode and is of the Panda type (see Figure 2.2(b)). The measured RIP of the Panda fibre along the axis containing the stress applying parts (SAPs) is given in Figure 4.6(a). Circular symmetry was once again assumed. The SAP is indicated by the large area of decreased refractive index (due to the presence of B_2O_3). Orthogonal to the axis shown in Figure 4.6(a), the RIP looks exactly the same apart from the absence of the SAP (i.e. a flat cladding).

In contrast to the previous dispersion simulations, the PM fibre was modelled by approximating the measured RIP with index steps (see dashed lines in Figure 4.6(a)). Following the procedure outlined in Section 2.1.3, the modal birefringence was calculated. For this purpose, Young's modulus and the Poisson ratio for the core, cladding and SAPs were approximated by the silica values of $E = 7.8\times10^{10}$ N/m^2 and $\nu = 0.186$, respectively [6], [7]. The relative stress-optic coefficient was taken as $C = 3.43\times10^{-12}$ m^2/N [7]. Since the correct thermal expansion coefficients for the respective fibre materials depend on their doping concentrations, the procedure at the start of Section 4.1 was supplemented by the following [8]:

$$\alpha = (1 - m_+)\alpha_0 + m_+\alpha_+ \tag{4.3}$$

Here, m_+ again denotes the doping concentration, whilst α_0 and α_+ are the thermal expansion coefficients of the host material (silica) and dopant, respectively. The α values for pure SiO_2, GeO_2 and B_2O_3 are 5.4×10^{-7} $^oC^{-1}$, 7×10^{-6} $^oC^{-1}$ and 10×10^{-6} $^oC^{-1}$,

respectively [8]. The difference between the drawing temperature and room temperature was taken as 1300 ^{o}C.

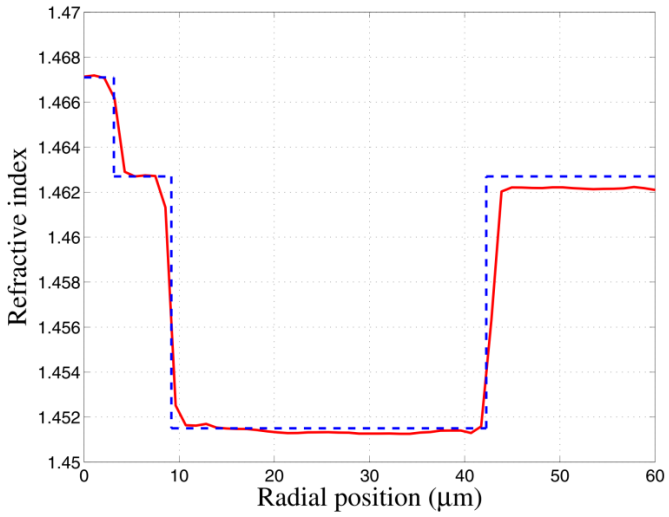

(a)

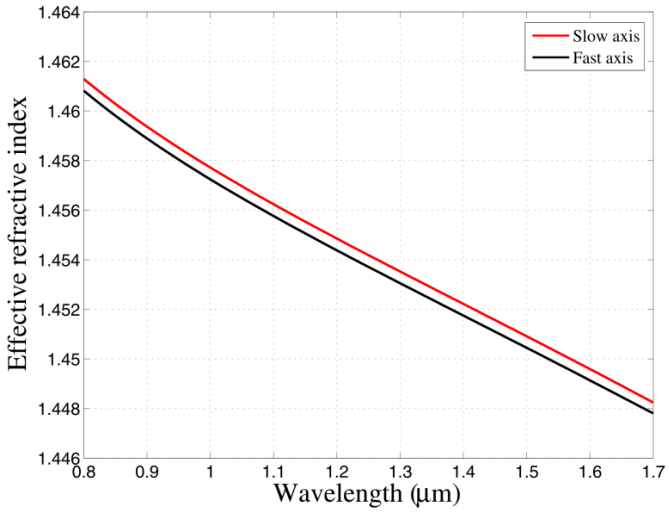

(b)

Figure 4.6: (a) RIP of Panda fibre along the axis containing the SAPs. (b) Numerically calculated effective refractive index of the slow- and fast axes, showing the birefringence responsible for maintaining the polarization.

The wavelength dependence of the calculated effective refractive index for the two orthogonal polarization components of the PM fibre's fundamental mode is shown in Figure 4.6(b). The upper curve, for which the effective refractive index is larger, corresponds to the slow axis of the fibre. The COMSOL simulation gave a value of $B_m = 4.77\times10^{-4}$ for the modal birefringence at λ = 1000 nm. This value was found to be in good agreement with that obtained from a measurement of the beat length of this fibre

($B_m = \lambda/L_B = 4.84\times10^{-4}$), as well as that calculated from an analytical expression using the same parameter values ($B_0 = 4.84\times10^{-4}$) [9]. The modal birefringence shows only a weak dependence on wavelength.

The discussion of Section 2.3.2 explained how the different terms in the expansion of the linear phase mismatch can be balanced by polarizing the normal-dispersion-regime pump-wave along the slow fibre axis. The calculated dispersions for the slow and fast axes were therefore used to evaluate the phase-matching properties of the PM fibre, according to $\Delta\beta = \left[\tilde{n}_a^y\omega_a + \tilde{n}_s^y\omega_s - 2\tilde{n}_p^x\omega_p\right]/c$ (also see equation 2.62). Figure 4.7(a) shows the phase mismatch, as a function of frequency-shift, for λ_p = 1080 nm. The general trend in the phase mismatch resembles that of Figure 4.4(a) and yields a zero value at a frequency-shift of 78.5 THz. The corresponding phase-matched wavelengths are λ_a = 842 nm and λ_s = 1506 nm. In analogy to Figure 4.4(c), Figure 4.7(b) gives the phase-matched Stokes and anti-Stokes wavelengths for pump wavelengths ranging from 1040 nm to 1140 nm.

The FWM overlap integral for the birefringence phase-matching process corresponding to Figure 4.7(a) has a value of A_{eff} = 46 μm^2. This value is significantly better than that of the Adjusted Freelight fibre and compares well to the hypothetical fundamental mode process of Section 4.1. It is however instructive to also consider the solutions to the coupled amplitude equation. This is done in the following section.

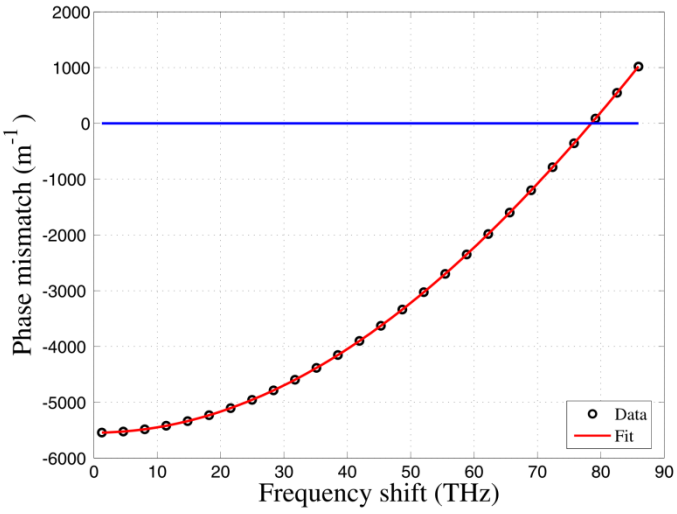

(a)

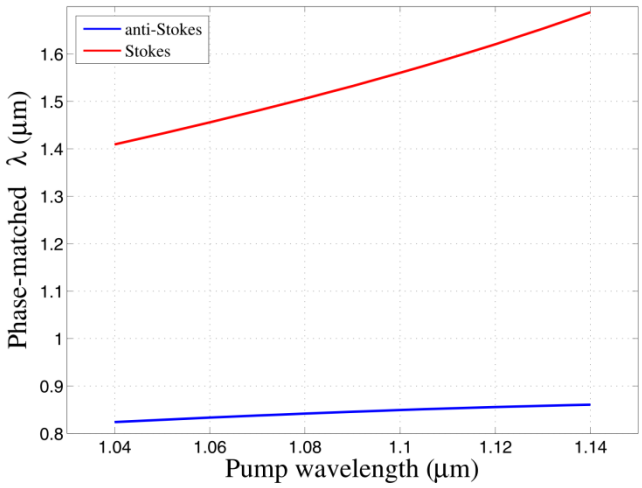

(b)

Figure 4.7: (a) Birefringence phase-matching at λ_p=1080 nm in a PM fibre. (b) Phase-matching diagram for the pump polarized along the slow axis of a PM fibre.

4.1.2 Numerical Solutions to the Coupled Amplitude Equations

Armed with the calculated overlap integral values, the theory of Chapter 2.3 was applied to the multi-mode (MM) and polarization maintaining (PM) fibres. Whilst the theory is only approximate in the sense that it assumes perfectly uniform fibres, it still provides a basis for comparison.

4.1.2.1 Scalar OPA solution

The coupled amplitude equation formulism describes the power and phase evolution of the interacting LP modes under the assumption that the relevant waves remain co-polarized along the propagation distance. It is important to note that this assumption is violated for the MM fibre in question. The resulting solutions should therefore be considered as indicative of the potential of the fibre, with the understanding that the fibre length required for near-complete pump depletion may be significantly longer in reality.

In accordance with the examples in Chapter 2, the calculation used a constant value, of $n_2 = 2.6\times10^{-20}$ m^2/W, for the nonlinear index coefficient of silica [4]. Particularly for this case, where the overlap integrals vary significantly depending on the combination of interacting modes (SPM, XPM and FWM), the definition of γ precludes its use. The individual values of the overlap integrals were therefore inserted

into equations 2.47 to 2.49. Since the targeted Stokes and anti-Stokes wavelengths are both in spectral regions where seed sources are available, the Stokes wave was arbitrarily chosen as the input wave, whilst the anti-Stokes wave was assumed to build up from noise. The pump power at the input to the fibre was chosen to be consistent with the requirements identified in Chapter 3. The OPA simulation therefore used P_p = 1 kW, P_s = 10 mW and P_a = 0.1 μW [10].

The result, obtained at an optimum value for $\Delta\beta=\Delta\beta_M+\Delta\beta_W$, of -0.104 m^{-1}, is shown in Figure 4.8. The peak pump-to-anti-Stokes conversion efficiency is 62.3%, which corresponds to a maximum pump depletion of 99.97% after a propagation length of 45 m. As this fibre length may lead to non-negligible losses, particularly towards the short-wavelength side of the spectrum, the solution was re-calculated with loss included, as outlined in Section 2.3. For this purpose, the linear attenuation constants (α_k) were approximated as 0.203 km^{-1}, 0.514 km^{-1} and 0.334 km^{-1} (or 0.88, 2.23 and 1.45 in units of dB/km) at the pump, anti-Stokes and Stokes wavelengths, respectively [11]. The result closely resembles that of Figure 4.8 and yields a peak pump-to-anti-Stokes conversion efficiency and maximum pump depletion of 61.5% and 98.72%, respectively. In accordance with this relative reduction in power transfer, the optimum fibre length for the process is reduced to 40 m. Although the power transfer is reversed for longer fibre lengths, the calculation indicates a conversion efficiency of 61.1% at 45 m. It is therefore clear that, for the relatively low values applicable to our fibre, the influence of loss may be neglected as a first approximation.

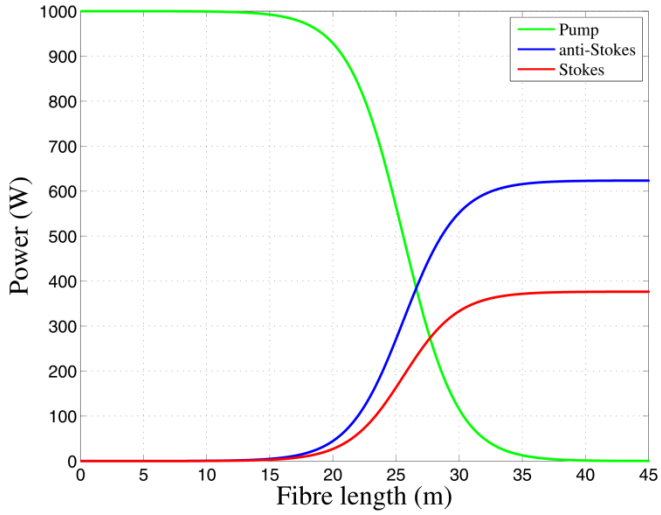

Figure 4.8: Optimized result for an OPA using the Adjusted Freelight multi-mode fibre: P_p = 1 kW.

4.1.2.2 Vector OPA solution

For a PM fibre with the pump- and daughter waves polarized along the slow and fast axes, respectively, the scalar coupled amplitude equations need to be adjusted. A vector equivalent to the equations of Chapter 2 may be obtained by replacing A_k with $\overrightarrow{A_k} = A_k \hat{e}_k$, where A_k is the scalar amplitude and $\hat{e}_k$ is the associated normalized Jones vector. By applying a vector operation [12],

$$[\hat{e}_i, \hat{e}_j, \hat{e}_k, \hat{e}_l] = \frac{1}{3}\left[(\hat{e}_i \cdot \hat{e}_j)(\hat{e}_k \cdot \hat{e}_l) + (\hat{e}_j \cdot \hat{e}_k)(\hat{e}_i \cdot \hat{e}_l) + (\hat{e}_k \cdot \hat{e}_i)(\hat{e}_j \cdot \hat{e}_l)\right] \tag{4.4}$$

to the SPM, XPM and FWM terms, it can be shown that all XPM and FWM terms, except for the XPM interaction between the co-polarized signal and idler, are multiplied by a factor of 1/3. This factor of 1/3 has its origins in the fact that the perpendicular magnitude of $\chi^{(3)}$ is roughly three times smaller than its parallel magnitude. With these scaling factors, the coupled amplitude equations may then be solved as before.

The solution for the PM fibre was calculated using the parameter values of the preceding section along with the appropriate overlap integrals. The result for $\Delta\beta$=0.245 m^{-1} follows in Figure 4.9. A maximum pump-to-anti-Stokes conversion efficiency of 45.6% occurs after 42.5 m (black dashed line). Notably, the maximum achievable pump depletion for this process is 71.1% (compare to Figure 4.8).

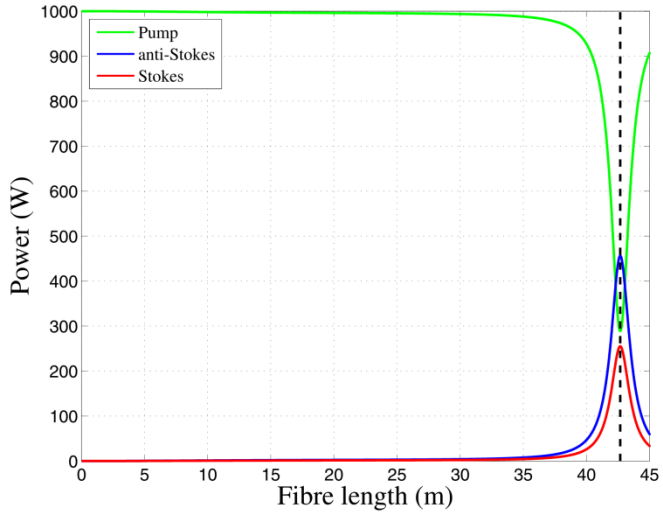

Figure 4.9: Optimized result for an OPA using the Fujikura PM fibre: P_p = 1 kW.

It is furthermore of interest that, whilst the initial power transfer is slow, the majority of power is transferred from pump to Stokes and anti-Stokes (and vice versa) over a short fibre length. The resulting power *inversion* is therefore short-lived and in stark contrast to the case of Figure 4.8.

4.1.2.3 Bandwidth considerations

On the basis of the preceding analysis, the Adjusted Freelight fibre, and its associated higher-order mode phase-matching, provides superior performance compared to the birefringence phase-matching process. A comparison between these approaches will however not be complete without due consideration to their parametric bandwidths (refer to Section 2.3.2). In addition to being a measure of how robust the FWM process will be under the influence of dispersion fluctuations, the parametric bandwidth also determines the FWM pump source requirements in terms of linewidth (refer to the discussions in Section 2.3.4 and the introduction to Chapter 3, respectively).

For the purpose of calculating the small-signal parametric bandwidth, equation 2.63 was used. Whilst an approximate functional expression for the mixing bandwidth ($\Delta\kappa$) exists (see Section 2.3.2), its value can easily be calculated from the simulations in Sections 4.1.2.1 and 4.1.2.2. The value of the derivative in equation 2.63 may similarly be calculated from Figure 4.7(a) and the corresponding result for the Adjusted Freelight fibre. The results are given in Table 4.1.

	MM fibre	PM fibre
$\Delta\kappa$ (m^{-1})	5.97×10^{-1}	2.52
$\left.\frac{d\Omega}{d(\Delta\beta)}\right\|_{\Delta\beta=0}$ (m/s)	6.30×10^{9}	7.55×10^{9}
$\Delta\Omega$ (GHz)	3.76	19.0

Table 4.1: Calculated parameters for the parametric bandwidth of the Adjusted Freelight and Fujikura PM fibres.

The parametric bandwidth for the Fujikura PM fibre is larger than that of the Adjusted Freelight fibre by roughly a factor of five. This may seem counter intuitive considering that the relevant birefringence phase-matching process yields gain over the range

$-2\gamma P_p/3 < \Delta\beta < 2\gamma P_p$, compared to the $-4\gamma P_p < \Delta\beta < 0$ associated with co-polarized waves (refer to the discussion in Section 2.3.2). The result is however consistent with the superior overlap between the interacting fundamental modes of the birefringence phase-matching process (see Sections 4.1.1.1 and 4.1.1.2).

As a result of the importance of the parametric bandwidth for FWM build-up in real fibres, the Fujikura PM fibre was chosen for the experimental phase of the OPA investigation. This decision was additionally motivated by the Fujikura fibre being readily available. In contrast, the Adjusted Freelight fibre would have required precision fabrication, not to mention the fact that the use of higher-order modes would have lead to significant complications with regards to launching the pump and seed light (particularly in an all-fibre configuration). Other practical considerations, such as the influence of bend-loss on the propagation characteristics of the involved higher-order modes, provided further incentive for the use of the Fujikura PM fibre.

4.2 Experimental Results

This section details the results from our experiments on fibre optical parametric amplification (OPA) and generation (OPG) using the Fujikura PM fibre as nonlinear converter. The discussion is separated into two parts. Section 4.2.1 gives an overview of the OPA experiments for which the MOPA, described in Section 3.2.1, was used as pump source. OPG experiments using alternative pump sources are reported in Section 4.2.2.

4.2.1 OPA Configuration

Several experiments were performed to investigate the plausibility of large frequency-shift parametric amplification using birefringence matching in the Fujikura PM fibre. The work presented in this section provides an overview of two of these experiments. Whereas both experiments made use of the same pump source, different seed sources were employed. The discussion is therefore two-fold and follows in Sections 4.2.1.1 and 4.2.1.2.

4.2.1.1 Narrow-Band Pulsed Seeding

In an initial approach, a tunable source was constructed for seeding at around the calculated Stokes wavelength (1506 nm). The experimental setup for the seed source, implementing the Raman amplifier configuration, is depicted by the red portion in Figure 4.10. The source consists of a directly modulated tunable laser (Photonetics Tunics-SW 3642HE 15 TLS) [13], with a wavelength around 1495 nm, and a co-propagating CW pump Raman laser (BFI Optilas FRL-DC) at 1405 nm [14]. The two waves are combined by a WDM-coupler before passing through 8 km of Freelight fibre (chosen purely for convenience). At the output from the Freelight fibre, a second WDM-coupler is employed to separate the Raman-amplified component from the residual pump light at 1405 nm. A polarization controller is included at the output from the Freelight fibre in order to control the launched polarization of the seed light upon combination with the linearly-polarized pump light from the MOPA in a PM WDM.

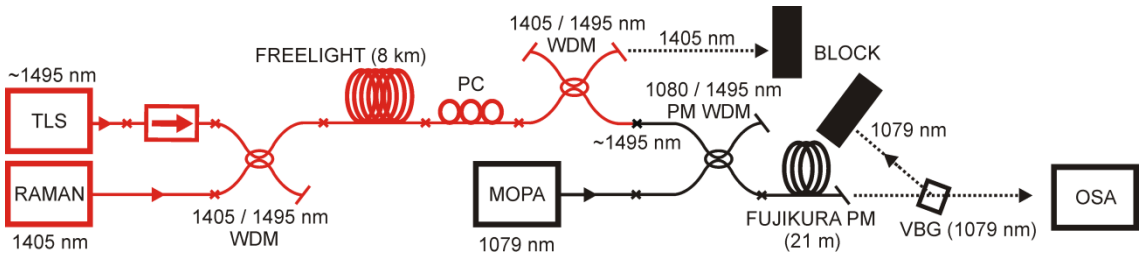

Figure 4.10: Experimental setup for an OPA constructed from 21 m of Fujikura PM fibre. Seed light at the Stokes wavelength around 1495 nm is provided by a Raman amplifier (red portion). Details on the configuration of the MOPA are provided in Chapter 3.2.

The applicable pump MOPA characteristics are described in Section 3.2.1. This particular configuration for the MOPA was typically operated at repetition rates of 5 MHz, with pulse widths of 2.5 ns. To facilitate optimum synchronisation between the pulses from the MOPA and the Raman amplifier seed source, the tunable laser was modulated using the same parameter values. The output spectrum for the tunable laser, as measured from the 1495 nm output-WDM, in the absence and presence of pump power, is shown in Figure 4.11. At a CW pump power of 2.85 W, the 1495 nm seed experiences a gain of 30 dB and is amplified to an average output power of 1.65 mW, or roughly 132 mW in terms of peak power.

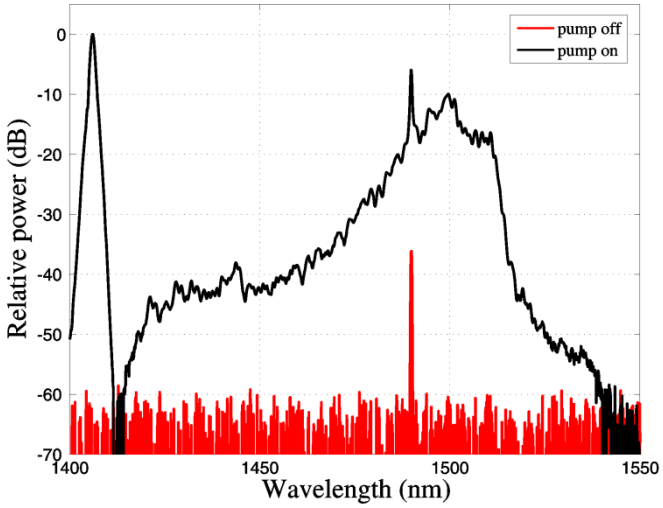

Figure 4.11: Output spectrum of the Raman amplifier, as measured from the output-WDM (spectral resolution: 0.5 nm). The tunable laser input power (red) experiences 30 dB gain at a CW pump power of 2.85 W (black).

The MOPA output power was typically limited to 4 W by the onset of significant SRS in the amplifier chain (refer to the discussion in Section 3.2.1). As such, the maximum pump peak power had a value of approximately 320 W. From the calculated result for a pump power of 1 kW (Figure 4.10) and the discussion in Chapter 2.3.1, it follows that this pump power would require a fibre length in excess of 120 m for near-complete pump depletion. However, calculations show that substantial pump depletion can be obtained for significantly shorter lengths of Fujikura PM fibre. This is illustrated in Figure 4.12(a), where a fibre length of 21 m leads to a pump-to-anti-Stokes conversion efficiency of 38.8% and 60.56% pump depletion. Therefore, considering that a shorter nonlinear converter also leads to a reduction in the severity of competing SRS, a slight reduction in pump depletion represents a reasonable trade-off. The experiment subsequently employed a 21 m length of Fujikura PM fibre (refer to Figure 4.10).

Figure 4.13 displays output spectra from the OPA experiment for a pump peak power of 320 W. In analogy to Chapter 3, a VBG was once more employed as a spectral filter. This time however, its intended purpose was to provide relative attenuation at the FWM pump wavelength of 1079 nm, to avoid saturation of the OSA detector (see Figure 4.10). Figure 4.13(a) shows the VBG transmission in the absence and presence of seeding at 1495 nm. Both spectra show two orders of Raman scattering at 1132 nm and 1191 nm. In addition, a single order of Raman anti-Stokes can be identified at about

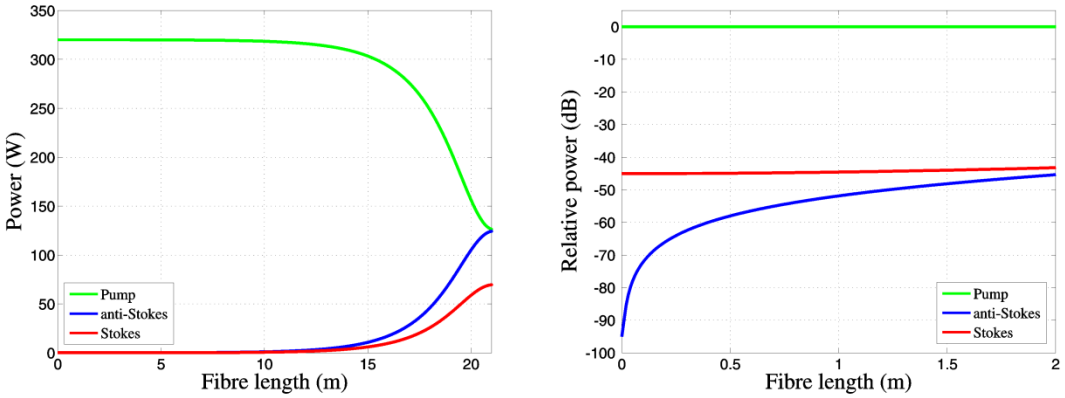

(a) (b)

Figure 4.12: Optimized results for an OPA using the Fujikura PM fibre. (a): P_p = 320 W and L = 21 m. (b) P_p = 320 W and L = 2 m (logarithmic scale). All other parameters are identical to those used in Section 4.1.2.2.

1038 nm. In the presence of seeding, the FWM anti-Stokes emerges at a wavelength of 844 nm, in excellent agreement with the theoretically predicted value (see Figure 4.7(b)). Figure 4.13(b) shows the dependence of the generated anti-Stokes on the seed wavelength. The anti-Stokes power reaches its maximum for a Stokes wavelength around 1494 nm and shows a relative reduction for shorter and longer seed wavelengths. Whereas the Stokes seed power is dependent on its wavelength, owing to the SRS gain profile (see Figure 4.11), this influence is relatively negligible. The trend in Figure 4.13(b) may therefore be associated with changes in the average phase mismatch over the length of the nonlinear converter.

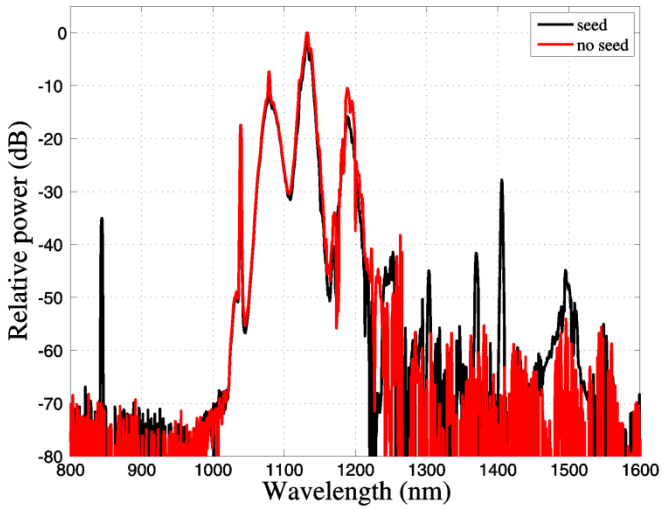

(a)

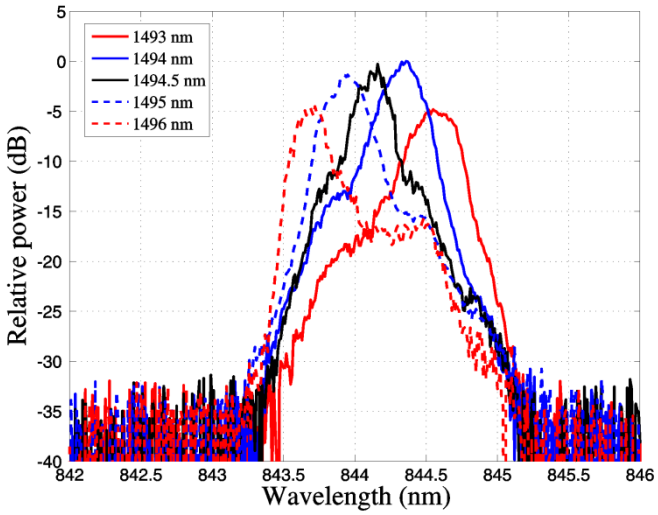

(b)

Figure 4.13: (a) Output spectra from 21 m of Fujikura fibre in the absence and presence of seeding at 1495 nm, for P_p = 320 W (spectral resolution: 2 nm). (b) High resolution spectra of the generated anti-Stokes, as a function of seed wavelength (spectral resolution: 0.1 nm).

The anti-Stokes power in Figure 4.13 is several orders of magnitude smaller than the calculated result in Figure 4.12(a). However, the experimental result compares relatively well to Figure 4.12(b), showing the calculated result for 2 m of Fujikura PM fibre. This comparison seems to imply that coherent build-up of the anti-Stokes power only occurs over lengths of up to 2 m, before the process is interrupted, resulting in an incoherent anti-Stokes wave after 21 m of propagation. Since this FWM process is characterised by a walk-off length of 118 m (equation 2.37), a discontinuity in phase-matching is the most likely cause of disruption to coherent power build-up. In turn, changes in phase-matching may be attributed to inhomogeneities in fibre dimensions, as discussed in Chapter 2.3.4. To investigate the influence of non-uniformities, the previously calculated frequency bandwidth for the birefringence-matching process (refer to Section 4.1.2.3) may be used to estimate the parametric gain's tolerance to core-size variations. This was done by increasing the core radius of the Fujikura PM fibre by 1% and calculating the resultant phase-matched wavelengths for λ_p = 1079 nm. The zero-mismatch frequency-shift (Ω_0) corresponding to the 1% increase was found to be 245.6 GHz larger than that associated with the original fibre dimensions. Assuming a linear relation between the magnitude of the core radius variation and the increase in the zero-mismatch frequency-shift, core radius variations in excess of roughly 0.1% (0.003 μm) will disrupt the gain. Physically, the core radius variation shifts the newly

generated signal- and idler waves out of the existing gain bandwidth. Although the signal- and idler waves still experience gain at the shifted wavelengths, the overall power transfer to the calculated wavelengths of Section 4.1.1.2 deteriorates. This dependence of the overall power transfer on the longitudinal homogeneity of the fibre may therefore lead to very different behaviour from that indicated in Figure 4.12(a) and the figures of Section 4.1.2.

4.2.1.2 Broad-Band CW Seeding

The experimental work of Section 4.2.1.1 concluded that parametric gain inside the Fujikura PM fibre is only piece-wise coherent, as a possible result of longitudinal fibre variations. In an effort to explore the validity of this hypothesis, a set of experiments, using different lengths of fibre, were conducted.

For the experimental results presented here, the peak power from the MOPA of Chapter 3.2.1 was increased by decreasing the PRF from 5 MHz to 2 MHz. To avoid the associated increased levels of nonlinear scattering, free-space VBG-filtering was employed (refer to the approach in Chapter 3.2.2). The filtered pump light was lens-coupled into a 1080/1495 nm PM WDM-coupler. The second WDM input port and combined output port was spliced to a seed source and the Fujikura fibre, respectively, as illustrated in Figure 4.10. Peak pump powers at the input to the Fujikura PM fibre was typically limited to an estimated 580 W.

Since the work of Section 4.2.1.1 established the optimum FWM Stokes wavelength, it was no longer necessary to employ a tunable seed source and simpler alternatives therefore became an option. To this end, a 1450 nm single-mode CW laser diode (Fitel FOL14xx series), was chosen [15]. By controlling the operating temperature, it proved straightforward to shift the spectral response to 1495 nm (at 54^{o}C), where the CW diode was typically operated at around 100 mW.

The output spectra from two lengths of Fujikura PM fibre, as measured through a VBG (refer to Figure 4.10), are given in Figure 4.14(a). Here, spectral measurements were performed in a consistent manner to allow a direct comparison. This is also true for the spectra compared in Figure 4.13(a). However, no particular effort was made to standardise spectral measurements across experiments. It is therefore difficult to compare Figures 4.13(a) and 4.14(a). Having said that, a number of qualitative

differences can be identified. Most notably, the result for 21 m of fibre (black curve) illustrates reduced power levels for the first and second order Raman Stokes as well as for the Raman anti-Stokes. This may seem surprising considering that the pump peak power increased from 320 W to 580 W. The result however highlights the value of filtering and its influence in terms of seeding at SRS wavelengths. It is furthermore interesting that the reduction in SRS and increased pump power did not result in a significant change in the anti-Stokes power, compared to that of Figure 4.13(a).

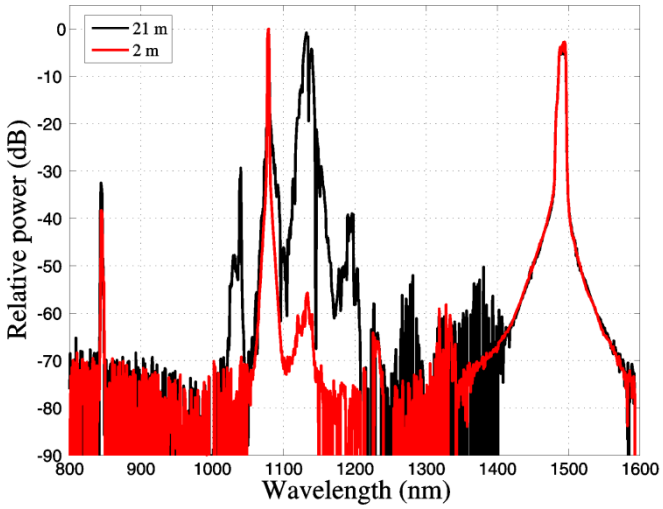

(a)

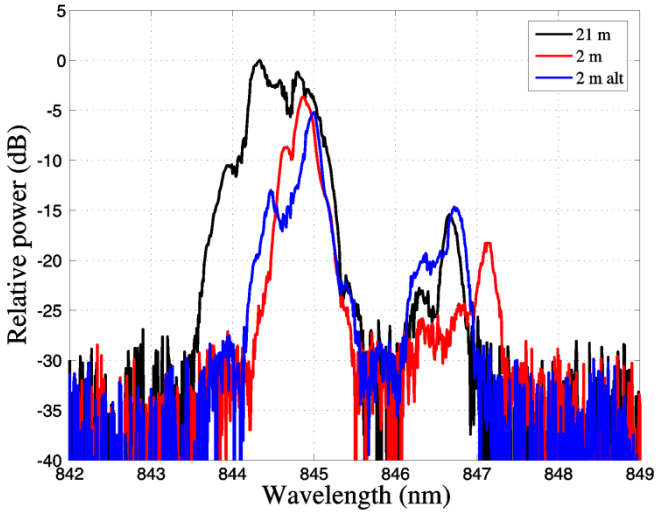

(b)

Figure 4.14: (a) Output spectra from 21 m (black) and 2 m (red) lengths of Fujikura fibre under CW seeding at the Stokes wavelength, for P_p = 580 W (spectral resolution: 2 nm). (b) High resolution spectra of the generated anti-Stokes for the cases of (a) and an alternative 2 m fibre sample (blue) (spectral resolution: 0.1 nm).

In accordance with theory, the spectrum from a 2 m length of Fujikura fibre shows a significant relative reduction in SRS (red curve). This is in contrast to a comparison of the calculated and measured relative power at the anti-Stokes wavelength (refer to Figure 4.12). The anti-Stokes power only experiences an approximate 5 dB decrease as the fibre length is reduced from 21 m to 2 m. This result therefore appears to corroborate the hypothesis that coherent parametric gain only occurs over fibre lengths of roughly 2 m. Figure 4.14(b) compares high resolution spectra of the anti-Stokes for different nonlinear converter lengths. In addition to the 21 m and 2 m fibre samples corresponding to Figure 4.14(a), the comparison includes a spectrum for a different 2 m fibre sample. Anti-Stokes waves from the 2 m fibre samples are not only associated with different powers, but also with different spectral distributions. These differences are consistent with relative differences in the phase-matching, and therefore dispersion, of the samples. In further support of this argument, the spectral width of the 21 m fibre sample is significantly larger than that of the 2 m samples. The 21 m fibre sample may therefore be regarded as a collection of shorter fibres, each with their own associated dispersion and anti-Stokes spectra. In this picture, the 5 dB increase associated with a 19 m gain in fibre length, is indicative of a fairly low degree of overlap in the parametric bandwidths of the constituent fibre samples. The conclusion must therefore be that the Fujikura PM fibre suffers from longitudinal inhomogeneities, relatively large compared to the parametric bandwidth associated with a frequency-shift of 78 THz.

4.2.2 OPG Configuration

The simplest way of reducing the disruptive influence of longitudinal fibre inhomogeneities is to increase the parametric bandwidth. In accordance with the discussion of Section 2.3.2, this can be achieved through an increase in pump power. The following sections briefly report on two experiments in which this approach was explored. Both experiments relied on the simplest possible configuration whereby a high-power pump source was lens-coupled into an un-seeded nonlinear converter, via polarizing optics.

4.2.2.1 Pico-Second MOPA Pump Source

In an initial approach at using a high-power source, a 1 m length of Fujikura PM fibre was pumped by 20 ps pulses from a YDF-based MOPA at 1060 nm. Details on this source, capable of delivering peak powers of up to 40 kW, are given in Ref. [16]. The fibre length was limited to 1 m by the walk-off length for the large frequency-shift process in the presence of 20 ps pump pulses.

In the absence of active cooling at the input to the Fujikura fibre, launched pump peak powers were typically limited to around 10 kW. At these power levels, the calculated parametric bandwidth approaches 0.5 nm. This relative increase in bandwidth should lead to a significant improvement in the fibre length over which coherent parametric gain occurs. However, upon pumping the fibre along the slow axis, the measured optical spectrum showed no sign of FWM (refer to red line in Figure 4.15). Instead, this output spectrum is characterised by significant spectral broadening and small features at the Raman Stokes and anti-Stokes wavelengths. The origin of the spectral broadening is rooted in the pulse shape from the MOPA's mode-locked seed laser. Whereas the MOPA of Chapter 3 delivers square-shaped pulses which are relatively robust against SPM-induced spectral broadening, this is not the case for the current pump source [4]. The incident pump linewidth has a value of roughly 0.4 nm and is easily accommodated by the pump acceptance bandwidth of roughly 0.8 nm. However, as a result of linewidth broadening, this scenario changes over the course of propagation through the fibre which results in a reduction to the effective length for the FWM process (refer to the discussion in Section 2.3.2) [3]. The influence of linewidth broadening may thus equivalently be described as a process that reduces the effective pump power at 1060 nm, leading to a decrease in the parametric bandwidth.

The blue (and black) line in Figure 4.15 shows the measured optical spectrum for the linearly polarized pump aligned at 45^{o} to the slow fibre axis. In addition to a reduction in the generated Raman Stokes, compared to the red line, this output spectrum contains relatively strong features around 1030 nm and 1090 nm. The symmetry of these features, with respect to the pump frequency, is consistent with fibre FWM. At the time, it was therefore decided to revisit the analysis of Section 4.1.1.2. Similar to the approach employed there, the phase mismatch for a non-degenerate FWM process, using two pump photons with opposite linear polarizations, were calculated over a range

of frequency-shift values. Phase-matching for this particular case, where a normal dispersion-regime pump wavelength is used, can only occur for a fast and slow polarized anti-Stokes and Stokes wave, respectively [17], [18]. The results, as a function of pump wavelength, are shown in Figure 4.16 (compare to Figure 4.7(b)). The calculated phase-matched wavelengths are in excellent agreement with those of Figure 4.15, thereby confirming this observation as the divided pump birefringence matching process alluded to in Section 2.3.2.

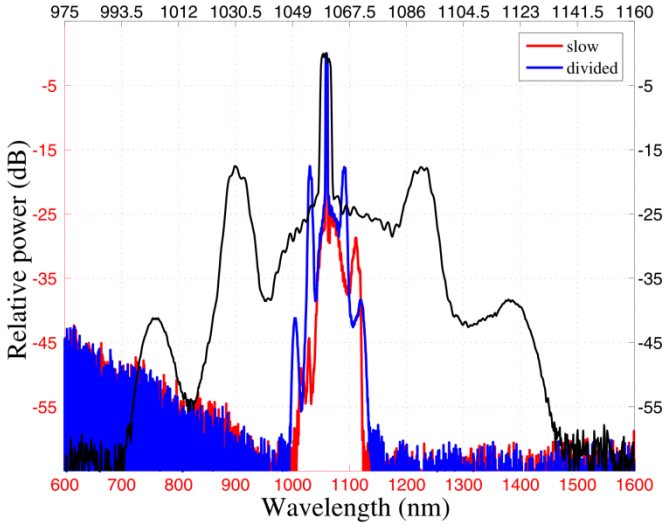

Figure 4.15: Output spectra from an un-seeded 1 m sample of Fujikura fibre, pumped by a high-power pico-second MOPA. Blue line (bottom axis): Incident pump polarization aligned to the slow fibre axis. Red line (bottom axis): Incident pump polarization aligned at 45^{o} to the slow fibre axis. Black line (top axis): Close-up of the small frequency-shift FWM process. In all cases the spectral resolution is 1 nm.

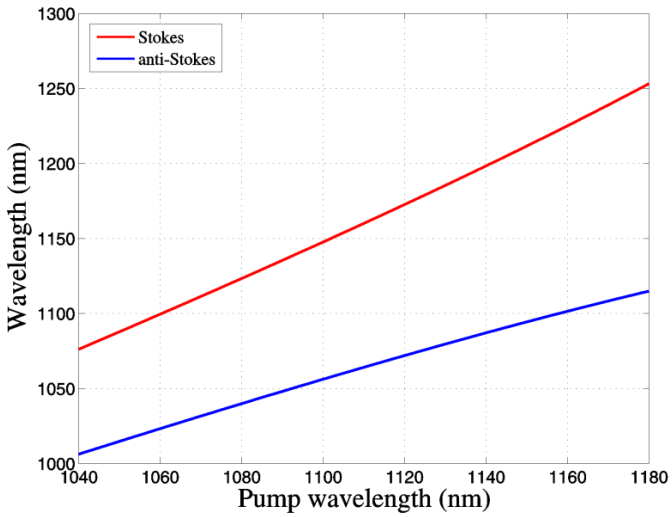

Figure 4.16: Phase-matching diagram for the small frequency-shift FWM process, where the pump power is divided between the slow and fast axis of the Fujikura PM fibre.

The divided pump birefringence matching process is characterised by a relatively small frequency-shift, compared to the degenerate process of interest. FWM based on this approach therefore exhibits relatively large parametric bandwidths and are subsequently more robust against the influence of fibre dimension variations (refer to Section 2.3.4). It is furthermore interesting to note that different combinations of interacting polarizations lead to changes in the solution to equation 4.4, which influences the coupled amplitude equations. However, since the small frequency-shift process is not the focus of this study, these changes will not be discussed here. The interested reader is referred to Ref. [12].

From Figure 4.15, the measured bandwidth of the generated FWM products is approximately 7 nm, in good agreement to a theoretical estimate. The associated parametric gain clearly exceeds that of competing SRS. This is in contrast to the case for which the pump polarization is aligned to the slow fibre axis, where insufficient coherence allows SRS to dominate. These experimental results therefore serve as an example of the importance of the parametric bandwidth and the requirement for a narrow linewidth, high peak power pump source.

4.2.2.2 Nd:YAG Pump Source

To assess the plausibility of large frequency-shift FWM in the Fujikura PM fibre, in the presence of a narrow linewidth, high peak power pump source, experiments employing a Nd:YAG laser were performed. The output from the 1064 nm Nd:YAG laser, characterised by a spectral linewidth of a few GHz, was lens-coupled into a 2 m length of Fujikura PM fibre. As before, launched peak powers were limited by the use of passive fibre cooling techniques. Nevertheless, pulse energies of up to 53 μJ (10 ns pulses at a PRF of 10 Hz) were successfully coupled into the fibre. The associated peak power was calculated from a measurement of the pulseshape. Although the peak power of the Gaussian pulse envelope only approached 3 kW, the pulse was found to contain sharp features of width ~100 ps and peak powers in the range 7 to 10 kW.

Spectral measurements were complicated by the low PRF of the pump source. This is evident from the noise-like features of the Fujikura output spectrum, in Figure 4.17. The result actually consists of two measurements. Two band-pass filters were used in separate measurements to attenuate the 1064 nm pump line, whilst providing high transmission across the FWM Stokes (1120-1600 nm) and anti-Stokes (760-1000 nm)

spectral bands. The resulting spectrum is therefore a merger of these measurements at a wavelength of 1000 nm (see red dashed line). Whilst the result shows efficient SRS, cascaded across multiple Stokes orders, other features are also resolved at 836 nm, 857 nm and 1455 nm. Anti-Stokes and Stokes wavelengths of 836 nm and 1455 nm, respectively, are consistent with the calculated result in Figure 4.7(b). Since the measurement only shows a peak for the FWM Stokes, it has to be concluded that the feature at 857 nm is in fact SRS generated from the FWM anti-Stokes at 836 nm.

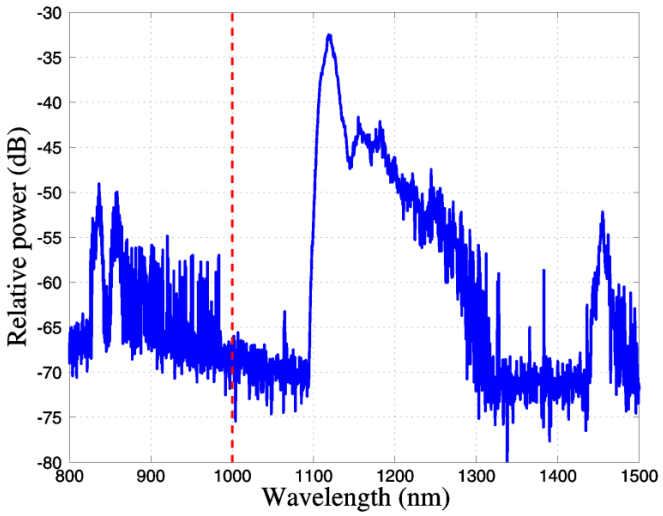

Figure 4.17: Output spectrum from an un-seeded 2 m sample of Fujikura fibre, using a narrow linewidth high-energy Nd:YAG pump source (spectral resolution: 2 nm).

Temporal analysis of the Fujikura output revealed a correlation between the generated Stokes and anti-Stokes pulses and the spikes in the pump pulses. This implies that the observed FWM is not a result of the pump pulse envelope, but instead originates from 100 ps pulses. This realisation is important, since the results are now comparable to those of the preceding section, with the most notable difference being the pump linewidth. Although a 100 ps pump pulse in 2 m length of Fujikura PM fibre should lead to walk-off limited FWM, similar results from a 1 m sample showed reduced parametric conversion. It therefore appears that the parametric gain in the 2 m fibre sample still only experienced piece-wise coherence. Based on these findings, it can be concluded that, whilst a narrow linewidth pump certainly can lead to noise-seeded large frequency-shift parametric gain, the peak power required to overcome fibre inhomogeneities exceeds 10 kW.

4.3 Summary

This chapter gave an overview of the approach and results of our investigation into large frequency-shift FWM through the use of conventional, non-microstructured fibre. Initial work was focussed on the refinement of a procedure whereby the chromatic dispersion could be calculated from the refractive index profile of a fibre. The chromatic dispersion was subsequently used to determine the wavelengths for which phase-matching can be achieved in a given fibre, at a pump wavelength in the range 1060-1080 nm. As a result of the zero-dispersion wavelength associated with silica-based conventional fibre, this analysis concluded that the use of higher-order spatial modes or different polarization modes were the only viable options. Both these options were then explored in terms of readily available fibres.

Calculations for the so-called Adjusted Freelight multi-mode fibre and the Fujikura polarization-maintaining (PM) fibre showed phase-matching at frequency-shift values of 70 THz and 78.5 THz, respectively. The overlap between the interacting modes of the Fujikura PM fibre was found to be superior to that of the multi-mode fibre. Despite this, the multi-mode fibre gave almost complete pump depletion, compared to only 71% for the Fujikura PM fibre over a similar fibre length. However, the mode overlap also determines the parametric bandwidth, for which the value of the Fujikura PM fibre was larger by an order of magnitude. Based primarily on this finding and the importance of reducing the influence of longitudinal inhomogeneities, the Fujikura PM fibre was chosen for the experimental phase of the investigation.

Experiments using the Fujikura PM fibre were performed in optical parametric amplifier (seeded) and generator (un-seeded) configurations. The OPA experiments made use of the purpose-built pump MOPA of Chapter 3. Whereas the generated anti-Stokes power was very small compared to analytical and numerical predictions, its wavelength was in excellent agreement with the calculated value. Additional experiments on shorter lengths of Fujikura PM fibre verified that the FWM process was subject to piece-wise coherent build-up, as a result of longitudinal inhomogeneities. To increase the parametric bandwidth in a bid to circumvent this limitation, subsequent experiments employed high-power pump sources. The first of these OPG experiments was unsuccessful in generating observable light at the Stokes or anti-Stokes wavelength.

This was attributed to the relatively large linewidth of the pump MOPA, as well as its susceptibility to spectral broadening due to self-phase modulation (SPM). A second experiment therefore made use of a narrow linewidth Nd:YAG pump source. Whilst this laser had a pulse width of 10 ns, the pulse shape was compromised by the presence of several high-power 100 ps features. It was however these features which succeeded in generating low-power FWM products at the anticipated wavelengths. This result was important, since it served as an indication of the plausibility of large frequency-shift FWM in the Fujikura PM fibre. This chapter therefore concludes that the inhomogeneities in the Fujikura fibre precludes large frequency-shift FWM at reasonable pump peak powers (<10 kW).

4.4 References

[1] L.G. Cohen, "Comparison of single-mode fiber dispersion measurement techniques," *J. Lightw. Technol.*, vol. LT-3, no. 5, pp. 958-966 (1985).

[2] R.H. Stolen, "Phase-matched-stimulated four-photon mixing in silica-fiber waveguides," *IEEE J. Quantum Electron.*, vol. QE-11, no. 3, pp. 100-103 (1975).

[3] R.H. Stolen and J.E. Bjorkholm, "Parametric amplification and frequency conversion in optical fibers," *IEEE J. Quantum Electron.*, vol. QE-18, no. 7, pp. 1062-1072 (1982).

[4] G.P. Agrawal, *Nonlinear Fiber Optics*, 3rd ed., Academic Press, 2001.

[5] R.H. Stolen, M.A. Bösch and C. Lin, "Phase matching in birefringent fibers," *Opt. Lett.*, vol. 6, no. 5, pp. 213-215 (1981).

[6] K. Okamoto, T. Hosaka and T. Edahiro, "Stress analysis of optical fibers by a finite element method," *IEEE J. Quantum Electron.*, vol. QE-17, no.10, pp. 2123-2129 (1981).

[7] K. Zheng, D.-Y. Chang, Y.-J. Fu, H. Wei, Y. Wei, F.-P. Yan, S.-Q. Lou, T.-G. Ning, W. Jian and S.-S. Jian, "Design and fabrication of panda-type erbium-doped polarization-maintaining fibres," *Chinese Physics*, vol. 16, no. 2, pp. 478-484 (2007).

[8] I.P Kaminow and V. Ramaswamy, "Single-polarization optical fibres: Slab model," *Appl. Phys. Lett.*, vol. 34, no. 4, pp. 268-270 (1979).

[9] P.L. Chu and R.A. Sammut, " Analytical method for calculation of stresses and material birefringence in polarization-maintaining optical fiber," *J. Lightw. Technol.*, vol. LT-2, no. 5, pp. 650-662 (1984).

[10] A. Vatarescu, "Light conversion in nonlinear monomode optical fibers," *J. Lightw. Technol.*, vol. LT-5, no. 12, pp. 1652-1659 (1987).

[11] M. Nakazawa and M. Tokuda, "Measurement of the fiber loss spectrum using fiber Raman optical-time-domain reflectometry," *Appl. Opt.*, vol. 22, no.12, pp. 1910-1914 (1983).

[12] M.E. Marhic, Fiber Optical Parametric Amplifiers, Oscillators and Related Devices, Cambridge Univ. Press, 2008.

[13] See for example: www.assetrelay.com/products/Photonetics-TUNICS%252dSW-3642HE-15-TLS.html

[14] Information available at: www.bfioptilas.com
[15] Information available at: www.furukawa.co.jp/fitel/
[16] K.K. Chen, J.H.V. Price, S. Alam, J.R. Hayes, D. Lin, A. Malinowski and D.J. Richardson, "Polarisation maintaining 100 W Yb-fibre MOPA producing μJ pulses tunable in duration from 1 to 21 ps," *Opt. Express*, vol.18, no. 14, pp. 14385-14394 (2010).
[17] R.K. Jain and K. Stenersen, "Phase-matched four-photon mixing processes in birefringent fibers," *Appl. Phys. B*, vol. 35, pp. 49-57 (1984).
[18] P.N. Morgan and J.M. Liu, "Parametric four-photon mixing followed by stimulated Raman scattering with optical pulses in birefringent optical fibers," *IEEE J. Quantum Electron.*, vol. 27, no. 4, pp. 1011-1021 (1991).

Chapter 5

OPO Using Photonic Crystal Fibre

Although the results for the Fujikura fibre illustrated its potential use as an OPA, the conversion efficiencies were low at the pump powers employed by us. This was tentatively attributed primarily to longitudinal fluctuations in the fibre diameter and the resulting dominance of competing SRS. To circumvent the limitations imposed by longitudinal fluctuations, it therefore became necessary to consider alternative nonlinear converter fibres. To this end, we considered photonic crystal fibres (PCF) [1]. Section 5.1 gives calculated results for the dispersion and phase-matching of the PCF chosen for our experiments. Following that, Sections 5.2 through 5.4 discusses the different experimental arrangements used in our investigation of PCF-based FWM. The chapter concludes with an overview of the main results and potential ways of improving the performance of these fibre-based FWM devices.

5.1 Dispersion and Phase-Matching Calculations

The air-holes in the cladding of a PCF allow unprecedented customization of the fibre's dispersion through appropriate design. It is therefore possible to shift the zero-dispersion wavelength (ZDW) to values below the ~1300 nm limit that applies to conventional silica step-index fibres (refer to Section 2.1.4). In this way, it has been shown that large frequency-shift FWM can be achieved by positioning the pump wavelength within the PCF's normal dispersion regime (refer to Section 2.3.2) [2]. In

fact, recent results have shown that this method of phase-matching can lead to exceptional parametric conversion efficiencies over frequency-shifts exceeding 100 THz [3] - [5].

After considering a number of PCFs, using the methods described in Section 2.1.4 and 4.1, a large mode-area fibre from NKT Photonics was selected. This fibre, designated PCF-LMA8, is characterized by $\Lambda = 5.6$ μm and $d/\Lambda = 0.49$ (where Λ and d are the pitch and diameter of the PCF air-holes, respectively).

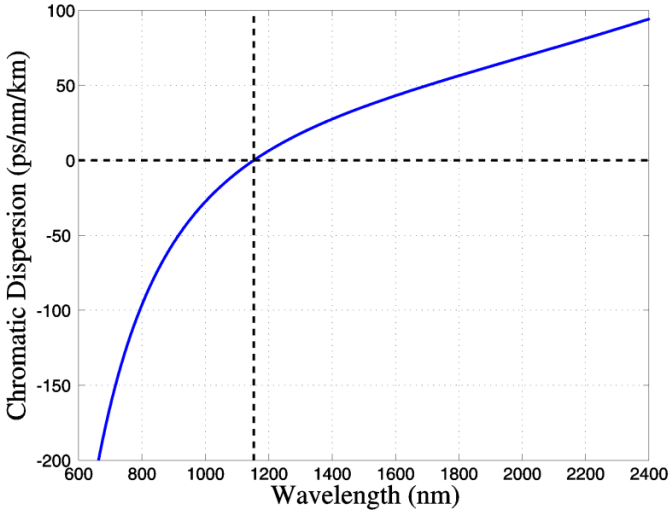

(a)

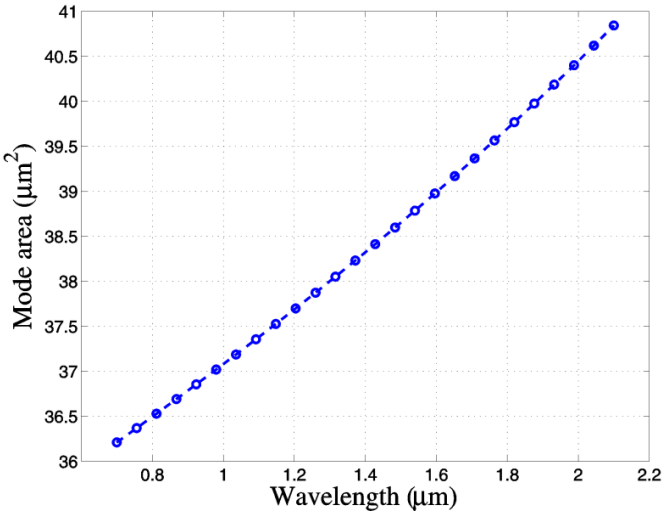

(b)

Figure 5.1: (a) Calculated chromatic dispersion and (b) mode-area as a function of wavelength for PCF-LMA8.

The calculated dispersion is shown in Figure 5.1(a) and yields a ZDW of 1153 nm. This value for the ZDW is well-suited to large frequency-shift FWM, since it allows normal-dispersion-regime pumping by high-power ytterbium-doped laser sources (refer to Section 2.4). Another attractive property of this PCF is that it exhibits single-mode operation over the full wavelength range of interest (600 – 2500 nm). Of particular interest is that the mode-field diameter, and consequently the effective mode-area, remains approximately constant over this range (see Figure 5.1(b)). As a result, the FWM conversion efficiency is improved, owing to a higher degree of spatial overlap between the interacting modes. It is furthermore notable that large mode-area PCFs are relatively insensitive against the influence of longitudinal inhomogeneities, compared to highly-nonlinear PCF varieties [5].

The dispersion data of Figure 5.1 was used to calculate the phase mismatch for the PCF-LMA8. In contrast to the Fujikura PM fibre, the nonlinear contribution to the phase mismatch may be important for the calculation of the phase-matched wavelengths in the PCF. This is due to the fact that the linear contribution to the phase mismatch converges to zero as the pump wavelength approaches the ZDW. The phase mismatch was therefore calculated for a typical pump peak power of 1 kW (refer to Chapter 3). For this purpose, the nonlinear parameter of the PCF was approximated as $\gamma = 3.9 \times 10^{-3}$ $m^{-1}W^{-1}$, by taking $n_2 = 2.6\times10^{-20}$ m^2/W and by using a nominal value of 38.5 μm^2 for A_{eff}. Figure 5.2(a) shows the phase mismatch as a function of frequency-shift for a pump wavelength of 1079 nm.

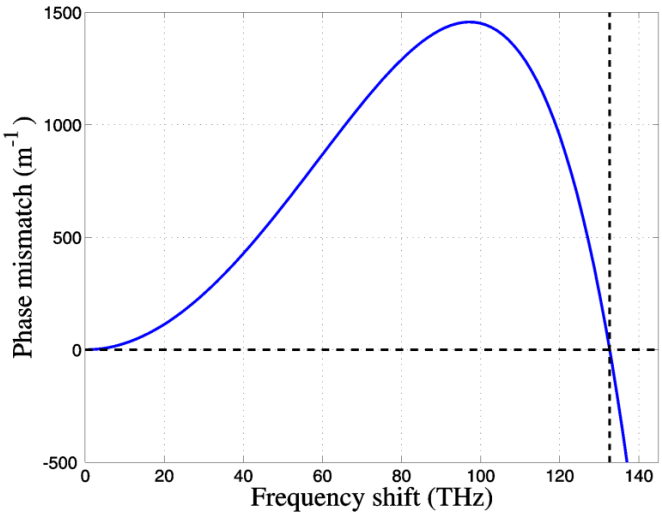

(a)

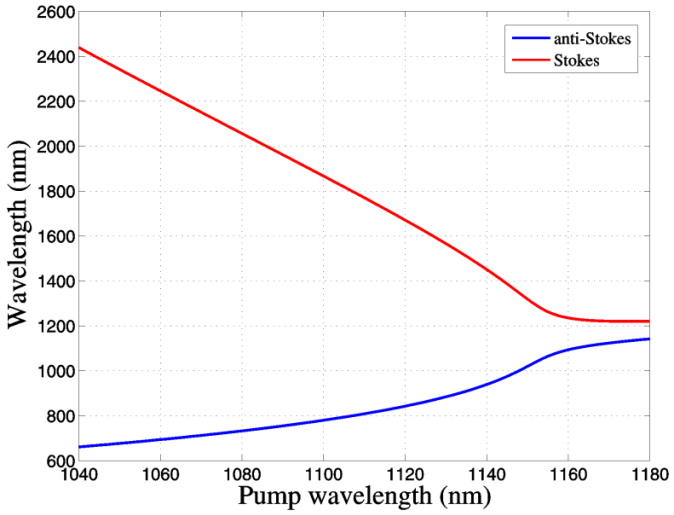

(b)

Figure 5.2: (a) Calculated PCF-LMA8 phase mismatch as a function of frequency-shift for a pump wavelength of 1079 nm. (b) Phase-matching diagram at a pump peak power of 1 kW.

Phase-matching is predicted at a frequency-shift of ~132 THz, corresponding to Stokes and anti-Stokes wavelengths of 2066 nm and 730 nm, respectively. The phase-matched wavelengths as a function of pump wavelength are given in Figure 5.2(b). This phase-matching diagram contrasts the frequency-shifts achieved from pumping in the normal or anomalous dispersion regime and emphasizes the significance of the zero-dispersion wavelength for fibre FWM. Whereas the pump power significantly influences the magnitude of the frequency-shift when pumping close to the ZDW, the nonlinear contribution to the phase mismatch becomes negligible for the pump powers and pump-wavelength-ZDW separation used in this chapter.

5.2 Single-Pass Configuration

As a first approach, the fibre MOPA, detailed in Section 3.2.2, was spliced to an 18 m length of PCF-LMA8 to investigate the system's single-pass FWM performance. To maximise the peak power at the 1079 nm MOPA wavelength, the system was adjusted to produce 1 ns pulses at a PRF of 1 MHz. The resulting peak power at the input to the PCF was typically no more than 2.2 kW within the ~40 pm linewidth at 1079 nm

From the numerical solution to the coupled amplitude equations (see Chapter 2), Figure 5.3 shows the ideal power transfer for a pump peak power of 1 kW. According to the calculated result, 10 m of PCF should be sufficient for almost-complete pump depletion at power levels well below that accessible from our MOPA. However, the measured PCF output spectrum, given in Figure 5.4, shows a supercontinuum (SC) stretching from 615 nm to beyond the long-wavelength limit of the spectrum analyser (1750 nm). In addition to the pump wave and Raman Stokes at 1079 nm and 1131 nm, respectively, an anti-Stokes wave at 715 nm (142 THz frequency-shift) can clearly be identified. Although this value is in good agreement with that predicted by Figure 5.2, the anti-Stokes conversion efficiency is very small. The small discrepancy in the phase-matched frequency-shift may well be due to tiny differences in the specified and actual values for the structural parameters of the PCF. However, the large contrast between the theoretically predicted power transfer and the spectrum in Figure 5.4 emphasizes the importance of discriminating against competing nonlinear processes. As the first order Raman Stokes cascades to higher orders, located in the anomalous dispersion regime, the spectrum broadens rapidly as it propagates down the fibre. Suppression of the Raman Stokes, through the prevention of seeding (for example), is therefore crucial.

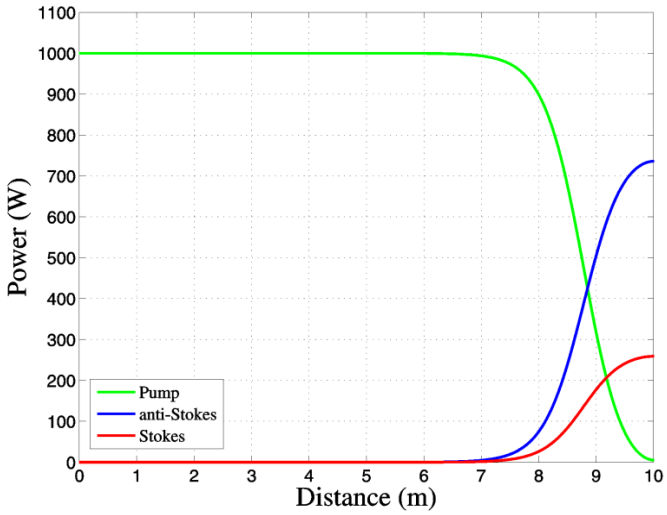

Figure 5.3: Optimised result for an OPA using the PCF-LMA8 , at a pump power of 1 kW.

In accordance with the experimental work of Chapter 4, a spectral filter at the output of the MOPA can suppress seeding of the Raman Stokes. However, whilst spectral filtering can prevent (unwanted) MOPA nonlinearities from seeding unwanted nonlinear

conversion inside the PCF, such conversion occurs even in the absence of seeding at sufficiently high peak powers. To mitigate this limitation, the current optical parametric generator may be reconfigured into a cavity [6]. In this configuration, a fraction of the desired anti-Stokes output is re-launched into the PCF. This then seeds further desired nonlinear conversion. Thus, the so-called optical parametric oscillator (OPO) has been demonstrated as a means of lowering the parametric threshold [2], and thereby the power requirements for FWM.

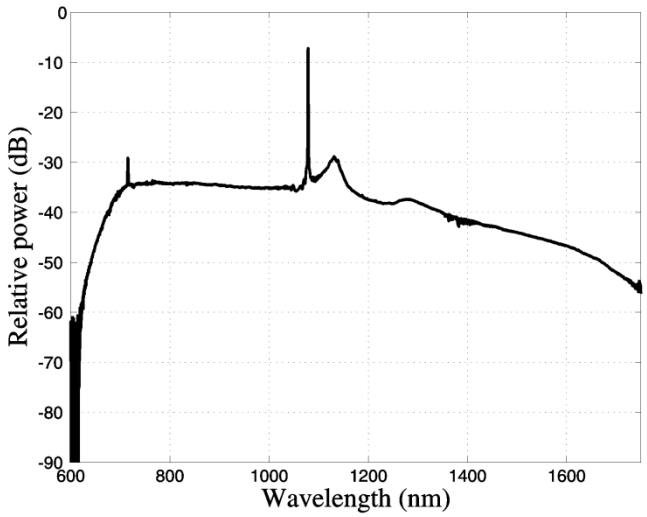

Figure 5.4: Supercontinuum generated in the PCF-LMA8 at a pump power of 2.17 kW. The spectrum shows a sharp feature at 715 nm, together with features at the pump (1079 nm) and Raman Stokes (1131 nm) wavelengths (spectral resolution: 1 nm).

5.3 Optical Parametric Oscillator Configuration

This section gives an overview of our implementation of fibre optical parametric oscillation, using the PCF-LMA8 as nonlinear converter. Section 5.3.1 starts off with a brief discussion on calculated results for the fibre of choice. Following this, Sections 5.3.2 and 5.3.3 reports on experimental results obtained through the use of a free-space cavity and all-fibre cavity, respectively. These results also provide a basis for comparison to the results following in Section 5.4. Finally, Section 5.3.4 comments on related issues and challenges of this approach.

5.3.1 Theoretical Considerations

The theory that governs the dynamics inside an optical parametric oscillator was treated in Section 2.3.3. For the simplest configuration of a linear cavity, the power transfer between the relevant waves are still described by the coupled amplitude equations (refer to Chapter 2.3), whilst the influence of resonant feedback is included through the steady state condition, $P_r(L)F = P_r(0)$. In this condition, L, F and r denote the total cavity length, feedback and resonant FWM wavelength, respectively. Such a bi-directional cavity will give rise to SPM and XPM interactions between the forward and backward propagating waves. However, for our particular case of pump pulses that are short compared to the cavity length, the influence of interactions between counter-propagating pulses may be disregarded from the theory.

For a given set of parameters, the relevant equations are solved in an iterative manner to find the value of $P_r(0)$ for which the steady state condition is satisfied. This procedure was performed to investigate the performance that can be expected from an LMA8-based OPO. In accordance with the calculations of Section 2.3.1, certain effects of the difference in wavelength between the Stokes and anti-Stokes (AS) waves were neglected. This assumption once again enabled the use of a nominal nonlinear parameter of $\gamma = 3.9 \times 10^{-3}$ $\mathrm{m^{-1}W^{-1}}$ (refer to Section 5.1). It furthermore allows for a general discussion on the results, since the choice of resonant wavelength is irrelevant.

Results for a pump peak power of 1 kW are shown in Figure 5.5. The quantity of interest is the conversion efficiency, defined as the ratio of Stokes (or AS) output power to pump input power, and displayed as a function of PCF-LMA8 length and the cavity's out-coupling ratio ($T = 1 - F$). Figure 5.5(a) gives the result for a linear phase mismatch value of $\Delta\beta = -2\gamma P_p$. As discussed in Chapter 2, this value corresponds to maximum gain, provided that pump depletion remains negligible. The result illustrates that the maximum conversion efficiency can be achieved over a range of fibre lengths and associated out-coupling ratios. As expected, a shorter fibre length requires a larger feedback, and vice versa. It is furthermore interesting to note that a secondary region of maxima is located towards longer fibre lengths. These maxima occur as a result of the periodic nature of the solutions to the coupled amplitude equations (refer to Section 2.3.1). Importantly, the maximum conversion efficiency only reaches ~28%, whereas the theoretical limit is 50%.

Seeing that pump depletion is clearly not negligible, the assumed value for Δβ no longer leads to maximum gain. This is illustrated in Figure 5.5(b), for which Δβ was arbitrarily chosen as $-1.6\ \mathrm{m}^{-1}$. In this case, the maximum conversion efficiency approaches the theoretical limit.

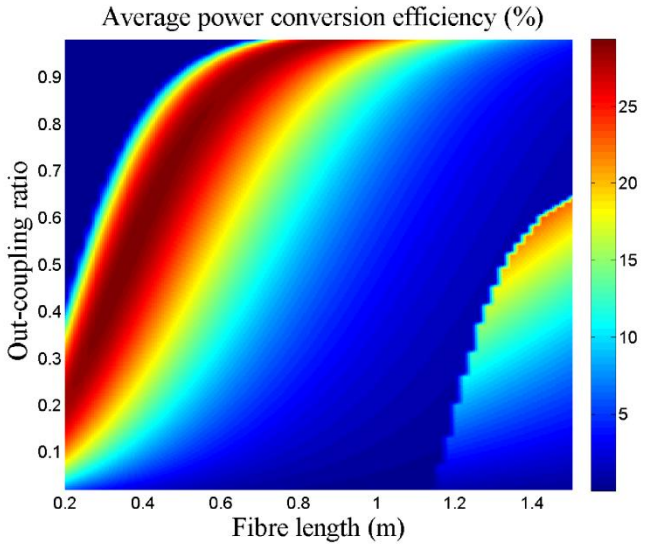

(a)

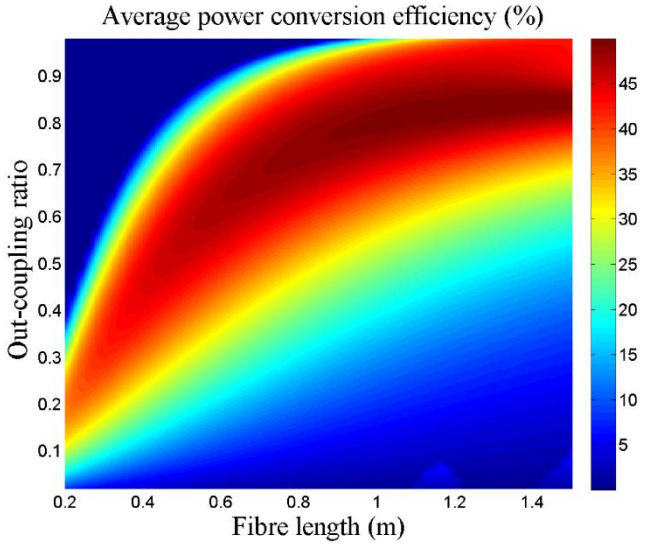

(b)

Figure 5.5: Pump-to-anti-Stokes average power conversion efficiency, as a function of PCF-LMA8 length and out-coupling ratio, for (a) $\Delta\beta = -2\gamma P_{p,0}$, and (b) $\Delta\beta = -1.6\ \mathrm{m}^{-1}$. The magnitude of the conversion efficiency is displayed on the z-axis (refer to right-hand side colour index).

The most important feature of the calculated OPO results is the relative reduction in fibre length required for significant pump depletion (compare to Figure 5.3). The results furthermore illustrate the influence of a non-zero phase mismatch on the peak

conversion efficiency within an oscillator. This is of particular interest to all practical optical parametric oscillators, where longitudinal inhomogeneities are present to some degree. For this case, the observed Stokes and AS waves at the output from the fibre will correspond to those wavelengths for which the average phase mismatch over the full fibre length is a minimum (see for example, Figure 5.5(a)). In the worst-case scenario, variations along the fibre can result in partially coherent build-up, in which case the expected oscillator dynamics will be dramatically different from that depicted in Figure 5 (refer to Section 4.2).

5.3.2 Free-Space Cavity Experiments

A schematic representation of our initial OPO cavity, constructed using available free-space components, is shown in Figure 5.6. The MOPA output is launched through a free-space isolator, before being diffracted by a volume Bragg-grating (VBG) with a bandwidth of ~0.5 nm (refer to Section 3.2.2). In accordance with the conclusion of Section 5.2, the VBG serves as a spectral filter to suppress seeding at SRS wavelengths inside the nonlinear converter. A half-wave plate is used to rotate the polarization angle of the linearly polarized MOPA output, before it is coupled into the free-space cavity.

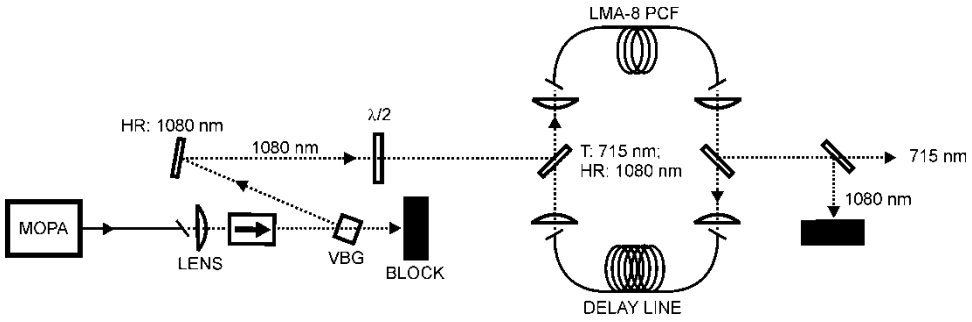

Figure 5.6: Schematic of the free-space OPO. A volume Bragg-grating (VBG) is used as a spectral filter to remove unwanted seed light at SRS wavelengths, whilst a half-wave plate provides partial control of the incident pump polarization. Dichroic mirrors with a high reflectivity (HR) at 1080 nm, and partial transmission (T) at 715 nm, provide resonant feedback at the FWM anti-Stokes wavelength.

The OPO cavity is formed using two dichroic mirrors that are highly reflective at 1079 nm and partially transmitting (~70%) at the established anti-Stokes wavelength of 715 nm. An 18 m length of PCF, together with a delay line, consisting of ~203 m of HI1060 fibre (Corning), completes the cavity and yields a round-trip frequency similar to the MOPA's PRF. Rough alignment of the cavity at the resonant wavelength of 715

nm was achieved using a SC source and a Si-detector. The estimated cavity round-trip loss however remained high (~13 dB), owing primarily to coupling-losses, but also to reflections at the dichroic mirror at the output from the delay line. Precise synchronization of the AS pulses was achieved by scanning the PRF of the MOPA, via the sampling rate of the arbitrary waveform generator (Tektronix AWG710), whilst monitoring the OPO output on an OSA. In this way, the resonant PRF was determined to be 904 kHz.

A comparison of the OPO output for the cases with and without synchronized feedback is shown in Figure 5.7(a). The spectra were recorded for an input peak power of 1.23 kW. The gain at the AS wavelength is 21 dB with respect to the unsynchronized case, whilst its linewidth was measured to be ~1.5 nm (0.1 nm spectral resolution). From the spectra, it is clear that a SC is still generated within the PCF-LMA8, although the shape is severely distorted by the spectral properties of the dichroic mirrors. The small signal parametric bandwidth at the AS wavelength, for this power level, was calculated as 0.16 nm (refer to Chapter 2). Since the pump linewidth is narrower than the associated pump acceptance bandwidth, it stands to reason that fibre inhomogeneities may be responsible for the broadened AS linewidth (refer to Chapter 4.2.1.2). However, the asymmetry of the broadened AS line is consistent with the influence of XPM and SPM [7].

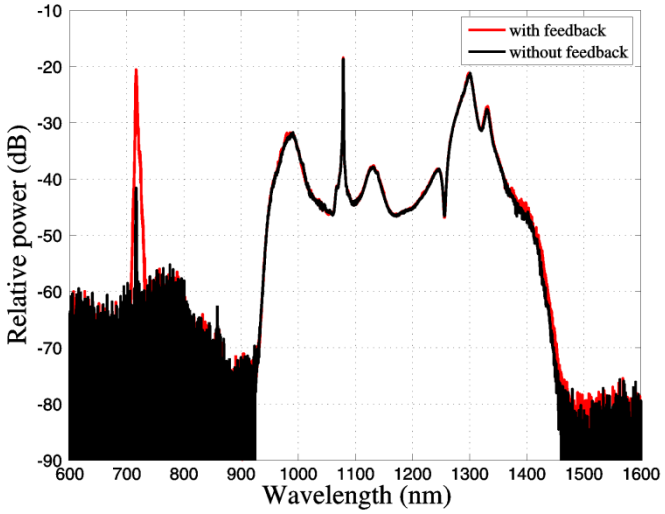

(a)

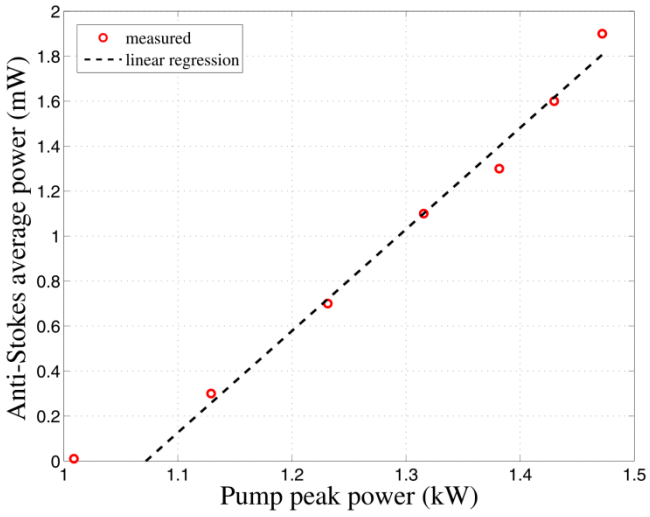

(b)

Figure 5.7: (a) Free-space OPO output spectra in the absence and presence of synchronized feedback, for a pump power of ~1.23 kW (spectral resolution: 1 nm). Synchronization is achieved at a MOPA PRF of 904 kHz. (b) Output power at the anti-Stokes wavelength, measured with the aid of a bulk diffraction grating and a broadband thermal power meter.

Figure 5.7(b) shows the dependence of the AS average power on the PCF input peak power. Power measurements were performed by imaging the OPO output onto a bulk diffraction grating for the purpose of isolating the AS. A thermal power meter with a flat spectral response (Melles Griot, 13PM001) was used at all times. The oscillation threshold is reached at a pump power of around 1.07 kW, after which the OPO output increases linearly up to the maximum pump power. The maximum output power of 1.9 mW translates into a total AS power of ~9 mW at the PCF output, giving rise to a pump-to-anti-Stokes average power conversion efficiency of ~0.6%.

5.3.3 Fibre Cavity Experiments

The free-space cavity fibre OPO gave a relatively low conversion efficiency, but nevertheless confirmed that a PCF-LMA8-based OPO can reach the oscillation threshold, using the MOPA of Section 3.2.2 as a pump source. In order to decrease the cavity loss and to converge on the ideal of an all-fibre OPO, the setup of Figure 5.8 was adopted. Shown here, is an all-fibre cavity OPO, using the same launch configuration as that of Figure 5.6. In this case, the dichroic mirrors were replaced by WDM-couplers, centred at 1079 nm and 715 nm. Since both WDM-couplers have a high extinction ratio

at 715 nm, a tap-coupler was used to extract 10% of the 715 nm light from the cavity. A second tap-coupler was furthermore employed for the purpose of studying the effect of higher output-coupling on the oscillator's threshold. It also simplifies power measurements as a result of the coupler's spectral discrimination. To enable a direct comparison to the free-space cavity OPO results, the PCF and delay line lengths were kept the same. The resultant cavity round-trip loss, dominated by splice-loss and attenuation in the delay fibre, was estimated at ~6 dB.

Pump light was launched into the OPO through the input-WDM-coupler. The WDM pigtails were kept as short as possible to prevent the build-up of significant Raman scattering inside these fibres. Seeding at SRS wavelengths inside the PCF was further reduced through an increase in the MOPA's PRF from 904 kHz (Section 5.3.2) to 1.73 MHz, resulting in a decreased pump peak power. The extra fibre, added to the cavity in the form of couplers, resulted in a decrease of the cavity's round-trip frequency from 904 kHz to 865 kHz. The new value for the PRF therefore enabled synchronization at double the cavity's round-trip frequency. This meant that the cavity now contained two pump pulses at any given time.

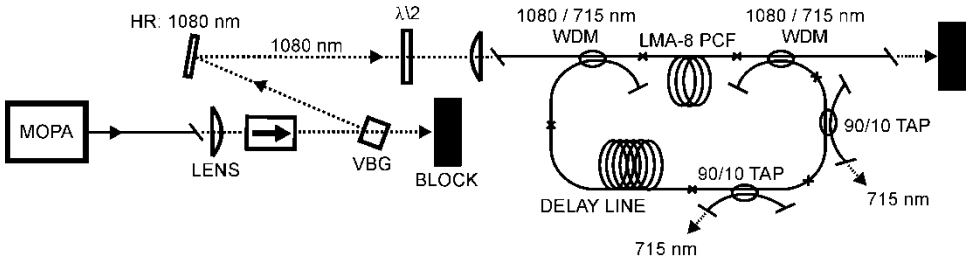

Figure 5.8: Schematic of the all-fibre cavity OPO. The pump launch setup is identical to that of Figure 5.6. WDM-couplers are used to couple light into and out of the cavity, whilst two tap-couplers remove a total of 19% of the anti-Stokes power from the cavity. The tap-couplers are associated with extremely high losses at the Stokes wavelength (2.2 μm), thereby ensuring singly-resonant operation of the OPO.

Figure 5.9 shows the effect of synchronized feedback on the AS power, as measured from the first of two tap-couplers in the all-fibre cavity OPO (compare to Figure 5.7). At a PCF input peak power of 0.46 kW, the AS wave increases by over 53 dB over its single-pass power. The increase in the FWM AS power, compared to the free-space cavity OPO case, is evident from the multiple Raman Stokes orders that it generates within the cavity's delay line. Once again, the AS linewidth of ~0.8 nm (0.1 nm spectral resolution) is an order of magnitude larger than the 60 pm predicted by

theory. In addition to the desired FWM, several other interesting features can be identified from Figure 5.9. Two peaks about the 1079 nm pump wavelength, at a frequency-shift of ~2.6 THz, is consistent with a FWM process. The efficiency of this process shows a dependence on the input pump polarization angle and is therefore thought to derive from polarization modulation instability within the HI1060 WDM-pigtails [8]. Apart from the first-order Raman Stokes, a Raman anti-Stokes wave is also observed. The enhancement of this Raman anti-Stokes wave in the presence of synchronized feedback is a well-known phenomenon and is attributed to the interaction between SRS and FWM [9]. The long-wavelength edge of the spectrum in Figure 5.9 remains unchanged as the PCF input pump power is increased. This is due to the large bending loss of the tap-coupler pigtails (Nufern HP-780) at wavelengths longer than 1200 nm. Since the resultant loss for the FWM Stokes is very high, the tap-coupler effectively ensures that the OPO is singly-resonant [10].

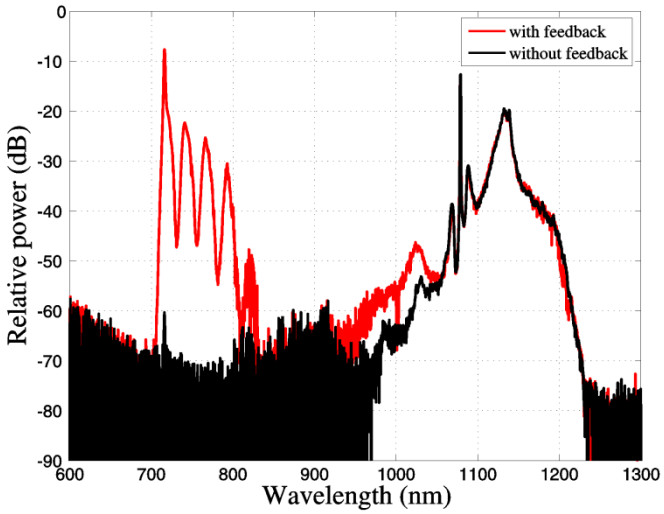

Figure 5.9: All-fibre cavity OPO output spectra, as measured from the first tap-coupler, in the absence, and presence of synchronized feedback at a pump peak power of 0.46 kW (spectral resolution: 1 nm). Synchronization is achieved at a MOPA PRF of 1.73 MHz, corresponding to half the cavity round-trip time. Note that the output-end WDM coupler attenuates wavelengths around the pump relative to those around the anti-stokes.

The average power at the AS wavelength, including that of its associated Raman orders, was measured from the second tap-coupler as a function of input pump peak power. Figure 5.10(b) gives a threshold pump power of 0.43 kW, whilst the maximum average output power of 10.8 mW is reached at a pump peak power of 1.09 kW. The

output spectrum from the second tap-coupler, at a pump power of 1.09 kW, is shown in Figure 5.10(a). From a comparison to Figure 5.9, it is clear that the coupler attenuates the long-wavelength part of the spectrum by ~20 dB. It is this spectral discrimination that allowed us to measure the AS power from this coupler. However, since five orders of SRS were efficiently generated from the AS peak at 715 nm, integration of the spectrum confirmed that only 46% of the measured power was in fact located at the AS wavelength.

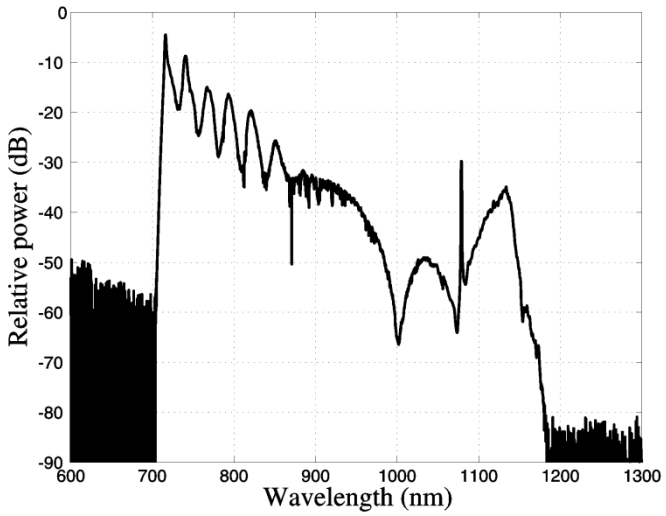

(a)

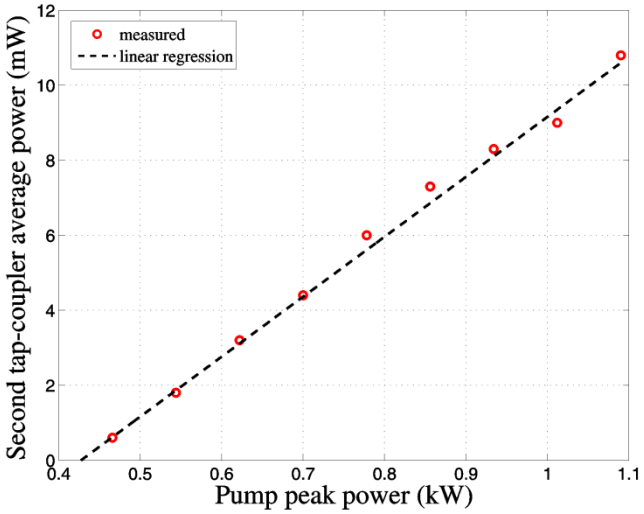

(b)

Figure 5.10: (a) All-fibre cavity OPO output spectrum at a pump power of 1.09 kW, as measured from the second tap-coupler (spectral resolution: 1 nm). (b) Second tap-coupler output power as a function of pump peak power. The maximum pump-to-anti-Stokes conversion efficiency was calculated to be 4.6%.

From the out-coupling ratios (both 10%), the calculated combined AS output power from both couplers at a pump power of 1.09 kW is 10.5 mW, whilst the total AS power from the PCF reaches 78 mW. The associated conversion efficiency is 4.6%.

It may be reasoned that the five orders of cascaded SRS in the sub-900 nm portion of the spectrum have their origin in the FWM AS at 715 nm, which had to serve as the pump source for the process. In this case, one can argue that the actual pump-to-anti-Stokes conversion efficiency is likely twice as high, or ~9%. However, the fact remains that cascaded SRS in the long OPO cavity is depleting the AS at 715 nm. For this reason, the power at 715 nm cannot simply be improved by using higher pump powers at the PCF input. The preceding measurements were therefore repeated with a 75 m delay line and a cavity synchronized at a MOPA PRF of 1.95 MHz (corresponding to the cavity round-trip time). Although the results were qualitatively no different from those reported in Figures 5.9 and 5.10, the spectra from the tap-couplers showed slightly reduced power levels for the Raman orders. The conclusion must then be that SRS in the delay line represents a limit to the power scaling of this OPO.

Several options are available for getting around the limitation of AS-generated SRS. An alternative to using a shorter delay may involve intra-cavity filtering at the AS-SRS wavelengths. The implementation of this approach is common with fibre OPO devices pumped in the anomalous dispersion regime [11], [12]. Another option to mitigate SRS in the delay fibre would be to decrease the power there, by using a higher output-coupling ratio. A drawback is that it will lead to a higher pump threshold power, but provided it is possible to operate well above threshold, a higher output power will be possible before SRS occurs. I will return to these issues in Section 5.4, where the OPO's dependence on a variety of parameters are considered.

5.3.4 Discussion

Although 9% is a respectable conversion efficiency, it is still below what has been demonstrated in parametric oscillators with smaller wavelength shifts [13]. It is also smaller than the Raman conversion efficiency to 1132 nm, despite the intrinsically larger gain and smaller polarization dependence of the parametric process [14]. As already mentioned, inadequate phase-matching is a possible explanation for this. The underlying reason for inadequate phase-matching is most likely related to the influence

of longitudinal fibre inhomogeneities and the small parametric bandwidth associated with the large frequency-shift process and the relatively low pump powers used.

An investigation into the temporal behaviour of the output from the OPO of Section 5.3.3 revealed that not every pump pulse is converted into a corresponding AS pulse. Although variations along the length of the fibre are known to result in decreased parametric conversion, they cannot on their own explain pulse-to-pulse variations. Although the pump peak power does vary somewhat from pulse to pulse, these variations were small compared to the AS variations. We suspect that these were caused by the evolution of the relative polarization of the interacting waves. The theoretical work of Lin and Agrawal suggests that birefringence and polarization mode dispersion (PMD) not only lead to a decrease in the average parametric gain, but also to considerable power fluctuations in the generated sidebands [15]. These fluctuations, which were found to scale with the magnitude of the frequency-shift [15], may therefore account for the pulse-to-pulse variation detected from our OPO. Since the OPO of the current work is significantly different from the generic FWM treated in Ref. [15], a detailed investigation into the influence of polarization is needed for further insight in our case. This topic will be revisited in Chapter 7.

In an attempt to improve the temporal instabilities of the pump MOPA, the 1079 nm YDFL seed was replaced with a 1064 nm Q-photonics diode. This wavelength was chosen since it enabled the use of an all-fibre band-pass-filter-integrated isolator, thereby allowing the MOPA to be spliced to the input WDM of the OPO cavity. The move to an all-fibre system improved the stability of the pump source by removing the influence of temperature drift at what used to be a free-space pump launch (refer to Section 5.3.3). With the pump wavelength moving to 1064 nm, the calculated frequency-shift increases to give Stokes and AS wavelengths of 2323 nm and 690 nm, respectively. However, the frequency-shift may actually be larger by up to 2%, judging by the discrepancy between the calculated and experimental AS wavelengths for the case of a 1079 nm pump wavelength (refer to Sections 5.1 and 5.2). The increased frequency-shift introduces a host of potential complications. Firstly, since the Stokes wavelength is approaching 2.5 μm, it is moving into a regime where the transparency of silica can no longer be assumed to be perfect. Several studies in the fibre FWM literature have been aimed at exploring the importance of Stokes loss (or AS loss) on the conversion from the pump to the AS wave (or Stokes wave). It has, for instance,

been suggested that loss at one of the daughter waves would lead to a reduced peak conversion efficiency, but an increased parametric bandwidth [16]. Other studies have however concluded that the effect of loss will essentially remain negligible within a silica PCF at Stokes wavelengths as high as 3 μm [4], [5]. A second complication of an increased frequency-shift is an increased sensitivity of the phase-matched wavelengths to fluctuations in the fibre dimensions. It is then altogether not surprising that the parametric oscillator threshold could not be reached for the case of a 1064 nm MOPA seed. The experiment did however serve as a guideline to what a realistic tuning range for a tunable OPO may constitute. It also strengthened the belief that fibre non-uniformity is a severe limitation to the conversion efficiency inside the PCF-LMA8 at the pump powers of interest.

The impact of longitudinal non-uniformity in the PCF, on the FWM process, can possibly be reduced through the use of fibres with increased mode-areas. This is because the dispersion of these fibres has a smaller contribution from waveguiding and consequently shows a reduced dependence on the exact waveguide dimensions. However, a larger core will reduce the signal intensity, and this increases the threshold. While this can be compensated for by a longer fibre, an increased fibre length will result in a reduction in the phase-matching bandwidth which increases the sensitivity to fluctuations. Furthermore, since waveguide dispersion is responsible for a shift of the zero-dispersion wavelength to values below that of bulk silica, a reduction in its effect would result in an increased phase-matched frequency-shift when pumping at 1079 nm [5]. This increase in frequency-shift will lead to an increased sensitivity to fibre non-uniformities [17], which will demand the use of higher pump powers to maintain the required parametric bandwidth for efficient conversion. Therefore, which fibre design allows for the lowest threshold in an OPO configuration is an open question that warrants further investigations and fell outside the scope of this thesis.

5.4 All-Fibre OPO

The investigation of Section 5.3 highlighted the requirement for a more stable pump source at a wavelength around 1080 nm. To this end, the MOPA was fitted with a 1080 nm Lumics seed diode. In accordance with our intention of an all-fibre experimental setup, a band-pass-filter-integrated fibre-isolator at a centre wavelength of 1080 nm (10

nm FWHM) was developed in partnership with Shinkosha. Details on the performance of the resultant MOPA are provided in Section 3.2.3.

A schematic representation of the full experimental setup is shown in Figure 5.11. To provide full polarization control of the launched pump power and the AS feedback power, mechanical polarization controllers were employed at the output from the MOPA and directly following the second tap-coupler (also refer to Figure 5.8). The general setup depicted in Figure 5.11 was used as the basis for an investigation into various aspects of PCF-based OPOs. The following sections aim to give an overview of our resulting findings and are structured according to:

5.4.1 Influence of Out-Coupling Ratio

5.4.2 Influence of PCF Length

5.4.3 Intra-Cavity Filtering

5.4.4 Pump Pulse Width

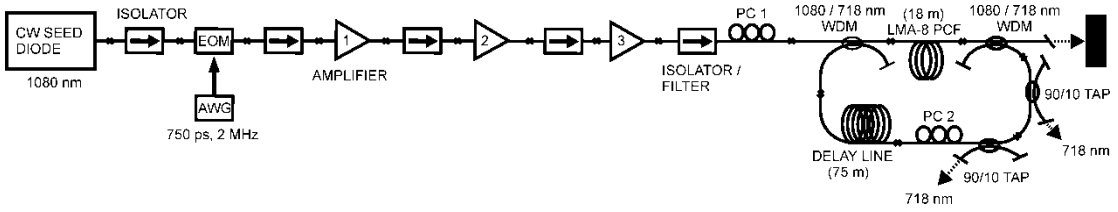

Figure 5.11: Schematic of the all-fibre Pump-OPO system at 1080 nm. A fiberized isolator with built-in band-pass filter allows maximum suppression of out-of-band ASE and SRS and yields improved stability and robustness.

5.4.1 Influence of Out-Coupling Ratio

Experiments on the all-fibre OPO, using an 18 m length of PCF-LMA8, were performed for two AS out-coupling ratios. Whilst the first tap-coupler had a fixed out-coupling ratio of 10%, the second tap-coupler was configured for 10% or 90% to yield total out-coupling ratios of 19% or 91%, respectively. The resultant output spectra, as measured from the second tap-coupler, are given in Figure 5.12(a). For these spectra, the MOPA was configured for a pump peak power of ~1 kW at the PCF input (750 ps pulses at a PRF of 2 MHz). The results illustrate the effects of a higher intra-cavity AS power. With an out-coupling ratio of 19%, the AS peak power is significantly higher upon entering the 75 m delay fibre, resulting in noticeable broadening of the AS spectrum as

well as SRS. These mechanisms therefore effectively limit the circulating AS power within the parametric bandwidth.

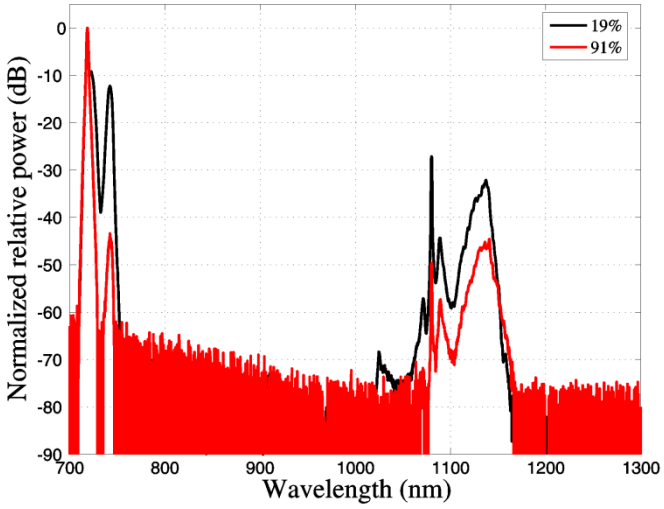

(a)

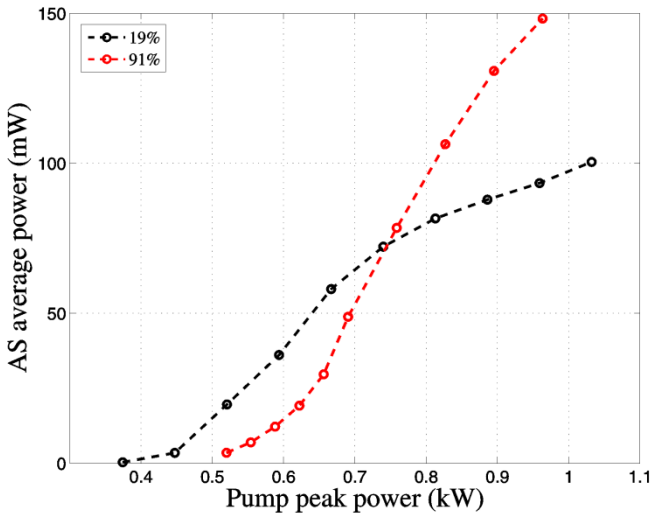

(b)

Figure 5.12: (a) Comparison of OPO output spectra for two values of the out-coupling ratio, as measured from the second tap-coupler at a pump power of ~1 kW (spectral resolution: 1 nm). (b) Corresponding total anti-Stokes average power at the PCF output, inferred from the measured out-coupled power.

The ~1 kW of launched pump power was the highest achievable for the pump pulse duration and PRF we used. This was limited by the power handling of the final isolator, specified as 2 W average power. From the measured average AS output power, we were able to infer the total AS power at the output from the PCF. Figure 5.12(b)

compares these values for both out-coupling ratios. Although having a higher pump threshold value, as can be expected due to the increase in cavity round-trip loss, the cavity with 91% output-coupling reaches a considerably higher maximum AS power than the lower loss cavity. As suggested by the slope of the red curve in Figure 5.12(b), the output power is limited by the available pump power. However, it is to be expected that the case of 91% output-coupling will eventually also be subjected to the spectral broadening associated with the 19% output-coupling ratio. The onset of spectral broadening should then be delayed through the use of delay fibres with shorter lengths or larger mode-field diameters. Experiments using relatively short delay fibres have confirmed that a longer delay line may in fact be preferred, which points to the existence of an optimum length (refer to Section 5.4.3).

The PCF subsequently gave a maximum average output power of 148 mW, which translates to an average-power in-fibre pump-to-anti-Stokes conversion efficiency of 10.3%. Although this result is, in terms of conversion efficiency, only marginally better than that achieved for the free-space pump launch OPO, it clearly shows a significantly better spectral density as only a single order of Raman Stokes is present for both coupling-ratios. This result in itself represents the highest fibre OPO conversion efficiency, for such a large frequency-shift, to date. It also conclusively illustrates the potential for robust all-fibre OPO systems.

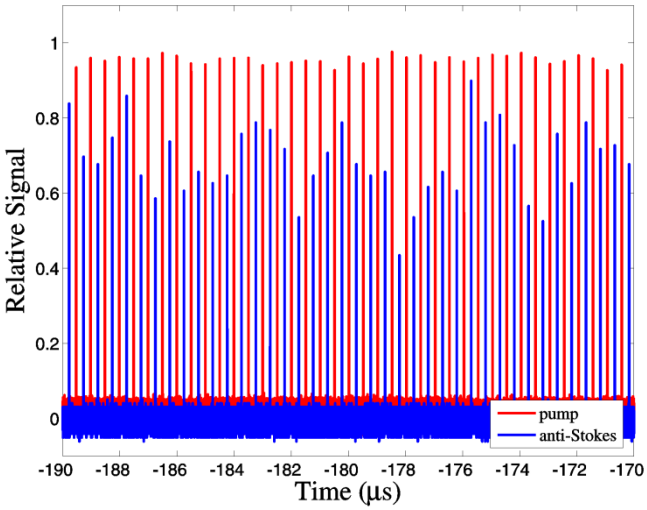

Figure 5.13: Temporal behaviour of the pump and generated anti-Stokes at an incident pump power of 1 kW. A measurement bandwidth of 20 GHz and sampling of 50 GSa/s were used.

Figure 5.13 gives an example of the temporal behaviour of both the pump MOPA (red) and the AS output at 719 nm (blue). The measurement was performed at the maximum pump power and made use of two 24 GHz photo-detectors (Discovery Semiconductors DSC30S [18] and New Focus Model 1414 [19]) and a 20 GHz real-time oscilloscope with a sampling rate of 50 GHz (Tektronix DSA72004B [20]). Thus, all peaks are well resolved. In contrast to the case with 1079-nm fibre-laser seeding, the pump pulses are very stable. Although relatively small pulse-to-pulse amplitude variations are still present, these variations cannot be correlated to those of the corresponding AS pulses. As the pump power is reduced to lower values, the severity of the pulse-to-pulse amplitude fluctuations for the AS wave increases significantly. This behaviour is to be expected closer to the parametric threshold, since certain pulses may only just reach threshold, whilst others may remain just below threshold.

The comparison in Figure 5.12 clearly shows that the out-coupling ratio has a strong influence on the dynamics inside the OPO. In light of this, it would have been interesting to compare the results to those using different out-coupling ratios. Unfortunately, alternative WDM couplers were not available for such an experiment. The analysis was however extended to consider how the performance of OPOs, based on different PCF nonlinear converter lengths, compare for the accessible out-coupling ratios. These results are presented next, in Section 5.4.2.

5.4.2 Influence of PCF Length

If the parametric gain in our OPO is indeed subject to degradation as a result of polarization effects and longitudinal inhomogeneity along the PCF, it seems probable that small contributions distributed over the length of the PCF will add up to produce the observed FWM at the wavelengths which have the highest degree of effective phase-matching (refer to Chapter 4.2.1). The presence of such a distributed gain may thus be an argument for the use of an even longer PCF. Although the use of very long fibres (even several times the walk-off length) has not been reported for a PCF-based OPO, Sloanes *et al*. have reported relatively high conversion efficiencies for a PCF-based optical parametric amplifier of this type [21], with what appears to be incoherent growth of the AS power. Translating this to an OPO, a longer PCF should help to reduce the pump threshold, which is an important consideration. However, once the fibre becomes too long, large frequency-shift FWM is dominated by the relative

strength of nonlinear processes that do not require active phase-matching. This places an upper limit on the fibre length, and therefore a lower limit on the threshold that can be realised. By contrast, in longer pump-wavelength OPOs, the desired FWM have been demonstrated to dominate even in km-long fibres [22].

To investigate the influence of the nonlinear converter length on the dynamics within the OPO, a series of experiments were performed. In contrast to the experiments of Sloanes *et al.*, it is not only the absolute length of the nonlinear converter that impacts on the performance of a fibre OPO, but also its relative length compared to that of the full cavity. In this section we consider how these parameters combine to influence the OPO output power, spectral attributes and temporal qualities.

Experiments on PCF lengths shorter than 18 m gave very low conversion efficiencies, provided that threshold could be reached at the pump peak powers accessible from the all-fibre MOPA, operated with 750 ps pulses at 2 MHz. For the case of an 11 m length of PCF, operated in a cavity configured for 91% out-coupling, the threshold pump power had a value of about 800 W. The associated threshold-power fibre-length product is in good agreement with the corresponding value for the 18 m PCF length (red curve in Figure 5.12(b)). This result is however somewhat surprising. Figure 5.14 shows the calculated relative group delay of PCF-LMA8 and indicates differences of 46 ps/m and 23 ps/m between the pump and Stokes waves, and the pump and AS waves, respectively. Since the FWM process will be limited by the largest of these, the calculated walk-off length for 750 ps pump pulses yields 16.3 m.

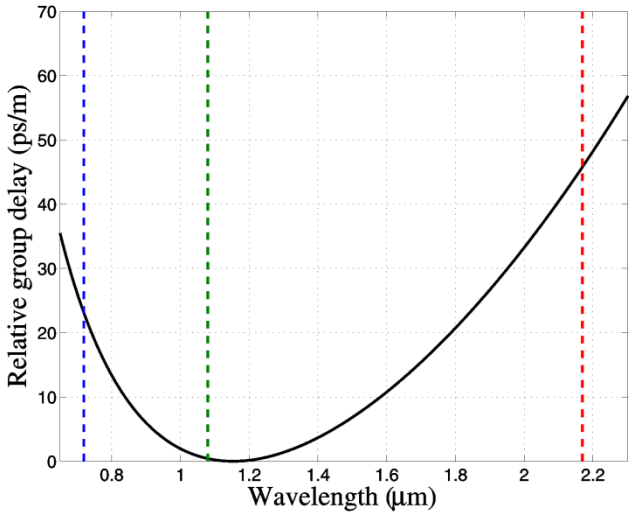

Figure 5.14: Calculated group delay for the PCF-LMA8, indicating the three relevant FWM wavelengths.

This length, which is the length after which the pump and Stokes pulses will be completely separated, is possibly longer than the actual fibre length over which the pulses will exchange energy, due to the additional influence of temporal gain narrowing. Temporal gain narrowing describes the process whereby the shape of the pump pulse is distorted by the exponential FWM gain and where only those parts of the pulse, where the instantaneous power exceeds the parametric threshold, are converted. Both walk-off and gain narrowing are likely responsible for the relative compression in the comparison of Figure 5.15, which shows a pump pulse (750 ps) and its associated AS pulse (200 ps) for the case of the above-mentioned experiment using 18 m of PCF. Since walk-off should have a more severe impact for a longer nonlinear converter, one might expect the threshold-power fibre-length product for the 11 m PCF to be noticeably less than that for the case of 18 m PCF. Even more so, considering that, from a practical perspective, the conversion efficiency in a shorter fibre should be less susceptible to the influence of longitudinal inhomogeneity. However, as it stands, the experiment adds value to the notion that the longitudinal inhomogeneity in the PCF-LMA8 is distributed, i.e. has a high spatial frequency [23], [17].

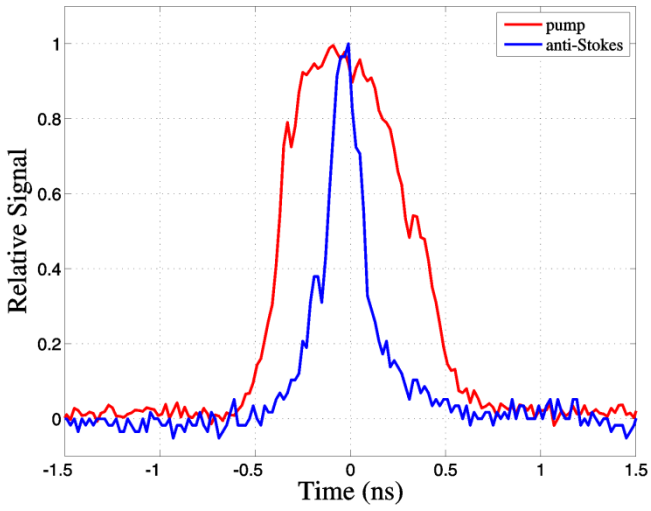

Figure 5.15: Comparison of the pump and anti-Stokes pulse widths for 18 m of PCF-LMA8. A measurement bandwidth of 20 GHz and a sampling of 50 GSa/s were used.

In accordance with the preceding conclusion, I was unable to reach threshold for a cavity consisting of 7 m PCF-LMA8. From the established threshold-power fibre-length product, the required pump power is 1.28 kW, compared to the ~1 kW accessible from the all-fibre MOPA. Despite attempts at increasing the pump peak power, by means of

decreasing the pump pulse width to values below 300 ps (at a PRF of 2 MHz), threshold still could not be reached. The exact reasons for this are not understood, although one hypothesis is that the temporally compressed circulating AS pulses are not synchronized appropriately as a result of timing jitter of the arbitrary waveform generator used to modulate the EOM. Measurements of the timing jitter typically showed a Gaussian distribution for the repetition rate, with a standard deviation of ~20 ps. Assuming a similar ratio for the pump-to-anti-Stokes pulse compression, the AS pulse width may be below 100 ps, in which case the timing jitter of the AWG can have a significant effect on the synchronous feedback of the OPO.

The in-fibre pump-to-anti-Stokes average power conversion efficiency for the 11 m PCF only reached a maximum value of 1.2%. Since this value is limited by the available pump peak power, the experimental setup was reconfigured to extend the investigation. To this end, the delay line was removed from the cavity, reducing the cavity length to 18.6 m. To accommodate the associated cavity round-trip time and to increase the pulse peak power, for a 750 ps pulse width, the MOPA seed was modulated in burst-mode. In the presence of gain saturation within the MOPA amplifiers, measures had to be taken in order to ensure that the OPO input pump pulses within each burst have comparable peak powers. This was accomplished through shaping of the group of pulses that constitutes the pump seed burst. Figure 5.16(a) shows the output from the first MOPA amplifier for two differently shaped input waveforms. Both burst-mode waveforms shown here have 20 pulses per burst, with an intra-burst pulse repetition period of ~93 ns and a burst delay of 15 μs, resulting in an average PRF of 1.33 MHz. Whilst the green waveform in Figure 5.16(a), designated *shape 2*, was chosen arbitrarily, the black waveform, called *shape 1*, was calculated according to the approach set forth in the work of Malinowski *et al.* [24]. In Ref. [24], the authors illustrate that the input pulse (or burst) shape, required for a desired output pulse shape, can be calculated if values for the small-signal gain and saturation energy of the amplifier system are known. It is shown that these values can be obtained from a fitting procedure to the output pulse from the amplifier system, for a known test input pulse.

Figures 5.16(b) and (c) show the resultant temporal behaviour at the OPO output for the pump wave (red) and AS wave (blue), for *shape 2* and *shape 1* in Figure 5.16 (a), respectively. The pump wave was measured at the 1080 nm port of the cavity's output WDM-coupler, whilst the AS wave was measured from the second tap-coupler,

configured for a 90% out-coupling ratio. From Figures 5.16(b) and (c), it follows that the two seed burst-shapes leads to notable differences in the shape of the output pump burst. *Shape 2* has the majority of its high peak power pulses located towards the trailing edge of the pulse, with *shape 1* favouring the leading edge. This difference clearly plays an important role in the number of round-trips it takes for the AS light to reach the measurement threshold. As such, *shape 1* gave superior OPO performance and was also found to give a higher average power conversion efficiency. The results from *shape 1* are compatible with those from a continuous pump pulsetrain, provided that we neglect the small number of pulses in every burst, required for the AS to build up from noise. The burst-mode data can therefore be used to supplement our initial measurement, to provide a proper comparison to the data for other PCF lengths.

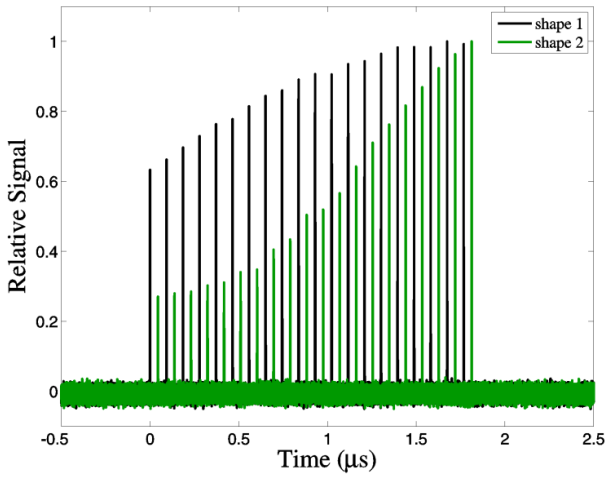

(a)

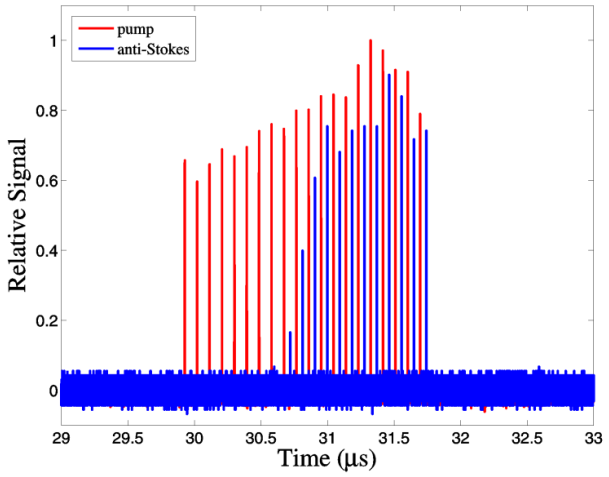

(b)

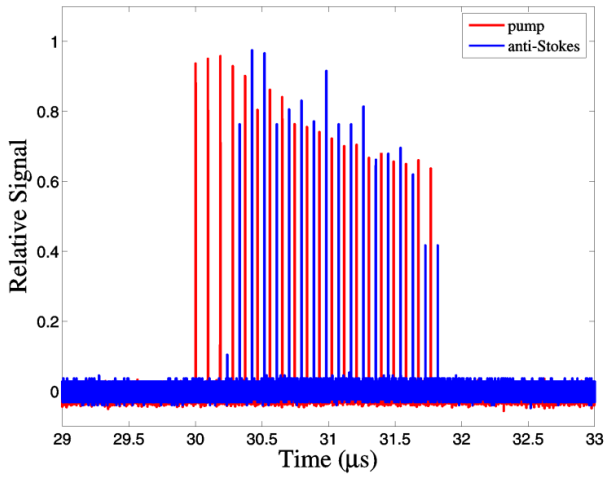

(c)

Figure 5.16: Influence of MOPA seed burst-shape on the MOPA output burst-shape and generated anti-Stokes burst, for a PCF length of 11 m. (a) Two examples of MOPA seed burst-shapes. (b) Output for *shape 2*. (c) Output for *shape 1*. All measurements made using a bandwidth of 20 GHz and a sampling of 50 GSa/s.

To investigate the OPO performance for cavities using longer lengths of PCF, the MOPA was reconfigured to its previous operating state with continuous modulation. To ensure that the results are comparable to each other and to that of the 18 m length of PCF, each cavity's round-trip length was supplemented with a delay fibre, as required, to yield 108 m. The associated pump pulses had a width of ~800 ps and a PRF of 1.85 MHz. Provided that the parametric threshold could be achieved, measurements were performed for two out-coupling ratios (19% and 91%). Sets of results for all the available PCF lengths, for both out-coupling ratios, are given in Figure 5.17(a) and (b). As before, the y-axis gives the AS average power at the PCF output, as calculated from the measured power at the second tap-coupler. The results of Figure 5.17 show superior OPO performance for PCF lengths shorter than 35 m. Whereas cavities containing 65 m and 100 m of PCF show saturation of the converted power for the case of 19% out-coupling, we were unable to reach threshold at 91% out-coupling. Interestingly, Figure 5.17(a) shows threshold pump powers that appear to be almost invariant to the length of the nonlinear converter. This is in contrast to Figure 5.17(b) (with 91% output coupling), where the cavity containing 18 m PCF has a threshold power quite similar to those of (a), whilst this value increases significantly for PCF lengths of both 35 m and 11 m. This behaviour suggests that the dynamics inside the OPO show a greater sensitivity to competing nonlinearities as the cavity loss increases.

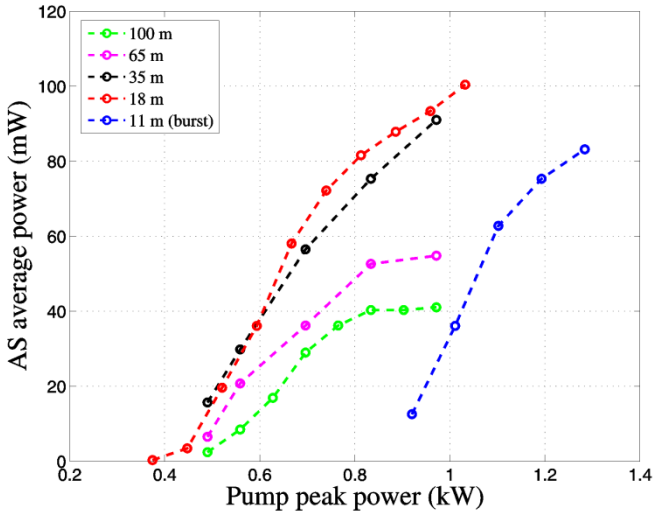

(a)

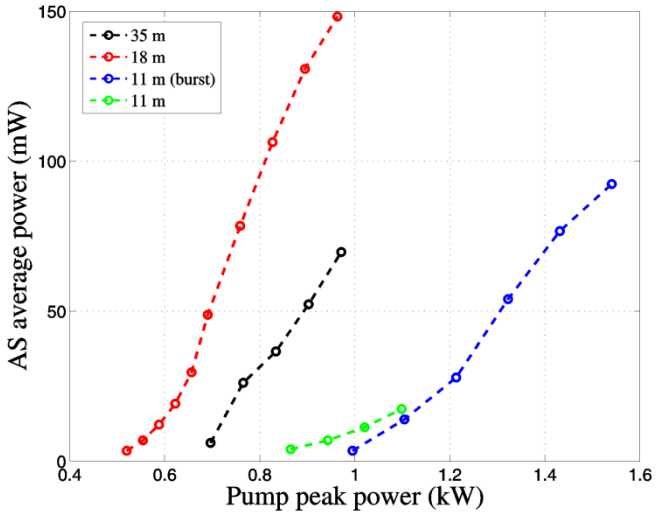

(b)

Figure 5.17: Comparison of the anti-Stokes PCF output average power for several lengths of LMA8, for cavities configured to (a) 19% out-coupling and (b) 91% out-coupling. A pump pulse width, ranging between 750 ps and 800 ps, and a PRF, ranging between 1.85 MHz and 2 MHz, is used throughout, apart from the specified burst-mode results.

It is worth noting that the slope of the burst-mode result for the 11 m nonlinear converter is in good agreement with the corresponding continuous pump pulsetrain result (refer to Figure 5.17(b)). Although the burst-mode result shows a slightly larger threshold value, it is to be expected, since the AS pulse has to build up from noise in every burst, as indicated by the missing blue pulses in Figure 5.16(c).

Figure 5.18 gives a direct comparison of the calculated AS average powers at the output of an 11 m PCF (burst-mode) and a 35 m PCF, for both out-coupling ratios. For

both PCF lengths, Figure 5.18 illustrates superior slope efficiency for the higher out-coupling ratio. Although this effect is less pronounced than in Figure 5.12(b), for the 18 m PCF cavity, the result is consistent with AS gain saturation as a result of secondary nonlinear effects caused by high intra-cavity AS powers. By extrapolating the measured data, it furthermore follows that the increase in threshold pump power, associated with the increased out-coupling ratio, becomes larger for longer nonlinear converters.

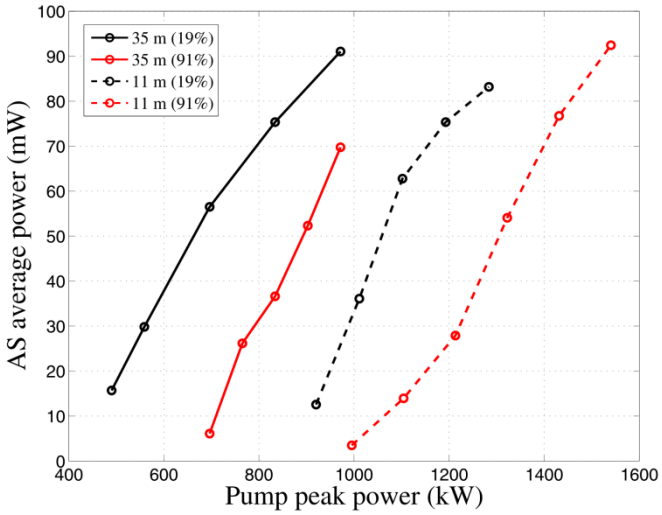

Figure 5.18: Comparison of the inferred total anti-Stokes average power at the output of 11 m and 35 m lengths of PCF, for OPO cavities configured for an out-coupling ratio of 19% (black) and 91% (red), respectively.

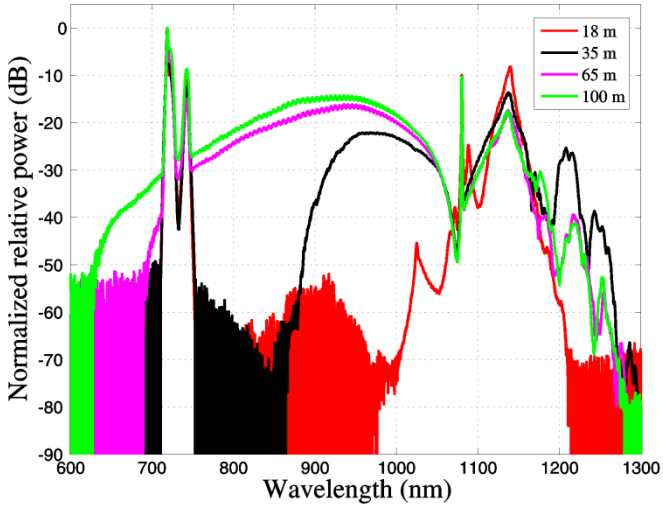

Figure 5.19: Comparison of OPO output spectra for four lengths of PCF-LMA8 with the cavity configured for 19 % out-coupling. The measurements were taken from the first tap-coupler at a pump power of ~1 kW (spectral resolution: 1 nm).

The findings related to Figure 5.18 are consistent with Figure 5.19, which shows an ever-increasing influence of competing nonlinearities, with increased PCF length. The spectra were measured from the first tap-coupler at the maximum pump power.

The results from Figures 5.17 through 5.19 are compatible with the hypothesis that a distributed, partially coherent gain may be responsible for the observed AS build-up. However, in contrast with the results achieved by Sloanes *et al.* for an OPA [21], the OPO conversion efficiency does not simply increase for longer nonlinear converters. Figure 5.20 shows the maximum pump-to-anti-Stokes average power conversion efficiency over the range of nonlinear converters for which measurement were made, irrespective of the out-coupling ratio used. Here, we find that the conversion efficiency has a sharp leading edge, peaking at 18 m, after which it slowly decays with fibre length. This result once again points to a scenario where the parametric gain benefits from the added PCF length, despite the influence of walk-off, but only up to the point where competing nonlinear processes such as SRS start to dominate as a result of their independence from phase-matching. Since Figure 5.14 gives the walk-off between the pump and first-order Raman Stokes as 0.4 ps/m, this effect is essentially negligible for the pump pulse widths employed here.

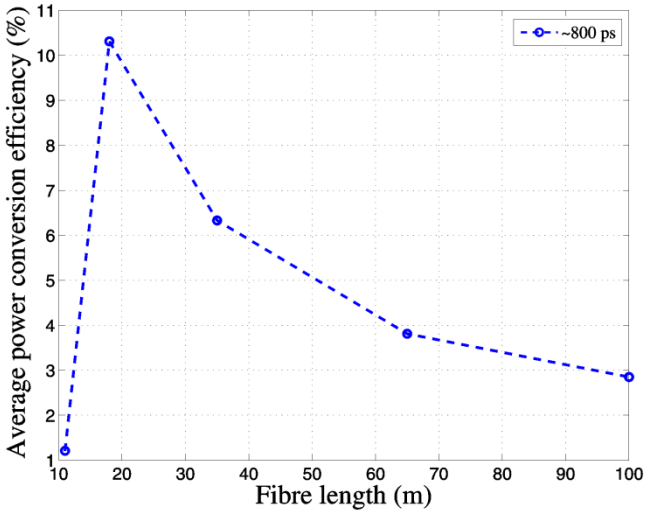

Figure 5.20: Influence of PCF-LMA8 length on OPO average power conversion efficiency, for a pump pulse width of approximately 800 ps.

The contrast with the results of Ref. [21] is not altogether surprising, seeing that the dynamics inside an oscillator is significantly more intricate. Furthermore, the fibre used

in their experiments gave phase-matching at a frequency-shift of ~54 THz, which would have resulted in a relatively large parametric bandwidth, in turn making the FWM process more competitive in a non-uniform fibre.

5.4.3 Intra-Cavity Filtering

During the course of investigating the spectral properties of the converted AS waves for different PCF lengths, an interesting observation was made. Figure 5.21 shows OPO output spectra, from a cavity configured for 91% out-coupling, for 18 m (red), as well as 11 m (blue) lengths of PCF. The 11 m result corresponds to the burst-mode-operated OPO experiment (refer to Section 5.4.2). A typical pump pulse and generated AS pulse for the 18 m and 11 m results are shown in Figures 5.15 and 5.22, respectively. Compared to the 18 m result, the AS pulse width associated with the 11 m result is relative large (~350 ps). This observation is consistent with a reduction in walk-off within the 11 m PCF. However, the increased AS broadening and AS-generated SRS for the 11 m result of Figure 5.21 are inconsistent with the reduced AS peak power (refer to Figure 5.17(b)) and the associated experimental setup's absence of a delay fibre. At first, this observation was believed to be related to the higher AS pulse energy, associated with the burst-mode result. However, further calculations revealed a more complex underlying dynamic.

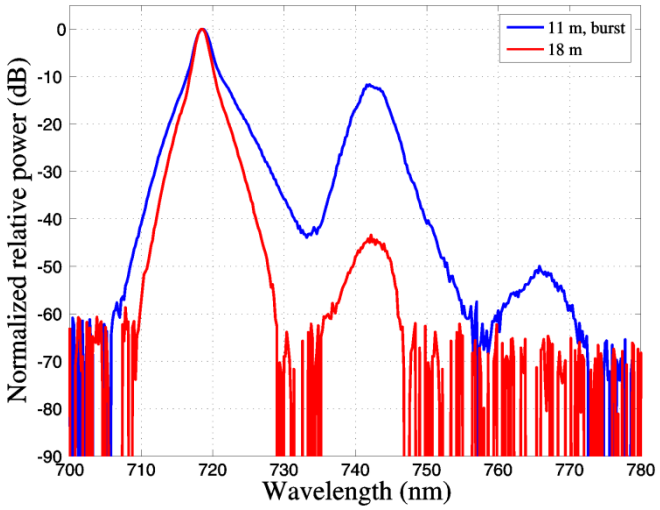

Figure 5.21: Comparison of the anti-Stokes output spectra generated for 18 m (red) and 11 m (burst-mode, blue) PCF-LMA8 lengths, at their respective maximum conversion efficiencies. The out-coupling ratio for both cases is 91% (spectral resolution: 1 nm).

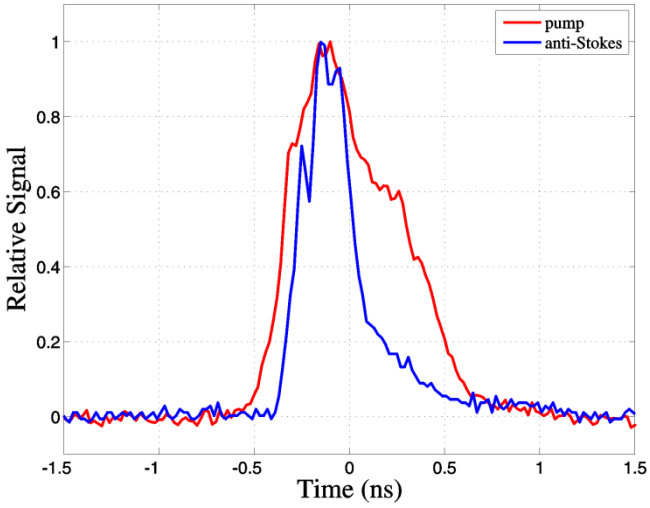

Figure 5.22: Comparison of the pump and anti-Stokes pulse widths for 11 m of PCF-LMA8, operated as a burst-mode OPO. A measurement bandwidth of 20 GHz and a sampling of 50 GSa/s were used.

The analysis started by calculating the round-trip group delay for both OPO cavities associated with the results in Figure 5.21. For this purpose, the group delay values in Figure 5.14 were used for the PCF, whilst the values for the remainder of the cavity were approximated using those of bulk silica. The round-trip group delay values were next employed to calculate the walk-off lengths between the AS and AS-generated SRS waves, for both cavities. Choosing these values as approximations to the effective interaction lengths (refer to equation 2.35), allowed us to calculate the AS-generated Raman gain for the respective cavities. The applicable AS peak power was approximated by path-averaging the value over the length of each cavity, taking account of the loss mechanisms throughout. This approach, which accounts for the differing AS pulse widths, PCF lengths, round-trip lengths and AS peak powers, successfully explained the observation of Figure 5.21 as follows. In the presence of a 75 m delay fibre (18 m result), the AS and AS-generated SRS experiences a relative round-trip delay of ~360 ps, which exceeds the AS pulse width for this case. Since the cavity is longer, the path averaged AS power is also lower, compared to the 11 m PCF cavity. The end result is a relatively increased SRS threshold. In contrast, the round-trip delay for a cavity round-trip length of 18.6 m is only ~60 ps, which is short compared to the AS pulse width of ~350 ps, and the SRS threshold is therefore significantly lowered. It is therefore clear that the length of the delay fibre presents a trade-off. On the one hand, its absence is desired, since it will contribute to AS-generated SRS for relatively

efficient cavities operating at acceptable thresholds. On the other hand, the delay fibre is seen to act as a temporal filter that increases the SRS threshold at the AS wavelength.

When the use of a short delay fibre is preferable, spectral filtering of the cavity feedback is seemingly the only appropriate alternative to temporal filtering, for the suppression of FWM AS-generated SRS. To explore this, a free-space band-pass filter was inserted into the cavity. The free-space path was constructed between the tap-couplers in the experimental setup of Figure 5.11. Figure 5.23 shows the transmission spectrum of the band-pass filter. It has a 3 dB bandwidth of 10 nm. The filter can be rotated with respect to the incident light to suppress AS-generated SRS by up to 30 dB (red dashed line), relative to the peak transmission (blue dashed line). Whilst this value is relatively small compared to the calculated suppression achieved through so-called temporal filtering (> 60 dB), these band-pass filters can be cascaded for greater effect.

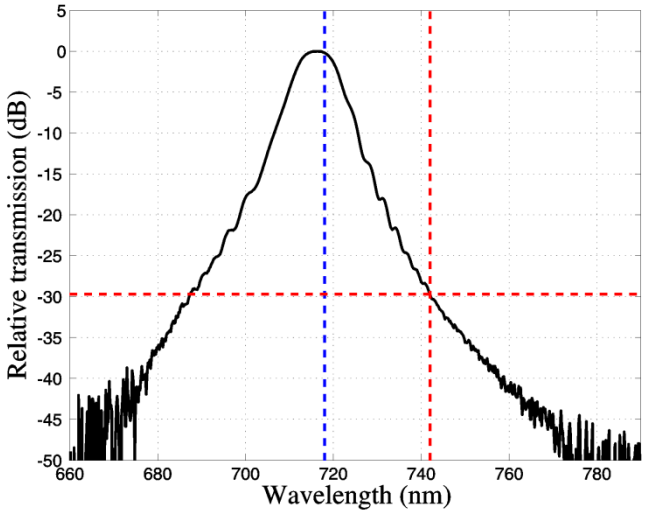

Figure 5.23: Transmission spectrum of the band-pass filter inserted into the OPO cavity feedback (spectral resolution: 1 nm). Red dashed lines indicate the position and relative suppression of the FWM anti-Stokes pumped first-order Raman Stokes.

One drawback of the device in Figure 5.23 is its insertion loss, measured as 2.2 dB. In combination with the requirement for a free-space path, for which we only managed a re-launch efficiency of 71%, the value for the loss effectively becomes 3.7 dB. This value is large and has a direct effect on the FWM conversion efficiency, in a cavity already characterised by relatively high losses (10-11 dB). For this reason, the free-space band-pass filter was used in a cavity with both tap-couplers configured for 10% out-coupling. The experimental setup furthermore employed a 35 m length of PCF

and a delay line of 65 m, thereby accommodating a comparison to the findings of Figure 5.17. This comparison is given in Figure 5.24 and shows an increase in the threshold pump power for the case with intra-cavity filtering, in accordance with the increased cavity loss. Importantly though, the slope efficiency for the case with filtering (red) exceeds that of the case without filtering (black), which merits the use of a spectral filter. It is however notable that the slope efficiency for the OPO employing spectral filtering is still lower than that of the corresponding OPO using an output-coupling of 91% (see Figure 5.18).

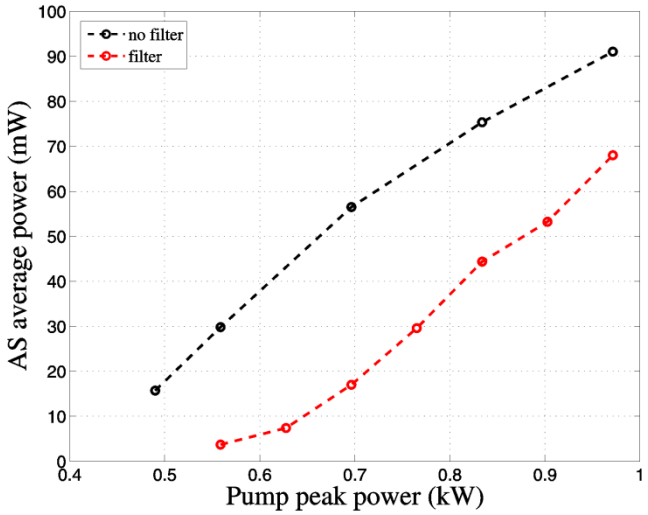

Figure 5.24: Comparison of the anti-Stokes average power for the case of a 35 m length of PCF-LMA8, in the absence (black) and presence (red) of an intra-cavity free-space spectral filter.

5.4.4 Influence of Pump Pulse Width

Up to this point, the results reported for the all-fibre pump-OPO system have only involved pump pulse widths ranging between 700 and 800 ps. It has however been illustrated that, depending on the length of the nonlinear converter, the pump pulse width can significantly influence the pulse width of the oscillating AS wave. Since changes to the pulse width affect the AS peak power, it is pivotal to the interplay between the various nonlinear processes within the OPO. For this reason, experiments were also performed for pump pulse widths shorter, and longer, than those of the preceding sections.

Figure 5.25 compares the generated AS average power from the PCF output, for three different pulse widths, for cavities containing 18 m and 35 m PCF lengths.

Whereas the results of (a) relate to an 18 m PCF cavity with an out-coupling ratio of 91%, the 35 m PCF cavity in (b) corresponds to an out-coupling ratio of 19%. The results are difficult to explain. Figure 5.25(a) shows similar values for the threshold and slope efficiency of the OPO for pump pulse widths of 750 ps and 1 ns. This result suggests that both pulse widths are large enough not to be influenced by walk-off and that an increase from 750 ps to 1 ns only leads to a reduction in pump peak power. This is in contrast to the result for 535 ps pump pulses, where the average power conversion efficiency appears to suffer from the influence of walk-off. Figure 5.25(b) gives a more varied response for the different pump pulse widths. The dominant performance for the case of a 1.33 ns pulse width, over the case of an 800 ps pulse width, is consistent with an increase in walk-off length from 17.4 m to 28.9 m. However, the influence of walk-off cannot explain the relative superior performance for the case of 530 ps pump pulses (L_W = 11.5 m). It is furthermore surprising to find a contrast between the comparative (extrapolated) threshold pump powers for Figures 5.25(a) and (b). The results in (b) suggest that the threshold pump power remains roughly constant in the presence of walk-off, and that walk-off only leads to changes in the slope efficiency. However, for the case of (a), the result for 535 ps pump pulses is characterised by a significantly higher threshold pump power. Clearly, the differences between the two cases cannot simply be explained by the higher cavity round-trip loss associated with (a).

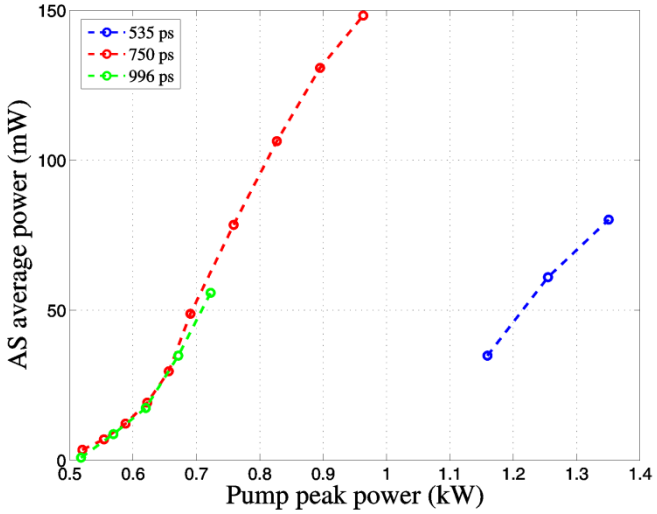

(a)

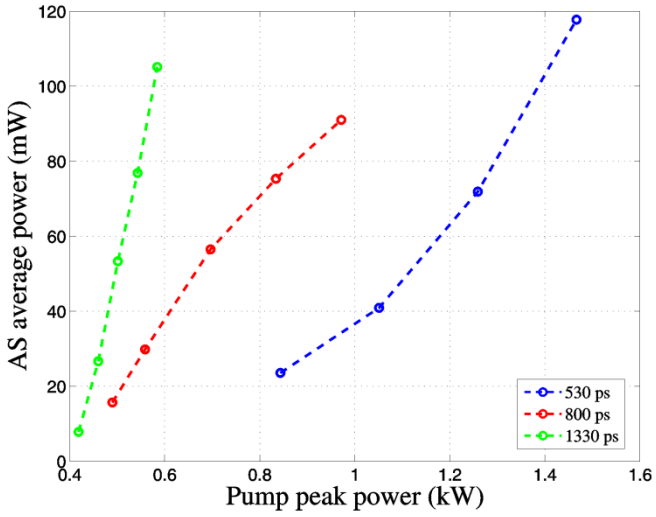

(b)

Figure 5.25: Anti-Stokes average power, as a function of pump peak power, for three values of the pump pulse width, for the cases of (a) 18 m and (b) 35 m of PCF-LMA8.

Figure 5.26 shows the maximum pump-to-anti-Stokes average power conversion efficiency, for pump pulses shorter and longer than those of the preceding sections, over the range of nonlinear converters for which measurement were made. The results show the values for optimum OPO performance, irrespective of the out-coupling ratio used. The corresponding result for ~800 ps pump pulses is included for comparison (refer to Figure 5.20). According to Figure 5.26, the AS conversion efficiencies for ~500 ps and >1 ns pulses have their optimal values for a PCF length of 35 m. It furthermore follows that OPOs using PCF lengths longer than (at most) 60 m, favour larger pump pulse widths. Figure 5.26 shows peak conversion efficiencies for ~800 ps and >1 ns pump pulses at fibre lengths roughly equal to their walk-off lengths. Results for both pulse widths indicate a gradual decay for longer lengths of PCF. This is in contrast with the results for 500 ps pump pulses, where the conversion efficiency at 18 m is less than that of 35 m. At the time of writing, there is no explanation for this perceived inconsistency in the results. It may be possible that the increase in the parametric bandwidth, due to the increased pump peak powers, results in a scenario where a greater percentage of the PCF contribute to AS build-up. Such a scenario would warrant experimental investigation for additional pump pulse widths and PCF lengths, about the values associated with the peak of the black curve in Figure 5.26.

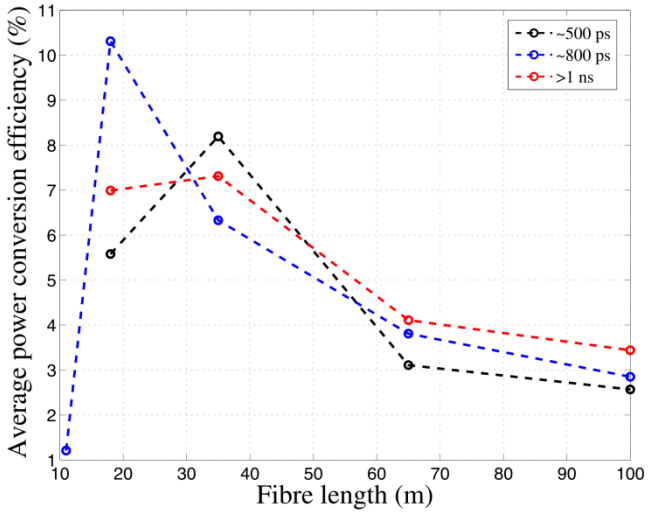

Figure 5.26: Influence of PCF-LMA8 length on OPO average power conversion efficiency, for pump pulse widths of approximately 500 ps (black), approximately 800 ps (blue) and larger than 1 ns (red).

5.5 Summary

In this chapter, I have investigated fibre optical parametric oscillators, using photonic crystal fibre as the nonlinear converter, as a source for spectrally distant wavelength conversion. In addition to analysing the PCF in terms of its properties as a nonlinear converter, several experiments were performed, aimed specifically at studying the performance of the fibre OPO under various conditions.

Initial experiments based on a single pass through the nonlinear converter, using free-space coupling optics, gave very low conversion efficiencies, but highlighted the requirement for appropriate spectral discrimination as well as seeding. Following the construction of a synchronously pumped fibre OPO, pump-to-anti-Stokes in-fibre average power conversion efficiencies as high as 4% was demonstrated. Although output spectra still showed signs of supercontinuum generation, as a result of fibre longitudinal inhomogeneities, cascaded SRS generated by the FWM AS provided encouragement.

Secondary experiments focussed on an all-fibre pump-OPO system and a pump source with superior temporal stability. This system was employed to study the dependence of the OPO conversion efficiency on the out-coupling ratio of the cavity, the length of the nonlinear converter as well as the pump pulse duration. It was found that a higher out-coupling ratio is important for the suppression of so-called secondary

nonlinear effects, pumped by the FWM AS. However, drawbacks included higher cavity losses, and subsequently, higher pump threshold power requirements. Experiments on OPOs using various nonlinear converter lengths demonstrated similar threshold pump powers for low values of the out-coupling ratio. In contrast, high out-coupling ratios lead to threshold values that were inversely proportional to the PCF length. The latter case is consistent with the expectation of a constant threshold-power-fibre-length product, but is somewhat surprising considering that the system is subject to pulse walk-off and longitudinal inhomogeneities. A tentative conclusion was that the longitudinal inhomogeneity in the PCF-LMA8 is characterised by a high spatial frequency. It was furthermore concluded that the OPO shows an increased sensitivity to competing nonlinearities as the cavity loss increases. The performance of the OPO, employing different lengths of PCF, was also evaluated for different pump pulse widths. The highest pump-to-anti-Stokes conversion efficiency of 10.3%, over a frequency separation of 142 THz, was found for pump pulses of 800 ps duration and a PCF length of 18 m. To the best of our knowledge, this result constitutes a record for all-fibre OPOs operating at frequency-shifts of this magnitude. In contrast, pump pulse durations of 500 ps and >1 ns gave their best conversion efficiencies for a PCF length of 35 m. Whilst the pump-to-anti-Stokes average power conversion efficiency was found to depend on the walk-off length between the pump and Stokes waves, for a specific pump pulse duration, the case of 500 ps pulses proved to be the exception. The exact reason for this remains unknown. However, it is likely due to the fact that the short pulse has a higher pump peak power, in combination with partially coherent build-up in segments of the full PCF length.

Experiments using the all-fibre setup furthermore highlighted the importance of some mechanism for intra-cavity filtering. As such, it was discovered that the delay line, used for the purpose of synchronous pumping, can act as a temporal filter through the process of dispersion. Since the delay line also leads to FWM anti-Stokes-generated SRS for the case of a sufficiently low out-coupling ratio, its length represents a trade-off. Measurements using a free-space spectral filter suggest that it can be used as an alternative to temporal filtering, should a short delay line be preferred. High insertion loss values, however prevent this from being a valid alternative in the current free-space configuration.

Current limitations for an efficient fibre OPO, operating at over ~140 THz, employing relatively low pump powers of around 1 kW from an all-fibre pump source, include the following. First and foremost is the longitudinal homogeneity of the fibre converter. As the parametric bandwidth associated with frequency-separations of 140 THz, at pump powers of 1 kW, is only a fraction of a nanometre, perturbations in the fibre dimensions have very strict tolerances. Although it may be possible to engineer the fibre around this limitation, it has never been demonstrated. This topic will be discussed in detail in the following chapter. Other limitations are those associated with competing nonlinearities like SRS, SPM and XPM. Care has to be taken to minimize SRS originating within the all-fibre pump source, since it can easily dominate over FWM, particularly in the presence of fibre longitudinal inhomogeneity. SPM and XPM degradation of the pump wave can for instance result in a broadened pump linewidth, which may exceed the parametric bandwidth, with similar consequences. A further requirement for an efficient OPO is cavity loss. Although competing nonlinearities can be classified as a loss mechanism, the word loss in this context refers to absorption and scattering losses within couplers and splices. A possible route to eliminating the severity of cavity losses is to employ a linear cavity fibre OPO, using fibre Bragg-gratings

5.6 References

[1] J.C. Knight, T.A. Birks, P. St. J. Russell and D.M. Atkin, "All-silica single-mode optical fiber with photonic crystal cladding," *Opt. Lett.*, vol. 21, no. 19, pp. 1547-1549 (1996).

[2] J.D. Harvey, R. Leonhardt, S. Coen, G.K.L. Wong, J.C. Knight, W.J. Wadsworth and P. St. J. Russell, "Scalar modulation instability in the normal dispersion regime by use of a photonic crystal fiber," *Opt. Lett.*, vol. 28, no. 22, pp. 2225-2227 (2003).

[3] W.J. Wadsworth, N. Joly, J.C. Knight, T.A. Birks, F. Biancalana and P .St. J. Russell, "Supercontinuum and four-wave mixing with Q-switched pulses in endlessly single-mode photonic crystal fibers," *Opt. Express*, vol. 12, no. 2, pp. 299-309 (2004).

[4] D. Nodop, C. Jauregui, D. Schimpf, J. Limpert and A. Tünnermann, "Efficient high-power generation of visible and mid-infrared light by degenerate four-wave mixing in a large-mode-area photonic-crystal fiber," *Opt. Lett.*, vol. 34, no. 22, pp. 3499-3501 (2009).

[5] L. Lavoute, J.C. Knight, P. Dupriez and W.J. Wadsworth, "High power red and near-IR generation using four wave mixing in all integrated fiber laser systems," *Opt. Express*, vol. 18, no. 15, pp. 16193-16205 (2010).

[6] W. Margulis and U. Österberg, "Four-photon fiber laser," *Opt. Lett.*, vol. 12, no. 7, pp. 519-521 (1987).

[7] G.P. Agrawal, Nonlinear Fiber Optics, 3rd ed., Academic Press, 2001.

[8] S.G. Murdoch, R. Leonhardt and J.D. Harvey, "Polarization modulation instability in weakly birefringent fibers," *Opt. Lett.*, vol. 20, no. 8, pp. 866-868 (1995).
[9] S. Coen, A.H.L. Chau, R. Leonhardt, J.D. Harvey, J.C. Knight, W.J. Wadsworth and P. St. J. Russell, "Supercontinuum generation by stimulated Raman scattering and parametric four-wave mixing in photonic crystal fibers," *J. Opt. Soc. Am. B*, vol. 19, no. 4, pp. 753-764 (2002).
[10] M.E. Marhic, Fiber Optical Parametric Amplifiers, Oscillators and Related Devices, Cambridge University Press, 2008.
[11] C.J.S. De Matos, J.R. Taylor and K.P. Hansen, "Continuous-wave, totally fiber integrated optical parametric oscillator using holey fiber," *Opt. Lett.*, vol. 29, no. 9, pp. 983-985 (2004).
[12] J.E. Sharping, M.A. Foster, A.L. Gaeta, J. Lasri, O. Lyngnes and K. Vogel, "Octave-spanning, high-power microstructure-fiber-based optical parametric oscillators," *Opt. Express*, vol. 15, no. 4, pp. 1474-1479 (2007).
[13] K. Cook, C. Xiong and W.J. Wadsworth, "Enhanced four-wave mixing and parametric oscillator in photonic crystal fiber," *J. Opt. A: Pure Appl. Opt.*, vol. 9, pp. 1095-1099 (2007).
[14] E.A. Golovchenko and A.N. Pilipetskii, "Unified analysis of four-photon mixing, modulation instability, and stimulated Raman scattering under various polarization conditions in fibers," *J. Opt. Soc. Am. B*, vol. 11, no. 1, pp. 92-101 (1994).
[15] Q. Lin and G.P. Agrawal, "Effects of polarization-mode dispersion on fiber-based parametric amplification and wavelength conversion," *Opt. Lett.*, vol. 29, no. 10, pp. 1114-1116 (2004).
[16] H. Liu, K. Xu, J. Wu, W. Li, Y. Li, X. Hong, Y. Zuo, J. Lin and Y. Dai, "Synthesis of flat and broadband parametric gain by idler loss in optical fiber," *OSA/CLEO 2011*, JThB80 (2011).
[17] J.S.Y. Chen, S.G. Murdoch, R. Leonhardt and J.D. Harvey, "Effect of dispersion fluctuations on widely tunable optical parametric amplification in photonic crystal fibers," *Opt. Express*, vol. 14, no. 20, pp. 9491-9501 (2006).
[18] Information available at: www.discoverysemi.com
[19] Information available at: : http://search.newport.com
[20] Information available at: www.tek.com/oscilloscope
[21] T. Sloanes, K. McEwan, B. Lowans and L. Michaille, "Optimisation of high average power optical parametric generation using a photonic crystal fiber," *Opt. Express*, vol. 16, no. 24, pp. 19724-19733 (2008).
[22] A. Gershikov, E. Shumakher, A. Willinger and G. Eisenstein, "Fiber parametric oscillator for the 2 μm wavelength range based on narrowband optical parametric amplification," *Opt. Lett.*, vol. 35, no. 19, pp. 3198-3200 (2010).
[23] M. Farahmand and M. De Sterke, "Parametric amplification in presence of dispersion fluctuations," *Opt. Express*, vol. 12, no. 1, pp. 136-142 (2004).
[24] A. Malinowski, K.T. Vu, K.K. Chen, J. Nilsson, Y. Jeong, S. Alam, D. Lin and D.J. Richardson, "High power pulsed fiber MOPA system incorporating electro-optic modulator based adaptive pulse shaping," *Opt. Express*, vol. 17, no. 23, pp. 20927-20937 (2009).

Chapter 6

Dispersion-Engineered PCF for Enhanced Parametric Bandwidth

Chapters 4 and 5 concluded that the conversion efficiency of large frequency-shift FWM in real fibres is severely limited by inadequate phase-matching. This was attributed primarily to the presence of longitudinal fluctuations in the fibre dimensions and refractive index profile. Particularly in experiments employing PCF nonlinear converters, this mechanism is often cited as the primary reason for discrepancies between theoretically predicted and experimentally observed conversion efficiencies. The parametric bandwidth, defined as the frequency range over which the phase mismatch remains sufficiently small, plays an important role in determining how sensitive a FWM process will be to longitudinal non-uniformities. Traditionally, progress in large frequency-shift FWM, pumped around 1 μm, had to rely on the use of higher peak powers and shorter lengths of PCF to increase the parametric bandwidth [1] – [3]. Since the use of high pump peak powers in a short fibre can preclude the implementation of an all-fibre solution, it is worth considering alternative methods of increasing the parametric bandwidth.

To this end, the current chapter investigates the possibility of increasing the parametric bandwidth through design of the PCF dispersion. The approach expands on the theoretical work of Lægsgaard who performed a similar analysis for single-material silica PCF [4], [5]. Here, it was shown that specific PCF designs lead to phase-matched FWM between group-velocity matched Stokes (down-converted frequency) and anti-

Stokes (up-converted frequency) waves, for pump wavelengths around 800 nm. We illustrate that this procedure for enhancing the parametric bandwidth can be extended to other pump wavelengths, particularly around 1 μm, by doping the core region of the silica PCF with germania. By exploring the parameter space, it is shown that various designs of this type can achieve a desired parametric bandwidth and frequency-shift. In addition to a decrease in sensitivity to longitudinal fluctuations, an increased parametric bandwidth leads to an increased pump acceptance bandwidth, which offers greater flexibility in the pump source technology available to large frequency-shift FWM applications.

The chapter is structured as follows. Sections 6.1 and 6.2 provide details on the fibre design methodology and solutions from the analysis, respectively. The stability of the general fibre design is considered in Section 6.3, where the discussion explores relevant issues such as the absolute and relative manufacturing tolerances. Here, as well as in the summary of Section 6.4, the question of whether the proposed design can reduce the severity of longitudinal inhomogeneities, is answered.

6.1 Numerical Approach

As a starting point, we consider the expression for the small-signal parametric gain bandwidth (also refer to Chapter 2.3.2) [6]:

$$\Delta\Omega = 2\left[\left(\frac{\pi}{L}\right)^2 + (\gamma P)^2\right]^{\frac{1}{2}} \frac{d\Omega}{d(\Delta\beta)_{\Delta\beta=0}} \tag{6.1}$$

The term in square brackets is the so-called mixing bandwidth and γ, L and P denote the nonlinear coefficient of the fibre, the fibre length and the applied pump power, respectively. The derivative outside the brackets depends on the functional relationship between the phase mismatch ($\Delta\beta$) and the frequency-shift (Ω), for which the following definitions hold (refer to Chapter 2.3):

$$\Delta\beta = \beta(\omega_s) + \beta(\omega_a) - 2\beta(\omega_p) \tag{6.2}$$

$$\Omega = \omega_p - \omega_s = \omega_a - \omega_p \tag{6.3}$$

As usual, β denotes the mode propagation constant associated with a particular angular frequency ω, where a subscript assignment of p, s or a indicates the pump wave, Stokes wave or anti-Stokes wave, respectively.

The parametric bandwidth defines the frequency range over which the phase mismatch is sufficiently small for the parametric gain to stay within (slightly less than) half its peak value. From the mixing bandwidth in equation 6.1 it is clear that the parametric bandwidth can be increased through an increase in pump power and a decrease in fibre length. However, an alternative method for increasing the parametric bandwidth is afforded by the derivative in equation 6.1. Although the fibre dispersion can be modified to a certain extent, through the application of tension, the controlled implementation of this technique is complicated and potentially expensive [7]. Consequently, the derivative in equation 6.1 is fixed for a given fibre and pump wavelength, and can only be optimised through appropriate design of the fibre dispersion prior to fabrication.

The approach whereby the fibre dispersion can be optimised was demonstrated in the theoretical work of Lægsgaard, where the author explored the parameter space of regular triangular lattice single-material silica PCF [4]. Lægsgaard concluded that with the proposed method, the dispersion required for an optimum parametric bandwidth can only be achieved for a specific range of pump wavelengths, which excluded those in excess of 1 μm. To overcome this limitation and to find similar solutions at pump wavelengths relevant to the work of this thesis, the current investigation focuses on silica PCF for which the core region is doped with germania. Studies on FWM in germania-doped PCF have been reported, most notably by Yatsenko *et al.*, who commented on the implications for dispersion engineering [8]. These fibres have also been fabricated by several groups [9], [10] and in some cases have even been demonstrated as sources for efficient FWM [11].

The PCF structure considered in this investigation is given in Figure 6.1. As for single-material PCF, the structure is characterised by the pitch (Λ) and diameter (d_h) of the air-holes in the cladding. Additionally, the core region with corresponding diameter (d_c), is assumed to be uniformly doped with germania. Both the doping-concentration and the diameter of the doped core will affect the fibre dispersion, with different

wavelength dependencies. Therefore, GeO_2-doping brings two additional degrees of freedom to the fibre design.

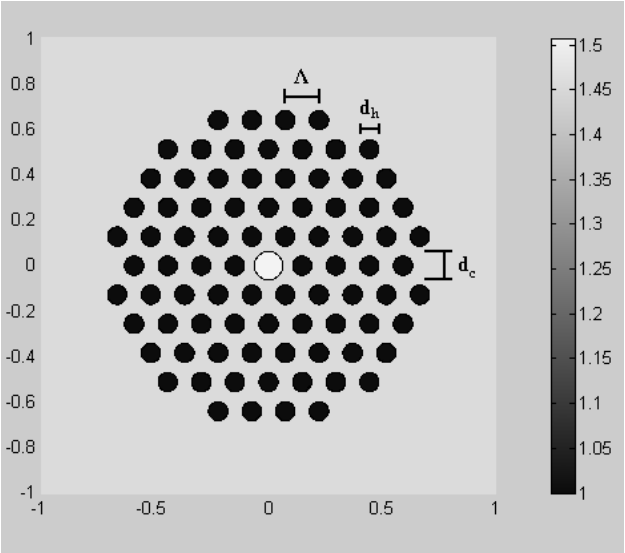

Figure 6.1: Structure of the GeO_2-doped silica PCF. The structure is characterized by the pitch (Λ) and diameter (d_h) of the air-holes, as well as the core diameter (d_c) and GeO_2-doping concentration.

The investigation into the dispersion properties of the structure in Figure 6.1 was conducted using a commercial finite-element-method package, *COMSOL* (refer to Chapter 2.1). Values for the material dispersion of GeO_2-doped silica at arbitrary doping concentrations were calculated using the Sellmeier equation and coefficients from Fleming [12]. The material refractive-index values were then incorporated into COMSOL, from which the mode propagation constants over the wavelength range of interest (700 – 2100 nm) were calculated. All PCFs in this study incorporated five rings of air-holes.

The calculated mode propagation constants allowed for the direct evaluation of the phase mismatch, according to equation 6.2. For the purpose of keeping the discussion general, the nonlinear contribution was excluded from the calculation of the phase mismatch (also refer to equation 2.57). Since the effect of the nonlinear contribution, at a given pump power, is simply to impose an offset on the calculated phase mismatch, it is straightforward to apply the general results to any desired pump power. Furthermore, while we only consider the fundamental spatial mode of the fibre, higher-order modes may well allow for additional phase-matching combination

6.2 Phase-Matching Results

The dispersive properties required for the optimisation of the parametric gain bandwidth can be explained at the hand of Figure 6.2. In order to facilitate a comparison to the single-material silica PCF, used in the experiments of Chapter 5, the pump wavelength was chosen as 1080 nm. Red curves represent the results for a GeO_2-doped PCF characterised by Λ=2.426 µm, d_h/Λ=0.49, d_c/d_h=0.5 and a doping concentration of 35% (mol). Similarly, blue curves show the comparative results for the silica PCF characterised by Λ=5.6 µm and d/Λ=0.49.

Figure 6.2(a) gives the calculated phase mismatch as a function of frequency-shift. The fibre parameters for the GeO_2-doped PCF were chosen to yield a phase-matched frequency-shift of ~130 THz, which is comparable to that of the single-material silica PCF. For the silica PCF the phase mismatch varies rapidly with frequency-shift about its zero value. This is in contrast to the GeO_2-doped PCF, where the phase mismatch curve reaches a turning point as it approaches the zero-mismatch value. The net result is a relatively slowly varying phase mismatch, which is responsible for an extended parametric bandwidth, in accordance with equation 6.1.

The relative differences in Figure 6.2(a) can be explained at the hand of Figure 6.2(b), showing the chromatic dispersion and group delay of the relevant fibres. Differences in the chromatic dispersion (solid lines) are pronounced on the long-wavelength side of the spectrum and are a result of the changing influence of the germania-doping in the core of the PCF (refer to Chapter 2.1.4). The group delay (dashed lines) displays a decreased slope for the GeO_2-doped PCF in the vicinity of 2 µm, as is evident from the chromatic dispersion which converges on a second ZDW. This effectively enables matching of the group velocity (GV) for the phase-matched Stokes and anti-Stokes waves of the germania-doped PCF, resulting in the behaviour seen in Figure 6.2(a).

Assuming a value of γ=4 $(W\ km)^{-1}$, which is expected for the all-silica PCF of Figure 6.2, and choosing a fibre length and pump power of 5 m and 1 kW, equation 6.1 may be evaluated for both fibres. Based on the calculated values for the derivative, the parametric bandwidth for the germania-doped PCF is found to be ~11.7 THz, compared to ~83 GHz for the all-silica PCF. Note that these numbers neglect the effect of an

increased γ-value, due to the larger nonlinear refractive index and smaller effective mode area, associated with the GeO_2-doped PCF [13].

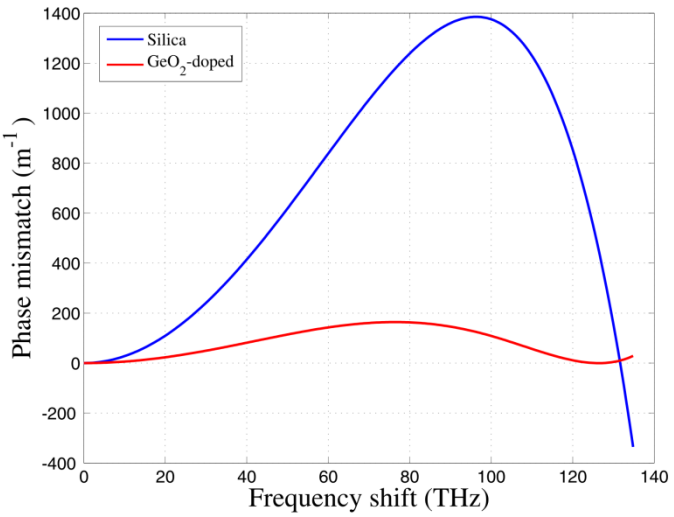

(a)

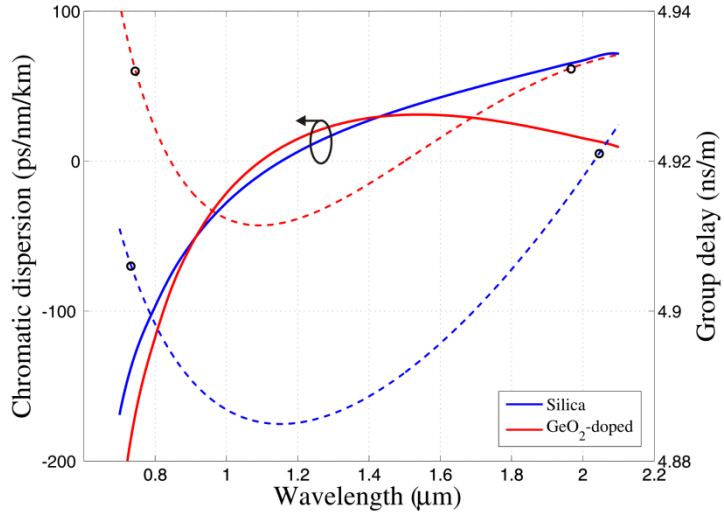

(b)

Figure 6.2: Comparison of the (a) phase mismatch (λ_p=1080 nm) as well as (b) chromatic dispersion and group delay of a commercial all-silica PCF (Λ=5.6 μm, d/Λ=0.49) and a GeO_2-doped silica PCF (Λ=2.426 μm, d_h/Λ=0.49, d_c/d_h=0.5, 35% (mol)).

Figure 6.3 expands on the results in Figure 6.2 and shows how the phase-matched Stokes and anti-Stokes wavelengths, for the silica PCF and GeO_2-doped PCF, depend on the chosen pump wavelength. In the absence of the nonlinear contribution to the phase mismatch, both fibres only have phase-matching solutions at frequency-shifts greater than zero when pumped in their respective normal-dispersion regimes (λ_p>1154 nm and λ_p>1096 nm for the silica and GeO_2-doped PCFs, respectively). However,

whereas the silica PCF only has a single pair of phase-matching solutions within the wavelength region of interest, the germania-doped PCF show two pairs of solutions in the vicinity of 1080 nm. The inset to Figure 6.3 clearly shows the convergence of the two pairs of phase-matching solutions at a pump wavelength of ~1080 nm, where the resultant Stokes and anti-Stokes waves are GV-matched.

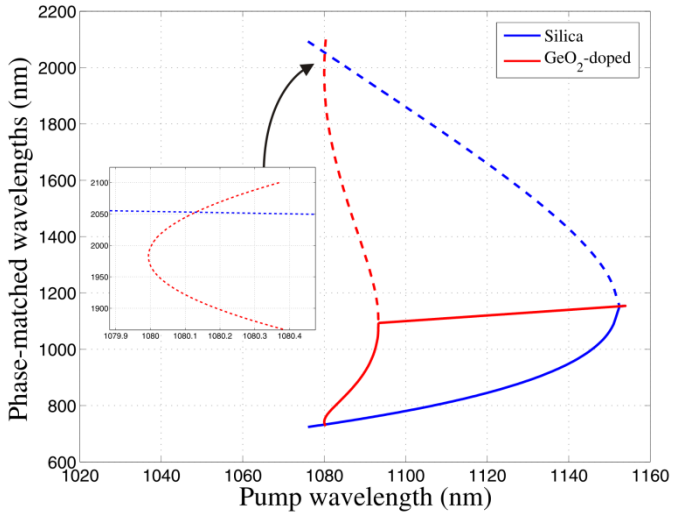

Figure 6.3: Phase-matched wavelengths for generated Stokes (dashed lines) and anti-Stokes (solid lines) waves as a function of pump wavelength, for the fibres of Figure 6.2.

The GeO_2-doped PCF of Figures 6.2 and 6.3 is only one example of a combination of design parameters that satisfy the criteria for an optimised parametric bandwidth. The example was chosen because the GV-matched phase-matched frequency-shift is comparable to that of an all-silica PCF of practical interest. However, as was the case for the solutions demonstrated in the work by Lægsgaard for silica PCF, combinations of design parameters may be found for similar solutions over a wide range of frequency-shifts. To this end, we systematically considered how these solutions depend on the GeO_2-doped PCF design parameters. The results will be discussed at the hand of Table 6.1.

Table 6.1 gives the design parameter values for a range of GeO_2-doped PCFs that lead to the solutions of interest for a pump wavelength of 1080 nm. Also given are the corresponding parameters for an all-silica PCF, at a pump wavelength of 800 nm, as in Ref. [4]. The tabled parameters for the fibres designated *PCF 1-5* and *Silica* are presented at the origin of Figure 6.4(a). The figure shows how the GV-matched phase-

matching solutions for each of the designated fibres depend on relative changes in the tabled structural parameters (Λ and d_h/Λ). Since d_c is coupled to d_h in the calculated results, its value effectively also varies by the percentage indicated on the figure's x-axis (apart from *Silica*). Figure 6.4(b) displays the phase-matched frequency-shift values associated with the GV-matched solutions in Figure 6.4(a). Here, the tabled parameters for the applicable fibres correspond to the lowest-valued phase-matched frequency-shifts.

Designation	**% (mol)**	**d_c/d_h**	**d_h/Λ**	**Λ (µm)**
Silica	-	-	0.550	1.282
PCF 1	35	2	0.467	1.597
PCF 2	35	1.5	0.524	1.518
PCF 3	35	1	0.570	1.538
PCF 4	35	0.75	0.540	1.705
PCF 5	35	0.5	0.348	2.230
PCF 6	45	1	0.630	1.440
PCF 7	25	1	0.490	1.786
PCF 8	15	1	0.365	2.097

Table 6.1: Parameter values for different designs of GeO_2-doped PCFs that yield group velocity matched phase-matching solutions, for a pump wavelength of 1080 nm. The parameters for the corresponding solutions in an all-silica PCF is also shown, for a pump wavelength of 800 nm. Note that the last two columns only indicate the solution parameters for the lowest-valued frequency-shift (origin in Figures 6.4(a) and 6.5(a)).

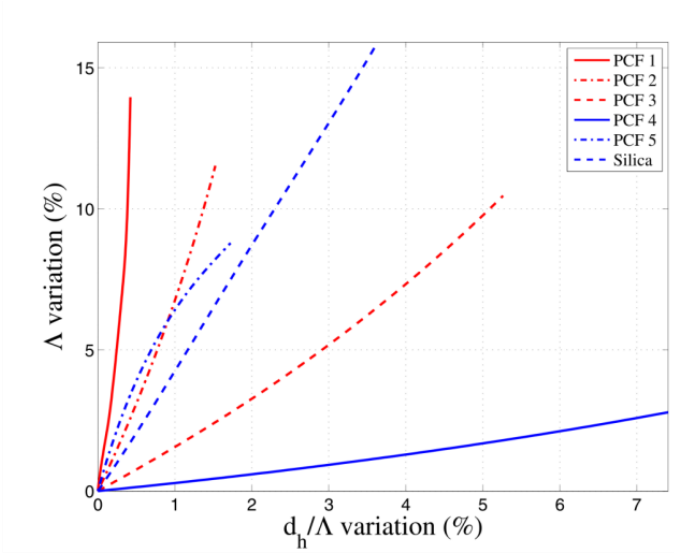

(a)

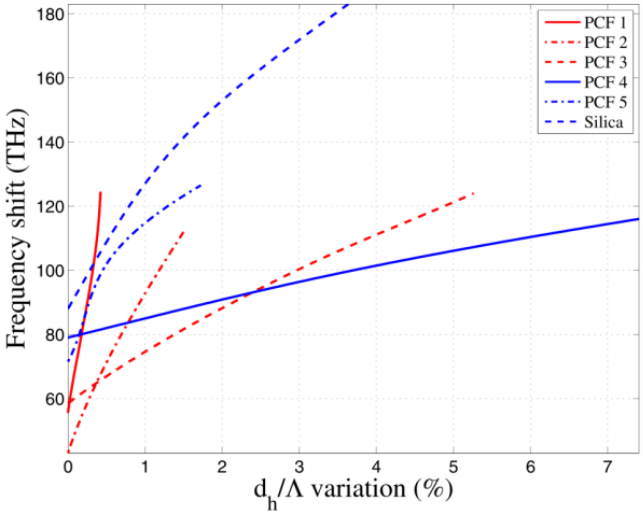

(b)

Figure 6.4: Constant GeO_2-doping concentration of 35% (mol). (a) Group velocity matched phase-matching solutions for *PCF 1-5* (λ_p=1080 nm), as well as that of an all-silica PCF (λ_p=800 nm), for the parameters given in Table 6.1. (b) Frequency-shifts corresponding to the solutions in (a).

From Figure 6.4 and Table 6.1 it is evident that the distribution of the solutions has a strong dependence on the relative diameter of the doped region. The frequency-shift associated with the solutions of *PCF 1*, for example, shows a very high sensitivity to variations in the normalised air-hole diameter. However, the associated variation in the pitch of the air-holes is large. This is in contrast to PCF 4, for which the frequency-shift varies gradually over the range of values for d_h/Λ, whilst the corresponding values of Λ only covers a relative change of 3%.

Figure 6.5 similarly compares *PCF 3* and *PCF 6-9* to each other and to the *Silica* PCF. In contrast to the fibres in Figure 6.4, the fibres compared here have the same ratio for d_c/d_h, whilst their doping concentration are different. Figure 6.5(a) gives the distribution of the solutions, whilst the associated frequency-shift values can be found in Figure 6.5(b). The solutions show a strong dependence on the doping concentration, but display a relatively predictable trend wherein a higher doping concentration leads to solutions at lower values of Λ and higher values of d_h/Λ, and subsequently d_c/Λ (refer to Table 6.1). As for Figure 6.4, the most important aspect of Figure 6.5 is the fact that several parameter combinations can be used to achieve an optimised parametric gain bandwidth at a desired frequency-shift. This enables the fibre designer to choose the most appropriate design for a particular application.

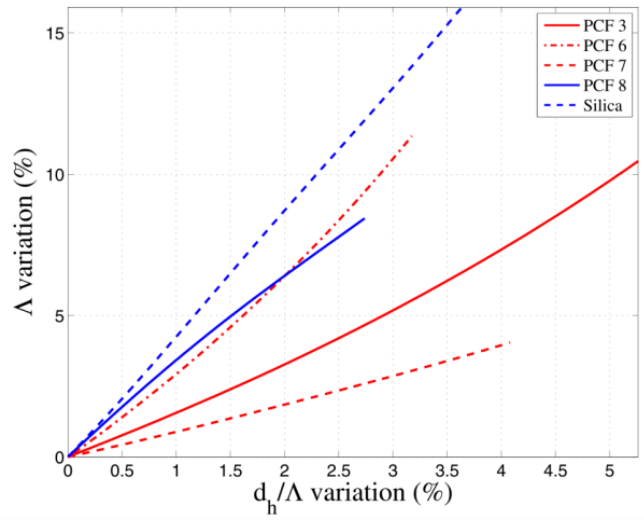

(a)

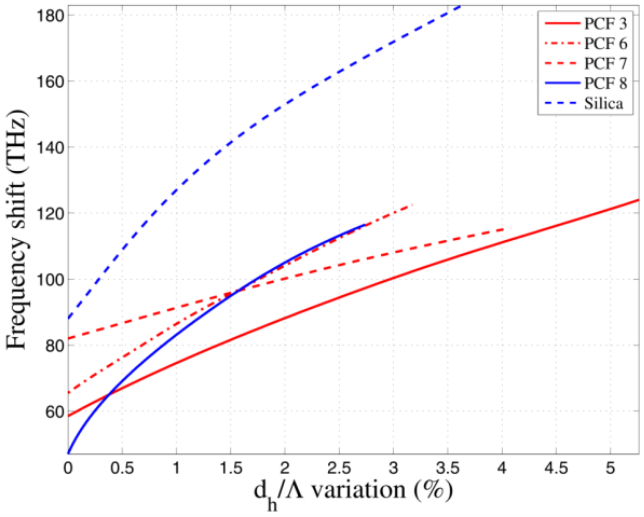

(b)

Figure 6.5: Constant d_c/d_h ratio. (a) Phase and group velocity matched solutions for *PCF 3* and *PCF 6-9* (λ_p=1080 nm), as well as that of an all-silica PCF (λ_p=800 nm), for the parameters given in Table 6.1. (b) Frequency-shifts corresponding to the solutions in (a).

6.3 Additional Considerations

An important consideration for the choice of a particular GV-matched phase-matching design is the associated sensitivity to variations in the structural parameters. To explore this aspect, the current section considers how the phase-matched frequency-shift and parametric bandwidth varies about the GV-matched solutions of *PCF 3* in Figures 6.4 and 6.5 (d_c/d_h=1 and 35% (mol))

Figure 6.6(a) considers solutions about Λ=1.6175 and d_h=0.95 and shows how the lowest-valued phase-matched frequency-shift changes as Λ and d_h (as well as d_c) depart from the reference values. Empty space on the graph indicates parameter combinations that do not allow for phase-matching within the wavelength region of interest. For the parameter combinations that do result in phase-matching, two distinct regions can be identified. The first region includes the origin and contains the GV-matched solutions on its left extremity. As the value of d_h (and d_c) increases, or the value of Λ decreases, relative to those of the GV-matched solutions, the lowest-valued phase-matched frequency-shift decreases. A second higher-valued phase-matched frequency-shift simultaneously increases, but is not displayed. For even larger departures from the GV-matched solutions, the lowest-valued phase-matched frequency-shift becomes zero, leaving only an increasing phase-matched frequency-shift. This transition region is presented by the hatched strip in Figure 6.6(a), since the steep gradient of the phase-matched frequency-shift made it very hard to accurately resolve the behaviour within this region. The remaining phase-matched frequency-shift now gives rise to the second phase-matching region, extending diagonally upwards from the lower left-hand corner. The right-hand side extremity of the second phase-matching region is defined primarily by the limits of the considered wavelength region, due to the large frequency-shifts associated with these phase-matching solutions. In contrast to the first phase-matching region, the frequency-shifts of the second region increases as d_h (and d_c) is increased, or Λ is decreased.

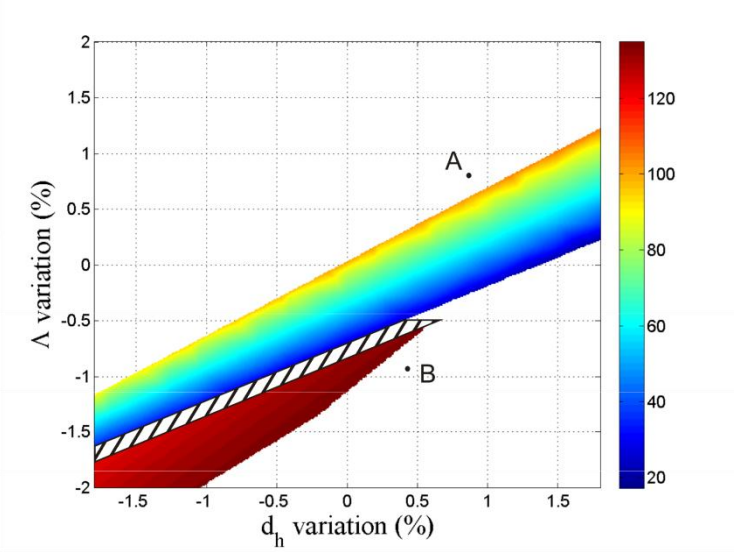

(a)

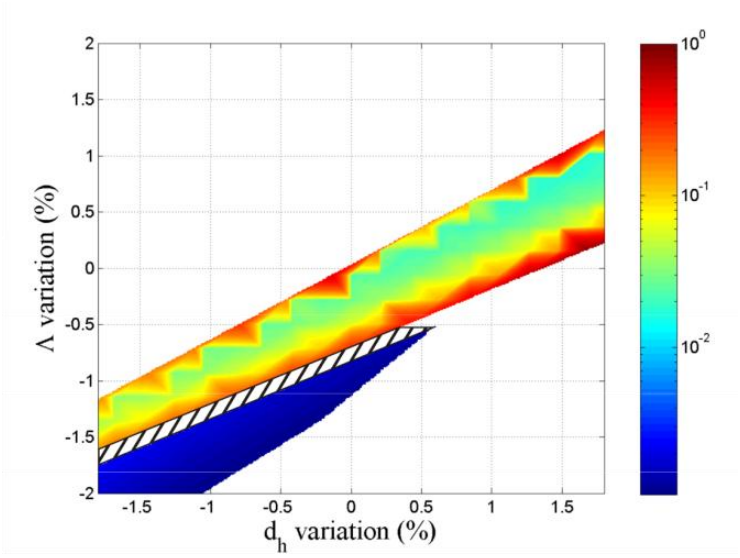

(b)

Figure 6.6: Phase-matching analysis of *PCF 3* in Table 6.1 (d_c/d_h=1, 35% (mol)), about Λ=1.6175 and d_h=0.95. (a) Phase-matched frequency-shift in units of THz (λ_p=1080 nm) as a function of percentage variation in Λ and d_h (and subsequently d_c), with respect to the reference values. (b) Corresponding normalised bandwidth for the phase-matched frequency-shift values in (a).

Figure 6.6(b) shows the normalized parametric bandwidth associated with the frequency-shifts in Figure 6.6(a). In the first phase-matching region, the parametric bandwidth is large for the GV-matched solutions (left extremity). As the frequency-shift decreases, the parametric bandwidth shows an initial decrease. However, as the frequency-shift is further decreased, the parametric bandwidth increases again, as is expected for normal dispersion regime pumping (refer to Chapter 2.3.2) [14]. The parametric bandwidth for the second phase-matching region is in stark contrast to that of the first, with values being up to three orders of magnitude smaller. These small bandwidths are in fact typical for large frequency-shifts and clearly illustrate the improvements possible with GV-matched phase-matching through the use of GeO_2-doped PCFs. Properly designed, these manage to maintain the large parametric bandwidths associated with FWM at small frequency-shifts, even at values in excess of 120 THz (refer to Figures 6.4 and 6.5). The largest GV-matched frequency-shift in Figure 6.6, of 105 THz, corresponds to anti-Stokes and Stokes wavelengths of 784 nm and 1736 nm, respectively.

The result of Figure 6.6 is crude in the sense that it assumes any variation in the air-hole diameter to be equal to the variation in the doping-diameter. Nevertheless, it gives an estimate of the degree of absolute manufacturing precision that would be

required for phase-matching within the first region, as outlined above. For the chosen fibre (d_c/d_h=1, 35% (mol)), the tolerance relative to the point Λ=1.6175 (0.4%) and d_h=0.9566 (0.7%) is ±0.4% in Λ and ±0.7% in d_h. These values do not account for a departure from the intended GeO_2-doping concentration or profile, which would certainly affect the behaviour (see Figure 6.5 and Table 6.1). It is furthermore important to note that the tolerance given above is very large compared to that required to approach exact GV-matched phase-matching.

The dependence on the absolute manufacturing precision can to some degree be reduced, particularly if ytterbium-doped pump sources are used. This stems from the large emission bandwidth of ytterbium-doped lasers and their subsequent suitability as tunable sources [15]. To illustrate the benefit of a tunable pump wavelength, Figure 6.7 shows how the phase mismatch of points A and B on Figure 6.6(a) are influenced when the pump wavelength is detuned from 1080 nm. At 1080 nm, neither A nor B result in any phase-matched solutions within the wavelength region of interest. However, by sweeping the pump wavelength from 1080 – 1086 nm (point A), or from 1080 – 1065 nm (point B), points A and B can be phase-matched over a wide range of frequency-shifts, including a characteristic value for which the group velocities are matched.

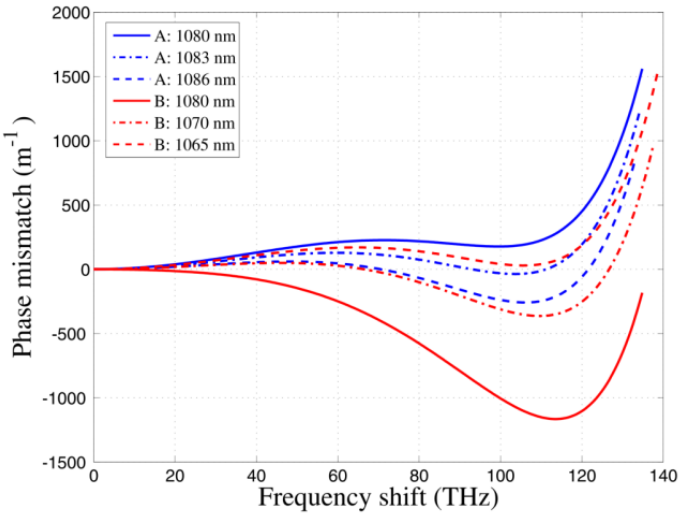

Figure 6.7: Phase mismatch as a function of frequency-shift for several pump wavelength values, for points A and B on Figure 6.6(a).

Figure 6.7 therefore illustrates that, by varying the pump wavelength, either the phase-matched frequency-shift (and indeed the Stokes and anti-stokes frequencies) or the

parametric bandwidth can, to some degree, be tailored (but not independently). Since the pump wavelengths in Figure 6.7 (1064 – 1086 nm) easily fall within the tuning range of a typical Yb-doped fibre source [15], wavelength tuning is ideally placed to alleviate the difficulty of attempts to enhance the parametric bandwidth through dispersion engineering.

The results in Figures 6.6(a) and (b) can now also be used to estimate the required relative manufacturing tolerance. Here, we are interested in the degree of structural variation, between different points along the length of the fibre, that can be tolerated before the difference in phase-matched frequency-shift exceeds that value for which the associated parametric bandwidths no longer overlap. This quantity will ultimately determine whether the approach of GV-matched phase-matching translates into a reduced sensitivity to longitudinal variations, relative to that associated with phase-matching in a conventional PCF. To enable a comparison, Figure 6.8 shows calculated results for the single-material silica PCF treated in Section 6.2 (refer to Figures 6.2 and 6.3). Structural parameters are displayed as a percentage change relative to the origin, where Λ=5.6 µm and d_h/Λ=0.49. As before, empty space indicates the absence of phase-matched frequency-shift values within the range 700 – 2100 nm, for a pump wavelength of 1080 nm. Also note that the parametric bandwidth in Figure 6.8(b) is normalised to the corresponding values in Figure 6.6(b).

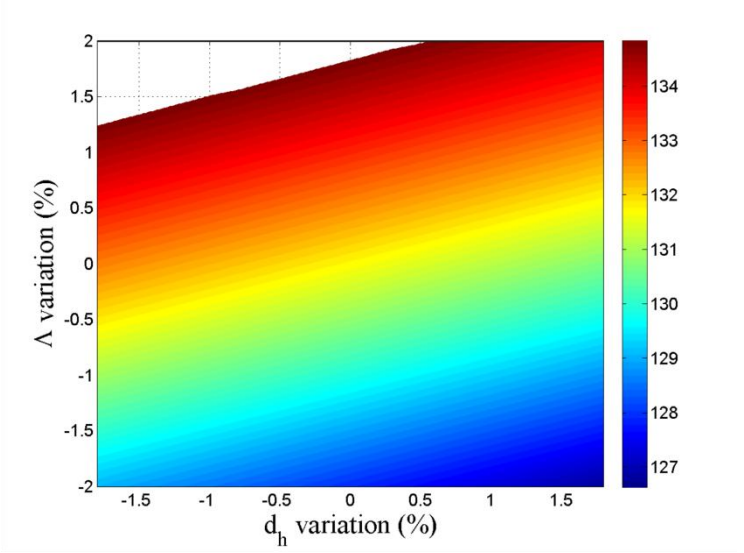

(a)

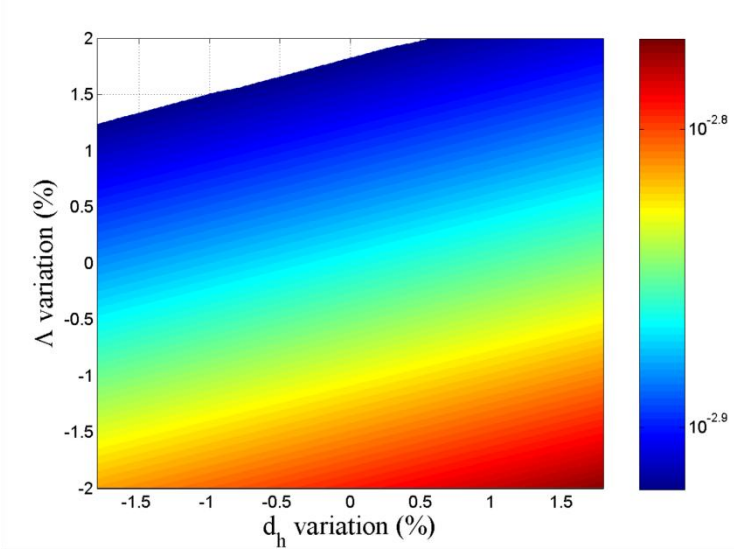

(b)

Figure 6.8: Phase-matching analysis of the silica PCF in Section 6.2, about Λ=5.6 µm and d_h/Λ=0.49. (a) Phase-matched frequency-shift in units of THz (λ_p=1080 nm) as a function of percentage variation in Λ and d_h, with respect to the reference values. (b) Corresponding bandwidth for the phase-matched frequency-shift values in (a). Note that, for comparative purposes, the bandwidth values are normalised to the corresponding values in Figure 6.6(b).

In contrast to the results of Figure 6.6, the silica PCF only yields a single phase-matched frequency-shift, for a given parameter combination, over the range of interest (i.e. a single phase-matching region). The phase-matched frequency-shift (Figure 6.8(a)) decreases monotonically for a reduction in Λ, or an increase in d_h, whilst the parametric gain bandwidth (Figure 6.8(b)) increases for reduced values of the frequency-shift (refer to Chapter 2.3.2). The range of phase-matched frequency-shift values and parametric gain bandwidth values in Figures 6.6 and 6.8 are significantly different. This is illustrated in the comparison of Table 6.2, where we consider the change in the phase-matched frequency-shift (Ω_0) and parametric bandwidth ($\Delta\Omega$) for a 0.3% variation in d_h, with respect to the origin in Figures 6.6 and 6.8. Here, the parametric bandwidth values were calculated from equation 6.1 by assuming a fibre length and pump power of 5 m and 1 kW, respectively (refer to Section 6.2). The range of 0.3% is convenient since the corresponding variation in the normalized parametric bandwidth of Figure 6.6(b) can be approximated as linear. This allows for straightforward evaluation of the derivative of the phase-matched frequency-shift and parametric bandwidth relative to the percentage variation in d_h. From Table 6.2, these values follow as -116.7 THz/% ($\frac{d\Omega_0}{dd_h}$) and -190.1 THz/% ($\frac{d\Delta\Omega}{dd_h}$) for *PCF 3* in Figure 6.6, as well as 666.7 GHz/% and 1.3 GHz/% for the

corresponding values of the silica PCF in Figure 6.8. The relative variation in d_h, that can be tolerated prior to a breakdown in phase-matching, can then be calculated by using $\Omega_0(0) - \Omega_0(d_h) = \Delta\Omega(d_h)$, and equations 6.4 and 6.5:

$$\Omega_0(0) - \Omega_0(d_h) = -\frac{\mathrm{d}\Omega_0}{\mathrm{d}d_h} d_h \tag{6.4}$$

$$\Delta\Omega(d_h) = \Delta\Omega(0) + \frac{\mathrm{d}\Delta\Omega}{\mathrm{d}d_h} d_h \tag{6.5}$$

For the fibres of Figures 6.6 and 6.8, these calculated values are 0.19% and 0.125%, respectively.

	Origin (d_h = 0)						**d_h = +0.3%**	
	Λ (μm)	d_h/Λ	d_c/d_h	GeO_2 (mol%)	Ω_0 (THz)	$\Delta\Omega$ (THz)	Ω_0 (THz)	$\Delta\Omega$ (THz)
Figure 6.6	1.6175	0.5873	1	35	105	58.20	70	1.16
Figure 6.8	5.6	0.49			131.7	0.0830	131.5	0.0834

Table 6.2: Values for the phase-matched frequency-shift (Ω_0) and parametric gain bandwidth ($\Delta\Omega$) before and after a 0.3% variation in the d_h structural parameter, relative to the origin in Figures 6.6 and 6.8, respectively.

This analysis therefore finds that group velocity matching, as an approach to optimise the parametric gain bandwidth, leads to a very slight reduction in the PCF's sensitivity to relative structural variations. It is however important to note that this conclusion is based on a comparison of two specific examples. The analysis furthermore only considers the fluctuations within a certain subset of the full parameter range contained in Figures 6.6 and 6.8. For a different parameter range, or for different PCFs, the conclusion may therefore differ significantly.

6.4 Summary

In this chapter GeO_2-doped PCF was investigated in terms of its suitability to provide large frequency-shift phase-matching at Stokes and anti-Stokes wavelengths that are also group velocity matched, for the purpose of extending the parametric bandwidth. Although phase-matching solutions of this kind have been reported for all-silica PCF, their applicability were limited to pump wavelengths below 1 μm. This therefore

excluded ytterbium-doped fibre pump sources, which has the potential to complement fibre parametric devices in ways not afforded by alternative pump wavelengths.

GeO_2-doped PCF was found to be suitable as a means of extending group velocity-matched phase-matching to pump wavelengths in excess of 1 μm. Using a pump wavelength of 1080 nm, calculations were carried out to examine the influence of the PCF structural parameters and the GeO_2-doping concentration on the frequency-shift for which GV-matched phase-matching is obtained. Here it was found that several combinations of the design parameters can be used to obtain a solution at a desired frequency-shift.

The phase-matched frequency-shift and associated parametric bandwidth, were next calculated over a range of values for Λ and d_h (and subsequently, d_c), for a chosen GeO_2-doped PCF design. In addition to illustrating the unique combination of a large frequency-shift and a large parametric bandwidth that results from group velocity matching of the FWM Stokes and anti-Stokes, this study enabled an estimation of the required absolute manufacturing precision. These values, found to be ±0.7% in d_h and ±0.4% in Λ, are specific to the considered parameter combination and can most likely be optimised by considering alternative combinations. Since the analysis makes certain simplifying assumptions, the actual values are likely considerably smaller than the calculated ones. However, our calculations show that this can, to some degree, be compensated through the use of a tunable pump source, which can be used to recover a GV-matched phase-matching solution, albeit not at the exact design frequency-shift.

Finally, the results from our preceding analysis were also used to estimate the relative structural variations that can be tolerated before the difference in phase-matched frequency-shift exceeds the parametric bandwidth. For comparison, this analysis was also performed for a silica PCF employed in an earlier chapter. The resulting relative tolerance values were found to be 0.19% and 0.125% for the GeO_2-doped PCF and silica PCF, respectively. These values are only approximate, but they do offer some insight. Whilst other fibre designs may yield better results, it currently appears as though the GV-matched FWM process will remain very sensitive to longitudinal variations in the fibre structure. It would nevertheless be interesting to compare various different GeO_2-doped PCF designs in terms of their relative manufacturing tolerances. However, due to time constraints, this exercise falls outside of the scope of this thesis.

6.5 References

[1] W.J. Wadsworth, N. Joly, J.C. Knight, T.A. Birks, F. Biancalana and P .St. J. Russell, "Supercontinuum and four-wave mixing with Q-switched pulses in endlessly single-mode photonic crystal fibers," *Opt. Express*, vol. 12, no. 2, pp. 299-309 (2004).

[2] D. Nodop, C. Jauregui, D. Schimpf, J. Limpert and A. Tünnermann, "Efficient high-power generation of visible and mid-infrared light by degenerate four-wave mixing in a large-mode-area photonic-crystal fiber," *Opt. Lett.*, vol. 34, no. 22, pp. 3499-3501 (2009).

[3] L. Lavoute, J.C. Knight, P. Dupriez and W.J. Wadsworth, "High power red and near-IR generation using four wave mixing in all integrated fiber laser systems," *Opt. Express*, vol. 18, no. 15, pp. 16193-16205 (2010).

[4] J. Lægsgaard, "Phase-matching conditions for single-pump parametric amplification in photonic crystal fibers," *J. Opt. A: Pure Appl. Opt.*, vol. 9, pp. 1105-1112 (2007).

[5] J. Lægsgaard, P.J. Roberts and M. Bache, "Tailoring the dispersion properties of photonic crystal fibers," *Opt. Quant. Electron.*, vol. 39, pp. 995-1008 (2007).

[6] R.H. Stolen and J.E. Bjorkholm, "Parametric amplification and frequency conversion in optical fibers," *IEEE J. of Quantum Electron.*, vol. QE-18, no. 7, pp. 1062-1072 (1982).

[7] E. Myslivets, C. Lundström, S. Moro, A.O.J. Wiberg, C.-S. Bres, N. Alic, P.A. Andrekson and S. Radic, "Dispersion fluctuation equalization nonlinear fibers by spatially controlled tension," *OFC 2010*, paper OTuA5.

[8] Y.P. Yatsenko and A.D. Pryamikov, "Parametric frequency conversion in photonic crystal fibres with germanosilicate core," *J. Opt. A: Pure Appl. Opt.*, vol. 9, pp. 716-722 (2007).

[9] Y.P. Yatsenko, A.F. Kosolapov, A.E. Levchenko, S.L. Semjonov and E.M. Dianov, "Broadband wavelength conversion in a germanosilicate-core photonic crystal fiber," *Opt. Lett.*, vol. 34, no. 17, pp. 2581-2583 (2009).

[10] K. Schuster, J. Kobelke, Y. Wang, A. Schwuchow, J. Kirchhof, H. Bartelt and S. Pissadakis, "Highly photosensitive PCFs with extremely germanium doped core," *Emerging Trends and Novel Materials in Photonics, International Commission for Optics Topical Meeting 2010*, CP1288.

[11] A. Labruyère, P. Leproux, V. Couderc, V. Tombelaine, J. Kobelke, K. Schuster, H. Bartelt, S. Hilaire, G. Huss and G. Mélin, "Structured-core GeO_2-doped photonic-crystal fibers for parametric and supercontinuum generation," *IEEE Photon. Technol. Lett.*, vol. 22, no. 16, pp. 1259-1261 (2010).

[12] J.W. Fleming, "Dispersion in GeO_2-SiO_2 glasses," *Appl. Opt.*, vol. 23, no. 24, pp. 4486-4493 (1984).

[13] A. Boskovic, S.V. Chernikov, J.R. Taylor, L. Gruner-Nielsen and O.A. Levring, "Direct continuous-wave measurement of n_2 in various types of telecommunication fiber at 1.55 μm," *Opt. Lett.*, vol. 21, no. 24, pp. 1966-1968 (1996).

[14] J.D. Harvey, R. Leonhardt, S. Coen, G.K.L. Wong, J.C. Knight, W.J. Wadsworth and P. St. J. Russell, "Scalar modulation instability in the normal dispersion regime by use of a photonic crystal fiber," *Opt. Lett.*, vol. 28, no. 22, pp. 2225-2227 (2003).

[15] J. Nilsson, W.A. Clarkson, R. Selvas, J.K. Sahu, P.W. Turner, S.-U. Alam and A.B. Grudinin, "High-power wavelength-tunable cladding-pumped rare-earth-doped silica fiber lasers," *Opt. Fiber Technol.*, vol. 10, pp. 5-30 (2004).

Chapter 7

Conclusions

7.1 Summary

The purpose of this thesis was to investigate methods whereby practical and efficient large frequency-shift fibre FWM can be realised at YDFA pump wavelengths. The use of an ytterbium fibre gain-medium was motivated by its flexibility as a high-power source, as well as its potential to enable fibre FWM up-conversion towards visible wavelengths. The prospect of large frequency-shift up-conversion, from a pump source that allows for all-fibre integration, may offer a viable alternative to bulk laser sources, which currently serve the spectral region of interest. In contrast to the high pump power approach followed in some of the previous investigations on this topic, this thesis considered the use of nanosecond pulses and modest pump peak powers (1 kW). This approach necessitated the use of longer nonlinear converter fibres, which in turn created the requirement for a highly uniform nonlinear converter. As such, this thesis considered the use of precision engineered conventional telecommunication fibres as well as microstructured fibres (i.e. photonic crystal fibres).

The use of conventional non-microstructured fibre as a route to phase-matched FWM was considered in Chapter 4. Here, a 1080 nm all-fibre MOPA, based on polarization-maintaining (PM) double-cladding ytterbium-doped fibre technology (refer to Chapter 3), was employed as pump source for a Fujikura PM nonlinear converter in an OPA configuration. This fibre and the phase-matching approach of using different polarization modes was earlier identified as the most suitable option for large

frequency-shift FWM, through numerical evaluation of the dispersion and phase-matching characteristics of a number of fibres. Although the Stokes-seeded OPA generated an anti-Stokes wave in excellent agreement with the calculated frequency-shift of 78.5 THz, the pump-to-anti-Stokes conversion efficiency was orders of magnitude below the calculated value for a 21 m length of Fujikura fibre. The conversion efficiency was however roughly consistent with that expected from a nonlinear converter length of 2 m, which implied piece-wise coherence for the conversion over a 21 m fibre length. This hypothesis was corroborated by the findings from experiments on a 2 m Fujikura sample, where the reduction in fibre length lead to a significant decrease in the anti-Stokes bandwidth, but only a 5 dB reduction in the peak spectral intensity. These observations were tentatively attributed to the combination of a small parametric bandwidth and variations of the dispersion (and phase-matching) along the fibre. In a bid to increase the parametric bandwidth to reduce the influence of longitudinal inhomogeneity, experiments in the OPG configuration explored the use of alternative high-power pump sources. Although these experiments were unsuccessful in generating significant anti-Stokes power, they did serve as confirmation of the strict requirements that large frequency-shift FWM places on the pump source, particularly in terms of linewidth, pulse-shape and temporal stability. Chapter 4 therefore concluded that phase-matching, through the use of polarization modes in the Fujikura PM fibre, did not offer a viable solution to large frequency-shift FWM at the pump powers available from the all-fibre MOPA at that time.

In Chapter 5, the use of higher-order dispersion phase-matching in a photonic crystal fibre (PCF) was investigated as a source for spectrally distant wavelength conversion. Experiments based on a single pass through the un-seeded nonlinear converter lead to the generation of an anti-Stokes (AS) at 715 nm, in good agreement to calculated results. The pump-to-anti-Stokes conversion efficiency was very low, but the result was useful in highlighting the requirement for appropriate spectral discrimination as well as seeding to reduce the influence of competing nonlinear processes. Following the construction of a synchronously pumped fibre OPO, pump-to-anti-Stokes in-fibre average power conversion efficiencies as high as 4% was demonstrated. Although output spectra still showed signs of supercontinuum generation, cascaded SRS, generated by the FWM AS, provided encouragement.

Subsequent experiments focussed on an all-fibre pump-OPO system and a pump MOPA with superior temporal stability. This system was employed to study the dependence of the OPO conversion efficiency on the out-coupling ratio of the cavity, the length of the nonlinear converter as well as the pump pulse duration. It was found that a higher out-coupling ratio is important for the suppression of so-called secondary nonlinear effects, pumped by the FWM AS. However, drawbacks included higher cavity losses, and subsequently, higher pump threshold power requirements. Experiments on OPOs using various nonlinear converter lengths demonstrated similar threshold pump powers for low values of the out-coupling ratio. In contrast, high out-coupling ratios lead to threshold values that were inversely proportional to the PCF length. The latter case is consistent with the expectation of a constant threshold-power-fibre-length product, but is somewhat surprising considering that the system is subject to pulse walk-off and longitudinal inhomogeneities. A tentative conclusion was that the longitudinal inhomogeneity in the PCF-LMA8 is characterised by a high spatial frequency. It was furthermore concluded that the OPO shows an increased sensitivity to competing nonlinearities as the cavity loss increases. The performance of the OPO, employing different lengths of PCF, was also evaluated for different pump pulse widths. The highest pump-to-anti-Stokes conversion efficiency of 10.3%, over a frequency separation of 142 THz, was found for pump pulses of 800 ps duration and a PCF length of 18 m. To the best of our knowledge, this result constitutes a record for all-fibre OPOs operating at frequency-shifts of this magnitude. In contrast, pump pulse durations of 500 ps and >1 ns gave their best conversion efficiencies for a PCF length of 35 m. Whilst the pump-to-anti-Stokes average power conversion efficiency was found to depend on the walk-off length between the pump and Stokes waves, for a specific pump pulse duration, the case of 500 ps pulses proved to be the exception. The exact reason for this remains unknown. However, it is likely due to the fact that the short pulse has a higher pump peak power, in combination with partially coherent build-up in segments of the full PCF length.

Experiments using the all-fibre pump-OPO setup highlighted the importance of some mechanism for intra-cavity filtering. As such, it was discovered that the delay line, used for the purpose of synchronous pumping, can act as a temporal filter through the process of dispersion. Since the delay line also leads to FWM anti-Stokes-generated SRS for the case of a sufficiently low out-coupling ratio, its length represents a trade-

off. Measurements using a free-space spectral filter suggest that it can be used as an alternative to temporal filtering, should a short delay line be preferred. High insertion loss values, however prevented this from being a valid alternative in our experiments.

The optical parametric devices investigated in Chapters 4 and 5 all suffered from longitudinal variations, to some extent. To reduce the sensitivity of the phase-matching process to these variations, it is common to increase the parametric bandwidth. This typically involves the use of higher pump powers and shorter nonlinear converters. However, as a higher pump power is in conflict with the objectives of this thesis, alternative methods of extending the parametric bandwidth had to be explored. To this end, Chapter 6 investigated GeO_2-doped PCF in terms of its ability to provide large frequency-shift phase-matching at Stokes and anti-Stokes wavelengths that are also group velocity matched. Although phase-matching solutions of this kind have been reported for all-silica PCF, their applicability were limited to pump wavelengths below 1 μm.

Using a numerical approach, GeO_2-doped PCF was found to be suitable as a means of extending group velocity-matched phase-matching to pump wavelengths in excess of 1 μm. Calculations were carried out to examine the influence of the PCF structural parameters and the GeO_2-doping concentration on the frequency-shift for which GV-matched phase-matching is obtained, assuming a 1080 nm pump wavelength. Here it was found that several combinations of the design parameters can be used to obtain a solution at a desired frequency-shift.

The phase-matched frequency-shift and associated parametric bandwidth, were next calculated over a range of values for Λ and d_h (and subsequently, d_c), for a chosen GeO_2-doped PCF design. In addition to illustrating the unique combination of a large frequency-shift and a large parametric bandwidth that results from group velocity matching of the FWM Stokes and anti-Stokes, this study enabled an estimation of the required absolute manufacturing precision. These values, found to be ±0.7% in d_h and ±0.4% in Λ, are specific to the considered parameter combination and can most likely be optimised by considering alternative combinations. Since the analysis make certain simplifying assumptions, the actual values are likely considerably smaller than the calculated ones. However, our calculations show that this can, to some degree, be

compensated through the use of a tunable pump source, which can be used to recover a GV-matched phase-matching solution, albeit not at the exact design frequency-shift.

Finally, the results from our preceding analysis were also used to estimate the relative structural variations that can be tolerated before the difference in phase-matched frequency-shift exceeds the parametric bandwidth. For comparison, this analysis was also performed for a silica PCF employed in an earlier chapter. The resulting relative tolerance values were found to be 0.19% and 0.125% for the GeO_2-doped PCF and silica PCF, respectively. These values are only approximate, but they do offer some insight. Whilst other fibre designs may yield better results, it currently appears as though the GV-matched FWM process will remain very sensitive to longitudinal variations in the fibre structure.

7.2 Future Work

The past decade has been productive in terms of research on fibre optical parametric amplifiers and oscillators, constructed from DSF or PCF. Particularly for large frequency-shift FWM, excellent conversion efficiencies have been achieved in PCF-based OPAs, using a variety of pump sources and phase-matching techniques. Similarly, all-fibre OPOs relying on DSF, and pump wavelengths in the region of 1550 nm, have demonstrated excellent wavelength tuneability and watt-level average output powers, albeit at relatively small frequency-shifts. It is however notable that little work has thus far been done on large frequency-shift OPOs at pump wavelengths in the 1 µm spectral region. This is likely a result of the success that single-pass devices have been enjoying. However, as these devices typically employ high peak-power pump sources, they tend to rely on hybrid free-space configurations, which limit their potential. The prospect of an efficient all-fibre OPO system holds several benefits of practical interest. In addition, the physics involved in an all-fibre pump-OPO device is significantly more interesting due to the complexities introduced by the interplay of dispersion, nonlinearity, cavity dynamics and phase-matching (which links to manufacturing precision). The combination of these effects is difficult to explain using available literature and requires a structured analysis of the various inter-dependencies. The work presented in the latter half of this thesis explored these inter-dependencies, but a significant amount of work is still required.

The influence of other unwanted nonlinear effects on the OPO gain is one example of an effect that should be studied more closely. SRS is perhaps the most important of these and has already been shown to have an intricate dependence on dispersion inside the cavity. A systematic approach using different nonlinear converter lengths and delay fibre lengths, at constant pump peak powers and pump pulse widths, should be very interesting. The influence of polarization is a related issue that requires particular attention in systems relying on non-PM fibres. This effect has been studied in single-pass fibre optical parametric devices, where it was found that the severity of polarization-related gain fluctuations scale with frequency-shift. A study on these effects in an oscillator with the added complexity of competing nonlinearities will be important for a detailed understanding of fibre OPOs.

It would furthermore be interesting to experimentally characterise the influence of longitudinal inhomogeneities on the OPO gain at different frequency-shifts and pump powers. Of particular interest is the role of the parametric gain bandwidth in mitigating the limitation imposed by these variations. This ties into an investigation on possible ways in which the OPO's sensitivity to longitudinal variations can be improved. One approach, explored in this thesis, focuses on doing this by expanding the parametric bandwidth through customization of the fibre dispersion. Although preliminary findings indicated that the implementation of this technique will be difficult, alternative designs may well exist and should be explored. The approach simultaneously provides an expanded pump-acceptance bandwidth, which may allow for greater freedom in the choice of pump source characteristics.

Finally, it is worth noting that the OPO explored in this thesis used one of several possible configurations, each of which will have their own trade-offs in terms of complexity versus flexibility. The combinations on offer from different oscillator arrangements (e.g. linear cavity) and different mechanisms for phase-matching should allow for an interesting comparison.

Publications

- **G.J. Van der Westhuizen** and J. Nilsson, "Fiber optical parametric oscillator for large frequency-shift wavelength conversion," *IEEE J. Quantum Electon.*, vol. 47, no. 11, pp. 1396-1403 (2011).

- **G.J. Van der Westhuizen** and J. Nilsson, "All-fiber optical parametric oscillator, pumped by an all-fiber Yb-based MOPA," *Conference on Lasers and Electro-Optics (CLEO)*, Baltimore (2011).

- **G.J. Van der Westhuizen** and J. Nilsson, "All-fibre OPO system for visible wavelengths," *International Quantum Electronics Conference (IQEC) and Conference on Lasers and Electro-Optics (CLEO) Pacific Rim*, Sydney (2011).

- Y. Jeong, C.A. Codemard, J. Ji, L.A. Vazquez-Zuniga, **G.J. Van der Westhuizen**, S. Yoo, A.J. Boyland, M.N. Petrovich, F. Poletti, G.M. Ponzo, J.K. Sahu, J. Nilsson, D.J. Richardson and D.N. Payne, "Novel fibre technology for high-power lasers," *Asia Communications and Photonics Conference and Exhibition (ACP)*, Shanghai (2010).

- Y. Jeong, C.A. Codemard, J. Ji, L.A. Vazquez-Zuniga, **G.J. Van der Westhuizen**, S. Yoo, A.J. Boyland, M.N. Petrovich, F. Poletti, J.K. Sahu, J. Nilsson, D.J. Richardson and D.N. Payne, "Recent changes in high power optical fibres," *in Proc. of ICOOPMA*, Budapest (2010).

- J. Nilsson, Y. Jeong, C.A. Codemard, C. Farrell, J. Ji, M.S.Z. Abidin, **G.J. Van der Westhuizen**, S. Yoo and J.K. Sahu, "High power fibre lasers: exploitation of unique properties," *Conference on Lasers and Electro-Optics Europe & 11th European Quantum Electronics Conference (CLEO/EQEC)*, Munich (2009).